

**DENSITY FLUCTUATION AND CORRELATION STUDY
OF MULTIPARTICLE PRODUCTION IN $^{28}\text{Si-Ag/Br}$
INTERACTION AT 14.5A GeV**

**A thesis submitted to the University of North Bengal
for the award of the degree of Doctor of Philosophy
in Physics**

BY

Provash Mali

SUPERVISOR

Prof. Amitabha Mukhopadhyay


**Department of Physics
University of North Bengal**

January 2016

DECLARATION

I declare that the thesis entitled, DENSITY FLUCTUATION AND CORRELATION STUDY OF MULTIPARTICLE PRODUCTION IN $^{28}\text{Si-Ag/Br}$ INTERACTION AT 14.5A GeV, has been prepared by me under the guidance of Dr. A. Mukhopadhyay, Professor of Physics, University of North Bengal. No part of this thesis has formed the basis of any previously awarded degree or fellowship.

Date: 05.02.2016


Provash Mallik

Department of Physics
University of North Bengal
Siliguri 734 013, Darjeeling, India

DEPARTMENT OF PHYSICS
UNIVERSITY OF NORTH BENGAL

P.O. North Bengal University, Siliguri, Darjeeling, West Bengal—734013, India

Website: www.nbu.ac.in



Phone: +91-353-2776338

Fax: +91-353-2699001

ENLIGHTENMENT TO PERFECTION

CERTIFICATE

I certify that Mr. Provash Mali has prepared the thesis entitled, *Density Fluctuation and Correlation Study of Multiparticle Production in $^{28}\text{Si-Ag/Br}$ Interaction at 14.5A GeV*, under my supervision for the award of the Ph.D. degree in Physics of the University of North Bengal. Mr. Mali has carried out this work at the Department of Physics of the University of North Bengal, and no part of this work has ever been used for the award of any other degree.

Date: 05 February 2016

Amitabha Mukhopadhyay

Amitabha Mukhopadhyay

Department of Physics
University of North Bengal
Siliguri 734 013, Darjeeling, India

To the memory of

my Dmma

Preface

One of the major challenges of present day fundamental research is to connect the science of ‘small’ with the science of ‘Big’. While the standard model of elementary particles based on the principles of local gauge invariance provides us with a solid foundation of the former, the ‘Big bang’ cosmology based on the principles of general theory of relativity can to a large extent explain the latter. The approaches are quite different and could not so far be brought under a common theoretical framework. It is generally believed that the entire universe, i.e. the spacetime, all matter and radiation came into being through the fragmentation of a very hot and dense primordial ‘fireball’ created in the Big bang. It is necessary to understand how the universe evolved during those initial moments of its birth. As the baby universe expanded and cooled, it underwent through a number of symmetry breaking processes like, the electroweak symmetry, the color SU(3) gauge symmetry, the chiral symmetry, and the matter–antimatter symmetry. From the time of electroweak decoupling (some pico-seconds) to hadronization (about 10 μ sec.) after the Big bang, the universe is believed to be filled up with a color conducting extended state comprising of weakly coupled quarks and gluons, a state popularly known as the quark-gluon plasma (QGP), and a state that can be characterized by using perturbative quantum chromodynamics (QCD). The universe that we live in today is overwhelmingly dominated by matter, which resulted from a very small aberration that took place during those early moments in the form of violation of CP symmetry. As our understanding of the fundamental laws of nature improves, and as newer experimental evidences allow us to modify and/or fine tune the theoretical concepts, we become more capable of looking back into those early evolutionary stages of the universe and unravel its mysteries with greater precision.

Soon after ideas like *asymptotic freedom* and *color confinement* were introduced, it was realized that the QCD vacuum can be heated to such high temperatures that some of the symmetries broken during the evolution of the primordial fireball can be restored, and a QGP-like state can be created even in a terrestrial laboratory when two heavy nuclei collide with each other at high energies, called the ‘little bang’. Any such terrestrially created fireball will however not only be much shorter lived ($t \sim 10^{-22}$ sec.) and much smaller in dimension ($r \sim 10$ fm.), but it would also be of much less density and less temperature than the primordial one. It was primarily due to the works of R. Hagedron we later realized that a transition from the QGP to color neutral hadrons can be extended to much lower temperatures ($T \sim$ rest energy of a π -meson), that is far away from the asymptotic freedom and that needs to be treated by invoking non-perturbative QCD. As

two nuclei impinge upon each other with high collision energies (say $\sqrt{s} \sim \text{TeV}$), anti-quarks and quarks will be produced with equal abundance, and the valence quarks present in the incoming nuclei will constitute only a small percentage of the total number of particles present in the nuclear/partonic fireball. Under such circumstances we expect an equilibrated state of high temperature and low baryo-chemical potential (μ_B). On the other hand at lower collision energies (say $\sqrt{s} \sim 10 \text{ GeV}$) the number of valence quarks present in the colliding nuclei will comprise a significant fraction of the total number of new quarks/anti-quarks created, and the intervening state, even though a color conducting one, should correspond to a lower temperature and higher value of μ_B . Such a state may prevail in the core of very compact astrophysical objects like neutron stars.

Over the last forty–fifty years an enormous amount of theoretical and experimental research have been undertaken in the field of high-energy heavy-ion interaction and QGP physics. Experiments have been performed by using various target-projectile combinations over a widely varying collision energies. New experimental facilities are still being created so that we get a complete ($\mu_B - T$) scan of the matter present in the fireball created in the little bang, or equivalently study the entire QCD phase diagram. On the theoretical side several signals that can identify the creation of a QGP-like state are suggested. Analysis of experimental data shows that perhaps the goal to create QGP in a terrestrial laboratory has already been accomplished. However, a complete characterization of such a short lived state extended only over an extremely minuscule of volume, is not an easy task. One has to understand that a high-energy heavy-ion interaction is a very complex dynamical process, where on an average a large number of background particles are produced, and an appropriate signal has to be filtered out only after eliminating a large amount of noise. Many of the theoretical predictions are based on lattice QCD (LQCD) calculations, which works well at high T and $\mu_B \approx 0$. At non-zero μ_B , LQCD has its own problems, a satisfactory solution for which is not yet found. Overall high-energy heavy-ion interaction is an exciting area of physics that needs command over several other areas like, nuclear physics, particle physics, astroparticle physics, theory of relativity, thermodynamics, statistical mechanics, relativistic fluid dynamics etc..

In a high-energy nucleus-nucleus (AB) collision a large number of new particles are produced, most of them are pions, and the phenomenon is known as multiparticle production. Till date the physics of multiparticle production is also not very comprehensively understood. Because of its implicit complexities, the problem needs to be probed from all possible angles. A lot of information related to the dynamics of multiparticle production can be extracted by studying the global properties of high-energy interaction like multiplicity distribution, rapidity distribution, transverse momentum distribution etc., or by studying the local properties like fluctuations in number densities. In the year 1983 an important observation was made

by the JACEE collaboration, where unnaturally large fluctuations in produced particle rapidity distributions were found in some cosmic-ray events, that cannot simply be an artifact of statistical coincidence. It has also been shown that the dynamical components of these unusually large particle density values, irrespective of their exact analytical form, abide by a power-law type of scale invariance with decreasing phase space resolution size. This observation lead to a paradigm shift in multiparticle research from studying global properties to studying local variables that are confined within limited regions of phase space. Various speculative proposals, conventional as well as exotic, have so far been put forward to explain this fluctuation phenomenon.

To characterize the particle density fluctuation and cluster formation we need to use suitable statistical tools. In this thesis we have used some of these methods and analyzed nuclear photo-emulsion data on the angular distribution of singly charged particles produced in a fixed target experiment on ^{28}Si -emulsion interaction at an incident energy of 14.5A GeV (Experiment No. E847 performed at the Alternating Gradient Synchrotron at the Brookhaven National Laboratory by the SUNY at Buffalo, USA, group). The experimental results are systematically compared with a Monte-Carlo model simulation based on Ultra-relativistic Quantum Molecular Dynamics (UrQMD). On a few occasions the ^{28}Si -Ag/Br results are also compared with ^{32}S -Ag/Br results at an incident energy of 200A GeV. The thesis starts with a brief introductory discussion on AB interaction at relativistic energy, where some qualitative description of the QGP state and the global scenario of past, present and future experimental facilities are reviewed. Some aspects of multiparticle data analysis techniques have been summarily outlined. In chapter two we briefly discuss the nuclear emulsion technique, the data collection process and the simulation method(s) adopted in the present investigation. The UrQMD model along with a charge reassignment algorithm that mimics the Bose-Einstein correlation as an after burner to the UrQMD output, have been outlined. Gross features of the data are also listed in this chapter. Based on the statistical techniques like intermittency, erraticity and multifractality, we present some results on different multiplicity moments and the scaling relations followed by them respectively, in chapter three, four and five. Each of these techniques deals with fluctuation study of particle densities in limited phase space intervals. In chapter six and seven we present our results, respectively on unusual azimuthal structure formation and wavelet analysis, where corresponding results of ^{32}S -Ag/Br interaction at 200A GeV are also incorporated. We have also performed a collective flow analysis of our ^{28}Si -Ag/Br data and compared them with those of ^{84}Kr -Ag/Br data at an incident energy of 1.52A GeV. However, to follow a convention of our university, in stead of discussing this work in a separate chapter, we have attached the corresponding photocopy of the published paper at the end. We conclude by making some critical observations on the major results of the entire investigation and have tried to identify some prospective areas of further study.

This thesis is based on my research efforts spanned over a period of last five years or so in the field of relativistic AB collision. In addition, at present I am also working on the multifractal characteristics of the time series data of different observables. So far I have eighteen (18) publications to my credit (as an author and/or a co-author), and nine (09) of them that constitutes the body of this thesis are listed below.

1. *Intermittency and erraticity of charged particles produced in $^{28}\text{Si-Ag/Br}$ interaction at $14.5A$ GeV* – P. Mali, A. Mukhopadhyay and G. Singh, *Can. J. Phys.* **89**, 949 (2011).
2. *Factorial correlator and short-range correlation of charged particles produced in $^{28}\text{Si-Ag/Br}$ interaction at $14.5A$ GeV* – P. Mali, A. Mukhopadhyay and G. Singh, *Phys. Scr.* **85**, 065202 (2012).
3. *Self-affine two-dimensional intermittency in $^{28}\text{Si-Ag/Br}$ interaction at $14.5A$ GeV* – P. Mali, A. Mukhopadhyay and G. Singh, *Acta. Phys. Pol.* **B 43**, 463 (2012).
4. *Multifractal analysis of charged particle distribution in $^{28}\text{Si-Ag/Br}$ interaction at $14.5A$ GeV* – P. Mali, A. Mukhopadhyay and G. Singh, *Fractals*, **20**, 13 (2012).
5. *Wavelet analysis of shower track distribution in high-energy nucleus-nucleus collisions* – P. Mali, S. Sarkar, A. Mukhopadhyay and G. Singh, *Adv. High Ener. Phys.*, **2013**, 759176 (2013).
6. *Azimuthal structure of charged particle emission in $^{28}\text{Si-Ag(Br)}$ interaction at $14.5A$ GeV and $^{32}\text{S-Ag(Br)}$ interaction at $200A$ GeV* – P. Mali, A. Mukhopadhyay and G. Singh, *Int. J. Mod. Phys.* **E 23(5)**, 1450027 (2014).
7. *Multifractal detrended fluctuation analysis of phase-space fluctuation in relativistic nuclear collisions* – P. Mali, S. Sarkar, S. Ghosh, A. Mukhopadhyay and G. Singh, *Physica A* **424**, 25 (2015).
8. *Multifractal detrended moving average analysis of particle density functions in relativistic nuclear collisions* – P. Mali, A. Mukhopadhyay and G. Singh, *Physica A* (in press, 2016) DOI: 10.1016/j.physa.2016.01.023
9. *Azimuthal correlation and collective behavior in nucleus-nucleus collisions* – P. Mali, A. Mukhopadhyay, S. Sarkar, G. Singh, *Phys. Atom. Nucl.* **78(2)**, 258 (2015).

Different chapters of the thesis is organized on the basis of the first eight (08) publications of the above list. However, as mentioned above, as per a norm of the University of North Bengal (UNB), which is to insert at least one reprint of the published papers, a photo-copy of the ninth publication is given at the end of the thesis. A full list of my publications is given in the list of publications section.

I would now like to take the opportunity to tie in some personal remarks. In the year 2006, I started my research career as a Junior Research Fellow at the Variable Energy Cyclotron Centre (VECC), Kolkata. At VECC I worked on low-energy experimental nuclear physics. Later in the year 2008 I moved on to join the Physics Department of UNB, and since the year 2010 I have been working on the physics analysis of experimental data on relativistic heavy-ion collision(s). The entire work presented here would have not been possible without the support, advice and encouragement that I have received from many persons during my research work. My primary thanks will go to my thesis supervisor, Professor Amitabha Mukhopadhyay of the Department of Physics, UNB for his guidance, encouragement and support. I deeply acknowledge the discussions I had with him right from my M.Sc. days, which kept me motivated all the time throughout my career. I would like to convey my sincere thanks to all my teachers and colleagues for their advice, support and words of encouragement. I express my deep sense of gratitude to Professor P. L. Jain of the State University of New York at Buffalo, USA for providing us with the emulsion plates and for allowing us to use the data collected thereof in the present investigation. My special thanks should also go to all my fellow friends of UNB. My friendship with Akhil, Souvik, Billo, Lal, Nairita, Rumisha and many others helped me to remain motivated during this challenging period. I wish to thank the supporting staff of the Department of Physics of UNB for their cooperation and help. I wish to take this opportunity also to thank my wonderful teachers at school and college who have inspired me at various stages of my life. I express my humble regards and sincere gratefulness to all my family members for their patience, love and continuous encouragement. Their inspiration and affection have helped me to overcome many hurdles in my life.

Raja Rammohunpur
January 2016

Provash Mali

Density Fluctuation and Correlation Study of Multiparticle Production in $^{28}\text{Si-Ag/Br}$ Interaction at 14.5A GeV

ABSTRACT

The present thesis is written on the basis of some results obtained from the physics analysis of local densities and cluster formation of singly charged particles produced in $^{28}\text{Si-Ag/Br}$ interaction at an incident energy in the laboratory system $E_{\text{lab}} = 14.5\text{A GeV}$. We systematically compare the experimental results with those obtained from a set of simulated data. A nuclear transport model namely the Ultra-relativistic Quantum Molecular Dynamics (UrQMD) is used for the simulation purpose. In addition a charge reassignment algorithm that mimics the Bose-Einstein Correlation (BEC) between identical mesons, considered to be primarily responsible for local cluster formation, has been implemented to the UrQMD output as an after burner. On a few occasions similar data on $^{32}\text{S-Ag/Br}$ interaction at $E_{\text{lab}} = 200\text{A GeV}$ have also been used for comparison purposes.

In **Chapter One** we review various issues related to high-energy nucleus-nucleus (AB) interaction, the main objective of which is to subject the nuclear matter to extreme thermodynamic conditions, so that one can create and characterize a color conducting extended QCD state like the Quark-gluon Plasma (QGP). The global scenario of high-energy heavy-ion experiments (past, present and future) is summarized. The kinematic variables required to describe various features of AB collision are introduced. Our present understanding of the spacetime evolution of AB collision are described. General features of QGP like its thermodynamics, its hydrodynamics, the QCD phase diagram, and the observables that are capable of diagnosing the formation of a QGP-like state are summarily outlined. Several Monte Carlo simulation methods commonly used to model high-energy AB collisions are briefly described. Finally, some statistical techniques employed to investigate multiparticle distribution are highlighted, with a special reference to the characterization of local fluctuations in particle number density. In **Chapter Two** the experimental aspects of the present investigation along with the simulation methods adopted are outlined. Salient features of nuclear photographic emulsion technique and the data collection process are summarily discussed. Gross features of the experimental and the simulated data samples on $^{28}\text{Si-Ag/Br}$ interaction at $E_{\text{lab}} = 14.5\text{A GeV}$ are presented.

Chapter Three presents an intermittency analysis on spatial fluctuations of the shower track density function in $^{28}\text{Si-Ag/Br}$ interaction at $E_{\text{lab}} = 14.5\text{A GeV}$. The experimental results are compared with the UrQMD simulation, with the UrQMD+BEC simulation, and on occasions with the results available from similar other experiments. Our analysis on the scaled factorial moments shows that small but significant nonstatistical components in the

fluctuations are present in the experimentally obtained particle densities that are self-similar in one-dimension (i.e., either in η or in φ), and self-affine in two-dimensions (η , φ). The factorial correlator, factorial cumulant and oscillatory moments are also determined. In most cases however, the UrQMD simulation fails to replicate the experiment, while inclusion of Bose-Einstein correlation in the UrQMD could recover only partially the difference between experiment and simulation. Event-by-event fluctuation study of factorial moments in the pseudorapidity space has been presented in **Chapter Four** in terms of erraticity moments for $^{28}\text{Si-Ag/Br}$ interaction at $E_{\text{lab}} = 14.5\text{A GeV}$. The erraticity parameters are extracted by analyzing the experimental data and two sets of simulated data. To check the noise level present in the experiment as well as in the simulations, we perform the same analysis for a set of purely random number generated events. The erraticity moments for all four data samples used in the analysis follow similar scaling-laws with phase space resolution size. Values of erraticity parameters suggest that the event-space fluctuation of factorial moments as predicted by the UrQMD and UrQMD+BEC models are closer to the experiment than their random number generated counterpart. The multifractal structure of the pseudorapidity density distribution of singly charged particles produced in $^{28}\text{Si-Ag/Br}$ interaction at $E_{\text{lab}} = 14.5\text{A GeV}$ is presented **Chapter Five**. Four different statistical techniques are used for this purpose. We observe that widely fluctuating density values that apparently lack any definite pattern, can be described in terms of a finite set of regularly behaving multifractal parameters. The analysis confirms the existence of a multifractal structure in the experimental as well as in the simulated data. We also observe that the differences between experiment and simulation, however large or small that may be, depend on the technique of analysis used.

In **Chapter Six** we look for unusual azimuthal structures of particle distribution within the framework of Cherenkov gluon emission and/or Mach shock wave formation in the nuclear/partonic medium. Shower track emission data of $^{28}\text{Si-Ag/Br}$ interaction at 14.5A GeV and $^{32}\text{S-Ag/Br}$ interaction at 200A GeV are used. Presence of unusual azimuthal structure in the data is established with respect to the model simulations. Our analysis confirms the presence of ‘jet-like’ structures in the central collisions for both interactions. As expected such structures are more pronounced in the ^{32}S data than in the ^{28}Si data. A continuous wavelet analysis is performed in **Chapter Seven** for pattern recognition of shower track emission data of $^{28}\text{Si-Ag/Br}$ interaction at 14.5A GeV and $^{32}\text{S-Ag/Br}$ interaction at 200A GeV . Making use of the event wise local maxima present in the scalograms, we try to identify the collective behavior in multiparticle production, if there is any. Statistically significant difference between the experiment and the simulation can be interpreted only in terms of some hitherto unknown dynamics of multiparticle production. We have also performed a collective flow analysis of our $^{28}\text{Si-Ag/Br}$ data and compared the results obtained thereof with those of $^{84}\text{Kr-Ag/Br}$ interaction at $E_{\text{lab}} = 1.52\text{A GeV}$. Evidences of collective flow are found

from both the data, of which $^{84}\text{Kr-Ag/Br}$ behave more systematically. However, to fulfill our university norm, in stead of making a separate chapter, a reprint of our published paper on this work has been attached at the end. The thesis concludes with a critical and analysis of our results that would help us better understand the underlying physics of multiparticle production at the collision energy range/colliding system(s) under consideration.

Contents

Declaration of Authorship	i
Certificate	ii
Preface	v
Abstract	x
List of Tables	xvi
List of Figures	xvii
1 Relativistic Nucleus-Nucleus Collision – an Overview	1
1.1 Introduction	1
1.2 Relativistic Kinematics	4
1.3 Nucleus-Nucleus Collision at High-energy	7
1.3.1 Space-time Evolution of AB Collision	13
1.3.2 Experimental Scenario	15
1.3.3 Experiment at the BNL-AGS	16
1.3.4 Experiment at the CERN-SPS	16
1.3.5 Experiment at the BNL-RHIC	17
1.3.6 Experiment at the CERN-LHC	20
1.3.7 The FAIR-CBM Experiment	21
1.4 Quark-Gluon Plasma	22
1.4.1 Fireball Thermodynamics	22
1.4.2 The Hydrodynamics	29
1.4.3 QCD Phase Diagram	32
1.4.4 Signals of QGP	34
1.5 Models of AB Interaction	39
1.5.1 RQMD and UrQMD	39
1.5.2 HIJING	40
1.5.3 AMPT	41
1.6 Multiparticle Production	42
1.6.1 Particle Density Fluctuation	42

2	Experiment and Simulation	52
2.1	Nuclear Emulsion	52
2.1.1	Particle Track Formation	53
2.1.2	Track Structure	54
2.2	The Microscopy	58
2.2.1	Scanning Emulsion Plates	60
2.3	Data Characteristics	61
2.4	Merits and Demerits of Emulsion Experiments	66
2.5	The Simulation	67
2.5.1	Modeling Bose-Einstein Correlation	71
2.5.2	Sampling $^{28}\text{Si-Ag/Br}$ Simulated Events	73
3	Intermittency in $^{28}\text{Si-Ag/Br}$ Interaction at 14.5A GeV	77
3.1	Introduction	77
3.2	Fluctuation of Particle Densities	79
3.2.1	Multiplicity Moments	80
3.2.2	Fluctuation in η -space	82
3.3	Scaled Factorial Moments	84
3.3.1	Intermittency in $1d$	85
3.3.2	Intermittency in $2d$	93
3.4	Factorial Correlators	99
3.4.1	Sum Rules	103
3.5	Factorial Cumulant Moments	104
3.6	Oscillatory Moment	106
3.7	Discussion	108
4	Erraticity in $^{28}\text{Si-Ag/Br}$ Interaction at 14.5A GeV	112
4.1	Introduction	112
4.2	Methodology and Results	114
4.3	Discussion	123
5	Multifractality in $^{28}\text{Si-Ag/Br}$ Interaction at 14.5A GeV	125
5.1	Introduction	125
5.2	Hwa's Moment	127
5.3	Takagi's Moment	133
5.4	Multifractal Detrended Fluctuation Analysis	137
5.4.1	Relation with Standard Multifractal Variables	139
5.4.2	Results of Multifractal Detrended Fluctuation Analysis	140
5.5	Multifractal Detrended Moving Average Analysis	143
5.5.1	Results of Multifractal Detrended Moving Average Analysis	145
5.6	Discussion	149

6	Azimuthal Structure of Particle Distribution in Relativistic Nucleus-Nucleus Collisions	153
6.1	Introduction	153
6.2	Methodology	155
6.3	Results	156
6.4	Discussion	166
7	Wavelet Analysis in Relativistic Nucleus-Nucleus Collisions	169
7.1	Introduction	169
7.2	Methodology	171
7.3	Results	174
7.4	Discussion	179
	Concluding Remarks	183
	List of Publications	188

List of Tables

1.1	Accelerator facilities in relativistic heavy-ion physics.	15
1.2	Four experiments at BNL-AGS: its major detector components and the important observations.	17
1.3	The Oxygen-Sulfur age ‘large’ experiments at CERN-SPS: its major detector component(s) and the important observation(s).	18
1.4	The Lead age experiments at CERN-SPS: its major detector component(s) and the important observation(s).	18
2.1	Chemical composition of standard emulsion.	54
3.1	The values of $1d$ intermittency exponent (ϕ_q) for order $q = 2 - 6$ in $^{28}\text{Si-Ag/Br}$ interaction at 14.5A GeV. The errors are of statistical origin only.	87
3.2	The values of multifractal specific heat calculated from the SFM analysis	92
3.3	The values of $2d$ intermittency exponent β_q of order $q = 2 - 4$ for self-similar partitioning of the (η, φ) space in $^{28}\text{Si-Ag/Br}$ interaction at 14.5A GeV.	94
3.4	The parameters of the quadratic Eq. (3.33) fit to the experimental data for various H values. The $\chi^2(dof)$ values showing the goodness of the fits are given.	97
3.5	The values of $2d$ intermittency exponents $\phi_q^{(2)}$ of order $q = 2 - 4$ for self-affine partitioning of the (η, φ) space in $^{28}\text{Si-Ag/Br}$ interaction at 14.5A GeV.	98
3.6	The ϕ_{pq} exponents of the FC scaling relation Eq. (3.39) for several different combinations of (p, q)	101
4.1	Values of b , $\tilde{\psi}(2, 2)$ and $\tilde{\mu}_2$ for the experiment, the UrQMD, the UrQMD+BEC . . .	117
4.2	Erraticity parameters in $^{28}\text{Si-Ag/Br}$ interaction at 14.5A GeV.	121
5.1	The values of the Lévy stable index (μ) obtained at two different regions of q . . .	133
5.2	The values of multifractal specific heat C calculated from the G_q and T_q moment analysis of the $^{28}\text{Si-Ag/Br}$ data at 14.5A GeV.	137
5.3	The values of the Hurst exponent H and the fractal dimension D_F calculated from the MF-DFA method for the $^{28}\text{Si-Ag/Br}$ interaction data at 14.5A GeV.	141

List of Figures

1.1	Summary of measurements of $\alpha_s(Q)$. The curves shown differ in their choice of the QCD scale parameter Λ_{QCD} [3].	3
1.2	Temperature history of the universe—from Big Bang to Little Bang.	4
1.3	Geometry of a nucleus-nucleus collision.	8
1.4	Multiplicity distribution as a tool to determine centrality of AB collision.	9
1.5	Stopping in nucleus-nucleus collisions.	12
1.6	Schematic of spacetime evolution of a high energy nucleus-nucleus collision in the center-of-mass frame of two colliding nuclei.	14
1.7	(a) Nuclear matter energy density and (b) pressure as a function of temperature from lattice calculation [30]. The arrows in the diagrams indicate the ideal Stefan-Boltzmann values.	25
1.8	Bjorken model of nucleus-nucleus collision.	32
1.9	Phase diagram of water (left). A schematic phase diagram of QCD matter (right).	33
2.1	Schematic of a secondary track geometry with respect to the projectile.	59
2.2	Plot of reaction cross-section with $A_p^{1/3} + A_t^{1/3}$ up to SPS energy	64
2.3	Distributions of (a) pseudorapidity and (b) azimuthal angle of shower tracks emitted from ^{28}Si -Ag/Br interaction at 14.5A GeV.	65
2.4	An illustration of the effect of the Bose-Einstein correlation algorithm. The phase space distribution of pi-mesons produced in the event generator (UrQMD) is modified by the after burner algorithm of BEC (UrQMD+BEC). Three color varieties represent the members of the pion family.	74
3.1	Pseudorapidity distribution of shower tracks of two high multiplicity events in ^{28}Si -Ag/Br interactions at 14.5A GeV. Note how the fluctuation increases with decreasing bin size from $\delta\eta = 0.2$ to $\delta\eta = 0.1$. n_s and n_h represent respectively the number of s -tracks and heavy fragments of the event. Gaussian fits to the distributions are shown.	83
3.2	Distributions of local pseudorapidity density of shower tracks in ^{28}Si -Ag/Br interactions at 14.5A GeV.	84

3.3	Variation of the event averaged SFM of shower tracks with phase space resolution in η -space. Straight lines best fitted to the data points are shown.	86
3.4	Same as Fig. 3.3 but in φ -space.	86
3.5	Normalized intermittency exponents as a function of order number q . Lines joining points are drawn to guide the eye.	88
3.6	Plots of d_q/d_2 as a function of order number q for the experiment—(a) curves represent the best fitted log-Lévy law, Eq. (3.27) and (b) curves represent the Ginzburg-Landau model, Eq. (3.28).	89
3.7	(a) Plot of λ_q with order number q . (b) Plot of intermittency strength α_q with q . (c) Plot of generalized Rényi dimension D_q with $\ln q/(q-1)$. The curves are drawn to guide the eye.	91
3.8	Plot of $2d$ -SFM for a self-similar partitioning of the (η, φ) plane. The lines represent linear regressions to the data points.	93
3.9	Plot of $2d$ -SFM of order $q = 2$ against (η, φ) -space resolution for several different values of H . The lines represent the quadratic function Eq. (3.33) with best fitted parameter set given in Table 3.4. First two data points are excluded from the fits.	96
3.10	$2d$ -SFM of order $q = 2 - 4$ against (η, φ) space resolution with two optimized values of H for which the power-law scaling of $F_2^{(2)}$ can be recovered at its best: (a) for $H = 0.5$ and (b) for $H = 2.5$	97
3.11	(a) $2d$ intermittency strength α_q in (η, φ) space with order q . (b) Anomalous fractal dimension d_q with order q . (c) The generalized dimension of (multi)fractality D_q with $\ln q/(q-1)$. The lines in (a) and (b) are drawn joining the data points, whereas those in (c) are linear regressions.	98
3.12	Factorial correlators with correlation length in η -space. The error bars are only of statistical origin. For clarity successive orders are shifted by one unit along the vertical axis as shown in the diagram.	101
3.13	Variation of $\phi_{p,q}/\phi_{1,1}$ against the product $p \cdot q$ for various combinations of p and q . The lines represent linear fit to the respective data points which confirm the validity of the α -model.	102
3.14	Factorial correlators with phase space resolution for two different values of correlation length $D = 0.05$ and 0.1 . The plots are for the experiment. The dashed lines are the best fitted horizontal lines to the data points.	102
3.15	The validity of the scaling relation Eq. (3.44) for (a) the experiment, (b) the UrQMD and (c) the UrQMD+BEC.	104
3.16	The normalized cumulant moments plotted against the phase space partition number in $^{28}\text{Si-Ag/Br}$ interaction at 14.5A GeV	106

3.17	The oscillatory moments H_q plotted with its rank q for the experiment (solid circle) and for the UrQMD (empty circle). The lines joining points are shown to guide the eye. The pseudorapidity cuts taken as (a) $\eta_0 - 0.25 \leq \eta \leq \eta_0 + 0.25$, (b) $\eta_0 - 0.5 \leq \eta \leq \eta_0 + 0.5$, (c) $\eta_0 - 0.75 \leq \eta \leq \eta_0 + 0.75$ and (d) $\eta_0 - 1.0 \leq \eta \leq \eta_0 + 1.0$.	107
4.1	Distributions of F_2^e in $^{28}\text{Si-Ag/Br}$ interaction at 14.5A GeV for two different values of η -space partition number $M = 5$ (a) and 10 (b).	115
4.2	Erraticity moments $C_{p,q}$ plotted as functions of phase space partition number M . The solid curves are drawn to guide the eye.	116
4.3	Plot of $\ln C_{2,2}$ and Σ_2 with $\ln f(M) = (\ln M)^b$. The lines represent best linear fits to the data points.	117
4.4	Plot of $\ln C_{p,2}$ with $\ln C_{2,2}$. The best fitted straight lines are shown.	118
4.5	Variation of $\chi(p, q)$ with p . The curves represent the best quadratic fits.	118
4.6	Plot of Σ_q with $\ln M$. The lines joining points are drawn to guide the eye.	119
4.7	Plot of Σ_q against Σ_2 . The lines represent the best linear fits to the data points for $M \leq 12$.	120
4.8	Plot of the entropy index $\tilde{\mu}_q$ against order number q calculated from (a) Eq. (4.9) and (b) Eq. (4.11). The lines joining the data points are shown.	121
5.1	Multifractal G_q moment plotted with phase space partition number in $^{28}\text{Si-Ag/Br}$ interaction at 14.5A GeV. Lines joining points are drawn to guide the eye.	128
5.2	(a) The event average mass exponent $\tau(q)$ and the Lipschitz-Hölder exponent α plotted against q . Note that the experiment (solid line), the UrQMD (dotted line) and the UrQMD+BEC (dashed line) are very close to each other. (b) The multifractal spectral function for the experiment (solid circles), the UrQMD (open circles) and the UrQMD+BEC (shaded circles).	129
5.3	Plots of $q - 1 - \tau^{\text{dyn}}(q)$, $q - 1 - \tau(q)$ and the intermittency exponent ϕ_q [21] versus order number q . In all diagrams lines joining points are drawn to guide the eye.	131
5.4	Plot of $\ln[B - \alpha]$ versus $\ln[1 - f(\alpha)]$. In all diagrams the dotted(solid) lines represent linear fits to the data points in the low(high)- q region.	132
5.5	Multifractal T_q moment as a function of number of counts in the phase space interval. The best fitted straight lines are shown in all diagrams.	135
5.6	Generalized dimensions D_q with order number q calculated from the SFM (solid circles) [21], G_q moment (open circles) and T_q moment (solid square) analysis. The lines joining points are shown to guide the eye.	136
5.7	Plot of D_q with $\ln q/(q - 1)$. The solid (open) circles are the results of the $G_q(T_q)$ moment analysis. The lines are the best linear fits to the data points.	136

5.8	Event averaged DFA fluctuation functions $\langle F_{q=2} \rangle$ plotted with phase space partition number. The lines represent the best linear fits to the data points in the linear region.	141
5.9	Event averaged MF-DFA1 fluctuation functions plotted with phase space partition number for integer $q \in [-5, +5]$ in $^{28}\text{Si-Ag/Br}$ interaction at 14.5A GeV. Lines joining points are drawn to guide the eye.	142
5.10	(a) Plot of $h(q)$ versus q , (b) $\tau(q)$ versus q , and (c) the singularity spectra $f(\alpha)$ obtained from the MF-DFA1 method. Lines joining points are shown.	142
5.11	Event averaged MF-DMA ($\theta = 0.5$) fluctuation functions for the window parameter $\theta = 0.5$. Lines joining points are drawn to guide the eye.	146
5.12	(a) Plot of $h(q)$ versus q , (b) $\tau(q)$ versus q , and (c) the singularity spectra obtained from the MF-DMA analysis with the window parameter $\theta = 0.5$. Line joining points are shown to guide the eye.	147
5.13	Generalized multifractal dimensions. The results of the MF-DMA (with $\theta = 0.5$) method are compared with those of the other methods. Lines joining points are drawn to guide the eye.	148
6.1	Schematic diagrams of an ideal (a) ring-like and (b) jet-like structure in the target azimuth.	156
6.2	A schematic of $S_2/\langle S_2 \rangle$ distributions from three effects, namely (1) ring-like effect distribution, (2) stochastic distribution and (3) jet-like effect distribution. The solid curve represents the resultant distribution.	157
6.3	Contribution of the ring-like effect to the experimental data on $^{208}\text{Pb-Ag/Br}$ interaction at 158A GeV/c as a function of the number of particles in a subgroup (N_d) for three different multiplicity groups [16].	158
6.4	Distributions of (a) the S_1 and (b) the S_2 parameters normalized by their respective stochastic values in $^{28}\text{Si-Ag/Br}$ interaction at 14.5A GeV.	159
6.5	Same as Fig. 6.4 but in $^{32}\text{S-Ag/Br}$ interaction at 200A GeV.	159
6.6	Average behavior of (a) the S_1 parameter and (b) the S_2 parameter in $^{28}\text{Si-Ag/Br}$ interaction at 14.5A GeV. Horizontal dashed lines follow Eq. (6.5). The effect of the BEC algorithm is shown in the bottom panel.	160
6.7	Same as Fig. 6.6 but in $^{32}\text{S-Ag/Br}$ interaction at 200A GeV.	161
6.8	Plot of (a) $\langle -\sum \ln(\Delta\varphi) \rangle$ and (b) $\langle \sum (\Delta\varphi)^2 \rangle$ as a function of $\Delta\eta$ and η_m in $^{28}\text{Si-Ag/Br}$ interaction at 14.5A GeV.	162
6.9	Same as Fig. 6.8 but in $^{32}\text{S-Ag/Br}$ interaction at 200A GeV.	162
6.10	Cluster density distributions for (a) the ring-like region, $S_2/\langle S_2 \rangle < 1$ and (b) the jet-like region, $S_2/\langle S_2 \rangle > 1$ in $^{28}\text{Si-Ag/Br}$ interaction at 14.5A GeV.	163
6.11	Same as Fig. 6.10 but in $^{32}\text{S-Ag/Br}$ interaction at 200A GeV.	163

6.12	Cluster size distributions for (a) the ring-like region, $S_2/\langle S_2 \rangle < 1$ and (b) the jet-like region, $S_2/\langle S_2 \rangle > 1$ in $^{28}\text{Si-Ag/Br}$ interaction at 14.5A GeV.	164
6.13	Same as Fig. 6.12 but in $^{32}\text{S-Ag/Br}$ interaction at 200A GeV.	165
6.14	Cluster mean η_m distributions for (a) $S_2/\langle S_2 \rangle < 0.9$, (b) $0.9 < S_2/\langle S_2 \rangle < 1.1$ and (c) $S_2/\langle S_2 \rangle > 1.1$ in $^{28}\text{Si-Ag/Br}$ interaction at 14.5A GeV.	166
6.15	Same as Fig. 6.14 but in $^{32}\text{S-Ag/Br}$ interaction at 200A GeV.	166
7.1	‘Before’ and ‘after’ illustrations of a nuclear magnetic resonance signal. The original signal is at the top and the denoised signal is at the bottom.	170
7.2	Several different families of wavelets. The number next to the wavelet name represents the number of vanishing moments (A stringent mathematical definition related to the number of wavelet coefficients) for the subclass of wavelet.	173
7.3	(a) First derivative and (b) second derivative (Mexican hat wavelet) of the Gaussian function.	174
7.4	g_2 wavelet pseudorapidity spectra in $^{28}\text{Si-Ag/Br}$ interaction at 14.5A GeV for different values of the scale parameter a	175
7.5	g_2 wavelet pseudorapidity spectra in $^{32}\text{S-Ag/Br}$ interaction at 200A GeV for different values of the scale parameter a	176
7.6	Wavelet pseudorapidity spectra for a high-multiplicity event in (a) $^{28}\text{Si-Ag/Br}$ interaction at 14.5A GeV and (b) $^{32}\text{S-Ag/Br}$ interaction at 200A GeV, the event multiplicities are respectively 146 and 379.	177
7.7	Scalograms of the events for which the wavelet pseudorapidity spectra are shown in Fig. 7.6.	177
7.8	Distributions of the local maxima (left panel) and minima (right panel) of the scalograms in $^{28}\text{Si-Ag/Br}$ interaction at 14.5A GeV.	178
7.9	Same as Fig. 7.8 but in $^{32}\text{S-Ag/Br}$ interaction at 200A GeV.	179
7.10	b_{max} distributions for different limiting values of a_{max} in $^{28}\text{Si-Ag/Br}$ interaction at 14.5A GeV. The distribution plots are so shifted as to avoid mutual overlapping.	180
7.11	Same as Fig. 7.10 but in $^{32}\text{S-Ag/Br}$ interaction at 200A GeV.	180
7.12	b_{max} distributions for different scale windows in $^{28}\text{Si-Ag/Br}$ interaction at 14.5A GeV. The distributions plots are so shifted as to avoid mutual overlapping.	181
7.13	Same as Fig. 7.12 but in $^{32}\text{S-Ag/Br}$ interaction at 200A GeV.	181

Chapter 1

Relativistic Nucleus-Nucleus Collision – an Overview

1.1 Introduction

QCD is the quantum field theory of strong interaction. The theory describes how partons (quarks and gluons), the fundamental constituents of all strongly interacting particles, namely the hadrons (which also include the nucleons), interact with each other. The idea of color degree of freedom plays an important role in strong interaction. Quarks carry three varieties of color, while all hadrons must be color neutral (singlet) composite objects in the same sense as all atoms are electrically neutral. The quarks interact with each other by exchanging gluons, the quanta of strong interaction, which themselves are color carrying objects. Unlike atoms the hadrons are guided by a phenomenon called the *asymptotic freedom* [1, 2], the basic essence of which is that the QCD interaction strongly depends on the length scale. For two colored particles the interaction is strong at large and weak at small separations. As a result, the partons are permanently confined within hadrons, and till date nobody has been able to isolate a quark. Fig. 1.1 shows how the QCD *running coupling constant* α_s varies with the momentum transfer Q [3]. Small values of α_s correspond to a large momentum transfer or equivalently a short distance when the partons are weakly interacting. Under such a situation the confinement phenomenon can be explained

in terms of a perturbative QCD (pQCD). On the other hand, at a low momentum transfer or equivalently at a large distance α_s is large, and the strongly coupled QCD state becomes highly nonperturbative. In the ideal QCD Lagrangian quarks are considered as massless point particles. However, a quark confined within a hadron can polarize the surrounding gluon field and acquire a dynamically generated effective mass, also known as the *constituent* mass, whose typical value for light quarks is about 350 MeV in baryons and slightly less in mesons [4]. The process of mass acquisition by fundamental particles like quarks and leptons, is largely (about 98%) due to spontaneous breaking of chiral symmetry and marginally (about 2%) due to the interaction with the Higgs field. A fascinating consequence of the idea of asymptotic freedom was recognized shortly after it was introduced. If the normal nuclear matter can be subjected to extremely high values of temperature and pressure, it becomes difficult for the constituent partons to remain within the confinements of individual color neutral hadrons. Under such circumstances the parton-parton coupling becomes loose while the quarks and gluons can move freely over a region that can perhaps be wider than the hadronic dimension (~ 1 fm.) at least by an order [5]. If the temperature is raised to a sufficiently high value say $T > 100 \text{ GeV}$: ($1 \text{ MeV} \approx 10^{10} \text{ K}$), the gluonic cloud surrounding the quarks will melt down, thereby restoring the chiral symmetry. At vanishing baryon density deconfinement and chiral symmetry restoration may take place simultaneously, while at high baryon density the former probably precedes the latter [6]. A color conducting deconfined state of weakly interacting partons comes as a solution of pQCD. A state similar to this perhaps filled up our entire universe at the very early stages of its creation—from the time of electro-weak decoupling (a few pico-secs) to hadronization (several micro-secs) after the *Big bang*. However, the highest limiting temperature at which a state of color neutral hadrons can survive is set at a much smaller value ($T \approx 170 \text{ MeV}$) [7]. Therefore, a confinement–deconfinement transition is possible even at a much lower temperature. Corresponding deconfined state may however not be so weakly coupled and needs to be treated non-perturbatively. In a different approach nuclear matter is squeezed so hard that a large number of constituent (valence) quarks are compelled to assemble in the close proximity of every other single quark, and none of them can anymore recognize which other quark(s) did it partner with in the original nucleon. Such a situation may also lead to the formation of a color conducting deconfined state at a much lower temperature but at a higher baryo-chemical potential ($\mu_B \sim$ several hundred MeV). A similar state perhaps forms the core of very compact astrophysical objects like the neutron stars, which having temperatures $T \sim 10^5 - 10^9 \text{ K}$ may be considered as cold in the partonic scale [8].

When two heavy nuclei with high incoming energies are allowed to impinge upon each other, a central ‘fireball’ is created. Depending purely on the initial conditions a local thermal and/or chemical equilibrium may be achieved. Under favorable thermodynamic conditions such an equilibrated state may undergo a transition from a state of interacting

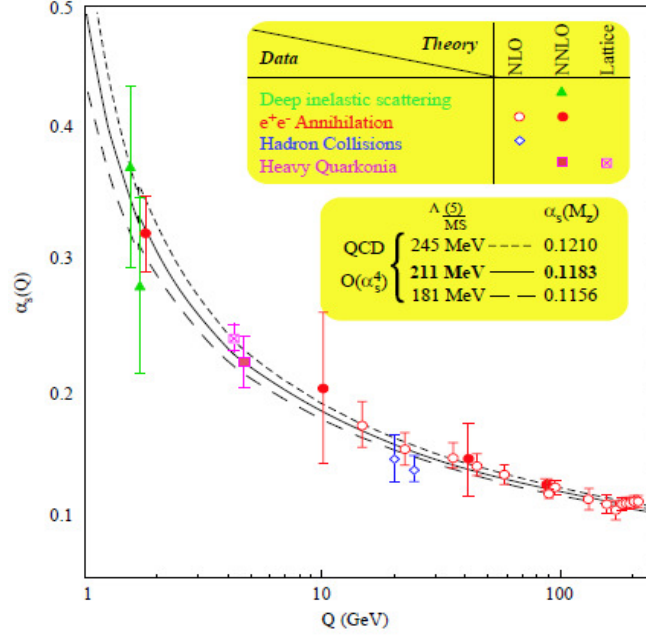


Figure 1.1: Summary of measurements of $\alpha_s(Q)$. The curves shown differ in their choice of the QCD scale parameter Λ_{QCD} [3].

nucleons to a color conducting state called the *Quark-gluon Plasma* (QGP) [5, 9, 10], where deconfined quarks and gluons can propagate over nuclear rather than merely nucleonic volumes. As indicated above, through AB interactions it is possible to recreate the initial evolutionary stages of our universe since it came into being, or to produce the state of matter similar to what probably fills up the core of very compact astrophysical objects, states that are otherwise experimentally inaccessible in every possible sense. The science of small elementary particles is therefore, deeply intertwined with the science of the large, the study of the origin and the evolution of the universe. Fig. 1.2 shows a schematic of the temperature history of our universe as it evolved with time after its creation [11]. At times $\sim 10 \mu\text{sec.}$ after the Big bang, at temperature $T \sim 200 \text{ MeV}$ the universe was in the state of QGP. In present-day experiments by colliding two heavy-ions at relativistic energies, we may try to recreate that kind of matter in the laboratory through a *Little bang*. One has to remember that any such terrestrially created fireball will certainly contain much less energy, and will be much shorter lived ($\sim 10^{-22} \text{ sec.}$) than the primordial one. As the infant universe expanded and cooled down, the plasma phase of matter went through a transition to form a variety of particles, most importantly the nucleons which constitute different forms of matter as we see them today. However, unless the system under consideration behaves like matter and not like individual particles or a group of particles, it is inappropriate to discuss the same in terms of phase transition or local equilibrium. A local equilibrium means that the lifetime of the fireball must be significantly larger than the inverse rate of binary collisions taking place within it. Each constituent particle should experience at least several collisions. It is also

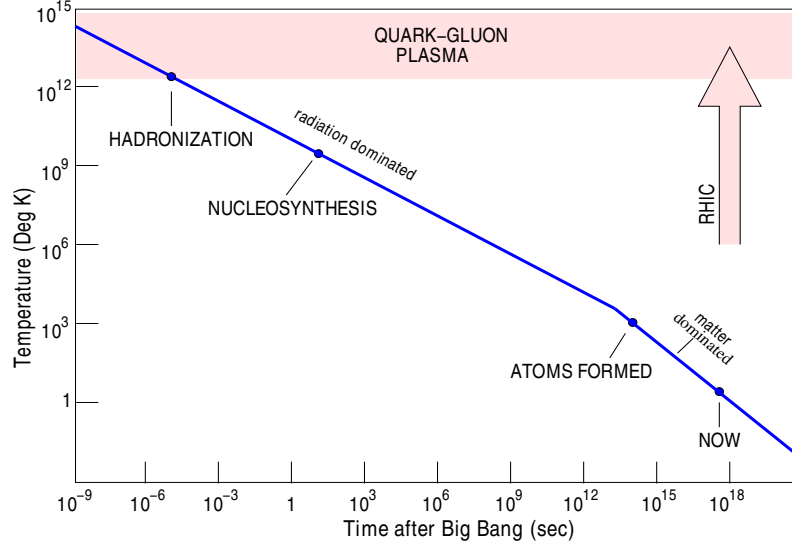


Figure 1.2: Temperature history of the universe—from Big Bang to Little Bang.

necessary to establish that the non-hadronic degrees of freedom present in the fireball form a statistical ensemble, so that concepts like temperature, chemical potential and flow velocity can be applied to the system, and the system can be characterized by an experimentally determinable equation of state. The measurements should further enable us to determine the physical characteristics of phase transition like its order, the critical temperature and the speed of sound in hadronic/partonic medium along with the nature of quasi-particle states [12]. For two reasons an interacting AB system is better suited than a proton-proton (pp) system in this regard. First, in a high-energy AB collision at the same incident energy per nucleon, the average multiplicity of the newly produced particles is much higher (as large as 10^4 per event at the highest possible collision energy achieved till date) than that of a pp collision. Thus the relative fluctuations of thermodynamic parameters that are usually required to characterize a state, will be less. Second, in the AB system there will be many rescattering among the nucleons of the colliding nuclei so that enough spacetime is available before a local equilibrium settles down within the radiation and matter mix-up prevailing in the central reaction zone, so that the same can be called ‘a state’ [13].

1.2 Relativistic Kinematics

High-energy interactions between particles should be studied by using such kinematic variables that have simple transformation properties as we move from one Lorentz frame to the other. The distribution functions plotted in terms of such variables in one frame of reference can then be very easily redrawn in another Lorentz transformed frame. Conventionally in a fixed target experiment measurements are made in the laboratory system (LS), and in a

collider experiment in the CM system (CMS) which for a symmetric (AA) collision coincides with the LS. Some of the commonly used kinematic variables in high-energy collisions are introduced below.

• **Energy in LS and CMS:** For a target fixed in the LS, the projectile (rest mass m_1 and incident energy E_1) and the target (rest mass m_2) four momenta may, respectively be denoted by:

$$p_1 = (E_1, \mathbf{p}_1) \quad \text{and} \quad p_2 = (m_2, \mathbf{0}) \quad (1.1)$$

the relativistic energy-momentum relation being effective for each particle. In the CMS both will have equal and opposite three momenta. Corresponding four momenta will be:

$$p_1^* = (E_1^*, \mathbf{p}_1^*) \quad \text{and} \quad p_2^* = (E_2^*, \mathbf{p}_2^* = -\mathbf{p}_1^*). \quad (1.2)$$

In the CMS the total four momenta (s) of the colliding system is

$$(p_1^* + p_2^*)^2 = (E_1^* + E_2^*)^2 - (\mathbf{p}_1^* + \mathbf{p}_2^*)^2 = (E_1^* + E_2^*)^2 = E_{cm}^2 \equiv s. \quad (1.3)$$

Therefore, \sqrt{s} denotes the total energy available in the CMS which is also called the invariant mass of the CMS. On the other hand in LS

$$(p_1 + p_2)^2 = (E_1 + m_2)^2 - \mathbf{p}_1^2 = m_1^2 + m_2^2 + 2m_2 E_1. \quad (1.4)$$

Therefore, using Lorentz invariance of \sqrt{s} one can write,

$$E_{cm} = \sqrt{s} = \sqrt{m_1^2 + m_2^2 + 2m_2 E_1} \quad (1.5)$$

In the LS the CMS moves in the direction of \mathbf{p}_1 with a Lorentz factor,

$$\gamma_{cm} = \frac{E_1 + m_2}{\sqrt{s}} \quad \Rightarrow \quad \sqrt{s} = \frac{E_{lab}}{\gamma_{cm}} \quad (1.6)$$

In a collider experiment if the incident energies are very high ($E_1, E_2 \gg m_1, m_2$),

$$E_{cm}^2 \approx 4 E_1 E_2 \quad \Rightarrow \quad E_{cm} \approx 2E$$

when $E_1 = E_2 = E$ say. Under a similar situation, $E_{cm} \approx \sqrt{2m_2 E_1}$ for a fixed target experiment. For a symmetric AA collision the total CM energy is related to the CM energy of an NN system ($\sqrt{s_{NN}}$) by, $\sqrt{s} = A\sqrt{s_{NN}}$ with a Lorentz factor

$$\gamma_{cm} = \frac{E}{M} = \frac{\sqrt{s}}{2A m_N} = \frac{\sqrt{s_{NN}}}{2m_N}, \quad (1.7)$$

where m_N is the mass of a nucleon. For asymmetric collisions however, it is difficult to fix the ‘effective’ CM frame which is dependent on the impact parameter of the collision. Therefore, the number of participating and spectator nucleons need to be determined first, posing extra problems particularly for soft processes. For hard processes that are more likely to be observed in central collisions, the NN frame still works.

• **Transverse Momentum:** The *transverse momentum* (\mathbf{p}_\perp) of a particle is the momentum component in a direction perpendicular to the beam direction. Obviously \mathbf{p}_\perp is related to the longitudinal component p_L as $|\mathbf{p}| = \sqrt{\mathbf{p}_\perp^2 + p_L^2}$. One can define the *transverse mass* (m_\perp) through $m_\perp = \sqrt{\mathbf{p}_\perp^2 + m^2}$, where m is the rest mass of the particle. The azimuthal angle (φ), defined over the transverse plane is introduced as, $\varphi = \tan^{-1}(p_y/p_x)$.

• **Rapidity Variable:** The *rapidity variable* (y), parameter of the ‘Lorentz boost’, can either be defined in terms of the energy-momentum components (E, \mathbf{p}) or in terms of the space-time components (t, \mathbf{x}) of a particle as,

$$y = \frac{1}{2} \ln \left(\frac{E + p_L}{E - p_L} \right) \quad \text{or} \quad y = \frac{1}{2} \ln \left(\frac{t + z}{t - z} \right) \quad (1.8)$$

Here p_L is the longitudinal component of the momentum and z is the space co-ordinate of a particle along the beam direction. y is a dimensionless quantity related to the ratio of the forward light-cone momentum (p_+) to the backward light-cone momentum (p_-) of the particle, can either be positive or negative. In the nonrelativistic limit, the rapidity of a particle traveling along the longitudinal direction is equal to the velocity of the particle in the unit of velocity of light in vacuum. One can easily show that, $E = m_\perp \cosh y$ and $p_L = m_\perp \sinh y$. The energy and momentum of the CMS in the LS, respectively are $\gamma_{cm}\sqrt{s}$ and $\beta_{cm}\gamma_{cm}\sqrt{s}$, where β_{cm} and γ_{cm} are, respectively the velocity and Lorentz factor of the CMS in the LS. Therefore the rapidity of the CMS in the LS is

$$y_{cm} = \frac{1}{2} \ln \left[\frac{\gamma_{cm}\sqrt{s} + \beta_{cm}\gamma_{cm}\sqrt{s}}{\gamma_{cm}\sqrt{s} - \beta_{cm}\gamma_{cm}\sqrt{s}} \right] = \frac{1}{2} \ln \left[\frac{1 + \beta_{cm}}{1 - \beta_{cm}} \right] \quad (1.9)$$

The rapidity of a particle is actually the relativistic realization of the velocity, and in one Lorentz frame it is related to the rapidity in the other by an additive constant. As for example the rapidity of a particle (y) in LS is related to the same (y^*) in CMS by the simple relation $y = y^* + y_{cm}$. Let us denote the projectile by P and the target by T . In a fixed target experiment $p_T = 0$, $E = m_P \cosh y_P$ and $p_L = m_P \sinh y_P$ for the incident particle, where m_P is its rest mass and y_P the rapidity. Therefore,

$$y_P = \cosh^{-1} \left(\frac{E}{m_P} \right) = \cosh^{-1} \left(\frac{\sqrt{s_{NN}}}{2m_N} \right) \quad \text{or} \quad y_P = \sinh^{-1} \left(\frac{p_L}{m_P} \right)$$

• **Pseudorapidity Variable:** In some experiments variables like E , \mathbf{p} or the rest mass of a particle may not be easily measured. In such cases it is convenient to use the *pseudorapidity* (η) variable to characterize the particle which requires only the measurement of the emission angle (θ) with respect to the beam direction. The η variable is defined as,

$$\eta = -\ln [\tan (\theta / 2)] \quad (1.10)$$

At high-energy ($|\mathbf{p}| \gg m$) the pseudorapidity can also be approximated to the rapidity,

$$\eta = \frac{1}{2} \ln \left(\frac{|\mathbf{p}| + p_L}{|\mathbf{p}| - p_L} \right) \approx y \quad (1.11)$$

Using Eq. (1.8) and Eq. (1.10) y and η can be expressed in terms of each other

$$y = \frac{1}{2} \ln \left[\frac{\sqrt{p_{\perp}^2 \cosh^2 \eta + m^2} + p_{\perp} \sinh \eta}{\sqrt{p_{\perp}^2 \cosh^2 \eta + m^2} - p_{\perp} \sinh \eta} \right]; \eta = \frac{1}{2} \ln \left[\frac{\sqrt{m_{\perp}^2 \cosh^2 y + m^2} + m_{\perp} \sinh y}{\sqrt{m_{\perp}^2 \cosh^2 y + m^2} - m_{\perp} \sinh y} \right].$$

The distribution of the number of detected particles (N) in terms of p_{\perp} and y can therefore, be related to the distribution in terms of p_{\perp} and η as,

$$\frac{d^2 N}{d\eta d\mathbf{p}_{\perp}} = \left(1 - \frac{m^2}{m_{\perp}^2 \cosh^2 y} \right)^{\frac{1}{2}} \frac{d^2 N}{dy d\mathbf{p}_{\perp}} \quad (1.12)$$

The differential $d^3 p/E$ is a Lorentz invariant quantity. One can express it as,

$$d^3 p/E = d\mathbf{p}_{\perp} dy = p_{\perp} dp_{\perp} d\varphi dy = m_{\perp} dm_{\perp} d\varphi dy. \quad (1.13)$$

The Lorentz invariant differential cross-section $E d^3 \sigma / dp^3 \equiv E d^3 N / dp^3$, also called the invariant yield, can now be expressed in terms of measurable quantities as,

$$E \frac{d^3 \sigma}{dp^3} \propto \frac{1}{m_{\perp}} \frac{d^3 N}{dm_{\perp} d\varphi dy} = \frac{1}{2\pi m_{\perp}} \frac{d^2 N}{dm_{\perp} dy} = \frac{1}{2\pi p_{\perp}} \frac{d^2 N}{dp_{\perp} dy}. \quad (1.14)$$

1.3 Nucleus-Nucleus Collision at High-energy

A high-energy AB collision is a highly complex dynamical event. The control parameters are the collision energy and the size of the colliding system. We expect that for the short-range hadronic interactions the collision geometry should determine the amount of matter participating in nuclear collisions. The collision geometry is a very important and therefore should be very carefully explored. The early age experimental results confirm the role of this simple geometric picture of nuclear collision dynamics. The reaction radius, defined as

the square root of the reaction cross section (σ), increases linearly with the geometric size of the colliding system described by the sum of their radii as [14],

$$\sigma^{1/2} \propto [A^{1/3} + B^{1/3}]. \quad (1.15)$$

This result confirms that for local deposition of energy and baryon number to take place the colliding nuclei need to ‘touch’ each other. At high energies in the laboratory system ($E_{\text{lab}} \sim$ a few GeV per nucleon) in the center of momentum frame, due to Lorentz boost both the colliding nuclei look like two discs, contracted along the direction of the boost with transverse radii respectively, say R_A and R_B , approaching each other. Figure 1.3 shows a schematic

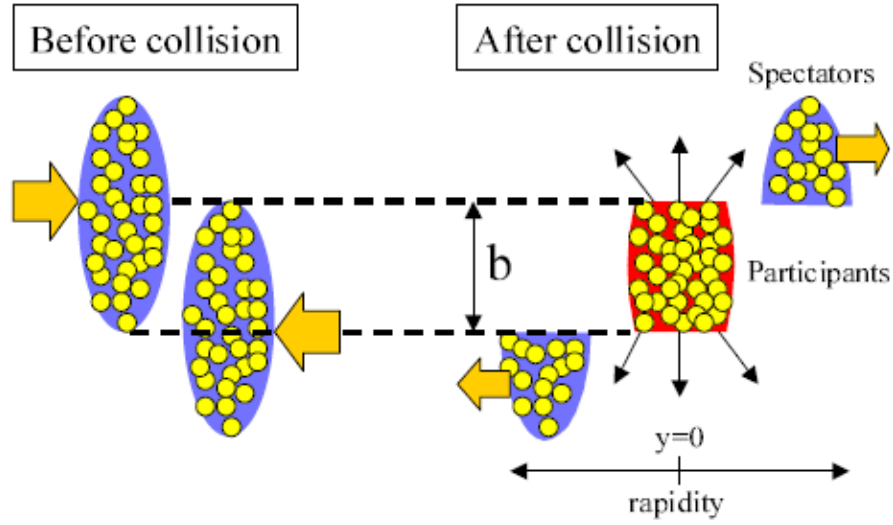


Figure 1.3: Geometry of a nucleus-nucleus collision.

drawing of such an interacting system. Nucleons that directly participate in the collision are called the ‘participants’, and the rest that do not participate are called the ‘spectators’. The number of participating nucleons (N_{part}) should in principle be geometrically determined from the impact parameter (b) of the collision, that in principle can vary between 0 and $R_A + R_B$. Collisions close to the $b \approx 0$ side are called central events, while those on the $b \approx R_A + R_B$ side are called peripheral events, and the entire set of events with $0 \leq b \leq R_A + R_B$ is called a minimum bias sample. However, b cannot be directly measured in an experiment. Generally, any observable that varies monotonically with b can be used to represent the impact parameter. The average charged particle multiplicity N_{ch} , the transverse energy (E_{\perp}) and the missing forward energy are suitable for this purpose. For most central collisions the missing forward energy approaches zero, thereby posing extra difficulty to use it as a trigger condition. Therefore, two assumptions are made: (i) on an average E_{\perp} released in a collision is proportional to N_{part} , and (ii) N_{ch} per collision is proportional to N_{part} . Now the minimum bias E_{\perp} or N_{ch} distribution can be used to

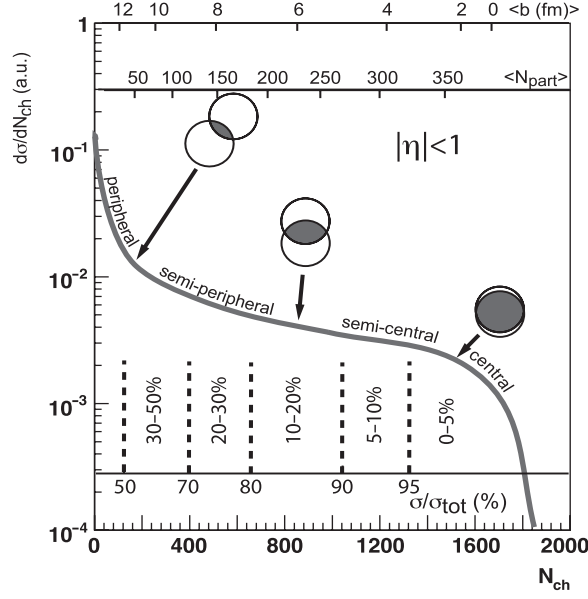


Figure 1.4: Multiplicity distribution as a tool to determine centrality of AB collision.

determine the average centrality of a sub-sample of events, while the energy carried in the extreme forward direction can be used to determine the number of spectator nucleons. As for example, events with the highest 5% value of N_{ch} should correspond to the 5% most central collisions. The correlation between centrality and the impact parameter can be established by Galuber-type Monte Carlo simulations and by employing Woods-Saxon type nuclear density profile [15]. The Glauber model treats the AB collision as a superposition of many NN collisions, assumes that at high-energies nucleons travel in straight lines (eikonal approximation), an inelastic NN collision takes place if two nucleons come within a distance $d \leq \sqrt{\sigma_{NN}^{inel}/\pi}$, and after each such collision if a hadron is excited, it will subsequently interact with other hadrons with the same cross-section as the original nucleons, σ_{NN}^{inel} being the NN inelastic scattering cross section. According to this model in hard processes, where large momentum transfer takes place, N_{part} proportionally varies with A , whereas the number of NN binary collisions N_{coll} grows as $A^{4/3}$. The correlation between N_{ch} , centrality and N_{part} is schematically shown Fig. 1.4 [15].

Each incoming nucleus can be looked upon as a coherent cloud of partons, more precisely as color-glass-condensates where the nucleons possess only longitudinal momentum/energy. The nucleons undergo successive collisions, as a result of which new (transverse) degrees of freedom are excited, and a significant fraction of the incoming kinetic energy is deposited in the central region leading to the formation of a high-energy, high-density fireball, a highly non-equilibrium state. This is still coherent and liberation of partons from this state takes a finite amount of proper time ($< \text{fm}/c$). Subsequent collisions among partons lead to a nearly thermalized (local thermalization) state. This happens at a time of the order of $1 \text{ fm}/c$, a less

understood aspect of the entire process. When the incident energy involved is extremely high ($\sqrt{s} \geq 200A$ GeV) and the participating nucleons are far apart in phase space, the colliding nuclei cannot stop each other and are said to be ‘transparent’ with respect to each other. As mentioned above, still significant amount of energy will be deposited in the central reaction zone which is gradually converted into formation of $q\bar{q}$ pairs. A large number of final state particles will be produced in the form of mesons, while the relative abundance of net baryon content of the state will be small. Models based on hydrodynamics are used for theoretical understanding of such states. Once again this may eventually lead to QGP formation at high temperature and small chemical potential, a state that perhaps has already been created in BNL Relativistic Heavy-ion Collider (RHIC) and in CERN Large Hadron Collider (LHC) experiments. Subsequent evolution of the system proceeds following a relativistic imperfect fluid dynamics.

On the other hand, if the nucleons stemming out of the projectile and target nuclei can significantly stop each other, we expect a baryon rich state to develop in the central reaction zone that may ultimately lead to a baryon rich QGP. Nuclear stopping is a measure of the efficiency of converting the incoming longitudinal energy into transverse degrees of freedom and slowing down of the incoming nucleus (nuclei). Using the Alternating Gradient Synchrotron (AGS) at Brookhaven National Laboratory (BNL) and Super-proton Synchrotron (SPS) at Center for Nuclear Research (CERN), in experiments up to 60A GeV collision energy involving ^{28}Si or ^{32}S projectiles almost complete stopping has been observed. Significant redistribution of the total initial baryon number carried by the interacting nucleons takes place, leading to a high baryo-chemical potential of the equilibrated state. The underlying physics issues are addressed through non-perturbative QCD and/or through hadronic transport models. In a symmetric collision ($A_P = A_T$), if a complete overlap between projectile and target is reached then the stopping is large, and such collisions are best for studying a free expansion of hot and dense nuclear matter in vacuum. Stopping is typically measured by the average rapidity loss defined as,

$$\langle \delta y \rangle = y_P - \langle y_b \rangle = y_P - \frac{2}{N_{part}} \int_0^{y_P} y \frac{dN_{b-\bar{b}}}{dy} dy, \quad (1.16)$$

where $\langle y_b \rangle$ is the net average baryon rapidity after the collision. The average scaled rapidity shift $\langle \delta y / y_P \rangle \approx 0.27$ does not significantly change up to SPS energy ($E_{lab} = 200A$ GeV) [16], which signifies that for comparable system sizes the normalized rapidity densities do not change with beam energy. Corresponding energy loss (ΔE) can also be estimated,

$$\Delta E = \int_{-y_P}^{y_P} \langle m_{\perp}(y) \rangle \frac{dN_{b-\bar{b}}}{dy} \cosh y dy, \quad (1.17)$$

which comes out to be $\Delta E = 25.7 \pm 2.1$ TeV at the top RHIC energy [17]. It should also be noted that an incomplete stopping and a longitudinally expanding source lead to similar rapidity distributions, an issue that should be properly taken care of.

The energy content available for particle production in an AB collision is the basic and most important quantity. This will depend globally on $\sqrt{s_{NN}}$ and collision centrality, and locally on p_\perp and y . The p_\perp spectra of produced particles can in general be divided into a low- p_\perp and a high- p_\perp part. The low- p_\perp part due to the random kinetic and collective motion of particles present in the fireball, has a thermal origin and can be described by an exponentially decaying function. The high- p_\perp part on the other hand is dominated by hard scatterings and requires a power-law. The inverse slope of the p_\perp spectrum is the ‘effective temperature’ (T_e) of the source (here the fireball) from which the particles are originating. T_e can be measured from the knowledge of $\langle p_\perp \rangle$ defined as,

$$\langle p_\perp \rangle = \frac{\int_0^\infty p_\perp \left(\frac{dN}{dp_\perp} \right) dp_\perp}{\int_0^\infty \left(\frac{dN}{dp_\perp} \right) dp_\perp} = \frac{\int_0^\infty p_\perp^2 f(p_\perp) dp_\perp}{\int_0^\infty p_\perp f(p_\perp) dp_\perp}. \quad (1.18)$$

Here $f(p_\perp)$ is the p_\perp distribution function that can be approximated by an exponential function as,

$$f(p_\perp) = \frac{dN}{d\mathbf{p}_\perp} = \frac{1}{2\pi} \left(\frac{dN}{p_\perp dp_\perp} \right) \propto \exp(-m_\perp/T_e). \quad (1.19)$$

One can use the above form of $f(p_\perp)$ to determine the average value of say m_\perp :

$$\langle m_\perp \rangle = \frac{\int_0^\infty p_\perp m_\perp \exp(-m_\perp/T_e) dp_\perp}{\int_0^\infty p_\perp \exp(-m_\perp/T_e) dp_\perp} = \frac{2T_e^2 + 2mT_e + m^2}{m + T_e}. \quad (1.20)$$

For $\langle p_\perp \rangle \gg$ the rest mass m of the particle under consideration, $\langle m_\perp \rangle \approx \langle p_\perp \rangle \approx 2T_e$. Integrating the invariant yield over the entire p_\perp region one gets the rapidity distribution dN/dy of produced particles. Significant amount of information on AB collisions can be extracted by studying the rapidity distribution. Particle identification is necessary for the purpose, which may not be possible in all experiments. Under such circumstances the pseudorapidity distributions are used. At very high-energies dN/dy should exhibit a plateau which due to the transformation given in Eq. (1.12) gets depleted by a small extent around $\eta^* = \eta - \eta_{cm} = 0$. In the CMS the depletion factor is $(1 - m^2 / \langle m_\perp^2 \rangle)^{1/2}$, whereas in the LS the peak of the distribution is located around half of the beam rapidity $y_P/2$, and the depletion factor is $[1 - m^2 / \{ \langle m_\perp^2 \rangle \cosh^2(y_P/2) \}]^{1/2}$. Due to additive nature of the rapidity variable its distribution remains unchanged as one moves from the LS to the CMS or vice versa. In any relativistic AB collision usually there is a central particle producing region which results from the nucleons directly participating in the collision, and two baryon rich fragmentation regions (target and projectile) that contain the spectator

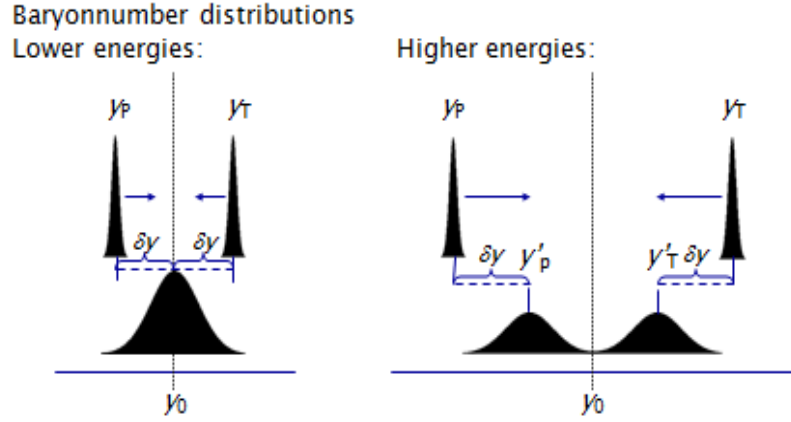


Figure 1.5: Stopping in nucleus-nucleus collisions.

nucleons. When the colliding nuclei are ‘transparent’ with respect to each other, they leave a trail of energy in the form of stretched out strings in between projectile and target rapidities. The strings subsequently fragment and the central region is populated (mostly) by different types of mesons. The baryons (nucleons) continue to move out of the central rapidity region apart from a down-shift in their rapidity values necessary for conservation of energy. On the other hand when the colliding nuclei substantially stop each other, the central rapidity region is filled up with both energy and baryons. Under the most extreme circumstances of complete stopping, the projectile and target baryons loose all memory of their initial states. Correspondingly, the difference (if there is any) between the energy and baryon number distributions in longitudinal and transverse directions with respect to the collision axis will be very little. These two extreme situations are schematically represented in Fig. 1.5. We understand that the rapidity gap $\Delta y = y_P - y_T$ i.e., the difference between the rapidity values of projectile and target, is important for characterizing the central region. For targets fixed in the LS $y_T = 0$ and $\Delta y = y_P$. Accordingly $\cosh \Delta y = E_P/m_P$. In collider experiments involving a head on symmetric colliding system, the CMS is at rest in LS and $\Delta y/2$ is the rapidity of projectile/target. With increasing \sqrt{s}_{NN} rapidity gap is found to increase as, $\Delta y \propto \ln \sqrt{s}$ [18], thereby enabling us to study the central region without having actually to account for particles spilling over from the fragmentation regions. Up to SPS energy the rapidity distribution do not show any plateau and can in stead be described by a single Gaussian having a width $\sigma(y)$ nearly proportional to Δy ($= 2 - 3$) rapidity units. Any system having a preferentially longitudinal expansion of the particle emitting source will therefore, have to have a reasonably large rapidity gap ($\Delta y > 3$) which occurs beyond the SPS energy. Experimental data suggest that nuclear/partonic stopping is present in the primordial, first generation collisions at the microscopic level. Rapidity distributions of particle multiplicity and/or transverse energy exhibit qualitatively similar shapes, which also evolve similarly with \sqrt{s} in pp , $p\bar{p}$ and e^+e^- reactions on one hand, and in central AB collisions on the other. One can formulate a nuclear modification factor for the bulk hadron

rapidity distributions as,

$$R_{AA} = \frac{dN_{ch}/dy \text{ in } AA}{0.5 N_{part} dN_{ch}/dy \text{ in } pp}, \quad (1.21)$$

where N_{part} is the average number of participating nucleons, and for AA collisions $0.5 N_{part}$ is the average number of opposing nucleon pairs. If the contribution to the total yield from each such opposing pairs is same as that from pp collision at same \sqrt{s} , then $R_{AA} = 1$. However, in RHIC and LHC experiments R_{AA} is found to be more than unity, thereby indicating higher stopping in nuclear collisions.

1.3.1 Space-time Evolution of AB Collision

In the CMS of a two-body collision the interacting nuclei follow trajectories very close to the light cone because their velocities are very close to that of the light [18]. We consider both longitudinal space co-ordinate (z) and the time (t) to be zero at the collision point. After the collision a large amount of the energy/matter density or both are deposited in the reaction zone around $z \sim 0$ [19]. If the energy/matter density is so large that the temperature/chemical potential of the created state exceeds the respective critical values required for a phase transition, one may achieve a state of deconfined quarks and gluons. Rescattering among the partons may then lead to thermalization and chemical equilibration. Subsequent expansion and cooling down of the medium will be governed by the equation of this deconfined state. As the system expands and cools down hadronization takes place. Assuming that an equilibrated color conducting deconfined state is created and based on some general arguments it is possible to roughly divide the entire sequence of evolution of a high-energy AB collision into several stages as illustrated in Fig. 1.6.

- (i) The initial collisions among the projectile and target nucleons take place during the passage time of the colliding nuclei, which is $\sim 2R/\gamma_{CM}$ for a symmetric and $\sim (R_A + R_B)/\gamma_{CM}$ for an asymmetric collision. Here R , R_A and R_B are the respective nuclear radii, and γ_{CM} is the Lorentz factor of the CMS in the LS. During this stage intense matter compression and heating take place. Due to inelastic processes initial longitudinal energy is converted to new internal and transverse degrees of freedom with breaking up of initial baryon structures. This initial stage of collision is labeled as a ‘pre-equilibrium’. Processes like parton-parton hard scattering predominantly take place in the overlap region of two colliding nuclei, depositing thereby a large amount of energy in the central ($z \sim 0$) region. The characteristic time of the pre-equilibration state is same as the passage time.
- (ii) After the short pre-equilibration time a ‘fireball’ is created, where depending on the initial conditions thermal and chemical equilibrium may be established. If a QGP like

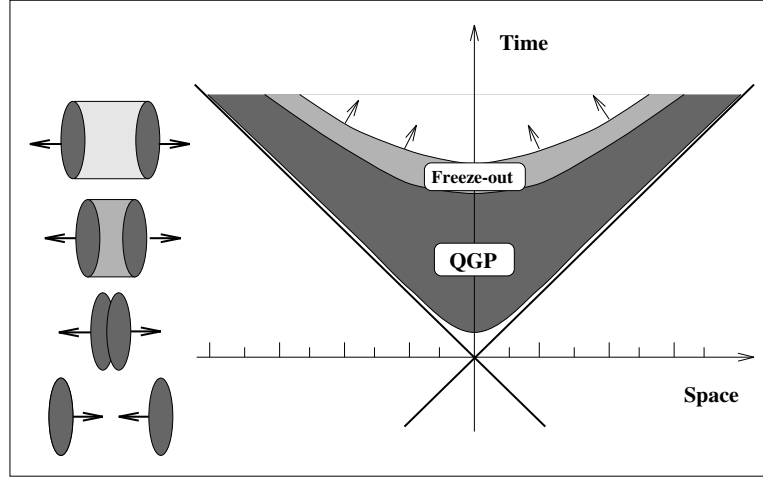


Figure 1.6: Schematic of spacetime evolution of a high energy nucleus-nucleus collision in the center-of-mass frame of two colliding nuclei.

state is formed it will be dominated by parton-parton and/or string-string scattering and the energy density is expected to reach a high value. The transition from a hadron gas to the QGP may occur at or around the Hagedron limit of temperature $T \approx 170$ MeV [7]. The precise value of the transition temperature (T_c) and how high the temperature must rise before the plasma can be considered as weakly coupled, can only be determined by an accurate and nonperturbative simulation of the QCD equation of state. Subsequently the volume of the QGP state rapidly expands and the energy density, temperature and/or baryon density of the fireball decrease. The high energetic quarks and gluons may also produce ‘jets’ which propagate through the medium so created.

- (iii) If a first-order phase transition is assumed, a ‘mixed phase’ is expected to exist between the QGP and the hadronic state, in which quarks and gluons are again confined into hadrons at a critical point. At the mixed phase the entropy density is transferred to lower degrees of freedom and therefore, the system is prevented from a fast expansion and cooling due to the ‘softest point’ defined by a minimum value of energy density/pressure (ε/p) in the equation of state. This leads to a maximum in the lifetime of the mixed phase, which is expected to last for a relatively long time ($\tau > 10$ fm/c) during the softening of the equation of state.
- (iv) The expanding fireball first reaches a chemical freeze-out stage when the inelastic interaction between the partons cease to take place and the relative abundance of every single particle species does no more change. The partons gradually start to recombine and produce different varieties of color neutral particles. In the hadronic phase the system maintains a collective expansion via hadron-hadron elastic interactions, thereby decreasing the temperature of the fireball. As the elastic collisions between

the particles slow down, the expanding system reaches a stage of kinetic freeze-out, and the final state particles freely stream out from the medium.

1.3.2 Experimental Scenario

The experimental studies on high-energy AB interaction has been carried out over about the last four decades. In the early days of high-energy heavy-ion and not so heavy-ion physics, the experimental scenario was dominated by some fixed target programmes like, (i) the Bevatron at Lawrence Berkeley National Laboratory (LBNL), (ii) the Synchrophasotron at Joint Institute of Nuclear Research (JINR), (iii) the Alternating Gradient Synchrotron (AGS) at Brookhaven National Laboratory (BNL) and (iv) the Super Proton Synchrotron (SPS) at CERN. Despite some experimental results suggesting early signal(s) of QGP formation [20], a clear signal in this regard was not confirmed in these fixed target experiments.

Table 1.1: Accelerator facilities in relativistic heavy-ion physics.

Accelerator	Start Year	Max. Energy	Projectiles	Experiment type
Bevalac Berkeley	1984	$< 2A$ GeV	^{12}C , ^{40}Ca , ^{84}Kr , ^{238}U	Fixed target
Synchrophasotron JINR, Dubna	1975	4.5A GeV	^{12}C , ^{24}Mg , ^{20}Ne , ^{28}Si	Fixed target
BNL-AGS Brookhaven	1986	14.6A GeV	^{28}Si	Fixed target
BNL-AGS Brookhaven	1992	11A GeV	^{197}Au	Fixed target
CERN-SPS Geneva	1986	200A GeV	^{16}O , ^{32}S	Fixed target
CERN-SPS Geneva	1994	200A GeV	^{208}Pb	Fixed target
GSI-SIS Darmstadt	2002	2A GeV	^{84}Kr , ^{197}Au	Fixed target
BNL-RHIC Brookhaven	2002	$\sqrt{s_{NN}} = 200$ GeV	^{39}Cu , ^{197}Au	Collider
CERN-LHC Geneva	2008	$\sqrt{s_{NN}} = 5.5$ TeV	^{16}O , Ar, Pb	Collider
GSI-SIS300 Darmstadt	2017	45A GeV	^{59}Ni , ^{197}Au	Fixed target
NICA JINR, Dubna	2017	$\sqrt{s_{NN}} \sim 5A$ GeV	^{197}Au , ^{238}U	Collider

At the beginning of 21st century the experimental study of high-energy nuclear collisions entered into a new era with the Relativistic Heavy-Ion Collider (RHIC) started functioning at BNL. This was followed by the establishment of Large Hadron Collider (LHC) at CERN, making provision for collision energies higher than RHIC more than by an order. For the first time in any terrestrial laboratory, the experiments at RHIC and LHC started to confirm the creation of a color deconfined extended QCD state like the QGP at high temperature and low chemical potential. The analysis, refinement of accumulated data, and physics analysis are still going on. To complement the RHIC and LHC experiments and to study the QCD state of high baryo-chemical potential, the Compressed Baryonic Matter (CBM) experiment is being designed at the Facility for Anti-proton and Ion Research (FAIR) at GSI, Darmstadt, which is expected to be commissioned some time in 2017-'18 [21]. The major heavy-ion programmes undertaken till date are summarized in Table 1.1. Some of the major experimental facilities and their importance in high-energy heavy-ion research are summarily outlined within the limited scope of this thesis.

1.3.3 Experiment at the BNL-AGS

Since 1960, the Alternating Gradient Synchrotron (AGS) has been one of the world's premier particle accelerator facility. The AGS receives proton beam of energy 200 MeV from the linear accelerator (LINAC) of Brookhaven and accelerates it up to energy 33 GeV. The AGS Booster, constructed in 1991, further augments the capability of the AGS, enabling it to accelerate more intense proton beams as well as heavy-ions such to higher energies. Currently the AGS is being used as an injector for the RHIC. Some features of major experiments performed in the BNL-AGS like their major detector component(s) and observable(s), are given in Table 1.2. However, a large number of small experiments were also carried out at the BNL-AGS facility, and the present thesis is based mainly on the data collected from one such experiment (E847).

1.3.4 Experiment at the CERN-SPS

The Super Proton Synchrotron (SPS) was the second largest of CERN accelerators, and now it is embedded with the Large Hadron Collider (LHC). The SPS had about 7 KM circumference with 1317 conventional electromagnets including 744 dipoles to bend the beams round the ring. A proton beam of 400 GeV energy was first extracted from the SPS in 1976 with a flux of 5×10^{12} particles per pulse. Latter SPS was modified to accelerate heavy-ions. The ions partially stripped of their electrons originate from an electron cyclotron resonance, pass through a radio frequency quadrupole, and injected into a LINAC, where

Table 1.2: Four experiments at BNL-AGS: its major detector components and the important observations.

Experiment	Major detector(s)	Observation(s)
E787	Photomultiplier tube (PMT) Drift chamber YALO light pulser	rare decay, specially $K^+ \rightarrow \pi^+ \nu \bar{\nu}$
E802	Zero-degree calorimeter (ZDC) Pb-glass calorimeter (PBGL) Target multiplicity array (TMA) Magnetic spectrometer	E_{ZD}, ρ, η p, \bar{p}, d, π^\pm K^\pm spectrum
E810	Time projection chamber (TPC)	Momenta and angles of charged particles
E814	NaI+U calorimeter Target calorimeter (TCAL) Silicon multiplicity counter Participant calorimeter Forward spectrometer	Transverse energy E_\perp , multiplicity in the forward direction

they are accelerated to an energy of 4.2 MeV. To get rid of the remaining electrons the ions are then allowed to pass through a stripper foil, and then successively accelerated by the proton synchrotron booster and proton synchrotron. The ions come out of the proton synchrotron with an energy of 4.2A GeV, and then pass through another stripper, that completely ionizes them. They are then injected into the SPS and accelerated to the highest possible energies. The ions are extracted at seven different points. Many experiments were performed in the CERN-SPS over a period of almost 22 years. The experiments may be divided into two categories, the ‘Oxygen-Sulfur’ age and the ‘Lead’ age experiments. Short summary of some of the major heavy-ion experiments at CERN-SPS are given in Table 1.3 and Table 1.4 [22]. Like in the BNL-AGS case, many small experiments were performed using the SPS facility too.

1.3.5 Experiment at the BNL-RHIC

The Relativistic Heavy Ion Collider (RHIC) at Brookhaven National Laboratory is one of only two major collider facilities in the world, the other being the CERN-LHC. Also RHIC is the world’s first and only polarized proton collider. RHIC is composed of two independent rings of circumference 3.8 km. containing a total of 1740 superconducting magnets. In principle RHIC can collide any species of nucleon with any other. Since its inception the collider has so far operated at 15 different $\sqrt{s_{NN}}$ values at six different species combinations. The startup of the RHIC in the year 2000 provided a major advancement leading to the discovery of the QGP, which was announced in 2005. The results [23, 24] indicated that

Table 1.3: The Oxygen-Sulfur age ‘large’ experiments at CERN-SPS: its major detector component(s) and the important observation(s).

Experiment	Major detector(s)	Observation(s)
NA34	U-calorimeter Liquid Ar-calorimeter Si-pad detectors External spectrometer	E_{\perp} , $\rho(\eta)$, π^{-} , γ Low mass muon pairs
NA34	Zero degree calorimeter (ZDC) Right calorimeter Photon position detector Streamer chamber Vertex magnet	E_{ZD} , E_{\perp} , $\rho(\eta)$, π^{-} , p , γ , K_s^0 , Λ , $\bar{\Lambda}$
NA36	Time projection chamber	K_s^0 , Λ , $\bar{\Lambda}$, Ξ , Ω
NA38	Electromagnetic calorimeter Di-muon spectrometer	E_{\perp} , J/ψ , muon pair
WA80	ZDC, mid-rapidity calorimeter Mid-rapidity multiplicity detector Large angle multiplicity detector Pb-glass photon detector	E_{ZD} , E_{\perp} , n_{ch} $\rho(\eta)$, γ , π^0
NA85	Ω -spectrometer, MWPC	K^{+} , K^0 , Λ , $\bar{\Lambda}$, Ξ^{\pm}

Table 1.4: The Lead age experiments at CERN-SPS: its major detector component(s) and the important observation(s).

Experiment	Major detector(s)	Particles	$y(\text{lab})$
NA44	Focusing spectrometer Time of flight (TOF)	K^{+}	2.5 – 3.5
NA49	Time projection chamber	K^{+} , K^0 , ϕ Λ , $\bar{\Lambda}$, Ξ^{\pm}	3.0 – 5.0
NA50	Dimuon spectrometer	ϕ	3.0 – 4.0
NA52	Beam spectrometer	K^{+}	1.4 – 6.0
WA97	Silicon Telescope	K^{+} , K^0 , Λ , $\bar{\Lambda}$ Ξ^{\pm} , Ω^{\pm}	2.4 – 3.4

instead of behaving like a ‘gas’ of free quarks and gluons, the partonic matter created in RHIC at $\sqrt{s_{NN}} = 200$ GeV behaves more like an ‘imperfect fluid’. The matter is much more strongly interacting than what was originally expected and possesses a non-zero viscosity [12, 17, 25, 26], which inspired to give it the new name ‘sQGP’ (strongly interacting QGP) [27]. The properties are quite different from the properties of the state of matter created

in CERN-SPS, which also claimed of a ‘new state of matter’ [28]. However, the results in the past two years from Pb + Pb measurements at the CERN-LHC at $\sqrt{s_{NN}} = 2.76$ TeV confirm the RHIC discoveries [23, 24], and add some new information too. Four major collaborative experiments have so far been performed at RHIC. Very brief description of them are given below.

- **The BRAHMS Experiment:** The BRAHMS (Broad Range Hadron Magnetic Spectrometer) setup was one of the smaller detectors of the RHIC. The BRAHMS experiment was designed to measure charged hadrons over a wide range of rapidity and transverse momentum to study the reaction mechanisms of the relativistic heavy-ion interactions and the properties of a highly excited nuclear matter formed in these reactions. The experiment took its first data in the year 2000 and completed data-taking in 2006.

- **The PHOBOS Experiment:** The PHOBOS detector was designed to examine and analyze a very large number of Au ion collisions. For each collision, the detector gives a global picture of the consequences of collision and information about a small subset of the nuclear fragments ejected from the high-energy density region. PHOBOS consisted of many silicon pad detectors surrounding the interaction region. With these detectors it was possible to count the total number of produced particles and study their angular distribution. With this array PHOBOS looked for unusual features, like fluctuations in the number of particles or in their angular distributions. Fluctuations of global/local variables in an event can be a characteristic of phase transition. In order to obtain more detailed information about these events, the PHOBOS detector also has two high-quality magnetic spectrometers, which study 1% of the produced particles in detail. The PHOBOS experiment was able to measure quantities like temperature, size and density of the fireball produced in the collision. It also studied the ratios of various particles produced.

- **The STAR Experiment:** The Solenoidal Tracker at RHIC (STAR) is a detector which specializes in tracking the thousands of particles produced in each collision at RHIC. Unlike other physics experiments where a theoretical idea can be tested directly by a single measurement, STAR makes use of a variety of simultaneous studies in order to draw strong conclusions about the QGP. This is due both to the complexity of the system formed in the high-energy nuclear collision and the unexplored landscape of the physics we study. The STAR detector therefore consists of several types of detectors, each specializing in detecting certain types of particles or characterizing their motion. These detectors work together with an advanced data acquisition and subsequent physics analysis that allows final statements to be made about the collision.

- **The PHENIX Experiment:** The Pioneering High Energy Nuclear Interaction Experiments (PHENIX) is the largest of the four experiments that have taken data at the

RHIC. PHENIX is an exploratory experiment for the investigation of high-energy collisions of heavy-ions and protons. PHENIX is designed specifically to measure direct probes of the AB collisions such as electrons, muons, and photons. The primary goal of PHENIX is to discover and study the QGP. The PHENIX set-up consists of a collection of detectors, each of which performs a specific role in the measurement. The detectors are grouped into two central arms, which are capable of measuring a variety of particles including pions, protons, kaons, deuterons, photons, and electrons, and two muon arms which focus on the measurement of muon particles. There are also additional event characterization detectors that provide additional information about a collision, and a set of three huge magnets that bend the trajectories of the charged particles.

1.3.6 Experiment at the CERN-LHC

The Large Hadron Collider (LHC), the world's largest and most powerful particle accelerator, is the latest addition to CERN's accelerator complex. It consists of a 27 km. long ring of superconducting magnets with a number of accelerating structures to boost the energy of the particles along their path. In the LHC heavy-ion programs, beams of nuclei collide at 30 times higher energies than in RHIC. The objective is to produce nuclear matter at the highest temperatures and densities ever studied in the laboratory, and to investigate its properties in detail. This LHC facility is expected to lead to basic new insights into the nature of the strong interaction between fundamental particles. In the LHC heavy-ion programme three experiments, ALICE, ATLAS and CMS, aim to produce and study this extreme high temperature state of matter and provide novel access to the question of how most of the mass of visible matter in the universe was generated during the first microseconds after the Big-Bang. The ALICE along with LHCb have specialized detectors for analyzing the LHC collisions in relation to specific phenomena. Two further experiments, TOTEM and LHCf, are much smaller in size. They are designed to focus on 'forward particles' (protons or heavy-ions). These are particles that just brush past each other as the beams collide, rather than meeting head-on. Brief summary of the three major heavy-ion experiments at the LHC are given below.

- **The ATLAS Experiment:** ATLAS, being a general purpose detector system, investigates a wide range of physics, including the search for the Higgs boson, extra dimensions, and particles that could make up dark matter. ATLAS has recorded many sets of measurements on the particles created in collisions - their paths, energies, and identities. This is accomplished in ATLAS through six different detecting sub-systems that identify particles and measure their momentum and energy. Another vital element of ATLAS is the huge magnet system that bends the paths of charged particles for momentum measurement.

The interactions in the ATLAS detectors create an enormous data flow. To analyze these data, ATLAS developed a very advanced trigger and data acquisition system and a large computing system.

- **The ALICE Experiment:** The ALICE (A Large Ion Collider Experiment) experiment at LHC is designed to study the collisions of heaviest stable ions (Pb). ALICE studies the physics of strongly interacting matter at extreme energy densities, where the formation of the QGP is expected. For this purpose, ALICE carries out a comprehensive study of the hadrons, electrons, muons and photons produced in Pb + Pb collisions. ALICE is also studying proton-proton (pp) collisions both for the purpose of comparison with Pb + Pb collisions and for physics analysis where ALICE is competitive with other LHC experiments. At the beginning of 2013 just before the LHC shutdown, the ALICE experiment got another opportunity to collect exciting data with the asymmetric p + Pb collisions. These data are crucial for understanding the complexity of the Pb + Pb interaction in many levels and are a necessary supplement for the baseline of pp data. In fact, the data from the p + Pb collisions will represent an ultimate benchmark for the already published results from Pb + Pb collisions. It will definitely allow to decouple the cold nuclear matter effects and thus will shed light to our quest for the QGP.

- **The CMS Experiment:** The Compact Muon Solenoid (CMS) experiment also uses a general purpose detector to investigate a wide range of physics, including the search for Higgs boson, extra dimensions, and particles that could make up dark matter. Although it has the same scientific goals as the ATLAS experiment, it uses different technical solutions and design of its detector magnet system to achieve these. The CMS detector is built around a huge solenoid magnet. This takes the form of a cylindrical coil of superconducting cable that generates a magnetic field of about 4 T. The magnetic field is confined by a steel ‘yoke’ that forms the bulk of the detector’s weight of 12500 tones. An unusual feature of the CMS detector is that, instead of being built in-situ underground like the other giant detectors of the LHC experiments, it was constructed on the surface, before being lowered underground in 15 sections and reassembled.

1.3.7 The FAIR-CBM Experiment

The Compressed Baryonic Matter (CBM) experiment will be one of the major scientific programs in the future Facility for Antiproton and Ion Research (FAIR) in GSI, Darmstadt. Laid out as a fixed-target experiment, the CBM research program will explore the QCD phase diagram in the region of high baryon densities using proton-nucleus and AB collisions at beam energies between 10A to 45A GeV. This includes finding out an appropriate equation of state for the nuclear matter at high densities, search for the deconfinement, detailed study

of the QCD phase diagram and chiral phase transitions [21]. The CBM detector will be so designed as to measure both bulk observables with large acceptance and rare diagnostic probes like charmed particles and vector mesons decaying into lepton pairs. Hadronic, leptonic and photonic observables will be measured with large acceptance. The interaction rates are expected to reach 10 MHz, in order to measure extremely rare probes like charm near threshold. The CBM set-up requires development of novel detector systems, trigger and data acquisition concepts as well as innovative real-time reconstruction techniques.

1.4 Quark-Gluon Plasma

Lattice QCD (LQCD) calculations suggest that a change in the state of matter (phase transition), from a color neutral hadronic system to a color conducting gas of nearly free quarks and gluons, is possible through high-energy heavy-ion interactions. Using the latest accelerator facilities like RHIC and LHC in an AB collision it is possible to produce an intermediate ‘fireball’ of sufficiently high energy/matter density, so that one can call it a ‘state’ having definite equilibrium properties. Of course the ‘fireball’ is not a static system and evolves with time. To talk about its thermodynamics is certainly an oversimplification. Moreover, it has been experimentally established that the ‘fireball’ behaves more like an imperfect fluid possessing a small but finite viscosity, and not like an ideal gas. To begin with a static idealization of the system can still be very instructive. Complexities and finer details of a real system can always be added on at a later stage.

1.4.1 Fireball Thermodynamics

At very high temperature the average kinetic energy is much higher than the rest energy of weakly interacting particles. To an excellent approximation such a system can be treated as a hot relativistic free gas. If moreover, the energy density significantly dominates over matter/baryon number density, as it is the case in RHIC or LHC, then particles and antiparticles will have nearly equal number densities and they can be created or annihilated with equal ease. In such an environment the chemical potential μ can be neglected. On the other hand color deconfinement is also possible at finite chemical potential and at a comparatively low energy density (temperature). Therefore, the color neutral hadronic phase \leftrightarrow QGP phase transition can be studied under different circumstances, e.g., transition from an ideal gas of massless partons (i) to a gas of massless pions, (ii) to a nucleon gas at zero temperature, and (iii) to a system where both the temperature and the mass of the hadronic constituents are finite [29]. We shall discuss the thermodynamics of the first case with a little detail which again offers two possibilities, one for which $\mu_q = \mu_{\bar{q}} = 0$, and the other for which the

chemical potentials are not zero. For the other two cases only very brief references will be made.

• **Case (i)–massless particles with $\mu = 0$:** The number density of the i th species parton is given by,

$$n_i = \int \frac{d^3 p_i}{(2\pi)^3} \frac{1}{\exp(\beta E_i) \pm 1}, \quad (1.22)$$

where $\beta = T^{-1}$ and the $+$ ($-$) sign corresponds to fermions (bosons). If $\beta E_i < 1$ the results are different for fermions and bosons. Setting $p_i \approx E_i$ for relativistic particles and integrating over phase space we find,

$$n_i = \frac{\zeta(3)}{\pi^2} T^3 \text{ for bosons, and } n_i = \frac{3}{4} \frac{\zeta(3)}{\pi^2} T^3 \text{ for fermions} \quad (1.23)$$

where ζ is the Riemann function, $\zeta(3) \approx 1.202$. If $\beta E_i > 1$, then with increasing energy the ± 1 factor in the denominator gradually becomes insignificant, and both distributions get converted to a Maxwell-Boltzmann distribution, yielding identical results. The energy density for a free gas can be computed in a similar way

$$\varepsilon_i = \int \frac{d^3 p_i}{(2\pi)^3} \frac{E_i}{\exp(\beta E_i) \pm 1}. \quad (1.24)$$

The integral results in

$$\varepsilon_i(\text{bosons}) = \frac{\pi^2}{30} T^4, \quad \text{and} \quad \varepsilon_i(\text{fermions}) = \frac{7}{8} \frac{\pi^2}{30} T^4. \quad (1.25)$$

Taking the degeneracy factor g_i associated with the i th species into account and summing over all particle species we get

$$\varepsilon = \sum_i g_i \varepsilon_i = g^* \frac{\pi^2}{30} T^4 \quad (1.26)$$

where $g^* = (g_b + \frac{7}{8} g_f)$ with g_b and g_f are the degeneracy factors, respectively for bosons and fermions. Obviously g^* depends on different degrees of freedom like charge, spin, flavor, color etc., it is an increasing function with increasing temperature. Like at $T \geq 100$ GeV all particles of standard model should be present and contribute to the value of g^* . If QGP can be treated as a relativistic free parton gas then the contribution to g^* from gluons comes from 2 helicity states and 8 colors, while that from each flavor of quarks comes from 3 colors, 2 spin states and 2 charge states. Depending on whether $T >$ or $T <$ the mass of a strange quark there will either be 3 (u, d, s) or 2 (u, d) flavors present in the system. Therefore,

$$\varepsilon_{qgp}(3 \text{ flavor}) \approx 47.5 \frac{\pi^2}{30} T^4, \quad \text{and} \quad \varepsilon_{qgp}(2 \text{ flavor}) = 37 \frac{\pi^2}{30} T^4 \quad (1.27)$$

is consistent with the Stefan-Boltzmann formula. Correspondingly for a free partonic gas (i) pressure $p = \varepsilon/3$, (ii) the entropy per unit volume $s = (\varepsilon + P)/T = 4\varepsilon/3T$, and (iii) the entropy per particle

$$\left. \frac{s}{n} \right|_{\text{bosons}} = \frac{2\pi^4}{45\zeta(3)} \approx 3.6, \quad \text{and} \quad \left. \frac{s}{n} \right|_{\text{fermions}} = \frac{7}{6} \frac{2\pi^4}{45\zeta(3)} \approx 4.2. \quad (1.28)$$

For massless hadrons (pions) ($g_h = 3$) the numbers are

$$n_h = 3 \frac{\zeta(3)}{\pi^2} T^3; \quad p_h = \frac{\pi^2}{30} T^4 \quad (1.29)$$

In the framework of ‘Bag model’ for a QGP state comprised of (u, d, g)

$$p_{qgp} = 37 \frac{\pi^2}{90} T^4 - B \quad (1.30)$$

which under critical condition (maximum pressure) will be equal to p_h ,

$$p_h(T_c) = p_{qgp}(T_c) \Rightarrow T_c = \left(\frac{90}{34\pi^2} B \right)^{1/4} \approx 0.72 B^{1/4} \quad (1.31)$$

Taking the Bag constant (B) for normal hadronic matter $B^{1/4} \approx 200 \text{ MeV/fm}^3$, one gets $T_c \approx 144 \text{ MeV}$ at $\mu = 0$.

Figure 1.7(a) shows the calculated energy density ε as a function of temperature T [30]. At the critical temperature $T_c \sim 170 \text{ MeV}$, the energy density changes rapidly, indicating a rapid increase in the effective degrees of freedom. At T_c not only deconfinement occurs but also chiral symmetry is restored. The pressure variation with temperature is given in Fig. 1.7(b), where it can be seen that in comparison with the rapid increase of energy density, p/T^4 increases at a slower rate. Therefore the pressure gradient in the system ($dp/d\varepsilon$) is significantly reduced during phase transition.

• **Case (i)–massless particles with $\mu \neq 0$:** For non-zero chemical potential one should consider the ‘grand potential’

$$\Omega(T, V, \mu) = -T \ln Z(T, V, \mu) = E - TS - \mu N = -pV \quad (1.32)$$

where the ‘grand partition function’

$$Z(T, V, \mu) = \text{Tr} \exp \left[\frac{\hat{H} - \mu \hat{N}}{T} \right] = \exp \left[-\frac{\Omega(T, V, \mu)}{T} \right] \quad (1.33)$$

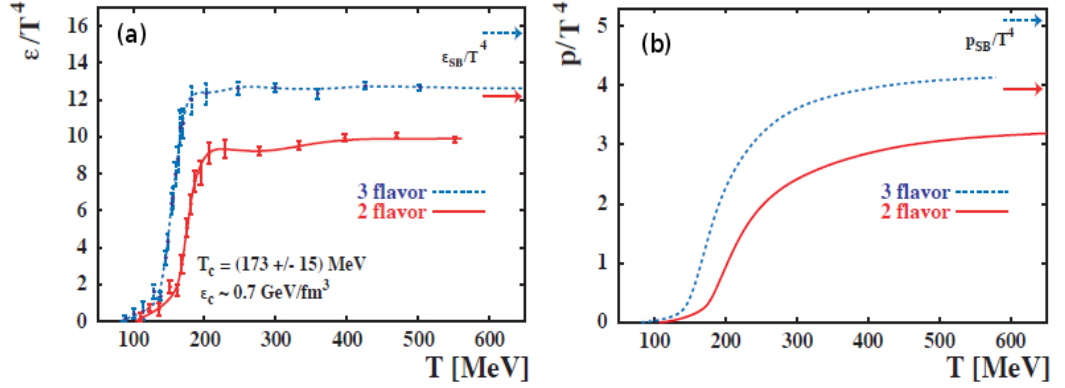


Figure 1.7: (a) Nuclear matter energy density and (b) pressure as a function of temperature from lattice calculation [30]. The arrows in the diagrams indicate the ideal Stefan-Boltzmann values.

and the relevant thermodynamic parameters are,

$$n = \frac{1}{V} \frac{\partial(T \ln Z)}{\partial \mu}, \quad p = \frac{\partial(T \ln Z)}{\partial V}, \quad s = \frac{1}{V} \frac{\partial(T \ln Z)}{\partial T} \quad \text{and} \quad \epsilon = \frac{T}{V} \frac{\partial(T \ln Z)}{\partial T} + \mu n$$

In terms of the occupation number distribution functions

$$\Omega = gVT \int \frac{d^3 p}{(2\pi)^3} \ln [1 \pm \exp \{-(E - \mu)/T\}] \quad (1.34)$$

For massless bosons (e.g., pions and gluons) one can still assume chemical potential to be zero. Also assuming that q and \bar{q} are always produced in pairs one can set $\mu_q = \mu_{\bar{q}}$. The integral that needs to be evaluated is therefore,

$$\begin{aligned} T \ln Z &= \frac{g_f V}{6\pi^2} \int p^3 \left[\frac{1}{\exp \{(E - \mu_q)/T\} + 1} + \frac{1}{\exp \{(E + \mu_q)/T\} + 1} \right] d^3 p \\ &= g_f V \left\{ \frac{7\pi^2}{360} T^4 + \frac{\mu_q^2}{12} T^2 + \frac{\mu_q^4}{24\pi^2} \right\}. \end{aligned} \quad (1.35)$$

Adding up the gluon term the total partition function for a massless quark-gluon systems comes out to be

$$\begin{aligned} T \ln Z|_{qgp} &= \frac{g_b V}{90} \pi^2 T^4 + g_f V \left\{ \frac{7\pi^2}{360} T^4 + \frac{\mu_q^2}{12} T^2 + \frac{\mu_q^4}{24\pi^2} \right\} \\ &= V \left(\frac{37\pi^2}{90} T^4 + \mu_q^2 T^2 + \frac{\mu_q^4}{2\pi^2} \right). \end{aligned} \quad (1.36)$$

Now the relevant thermodynamic parameters like, the net quark number density:

$$n_q = \left(\frac{T}{V} \right) \frac{\partial \ln Z|_{qgp}}{\partial \mu_q} = 2\mu_q \left(T^2 + \frac{\mu_q^2}{\pi^2} \right), \quad (1.37)$$

the energy density:

$$\varepsilon_{qgp} = \left(\frac{T^2}{V} \right) \frac{\partial}{\partial T} \ln Z|_{qgp} + \mu_q n_q = \frac{37 \pi^2}{30} T^4 + 3 \mu_q^2 T^2 + \frac{3 \mu_q^4}{2 \pi^2}, \quad (1.38)$$

the pressure:

$$P_{qgp} = \frac{T \ln Z|_{qgp}}{V} = \frac{37 \pi^2}{90} T^4 + 3 \mu_q^2 T^2 + \frac{3 \mu_q^4}{2 \pi^2}, \quad (1.39)$$

and finally the entropy density

$$s_{qgp} = \frac{\partial T \ln Z|_{qgp}}{\partial T} = \frac{74 \pi^2}{45} T^3 + 2 \mu_q T, \quad (1.40)$$

can easily be obtained. On the other hand the total number density of an ideal gas of massless quark, antiquark and gluons comes out as

$$n_{qgp} = \frac{34 \zeta(3)}{\pi^2} T^3 + 2 \mu_q^3, \quad (1.41)$$

and therefore, the ratio of the dominating terms proportional to T^3 is

$$\frac{s_{qgp}}{n_{qgp}} = \frac{74 \pi^4}{45 \cdot 34 \zeta(3)} \approx 3.92. \quad (1.42)$$

On the other hand for massless pions the corresponding numbers are:

$$\varepsilon_\pi = \frac{\pi^2}{10} T^4, \quad P_\pi = \frac{\pi^2}{30} T^4, \quad n_\pi = \frac{3 \zeta(3)}{\pi^2} T^3, \quad s_\pi = \frac{2 \pi^2}{15} T^3, \quad (1.43)$$

and the ratio $s_\pi/n_\pi \approx 3.6$, is only $\sim 9\%$ smaller than the QGP state, even though the plasma has a larger degree of freedom. Looking at the energy density and/or pressure expressions it is also evident that whether confined within a hadron or within a larger bag, a phase transition requires equal pressure across the transition region. Hence additional positive terms in the form of a potential energy has to be added / subtracted to the respective pion gas expressions and the energy density / pressure of a QGP state confined within a bag will be: $\varepsilon_{QGP} = \varepsilon_{qgp} + B$ and $P_{QGP} = P_{qgp} - B$. With a latent heat $L = 4B$ the phase transition is going to be of first order.

• **Case (ii)–nucleon gas at $T = 0$:** This situation is relevant in the context of the interior of a compact star. We have a QGP state with

$$\varepsilon_{QGP} = \frac{3 \mu_q^4}{2 \pi^2} - B, \quad P_{QGP} = \frac{\mu_q^4}{2 \pi^2} + B, \quad n_{QGP} = \frac{2 \mu_q^3}{\pi^2}, \quad s_{QGP} = 0. \quad (1.44)$$

The nucleons constitute a degenerate Fermi gas at $T = 0$ for which

$$T \ln Z|_N = \frac{g_N V}{6\pi^2} \int_0^\infty \frac{k^4 dk}{E} \frac{1}{\exp[E - \mu]/T + 1}, \quad (1.45)$$

where the nucleon degeneracy factor $g_N = 2$ (spin) $\times 2$ (isospin) $= 4$. The pressure P_N , the nucleon number density n_N and the energy density ε_N for such a system are given as

$$P_N = \frac{M^4}{6\pi^2} \left[r \sqrt{r^2 - 1} \left(r^2 - \frac{5}{2} \right) + \frac{3}{2} \ln(r + \sqrt{r^2 - 1}) \right], \quad (1.46)$$

$$n_N = \frac{T}{V} \frac{\partial \ln Z|_N}{\partial \mu} = \frac{2M^3}{3\pi^2} (r^2 - 1)^{3/2}, \quad (1.47)$$

$$\varepsilon_N = \frac{T^2}{V} \frac{\partial \ln Z|_N}{\partial T} = \mu n_N - P_N = \frac{2\mu}{3\pi^2} (\mu^2 - M^2)^{3/2} - P_N. \quad (1.48)$$

where M = nucleon mass, μ = nucleon chemical potential and $r = \mu/M$. The nucleon number density The latent heat of transition would be

$$\begin{aligned} L &= \varepsilon_{QGP} - \varepsilon_N = \frac{2\mu_q^4}{\pi^2} - \frac{2\mu}{3\pi^2} (\mu^2 - M^2)^{3/2} \\ &= \frac{2\mu_c}{3\pi^2} - \left[\left(\frac{\mu_c}{3} \right)^3 - (\mu_c^2 - M^2)^{3/2} \right], \end{aligned} \quad (1.49)$$

where to comply with the net baryon number conservation we have to set $\mu_c = 3\mu_q = \mu/3$.

• **Case (iii)–finite T , finite mass:** During hadronization of a QGP state at finite temperature a range of particles, mesons, baryons and their antiparticles comprised of up, down and strange quarks are produced. The QGP can still be considered as an ideal gas of massless partons. On the hadronic side the contribution from mesons (with zero chemical potential) comes as

$$T \ln Z|_M = \frac{g_M V}{6\pi^2} \int_0^\infty \frac{k^4 dk}{E} \frac{1}{\exp(E/T) - 1} = \frac{g_M V T^2 m^2}{2\pi^2} \sum_{n=1}^\infty K_2 \left(\frac{nm}{T} \right), \quad (1.50)$$

where m = meson mass, g_M = mesonic degrees of freedom and K_l is modified Bessel function of degree l . The pressure due to this meson gas is

$$P_M = \frac{T \ln Z|_M}{V} = \frac{g_M T^2 m^2}{2\pi^2} \sum_{n=1}^\infty K_2 \left(\frac{nm}{T} \right). \quad (1.51)$$

As $\mu_M = 0$ the energy density would be

$$\varepsilon_M = 3 P_M + \frac{g_M m^3 T}{2\pi^2} \sum_{n=1}^\infty \frac{1}{n} K_1 \left(\frac{nm}{T} \right), \quad (1.52)$$

and the entropy density

$$s_M = 3 \frac{P_M}{T} + \frac{g_M m^2}{2\pi^2} \sum_{n=1}^{\infty} \frac{1}{n} K_1 \left(\frac{nm}{T} \right). \quad (1.53)$$

Correspondingly, the baryon and antibaryon contributions are

$$\begin{aligned} T \ln Z_B &= \frac{g_B V}{6\pi^2} \int_0^{\infty} \frac{k^4 dk}{E} \left[\frac{1}{\exp \{(E - \mu_B)/T\} + 1} + \frac{1}{\exp \{(E + \mu_B)/T\} + 1} \right] \\ &= \frac{g_B M^2 T^2 V}{2\pi^2} \sum_{n=1}^{\infty} \frac{(-1)^{n-1}}{n^2} K_2 \left(\frac{nm}{T} \right) \times [\exp(n\mu/T) + \exp(-n\mu/T)] \end{aligned} \quad (1.54)$$

the pressure

$$P_B = \frac{g_B M^2 T^2}{2\pi^2} \sum_{n=1}^{\infty} \frac{(-1)^{n-1}}{n^2} K_2 \left(\frac{nm}{T} \right) \times [\exp(n\mu/T) + \exp(-n\mu/T)], \quad (1.55)$$

the number density

$$n_B = \frac{g_B M^2 T}{2\pi^2} \sum_{n=1}^{\infty} \frac{(-1)^{n-1}}{n} K_2 \left(\frac{nm}{T} \right) \times [\exp(n\mu/T) - \exp(-n\mu/T)], \quad (1.56)$$

the energy density

$$\begin{aligned} \varepsilon_B &= \frac{T^2}{V} \frac{\partial \ln Z_B}{\partial T} + \mu_B n_B \\ &= 3P_B + \frac{g_B M^3 T}{2\pi^2} \sum_{n=1}^{\infty} \frac{(-1)^{n-1}}{n} K_1 \left(\frac{nm}{T} \right) \times [\exp(n\mu/T) + \exp(-n\mu/T)] \end{aligned} \quad (1.57)$$

and finally the entropy density

$$s_B = 3 \frac{P_B}{T} + \frac{g_B M^3}{2\pi^2} \sum_{n=1}^{\infty} \frac{(-1)^{n-1}}{n} K_1 \left(\frac{nm}{T} \right) \times [\exp(n\mu/T) + \exp(-n\mu/T)]. \quad (1.58)$$

Both the meson and baryon contributions are to be included into the hadron gas. Setting $\mu_c = 3\mu_q = \mu_B$ and $T = T_c$ at the phase boundary one gets

$$P_{QGP} = P_B + P_M \quad \text{and} \quad L = \varepsilon_{QGP} - (\varepsilon_B + \varepsilon_M). \quad (1.59)$$

However, the fireball is a dynamically evolving system. Therefore, instead of using a static thermodynamic description, hydrodynamical models are always preferred.

1.4.2 The Hydrodynamics

Bulk of the particles produced (about 95%) in AB collisions are thermal pions ($p_{\perp} < 2$ GeV/c) associated with ‘soft’ processes. Their distribution will give us a first insight to the overall collision dynamics. The extreme view of complete stopping of the colliding nuclei was implicit in Fermi’s work [31] and described in the hydrodynamical model of Landau [32]. The entire initial longitudinal energy is inelastically transferred to produced particles and redistributed both in the transverse and longitudinal dimensions. In a symmetric AA collision Landau’s model not only assumes complete stopping of the reacting nucleons, but also an accumulation of matter and energy in a single mid-rapidity fireball that subsequently experiences hydrodynamical expansion like an ideal one-dimensional fluid. In this model the maximum achievable energy density is

$$\varepsilon_{\max} = \frac{E_{cm}}{V_A} = \frac{3 \gamma_{cm} \sqrt{s} N_{part}}{4\pi R^3} = \frac{3 s N_{part}}{4\pi m_N R^3}, \quad (1.60)$$

while the dispersion of the Gaussian follows, $\sigma^2 \propto \ln(\sqrt{s}/2m_N)$. A perfect fluid does not have any viscosity and therefore, does not produce any entropy. Using simple thermodynamics of an ideal gas of massless particles one can write

$$s \propto \varepsilon^{3/4} \quad \text{and} \quad T \propto \varepsilon^{1/4} \quad (1.61)$$

As the initial energy density $\varepsilon \propto E_{cm}^2$, and as according to the black body formula the number of produced particles is proportional to the entropy, the produced particle number comes out as, $N \propto E_{cm}^{1/2}$. As a consequence of initial Lorentz contraction, the intermediate fireball evolves predominantly in the longitudinal direction. Landau’s picture suffers from a limitation that the colliding nuclei must possess unrealistically large stopping power, which they don’t have. However, recent works show that combining a quark constituent picture with Landau’s hydrodynamical model, the \sqrt{s}_{NN} dependence of important global parameters like (i) pseudorapidity density of charged particles produced per participant pair, and (ii) charged particle mean multiplicity per participant pair, both measured in the midrapidity region of central AA collisions can be very accurately predicted over a wide collision energy range, \sqrt{s}_{NN} = a few GeV to a few TeV [33]. With increasing \sqrt{s}_{NN} while the midrapidity particle density is found to obey a linear-log increase, the multiplicity data increases following a second-order log-polynomial fit.

With increasing collision energy a non-Gaussian central peak develops into a double hump structure in the net baryon rapidity distribution that widens toward RHIC and LHC energies leaving a plateau in the mid-rapidity, thereby maintaining a boost invariance within the central rapidity region. The observed total E_{\perp} amounts only to a fraction (about 60%) of

its maximum value (E_{\perp}^{max}) that can result from complete stopping. The remaining part is therefore, used to sustain the longitudinal motion. As a result the central fireball fixed in the CMS gets converted to a longitudinally extended firetube i.e., a cylindrical volume containing high energy density, based on relativistic hydrodynamics an idea that was first introduced by Bjorken [19]. Hydrodynamics is a macroscopic approach to describe the dynamical evolution of the expansion stage of a heavy-ion collision. It is assumed that shortly after the collision the strongly interacting matter reaches a state of local thermal equilibrium and subsequently expands adiabatically. The evolution of the system is determined by its initial conditions and the equation of state (EoS) [34, 35], which relates the energy and the baryon density to the pressure exerted by the system, and which is subject to the constraints of local conservation of energy, momentum, and currents (e.g., baryon number). The energy-momentum tensor $T^{\mu\nu}$ and the current density j^{μ} of an ideal non-dissipative fluid are given by,

$$T^{\mu\nu}(x) = [\varepsilon(x) + p(x)]u^{\mu}(x)u^{\nu}(x) - g^{\mu\nu}p(x), \quad (1.62a)$$

$$j^{\mu}(x) = n(x)u^{\mu}(x), \quad (1.62b)$$

where $\varepsilon(x)$ is the energy density, $p(x)$ the pressure, and $n(x)$ the conserved number density at point x and $u^{\mu}(x) = \gamma(x) [1, \vec{v}(x)]$ is the local four velocity of the fluid. Note that $u^{\mu}u_{\mu} = 1$. The conservation laws are written in the form of continuity equations,

$$\partial_{\mu}T^{\mu\nu}(x) = 0 \quad \text{and} \quad \partial_{\mu}j^{\mu}(x) = 0. \quad (1.63)$$

The EoS describes how macroscopic pressure gradients generate collective flow. One has to solve,

$$\partial_{\mu} [(\varepsilon + P) u^{\mu} u^{\nu} - g^{\mu\nu} P] = 0. \quad (1.64)$$

Multiply with u_{ν} and use $u_{\nu} \partial_{\mu} u^{\nu} = 0$ to write

$$u^{\mu} \partial_{\mu} \varepsilon + (\varepsilon + P) \partial_{\mu} u^{\mu} = 0. \quad (1.65)$$

Dropping the transverse co-ordinates one can write,

$$t = \tau \cosh y \quad \text{and} \quad z = \tau \sinh y \quad (1.66)$$

in terms of the spacetime rapidity (y), so that $u^{\mu} = (t/\tau, 0, 0, z/\tau)$, where the Lorentz invariant proper time $\tau = t/\gamma = \sqrt{t^2 - z^2}$ and $u_z = z/t = \tanh y$ is the longitudinal velocity. The Bjorken equation

$$\frac{\partial \varepsilon}{\partial \tau} + \frac{\varepsilon + P}{\tau} = 0$$

can now be arrived at. One can also use $\varepsilon = \lambda P$, where $\lambda = dP/d\varepsilon = c_s^2$, the elastic wave

velocity in the medium, is a constant e.g., $c_s^2 = 1/3$ for an ideal gas of massless particles. Therefore,

$$\frac{\partial \varepsilon}{\partial \tau} + \frac{(1 + \lambda) \varepsilon}{\tau} = 0 \Rightarrow \varepsilon(\tau_f) = \varepsilon(\tau_i) \left(\frac{\tau_i}{\tau_f} \right)^{1+\lambda}. \quad (1.67)$$

From thermodynamics one can write

$$\varepsilon + P = T s + \mu_B n_B. \quad (1.68)$$

For zero net baryon density,

$$d\varepsilon = T ds \text{ and } s = \frac{(1 + \lambda) \varepsilon}{T} \Rightarrow s(\tau_f) = s(\tau_i) \left(\frac{\tau_i}{\tau_f} \right) \quad (1.69)$$

Also,

$$T \frac{ds}{d\tau} = \frac{d\varepsilon}{d\tau} = -\frac{(1 + \lambda) \varepsilon}{\tau} = -\frac{s T}{\tau} \quad (1.70)$$

$$\Rightarrow \frac{ds}{d\tau} + \frac{s}{\tau} = 0 \Rightarrow T(\tau) = (1 + \lambda) \frac{\varepsilon(\tau)}{s(\tau)} = T(\tau) \left(\frac{\tau_i}{\tau_f} \right)^\lambda \quad (1.71)$$

A phase transition from the QGP phase to a hadron gas causes a softening of the EoS. As the temperature crosses the critical temperature, the energy and entropy densities increase rapidly while the pressure rises slowly. The derivative of pressure to energy density (p/ε) has a minimum at the end of the mixed phase, known as the softest point. The diminishing driving force slows down the build-up of flow. The initial conditions which are input parameters, describe the starting time of the hydrodynamic evolution and the relevant macroscopic density distributions at that time. The hydrodynamic evolution is terminated by implementing the freeze out condition which describes the breakdown of local equilibrium due to decreasing local thermalization rates. In noncentral collisions, driven by its internal asymmetric pressure gradients, the system will expand more strongly in the direction of the reaction plane than perpendicular to the reaction plane. As time evolves, the system becomes less and less deformed. To estimate the initial energy density of a Bjorken-type fluid element therefore, one has to go to the fluid rest frame. All particles are originating from a cylindrical volume of cross-section area \mathcal{A} , which actually is the overlap area of the interacting nuclei, and of length $u_z t$. We concentrate on a thin slab of thickness dz centered between the two pancake-like moving nuclei (Fig. 1.8). The point of impact of the collision is assumed to be the origin ($z = 0$) of our frame of reference. Therefore $dz = \tau \cosh y dy$, and ignoring collisions between the produced hadrons, one can write the energy density as,

$$\varepsilon_{BJ} = \frac{\Delta E}{\Delta V} = \frac{E}{\mathcal{A}} \frac{dN}{dz} = \frac{m_\perp}{\pi R^2 \tau} \frac{dN}{dy} = \frac{1}{\pi R^2 \tau} \frac{dE_\perp}{dy}. \quad (1.72)$$

Taking the proper time $\tau \sim 1 \text{ fm}/c$ and (dN/dy) to be the central rapidity density of

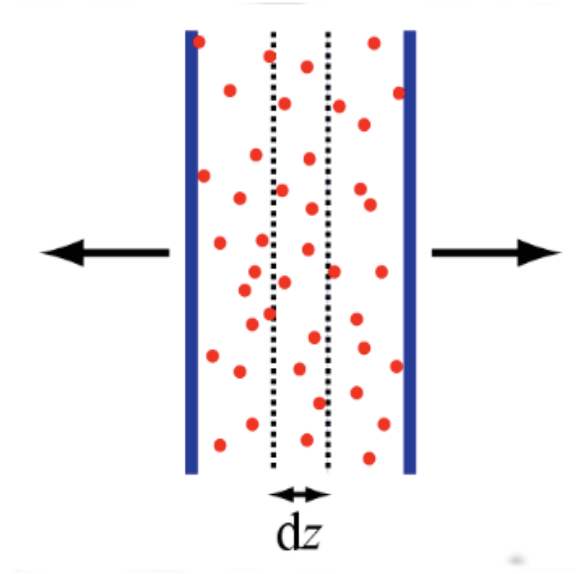


Figure 1.8: Bjorken model of nucleus-nucleus collision.

produced particles, this relation was first derived by Bjorken [19]. However, a perfect fluid must undergo an isentropic expansion, and the entropy of the expanding fireball S should be a conserved quantity. In terms of entropy density $s = S/V$ for one-dimensional expansion, therefore to compensate the Lorentz contraction a relation like $s_i \tau_i = s_f \tau_f$ should hold between an initial (τ_i) and final (τ_f) proper time. As it will be shown later, for massless particles, $\varepsilon = g \frac{\pi^2}{30} T^4$ and $s \propto T^3$, where T is the temperature and g is number of the degrees of freedom. Correspondingly,

$$T_i^3 \tau_i = T_f^3 \tau_f \Rightarrow \tau_f = \tau_i \left(\frac{T_i}{T_f} \right)^3 \quad \text{and} \quad \varepsilon_f = \varepsilon_i \left(\frac{\tau_i}{\tau_f} \right)^{4/3} \quad (1.73)$$

which is in contradiction with Bjorken's formula, $\varepsilon_{BJ} \sim \tau^{-1}$. The energy density formula should therefore, be modified as

$$\varepsilon = \frac{1}{\pi R^2 \tau_0} \frac{dE_\perp}{dy} \left(\frac{\tau_f}{\tau_i} \right)^{1/3} = 2 \varepsilon_{BJ}. \quad (1.74)$$

1.4.3 QCD Phase Diagram

The phase diagram (pressure vs temperature) of water has three broad regions separated by phase transition lines, the triple point where all three phases coexist, and the critical point where the vapor pressure curve terminates and two distinct coexisting phases, namely liquid and gas, become identical. Such a diagram is shown in the left panel of Fig. 1.9. In contrast the QCD phase diagram is known only schematically [11]. In high-energy AB collisions we expect two transitions to take place, one is the color deconfinement and the

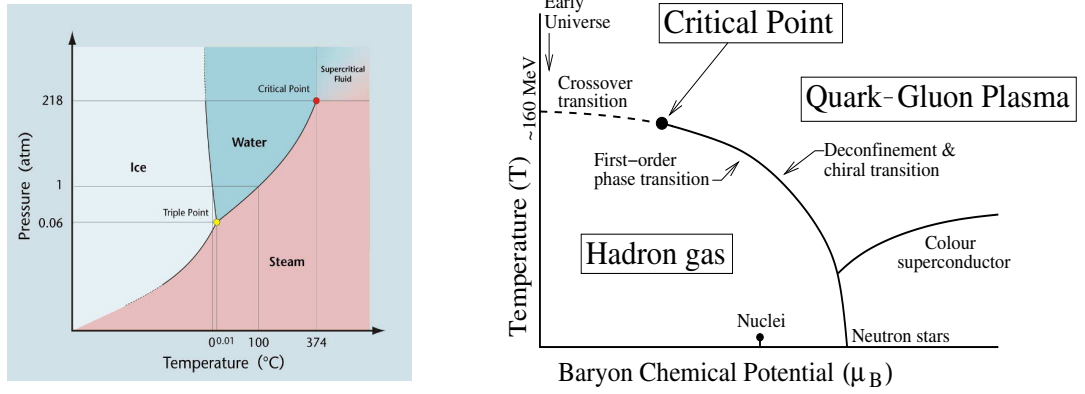


Figure 1.9: Phase diagram of water (left). A schematic phase diagram of QCD matter (right).

other is the restoration of chiral symmetry. The order parameters are the Polyakov loop for the former and quark condensate for the latter, neither of which can unfortunately be measured in experiments. LQCD and common wisdom however suggest that both should occur at a common T_c at least at small μ_B . LQCD also predicts a crossover transition around $T \sim 150 - 170$ MeV for vanishing μ_B . As mentioned, there are two extreme conditions of QGP to hadron phase transition, (i) at high temperature and at zero net baryon density, and (ii) at high baryon density and at zero temperature. For a system in between these two limits, there is a pressure arising from the thermal motion of the particles as well as from the degeneracy of the fermion gas. Thus, for a system having non-zero pressure and temperature, the critical temperature shall be placed in between the two extreme limits. The study of the intermediate region of the phase diagram is quite complicated as perturbation theory cannot be applied to QCD near T_c , and furthermore at finite baryon density the usual lattice approach fails [36, 37]. Therefore, one of the major objectives of high-energy heavy-ion physics is to explore the QCD phase diagram in the various temperatures and baryon density regions so as to confirm the existence of new phase of nuclear/partonic matter. Arguments based on a variety of other models indicate a first order phase transition as a function of T at finite μ_B , which one expects to terminate at a critical point [37]. The existence of the critical point, however, is not yet established in experiments. Apart from the region of color neutral hadrons at the low T and low μ_B , and the region of quarks and gluons at high T and high μ_B , there is also a region characterized by the color superconductivity, at high μ_B and low T . However, precise boundaries separating these regions are not yet known. Mapping the QCD phase diagram at least at a quantitative level, is possible by using LQCD. Although it allows first-principle calculations, there are technical difficulties for non-vanishing μ_B . There exist however, various other effective theories and phenomenological models [38] which form the basis of the schematic QCD phase diagram (μ_B against temperature T), shown very naively in the right panel of Fig. 1.9. Experimental tools available to explore such a diagram

are the relativistic heavy-ion accelerators. Apart from the terrestrial facilities, astronomy of neutron stars can also shed some light on the low T and high μ_B region of the phase diagram. Unlike a system in global equilibrium, here temperature and chemical potential may depend on space-time coordinates.

1.4.4 Signals of QGP

We know that the central fireball created in a high-energy AB collision expands very rapidly, and we observe as an outcome a large number of color neutral hadrons, leptons and photons streaming out of the collision debris. One needs to identify appropriate experimental tools (signals) for detecting the quark-gluon plasma, and to study its properties, if it is at all created. The problems associated with such a task are, (i) the volume filled up with QGP is at most several fermi in diameter and (ii) the time scale for which such a state exists ~ 5 to 10 fm/c [39, 40]. Moreover, signals of QGP are often shadowed under a huge background particles emitted from the hot hadronic gas. Different types of experimental probes have been put forward to examine different stages of the hot and dense matter as it expands and evolves back to normal color neutral hadronic state. There are some soft probes and some hard probes [35, 36]. Arranging in increasing order of hardness they are, (i) global observables—multiplicity distribution and rapidity distribution, (ii) geometry of emitting source—HBT, impact parameter via zero-degree energy flow, (iii) early state collective effects—elliptic flow, (iv) chiral symmetry restoration—neutral to charge ratios, resonance decays, (v) fluctuation phenomena—event-by-event particle composition and spectra, (vi) degrees of freedom as a function of T —hadron ratios and spectra, dilepton continuum, direct photons, (vii) deconfinement—charmonium and bottomonium spectroscopy, (viii) energy loss of partons in QGP—jet quenching, high p_\perp spectra, open charm and open beauty. A qualitative discussion on some of these are furnished below.

- **Hanbury-Brown–Twiss (HBT) Effect:** Identical particle correlation or interferometry, provides information on the reaction geometry, and hence provides important information about the spacetime dynamics and system lifetime of nuclear collisions. The information about the spacetime structure of the particle emitting source created in AB collisions obtained from the measured particle momenta, can be extracted by the method of the so called ‘two-particle intensity interferometry techniques’ also called the ‘Hanbury-Brown–Twiss’ (HBT) effect [41, 42]. The method was initially developed to measure the angular size of distant stars [43]. The two-particle correlation arises from the interference of particle wave-functions, where interference is defined as a phenomenon associated with the superposition of two or more waves. Such correlation depends on whether the particles are bosons or fermions. Also the degree of interference depends on the degree of coherence of the emitting

source of particles produced in such collisions, which reaches a maximum for a completely incoherent source. HBT is a useful method to understand the crucial reaction mechanism and equation of state (EoS) of the particle emitting source in relativistic heavy-ion collisions [44] where the QGP is expected to be formed. LQCD predicts a very soft EoS near about the QCD critical point ($T_c = 173 \pm 15$ MeV), and a sudden decrease in $dp/d\varepsilon$ ($= c_s^2$) value from what is obtained in the $T > 2T_c$ region [30], c_s being the speed of sound in QCD medium.

• **Collective Flow:** The particles produced in a high energy AB collision show a high degree of collective behavior which is termed as flow [45]. Due to spatial asymmetry of the overlapping volume of the colliding nuclei, the pressure gradient generated at an early stage of collision leads to an anisotropic transverse collective flow during the expansion of the hot and dense matter [46]. By characterizing asymmetric azimuthal distribution of particles emitted from non-central collisions, we can understand the extent of this outward pressure. When decomposed into Fourier components the invariant azimuthal distribution

$$\frac{d^3N}{d^3p} = \frac{1}{2\pi E p_\perp} \frac{d^2N}{dp_\perp dy} \left[1 + \sum_{i=1}^N 2v_n \cos\{n(\phi - \psi_{RP})\} \right] \quad (1.75)$$

has many non-zero coefficients. Here E , p_\perp , y , and ϕ are, respectively the energy, transverse momentum, rapidity and azimuthal angle of the produced particle, and ψ_{RP} is the azimuthal angle of the reaction plane which is defined as the plane spanned by the impact parameter vector and the beam direction. The first coefficient v_1 measures the ‘direct flow’ while the second coefficient v_2 is called the ‘elliptic flow’ and so on. The v_2 coefficient, almost in all high-energy AB collisions, is found to be the largest [47]. Such type of Fourier decomposition really measures particle emission directly correlated with the orientation of the density gradients as shown by the fact that v_2 for all charged particles at low transverse momenta scales linearly with the *eccentricity* of the overlap region of the colliding nuclei [48]. In the high- p_\perp region hadronization occurs through fragmentation, whereas in the medium- p_\perp region it is modeled by quark recombination or coalescence. The phenomenon of constituent quark number scaling provides experimental support to this model. When scaled by the constituent quark number, the v_2 against E_\perp curves merge into one universal curve, suggesting that elliptic flow actually develops at the quark level, and hadrons form through merger of constituent quarks.

• **Chiral Symmetry Restoration:** The approximate ‘chiral symmetry’ of QCD is spontaneously broken by the existence of a quark condensate in vacuum [39]. Due to large energy deposit in the collision zone of the relativistic collisions, if the QGP is formed then the medium would possess chiral symmetry. But the rapid expansion at earlier times suddenly reduces the temperature down, and the symmetry is spontaneously broken [49]. Lattice

simulations predict a very rapid drop of the scalar quark condensate $\langle q\bar{q} \rangle$ from its vacuum value to almost zero in a narrow temperature region around T_c . The temporary restoration of chiral symmetry in nuclear collisions may result in the formation of domains of disoriented chiral condensate [40].

- **Event-by-event Fluctuation:** Another set of global observables are related to *fluctuations*, which are of fundamental importance for studying perturbation to a thermodynamic system [39]. Several thermodynamic quantities show varying fluctuation patterns when the system undergoes a phase transition [50]. In the study of phase transition the measurement of particle number density, energy and charge fluctuations are relevant. Event-by-event fluctuations of thermodynamic quantities measured in high-energy heavy-ion collisions provide a reasonable framework for studying the nature of the QGP to hadron phase transition in the laboratory [51]. As for example, the fluctuations in the total charge contained in an ideal gas sub-system comprising of $N (= N_+ + N_-)$ particles is given by, $\langle \delta Q^2 \rangle = q^2 \langle N_+ + N_- \rangle$ where N_{\pm} are the number of positively and negatively charged particles. Obviously the above quantity is sensitive to the square of the charge q of the constituent particles, which should be smaller for a quark-gluon system than a color neutral hadronic system. The ration of charge fluctuation per entropy is four times larger in a pion gas than that in a 2-flavor QGP. Even if the contribution from hadronic resonances is taken into account the above factor reduces to three, thereby leaving a genuine signal for a QGP state.

- **Strangeness Enhancement:** The production of hadrons containing s quarks is normally suppressed in hadronic reactions compared with the production of hadrons containing only u and d valence quarks. This suppression increases with growing strangeness content of the produced hadrons. The theoretical studies have shown that strangeness is produced rapidly in the collisions of thermalized gluons, within the deconfined state formed in heavy-ion collisions [52, 53]. When QGP is formed, the production of hadrons carrying s quarks is expected to saturate because of s quark content of the plasma is rapidly equilibrated by $s\bar{s}$ pair production in the interaction between two gluons. So the yield of multi-strange baryons and strange antibaryons is predicted to be strongly enhanced [54] in a QGP medium. The deconfined state of QGP breaks up in a fast hadronization process with the enhancement of strange hadrons and strange anti-baryons, along with the rise of valence quark content of hadrons produced as the predicted property of deconfined phase [54]. This occurs due to the breakup of strangeness rich deconfined states (or hadronization), where several strange quarks are formed before and the independent reactions can combine into a multi-strange hadron.

- **Dilepton production:** Leptons are produced at an early stage of the collision and they can probe the very interior of the hottest stage of evolution of the fireball. The produced lepton pairs (l^{\pm}) carry information regarding the thermodynamical state of the medium at

the moment of their production. The production rate and the momentum distribution of the dilepton pairs depend on the momentum distribution of quarks and antiquarks present in the plasma, which in turn are governed by the thermodynamic condition [36]. In high energy AB collisions a probable formation of QGP is not the only source of dilepton production. There exist other processes, like the Drell-Yan process, which is important for large values of the invariant mass of the l^\pm pair [36, 55]. In the Drell-Yan process a valence quark of a nucleon of one of the colliding nuclei interacts with a sea antiquark of a nucleon belonging to the other nucleus. The $q\bar{q}$ pair annihilates to form a virtual photon (γ^*), which subsequently decays into a l^\pm pair. In addition a large fraction of the dilepton yield arises from the decay of long lived states, such as the neutral pions, eta, or the omega mesons. These resonances decay well outside the hot and compressed region and therefore, in order to extract information regarding the properties of hot and dense matter, a detailed analysis of the dilepton spectra, like in medium modification of hadron properties, is needed. In the low mass region, below the ϕ -meson mass limit, the most important production channels are, (i) delayed decay of $\eta, \Delta, \omega, a_1$ and (ii) direct decay of the vector mesons such as ρ, ω and Φ . Therefore, in order to separate out the portion of invariant mass spectrum of l^\pm due to QGP, it is essential to analyze the contribution from all other sources of dilepton production [55].

- **Thermal Photon production:** Photons are emitted throughout the expansion process, but their production is expected to be weighted more toward the hot and dense early stages of the collision. The photon production schemes in heavy-ion collision are complex in nature, and they may grossly be classified into four groups [56] namely, (i) the hard partonic scattering produces photons that falls off at large transverse momentum—such production rates can be calculated by making use of the perturbative QCD; (ii) photons are emitted in the collisions between quarks and gluons in the QGP medium—the energy spectrum of such photons is damped exponentially having a long tail extended up to several GeV; (iii) during hadronization the produced hadrons collide with other hadrons and resonances (ρ, ω)—such collisions may emit photons with energy values ranging from several hundred MeV to several GeV; (iv) photons can also be the decay products of the neutral mesons like π^0, η etc., emerging at the end of the thermal evolution and have energies in the range of $< 10^2$ MeV. Note that π^0 and η mesons can also be produced in hard partonic scattering at the early stage of the collision having several GeV of energy, and can subsequently decay into high p_\perp photons. These photons together with those mentioned in category (i) appears as a background to the thermal photons produced in category (ii) and (iii), which carry the information of the hot and dense matter produced in high-energy AB collisions [57].

- **Charmonium Production:** If a J/ψ particle, a bound state of $c\bar{c}$, is placed in QGP, the color charge of c will be screened by the quarks, antiquarks and the gluons on the plasma. The basic mechanism for deconfinement in the dense QGP is the Debye screening of the

quark color charge. The effect of Debye screening will modify the the long-range Coulomb potential into a short-range Yukawa potential with the range given by Debye screening length λ_D . Note that in a QGP the string tension between two quarks κ vanishes. When the screening radius becomes less than the binding radius of a quark-antiquark system, which means that it becomes less than the hadron radius, the confining force can no longer hold the quark-antiquark pair together and hence deconfinement sets in. The J/ψ has a radius of about 0.2 fm [58]. which is much smaller than the normal hadronic scale $\lambda_{QCD}^{-1} \approx 1$ fm. having a binding energy of 0.6 GeV which is larger than $\lambda_{QCD} \approx 0.2$ GeV. λ_{QCD} is called the QCD scale parameter to be determined from experiments. In AB collisions the J/ψ particles are produced in the initial stage of hard scattering. The suppression of J/ψ production in a quark-gluon plasma occurs because a $c\bar{c}$ pair formed by fusion of two gluons from the colliding nuclei cannot bind inside the quark-gluon plasma. Hence the effect of plasma will make the J/ψ unbound, thus the suppression of J/ψ production could be a possible signature of QGP formation [59]. There is however, an alternative proposition about charm production in AB collisions. As a hard process, charm production increases with collision energy at a much faster rate than that of the light quarks. At sufficiently high-energy the produced medium will therefore, contain more charm quarks than present in a QGP at chemical equilibrium. If these charm and anti-charm quarks combine at the hadronization point statistically to form charmonium states, the new combination mechanism should lead to a much enhanced J/ψ production rate, even if all primary (direct) J/ψ 's are dissociated [60]. The two predictions, sequential suppression against statistical regeneration, thus represent two really contradictory viewpoints, and the LHC results should be able to substantiate either (or both) of them [61].

- **Jet Quenching:** Hard-scattered partons (quarks and gluons) produced internally in AB collisions can be used to probe the medium in which it is produced. Nucleons belonging to the colliding nuclei may interact with each other and produce partons with large transverse momenta, which subsequently fragment and emerge as jets of particles in the final state. Hard partons are produced early in the collision, and therefore, they can probe the early stages of collision. Moreover, their production rate can be calculated using perturbative QCD. Partons/jets are color carrying objects and therefore, they interact strongly and lose more energy (or get quenched) in a QGP-like medium than in a color neutral hadronic matter. Among other factors the amount of energy loss depends on the path length the jet has to travel inside the medium. The yields of high- p_\perp pions and etas are found to be suppressed by a factor of about 5. Such suppressions are not seen either in $d + Au$ or in $p + Pb$ collisions where QGP formation is not expected, thereby ruling out suppression by cold nuclear matter [62]. These observations indicate that hard partons lose energy as they traverse the hot medium and jet suppression is therefore, a final-state effect. Jet quenching in hot dense matter can also be studied in terms of dihadron correlations as a function of

opening angle between a high- p_{\perp} trigger and associated particles. In the azimuthal plane of AB collisions there is always an enhanced high- p_{\perp} jet production in the near side than in the away side, a phenomenon that is absent in proton-proton or in proton-nucleus collisions. When soft (low- p_{\perp}) hadrons are included into trigger, jets appear in both near and away sides in all types of interactions.

1.5 Models of AB Interaction

In order to get a complete description of a high-energy AB collision, the QCD must be employed without any approximation. But as we know, due to the intrinsic complexities associated with the QCD, nonperturbative effects are to be treated through model calculations. Unfortunately, till date we do not have any complete model that describes all stages of space-time evolution process in an AB collision. The hadronic models, where an AB interaction is considered as a superposition of many NN interactions, try to simulate the entire history of the space-time evolution, and any deviation observed in comparison with measurement is considered as a collective effect. Models based on string fragmentation mechanism(s), parton shower cascade and transport mechanism focus on the initial pre-equilibrium stage of the interaction. Hydrodynamical model, on the other hand, mainly describes various equilibrium stages of the space-time evolution. In this section a brief description is given for some of the phenomenological models and theory that are currently being used by the heavy-ion community.

1.5.1 RQMD and UrQMD

The Relativistic Quantum Molecular Dynamics (RQMD) model is designed to give a complete description of an AB collision, that starts from the initial overlapping of the colliding nuclei and ends at the final freeze out state when strong interaction among the outgoing hadrons ceases to act. This is a semi-classical microscopic transport theory, where the incoming objects are represented by their classical trajectories and the interactions are treated stochastically [63]. The model nicely works in the BNL-AGS and CERN-SPS energy domains. At high-energy ($E_{\text{lab}} > 10A$ GeV) AB collisions, a Glauber type sequence of multiple scatterings is generated on the partonic level. Strings and resonances are excited in elementary NN collisions, where the strings can overlap to form chromoelectric flux tubes called the ‘ropes’. Secondary particles are produced through the fragmentation of resonances, strings and ropes. Subsequently, the fragmentation products interact with each other and also with the original nucleons, mostly via binary collisions. For this purpose a relativistic Boltzmann equation has to be solved for hadrons in the final stage of the collision.

These interactions drive the system toward equilibration and are the underlying mechanism which makes collective flow to develop even in the pre-equilibrium stage. In this model, the equilibrium pressure is simply due to an ideal gas of hadrons and resonances. The resulting equation of state in the cascade mode of RQMD is similar to the one in ref. [64].

The Ultra-relativistic Quantum Molecular Dynamics (UrQMD) [65] is based on analogous principles as the RQMD but with a vastly extended collision term. The range of applicability of UrQMD includes the SIS energy region ($\sqrt{s} \approx 2$ GeV) up to the RHIC energy ($\sqrt{s} = 200$ GeV). Currently, the model has been employed to simulate LHC events as well. In the UrQMD model the projectile and the target nuclei are treated according to a Fermi gas ansatz. In this scheme particle production at high-energy is implemented by the color string fragmentation mechanism similar to the Lund model [66]. The UrQMD code has been successfully used to reproduce the particle density distributions and the p_{\perp} spectra of various particle species in proton-proton, proton-nucleus and AB collisions. At $\sqrt{s_{NN}} \approx 10$ GeV the model can reproduce the elliptic flow parameter reasonably well. However, the model does not incorporate the symmetry aspects of the fields associated with the identical particles, and it predicts very small HBT radii. As the UrQMD code has been utilized to generate $^{28}\text{Si-Ag/Br}$ event sample at 14.5A GeV incident energy that has been used in the present investigation, we shall give a detailed description of the model in Section 2.5. The advantage of using transport models like RQMD or UrQMD is that they treat the final freeze-out stage dynamically, do not make any equilibrium assumption, and describe the dynamics of a hadron gas like system very well in and out of the chemical and/or thermal equilibrium. Therefore, AB interactions where it is less likely for the intermediate ‘fireball’ to reach a local equilibrium, these models are very useful.

1.5.2 HIJING

Heavy Ion Jet Interaction Generator (HIJING) [67] is a MC event generator developed to study jet and associated particle production in high-energy pp , pA and AB collisions. HIJING combines a QCD inspired model for jet production with the Lund FRITIOF [66] and Dual Parton model [68] for soft processes at intermediate energies ($\sqrt{s} \lesssim 20$ GeV/nucleon), and presents a successful implementation of pQCD process in PYTHIA model [69] for hadronic collisions. The model is designed mainly to explore the range of possible initial conditions that may occur in relativistic heavy-ion collisions. Nuclear shadowing of parton (specially the gluon) structure functions and a schematic model of final state interaction of high p_{\perp} jets in terms of an effective energy loss parameter dE/dz , have been included into the model to study the nuclear effects. To generate the initial phase space distribution for the parton cascade, the formation time for each parton is determined according to a

Lorentzian distribution with a half-width $t_f = E/m_\perp^2$, where E is the parton energy with transverse mass m_\perp . During the time of formation partons are considered to be part of the coherent cloud of parent nucleons and hence they do not suffer rescattering. Once the partons stop interacting, after an additional proper time of about 1.2 fm. they are converted into hadrons according to the HIJING fragmentation scheme.

1.5.3 AMPT

The AMPT (A Multi-Phase Transport) model [70] is an example of a hybrid type transport model. The initial conditions of AMPT are obtained from the HIJING that uses a Glauber formalism to determine the positions of participating nucleons. AMPT uses Zhang's Parton Cascade (ZPC) formalism [71] for fixing the scattering properties of partons. Note that the ZPC model includes only parton-parton elastic scattering with an in-medium cross section derived from pQCD along with an effective gluon screening mass taken as a parameter. After the minijet partons stop interacting, they are combined with their parent strings. The hadronization process is settled either by using the Lund fragmentation or by a quark coalescence scheme. The string fragmentation mechanism is same as that implemented in the PYTHIA program [72]. The final state hadronic scatterings are then modeled by a relativistic transport (ART) model [73]. In the AMPT model, there also exists a string melting scenario in which hadrons, that would have been produced from string fragmentation, are converted instead to valence quarks and antiquarks with their current quark masses [74]. Interactions among these partons are again described by the ZPC parton cascade model. As there are no inelastic scatterings, only quarks and antiquarks from the melted strings are present in the partonic matter. The transition from partonic matter to hadronic matter is achieved using a simple coalescence model, which combines two nearest quark and antiquark into mesons and three nearest quark(s) and/or antiquark(s) into baryons/antibaryons. The particle type is determined by the invariant mass of these partons. The users thus have a choice of using either of these two modes of particle production. In the default configuration of AMPT the energy of the so-called excited strings are not used in the partonic stage and only released in the hadronization stage, as it was implemented into the Lund string fragmentation model. On the other hand as mentioned above, in the string melting (SM) configuration of AMPT all excited strings are first converted (melted) into partons, and at the end of interaction stage the left over partons are combined into either mesons or baryons through a quark coalescence mechanism.

1.6 Multiparticle Production

A high-energy AB interaction is usually considered to be a superposition of many nucleon-nucleon (NN) collisions. In an AB collision each nucleon may rescatter several times and the produced partons from different NN collisions can also rescatter with each other before hadronization. Both these factors influence the particle production phenomena per participating nucleon in an AB interaction. In the final state a large number of particles comprising mostly of various types of hadrons, along with some photons and leptons are observed. The hadrons are created in the freeze-out stage which is a relatively late stage of the fireball expansion [75–77]. Therefore, they provide only indirect information of the intermediate equilibrated stage(s), if there is any. However, the hadrons are very abundant, they can be easily identified and their kinematic properties can be accurately measured. We can expect that there will be some rare but interesting events showing something exotic and unusual, while on the other a large majority of events will exhibit regular features e.g., a finite number of particles will come out with different energy-momentum values from each event. To extract any kind of nontrivial physics these regular events have to be subjected to rigorous statistical analysis. The particle number will vary from event to event which for a large event sample will result in a distribution of the particle multiplicity as well as distributions in terms of different kinematic variables. The primary objective of the present thesis is to analyze some of these distributions in a particular AB interaction, and therefore, in the following subsections we summarily outline some of the issues related to multiparticle production, some of which will subsequently be discussed in details.

1.6.1 Particle Density Fluctuation

The study of fluctuation of various final state observables drew an extra attention since the early days of high-energy collision experiments. Fluctuation in the density distribution of particles produced in AB collisions itself can render a lot of information on multiparticle dynamics, and this actually is the subject matter of our present investigation. Of course, there is always a trivial statistical component (noise) associated with the observed fluctuation that has to be carefully eliminated. The *nonstatistical* (also called *dynamical*) component of density fluctuation that results from some nontrivial dynamics is not yet fully understood. Efforts have been made to interpret the dynamical component of density fluctuation observed within narrow phase space intervals (local pattern) in AB interactions in terms of phenomena like (i) Bose-Einstein correlation, (ii) jet structure of particle emission, (iii) resonance decay, (iv) collective phenomena, (v) parton shower cascade mechanism and (vi) some exotic process like the thermal/non-thermal phase transition etc.. Various methods have been developed to characterize the dynamical component in terms of a small number

of well behaved parameters. A brief item-wise discussion on some of the statistical techniques used to study local density fluctuations of multiparticle production are summarily discussed below. Almost all of these issues will later be discussed in details with reference to the results obtained from the present investigation along with the corresponding physics analysis.

- **Intermittency:** The factorial moment of order q (a +ve integer) is defined as,

$$n^{[q]} = n(n-1) \cdots (n-q+1) \quad (1.76)$$

where n is the particle multiplicity in an arbitrary sub-interval (bin) of width say $\delta X = \Delta X/M$ of the variable X , ΔX being the overall domain of the variable under consideration which is divided into M non-overlapping equal sub-intervals. When properly normalized with respect to the average particle number per bin and averaged over a number of bins as well as over a large sample of events, the normalized factorial moment F_q scales with the phase space resolution size δX [78, 79]

$$F_q \propto \delta X^{-\phi_q} : \quad \delta X \rightarrow 0 \quad (1.77)$$

In multiparticle production physics the above relation for $\phi_q > 0$ is known as *intermittency*. The intermittency exponent ϕ_q used for characterizing turbulence in the theory of chaos to describe the development of a hydrodynamical system from a stable to a chaotic state, can analogously be used in particle production [80], and it can be determined from the asymptotic behavior of the scaling-law (1.77). For a *self-similar* density function F_q is found to follow such a scaling relation [78–80]. The technique first proposed by Bialas and Peschanski [78] to analyze a few high multiplicity JACEE events induced by high energy cosmic ray nuclei [81], has so far been extensively used to study local fluctuations of particle densities in high-energy collisions involving various combinations of target-projectile and collision energy (for review see refs. [82, 83]). In AB collisions the intermittency parameters may contain signatures of some kind of phase transition [84]. In view of self-similarity dominating the particle production process contradictory suggestions have also been made [85].

- **Cumulant Moment:** Evidence of genuine higher order particle correlations can be obtained only after subtracting their contribution originating from lower order(s). For this purpose one can study the *cumulant moments* (K_q) and the *oscillatory moments* (H_q). The F_q and the K_q moments are related by a recurrence relation

$$F_q = \sum_{j=1}^{q-1} \binom{q-1}{j-1} F_{q-j} K_j + K_q; \quad \text{for } q \geq 2. \quad (1.78)$$

H_q is now defined as the ratio $H_q = K_q/F_q$. According to a QCD parton shower cascade model [86] the H_q moments should oscillate with order number q about the $H_q = 0$ line. Almost all the correlation studies (just to cite a few of them [87–90]) have showed the validity of the α -model and some of them are also in agreement with the QCD based parton shower cascade model mentioned above [86].

- **Factorial Correlator:** While the SFM is used to look into the local (dynamical) density fluctuation, the two-fold factorial moment or *factorial correlator* (FC) provides a bin-to-bin correlation of fluctuations within an event. Hence, the FC provides information on the dynamics of particle production beyond that obtained from single particle inclusive spectra. According to the α -model of particle production [79], factorial correlator (F_{pq}) calculated for two equal sized non-overlapping bins (say m -th and m' -th) separated by a distance D called the correlation length, defined as

$$F_{pq} = \frac{\langle n_m^{[q]} n_{m'}^{[q]} \rangle}{\langle n_m^{[q]} \rangle \langle n_{m'}^{[q]} \rangle} \quad (1.79)$$

depends only on D and not on δX . F_{pq} follows a scaling relation like

$$F_{pq} \sim D^{-\phi_{pq}}. \quad (1.80)$$

The exponent ϕ_{pq} measures the correlation length, and according to the α -model the exponent ϕ_{pq} is expected to follow a relation like, $\phi_{pq} = (p.q) \phi_{11}$.

- **Self-Affinity:** The effect of intermittency is more prominent in higher dimensions [91]. This is due to the fact that the actual process of multiparticle production takes place in a three dimensional space, and a dimensional reduction in the analysis reduces the extent of fluctuation. It is also very unlikely and the actual fact of matter is that the distribution of particles is not isotropic in all (longitudinal and transverse) directions. As a result, the scaling-law Eq. (1.77) for a self-similar partitioning of phase space is not found to be exact in higher dimensions. Hence, the scaling behavior should be different in different directions, and in a higher dimensional analysis a scaling behavior like Eq. (1.77) can be retrieved only by incorporating unequal partitioning in different directions. This is known as *self-affine* scaling. The self-affine structure of phase space is characterized by a ‘roughness’ parameter called the *Hurst exponent* (H) [92]. For $H = 1$ self-affine partitioning reduces to self-similar one. The anomalous scaling of two dimensional SFM in AB collisions was studied in detail by the EMU01 collaboration for different projectiles and different incident energies in emulsion experiments [93]. The EMU01 analysis showed that in order to recover the scaling-law (1.77) the phase space should be divided finer in the longitudinal η direction than in the transverse φ direction.

• **Erraticity:** The *erraticity moment* C_{pq} first introduced in ref. [94] to investigate both the spatial density fluctuations and the event-to-event fluctuations. The moment C_{pq} is analytically connected with a parameter called the *entropy index* μ_q , a direct measure of the degree of fluctuation in event space. μ_q is also a suitable parameter for measuring the chaotic behavior in the QCD branching process [95], possessing another advantage that it can identify whether a branching process is initiated by a quark or by a gluon. Erraticity analysis has been performed at various energies [96–98]. The experimental results are compared with Monte-Carlo simulations. The brief observations of the erraticity analysis are (i) the experimental values of the entropy indices in all cases are non-zero and significantly greater than the simulated values, (ii) the experimental results more or less agree with the theoretical predictions, (iii) μ_q decreases with increasing square-root of event multiplicity ($\sqrt{N_{ch}}$), and (iv) the pattern is independent of the energy involved in interactions [96]. In case of pp collisions it is also noticed that the reaction may not be triggered by the QCD parton cascading.

• **Multifractality:** A highly fluctuating signal can also be characterized in terms of the theory of fractals. For a self-similar object a *fractal dimension* can characterize the system, whereas an irregular or a multifractal object requires a set/spectrum of such dimensions. Multifractality is understood to be one probable cause of the observed density fluctuations in high-energy collisions. A multifractal analysis of multiparticle distribution data is based on evaluating *Hwa's moment* (or frequency moments) G_q [99, 100] and *Takagi's moment* T_q [101]. The G_q moment analysis is affected by the finiteness of event multiplicity ($\langle N_{ch} \rangle$). In this method the statistical noise can be eliminated by generating a random number based simulated event sample without invoking any inter-particle correlation. On the other hand, Takagi's moment is not influenced by the finiteness of $\langle N_{ch} \rangle$, but the mechanism of eliminating noise has not yet developed. Another very popular technique of dynamical time series data analysis, the so-called multifractal detrended fluctuation analysis (MF-DFA) [102], has recently been implemented for the multifractal characterization of high-energy AB collision data [103]. The MF-DFA method is not yet fully customized for the multiparticle data analysis and only a couple of articles are found in the literature where the MF-DFA method is used to analyzed the Au + Au collision data at 200A GeV [103, 104].

• **Azimuthal Structure:** In order to look into the nature of particle production in the azimuthal plane, one can use the prescription of ref. [105] which is known as the ‘azimuthal structure analysis’. The objective of this analysis is to investigate whether the emitted particles prefer to come out in clusters (or subgroups) and if so, then whether the clusters are confined to narrow intervals of both longitudinal and transverse phase space variables i.e., *jet-like*, or confined only to a narrow interval of longitudinal variable but covers the entire allowed region of transverse one i.e., *ring-like*. The idea is based on a speculation that

either ‘Cherenkov gluon emission’ or a ‘Mach shock wave’ formation in nuclear/partonic medium [106] is responsible for such unusual structures. The EMU01 collaboration showed the presence of jet-like particle subgroups in ^{16}O and ^{32}S -induced interactions in nuclear emulsion experiments [105]. But the observation could be explained by the $\gamma \rightarrow e^-e^+$ conversion and interference between identical particles (HBT). In some other experiments however, presence of ring-like structure was observed [107–109].

• **Wavelet Analysis:** Wavelet transforms are a mathematical tool to perform signal analysis when signal frequency itself is a function of time. For certain classes of signals and images wavelet analysis provides more precise information about the signals. Recently, the technique has successfully been applied to analyze multiparticle emission data [110]. The wavelet analysis in high-energy collisions is based on the assumption that the dynamical fluctuation would be manifested by excess particles located at some characteristic position and at some characteristic resolution(s). Wavelet transform of a function of pseudorapidity say, $f(\eta)$ is given by [111]

$$W_\Psi(a, b)f(\eta) = \frac{1}{\sqrt{C_\Psi}} \int_{-\infty}^{+\infty} f(\eta)\Psi_{a,b}(\eta)d\eta, \quad (1.81)$$

where

$$\Psi_{a,b}(\eta) = a^{1/2}\Psi\left(\frac{\eta - b}{a}\right) \quad (1.82)$$

is called the mother wavelet, C_Ψ is a normalization constant. For continuous wavelets both the translation parameter b and the scale parameter a are continuous variables. The choice of a wavelet depends on the problem studied. Therefore, it is not unique. In multiparticle data analysis, the second derivative of the Gaussian function

$$g_2(x) = (1 - x^2) \exp(-x^2/2) \quad (1.83)$$

known as the ‘Mexican hat’ (MHAT), is usually chosen as the mother wavelet and the signal to be analyzed is the η -distribution. The irregularities are revealed in the wavelet pseudorapidity spectra within a particular scale region and they are interpreted as the preferred pseudorapidity values of the groups of emitted particles [107, 110]. Till date only a handful of results on wavelet analysis can be found in literature.

• **Void Analysis:** Multiparticle (rapidity) distributions in high-energy interactions exhibit both large spikes and deep valleys. From the perspective of underlying mechanism of multiparticle production both are equally important, and are complementary to each other. It is known that higher order cumulant correlation functions C_N can be constructed out of two-particle cumulant correlation functions C_2 [112]. Actually C_N is proportional to the product of $(N - 1)$ two-particle reduced cumulants summed over all permutations.

This scheme successfully implemented in both galaxy-galaxy and particle-particle correlation studies, is formally termed as ‘linked-pair ansatz’ in multiparticle phenomenology. The technique is based on finding out a rapidity gap distribution $P_0(\Delta y)$ that measures the chance of finding out no particle within certain rapidity interval (Δy) [113]. Based on the hierarchical model of particle correlations stated above, it has been shown that a scaling behavior of the void probability distribution provides a sensible proof of the linked-pair approximation. The analysis method has so far been successfully tested in several high-energy experiments.

Bibliography

- [1] D. J. Gross and F. Wilczek, *Phys. Rev. Lett.* **30**, 1343 (1973);
D. J. Gross and F. Wilczek, *Phys. Rev.* **D 8**, 3633 (1973).
- [2] H. Politzer, *Phys. Rev. Lett.* **30**, 1346 (1973).
- [3] S. Bethke, *Nucl. Phys. Proc.* **121** (Suppl.), 74 (2003).
- [4] F. Karsch, E. Laermann and A. Peikart, *Nucl. Phys.* **B605**, 579 (2001).
- [5] J. C. Collins and M. J. Perry, *Phys. Rev. Lett.* **34**, 1353 (1975);
N. Cabbibo and G. Parisi, *Phys. Lett.* **B 59**, 67 (1975).
- [6] T. Banks and A. Casher, *Nucl. Phys.* **B 109**, 103 (1980).
- [7] R. Hagedorn, *Nuovo Cim. Suppl.* **3**, 147 (1965)
R. Hagedorn and J. Rafelski, *Phys. Lett.* **B 97**, 136 (1980);
R. Hagedorn, *Z. Phys.* **C 17**, 265 (1983).
- [8] J. Berges, *Effective Theories of Matter (1)* (Lectures given at 11th Summer School and Symposium on Nuclear Physics, Seoul, Korea 1998) [arXiv:hep-ph/9902419].
- [9] E. V. Shuryak, *Phys. Lett.* **B 78**, 150 (1978); *Phys. Rep.* **61**, 71 (1980).
- [10] G. Chapline, M. Johnson, E. Teller *et al.*, *Phys. Rev.* **D 8**, 4302 (1973).
- [11] R. S. Bhalerao *Relativistic heavy-ion collisions* (Lectures given at the First Asia-Europe-Pacific School of High-Energy Physics, Japan, 2012) [arXiv:1404.3294v1].
- [12] K. Adcox *et al.* (PHENIX Collaboration), *Nucl. Phys.* **A 757**, 184 (2005).
- [13] P. Barun-Munzinger and J. Stachel, *Nature* **448**, 302 (2007).
- [14] F. Karsch, *Nucl. Phys.* **A 698**, 199c (2002).
- [15] M. Kliemant, R. Sahoo, T. Schuster and R. Stock, *Lect. Not. Phys.* **785**, 23 (2010)
in *The Physics of the Quark-Gluon Plasma: Introductory Lectures*, Eds. S. Sarkar, S. Satz and B. Sinha, (Springer-Verlag, Berlin, Germany, 2010).
- [16] N. Herrmann *et al.*, *Ann. Rev. Nucl. Part. Sci.* **49**, 581 (1999).
- [17] J. Adams *et al.* (STAR Collaboration), *Nucl. Phys.* **A 757**, 102 (2005).

- [18] J. Letessier and J. Rafelski, *Hadrons and Quark-Gluon Plasma*, (Cambridge University Press, Cambridge, UK, 2004).
- [19] J. D. Bjorken, *Phys. Rev. D* **27**, 140 (1983).
- [20] I. S. Hughes, *Elementary particles*, (Cambridge University Press, UK, 1991).
- [21] B. Friman, C. Höhne, J. Knoll, S. Leupold, J. Randrup, R. Rapp and P. Senger (Eds.), *The CBM Physics Book* (Springer, 2010).
- [22] H. Schopper and Luigi D. Lella (Eds.), *60 Years of CERN Experiments and Discoveries* (World Scientific Publishing Company, 2015).
- [23] M. J. Tannenbaum, arXiv:1201.5900[nucl-ex] (2012).
- [24] J. Rak and M. J. Tannenbaum, *High- p_T Physics in the Heavy Ion Era* (Cambridge University Press, Cambridge, UK, 2013).
- [25] I. Arsene *et al.* (BRAHMS Collaboration), *Nucl. Phys. A* **757**, 1 (2005).
- [26] B. B. Back *et al.* (PHOBOS Collaboration), *Nucl. Phys. A* **757**, 28 (2005).
- [27] D. Rischke and G. Levin, *Nucl. Phys. A* **750**, 1 (2005).
- [28] Press Conference, *A New State of Matter Created at CERN*, <http://newstate-matter.web.cern.ch/newstate-matter/Story.html>
- [29] R. Vogt, *Ultrarelativistic Heavy-Ion Collisions*, (Elsevier, Amsterdam, The Netherlands, 2007).
- [30] F. Karsch and E. Laermann, *Quark-Gluon Plasma*, Eds. R. C. Hwa and X. N. Wang, (World Scientific, Singapore, 2003).
- [31] E. Fermi, *Prog. Theo. Phys.*, **5**, 570 (1950); *ibid* **81**, 683 (1951).
- [32] L. D. Landau, *Izv. Akad. Nauk., Ser. Fiz.* **17**, 51 (1953);
S. Z. Belensky and L. D. Landau *Usp. Fiz. Nauk.* **56**, 309 (1955).
- [33] E. K. G. Sarkisyan and A. S. Sakharov, *Eur. Phys. J. C* **70**, 533 (2010);
A. N. Mishra, R. Sahoo, E. K. G. Sarkisyan and A. S. Sakharov, *Eur. Phys. J. C* **74**, 3147 (2014).
- [34] P. Kolb and U. Heinz, *Quark-Gluon Plasma 3*, Eds., R. C. Hwa and X. N. Wang (World Scientific, Singapore, 2003).
- [35] K. Yagi, T. Hatsuda and Y. Miake, *Quark-Gluon Plasma, From Big Bang to Little Bang* (Cambridge University Press, Cambridge, UK 2005).
- [36] C. Y. Wong, *Introduction to High-Energy Heavy-Ion Collisions* (World Scientific, 1994).
- [37] L. D. McLerran *et al.*, *Phys. Lett. B* **98**, 195 (1981); *Phys. Rev. D* **24**, 450 (1981);
J. Kuti, J. Polonyi and K. Szlachanyi, *Phys. Lett. B* **98**, 199 (1981).
- [38] H. Satz, Extreme States of Matters in Strong Interaction Physics, *Lect. Not. Phys.* **841**, 111 (Springer-Verlag Berlin Heidelberg, 2012);
A. Ayala *et al.*, *Nucl. Phys. B* **897**, 77 (2015).

- [39] B. Müller and J. L. Nagle, *Ann. Rev. Nucl. Part. Phys.* **56**, 93 (2006).
- [40] J. W. Harris and B. Müller, *Ann. Rev. Nucl. Part. Sci.* **46**, 71 (1996).
- [41] G. Goldhaber *et al.* *Phys. Rev.* **120**, 300 (1960).
- [42] U. A. Wiedemann and U. W. Heinz, *Phys. Rept.* **319**, 145 (1999).
- [43] R. Hanbury-Brown and R. Q. Twiss, *Nature* **178**, 1046 (1956).
- [44] U. A. Wiedemann, *Nucl. Phys. A* **661**, 65 (1999).
- [45] H. A. Gustafsson *et al.*, *Phys. Rev. Lett.* **52**, 1590 (1984).
- [46] J.-Y. Ollitrault, *Phys. Rev. D* **46**, 229 (1992).
- [47] K. H. Ackermann *et al.* (STAR Collaboration), *Phys. Rev. Lett.* **86**, 402 (2001).
- [48] C. Adler *et al.* (STAR Collaboration), *Phys. Rev. Lett.* **87**, 182301 (2001).
- [49] B. Mohanty and J. Serreau, *Phys. Rept.* **414**, 263 (2005).
- [50] T. K. Nayak, *J. Phys. G* **32**, S187 (2006).
- [51] V. Koch, M. Bleicher and S. Jeon, *Nucl. Phys. A* **698**, 261 (2002).
- [52] J. Rafelski, B. Muller, *Phys. Rev. Lett.* **48**, 1066 (1982) [Erra. *ibid* **56**, 2334 (1986)];
P. Koch, B. Muller and J. Rafelski, *Phys. Rep.* **142** (1986).
- [53] B. Sinha, *Phys. Lett. B* **135**, 169 (1984).
- [54] P. Koch, B. Muller and J. Rafelski, *Z. Phys. A* **324**, 453 (1986).
- [55] V. Koch, *Acta Phys. Polon. B* **29**, 3233 (1998).
- [56] P. Aurenche, arXiv:hep-ph/0201011; F. Arleo *et al.*, “Photon physics” section, CERN Yellow Report, 2004-009, arXiv:hep-ph/0311131 (2007).
- [57] T. Peitzmann and M. H. Thoma, *Phys. Rep.* **364**, 175 (2002);
D. Boyanovsky and H. J. de Vega, *Phys. Rev. D* **68**, 065018 (2003);
F.-M. Liu and K. Werner, *Phys. Rev. Lett.* **106**, 242301 (2011);
M. Wilde *et al.* (ALICE collaboration), *Nucl. Phys. A* **904**, 573c (2013).
- [58] K. Kanaya and H. Satz, *Phys. Rev. D* **34**, 3193 (1986);
T. A. DeGrand and C. E. DeTar, *Phys. Rev. D* **34**, 2469 (1986).
- [59] T. Matsui and H. Satz, *Phys. Lett. B* **178**, 416 (1986).
- [60] A. Adare *et al.* (PHENIX Collaboration), *Phys. Rev. Lett.* **98**, 232301 (2007).
- [61] P. Pillot (for the ALICE collaboration), *J. Phys. G* **38**, 124111 (2011);
A. Grelli (for the ALICE collaboration), *J. Phys. G* **316**, 012025c (2011).
- [62] J. D. Bjorken, Preprint FERMILAB-PUB-82-059-THY (1982);
K. Adcox (for the PHENIX Collaboration), *Nucl. Phys. A* **757**, 184 (2005);
K. Aamodt *et al.*, (ALICE Collaboration) *Phys. Lett. B* **696**, 30 (2011);
S. Chatrchyan *et al.* (CMS Collaboration), *Eur. Phys. J. C* **72**, 1945 (2012).

- [63] H. Sorge, *Phys. Rev. Lett.* **78**, 2309 (1997); *Phys. Lett.* **B 402**, 251 (1997).
- [64] H. Bebie, P. Gerber, J. L. Goity and H. Leutwyler, *Nucl. Phys.* **B 378**, 95 (1992).
- [65] S. A. Bass *et al.*, *Prog. Nucl. Part. Phys.* **41**, 255 (1998);
M. Bleicher *et al.*, *J. Phys.* **G 25**, 1859 (1999).
- [66] B. Andersson, G. Gustafson and B. Nilsson-Almqvist, *Nucl. Phys.* **B 281**, 289 (1987);
B. Nilsson-Almqvist and E. Stenlund, *Comp. Phys. Commun.* **43**, 387 (1987).
- [67] X. N. Wang and M. Gyulassy, *Phys. Rev.* **D 44**, 3501 (1991).
- [68] A. Capella, U. Sukhatme and J. Tran Thanh Van, *Z. Phys.* **C 3**, 329 (1980);
J. Ranft, *Phys. Rev.* **D 37**, 1842 (1988).
- [69] T. Sjöstrand, M. van Zijl, *Phys. Rev.* **D 36**, 2019 (1987).
- [70] Z.-W. Lin, C. M. Ko, B.-A. Li, B. Zhang, S. Pal, *Phys. Rev. C* **72**, 064901 (2005).
- [71] B. Zhang, *Comp. Phys. Commun.* **109**, 193 (1998).
- [72] T. Sjöstrand, *Comp. Phys. Commun.* **82**, 74 (1994).
- [73] B. A. Li and C. M. Ko, *Phys. Rev. C* **52**, 2037 (1995).
- [74] Zi-Wei Lin and C. M. Ko, *Phys. Rev. C* **65**, 034904 (2002).
- [75] N. Xu and M. Kaneta, *Nucl. Phys.* **A 698**, 306 (2002).
- [76] A. Andronic, P. Braun-Munzinger and J. Stachel, *Nucl. Phys.* **A 772**, 167 (2006).
- [77] J. Cleymans, H. Oeschler, K. Redlich and S. Wheaton, *J. Phys.* **G 32**, S165 (2006).
- [78] A. Bialas and R. Peschanski, *Nucl. Phys.* **B 273**, 703 (1986).
- [79] A. Bialas and R. Peschanski, *Nucl. Phys.* **B 308**, 857 (1988).
- [80] P. Carruthers *et al.*, *Phys. Lett.* **B 222**, 487 (1989).
- [81] T.H. Burnett *et al.* (JACEE Collaboration), *Phys. Rev. Lett.* **50**, 2062 (1962).
- [82] W. Kittel and E. A. De Wolf, *Soft Multihadron Dynamics* (World Scientific, 1995).
- [83] E. A. De Wolf, I. M. Dremin and W. Kittel, *Phys. Rep.* **270** 1 (1996).
- [84] A. Bialas and R. C. Hwa, *Phys. Lett.* **B 253**, 436 (1991).
- [85] R. C. Hwa (Ed.), *Quark-Gluon Plasma* (World Scientific, Singapore, 1990).
- [86] I. M. Dremin, *Phys. Lett.* **B 313**, 209 (1993).
- [87] M. I. Adamovich *et al.* (EMU01 Collaboration), *Nucl. Phys.* **B 388**, 3 (1992).
- [88] D. Ghosh *et al.*, *Phys. Rev. C* **52**, 2092 (1995).
- [89] M. K. Ghosh *et al.*, *J. Phys.* **G 34**, 177 (2007).
- [90] S. Islam and R. Hassan, *J. Phys.* **G 34**, 779 (2007).

- [91] W. Ochs, *Phys. Lett.* **B 247**, 101 (1990); *Z. Phys.* **C 50**, 339 (1991).
- [92] L. Liu, Y. Zhang, Y. Wu, *Z. Phys.* **C 69**, 323 (1996).
- [93] M. I. Adamovich *et al.* (EMU01 Collaboration), *Z. Phys.* **C 76**, 659 (1991).
- [94] Z. Cao and R. C. Hwa, *Phys. Rev. Lett.* **75**, 1268 (1995); *Phys. Rev.* **D 53**, 6608 (1996); *Phys. Rev.* **E 56**, 326 (1997).
- [95] A. Altarelli and G. Parisi, *Nucl. Phys.* **B 216**, 298 (1977).
- [96] W. Shaoshun and W. Zhaomin, *Phys. Rev.* **D 57**, 3036 (1998).
- [97] R. Hassan *et al.*, *J. Phys.* **G 28**, 2939 (2002).
- [98] D. Chanda *et al.*, *Phys. Rev.* **C 71**, 034904 (2005).
- [99] R. C. Hwa, *Phys. Rev.* **D 41**, 1456 (1990).
- [100] C. B. Chiu and R. C. Hwa, *Phys. Rev.* **D 43**, 100 (1991).
- [101] F. Takagi, *Phys. Rev. Lett.* **72** 32 (1994).
- [102] J. W. Kantelhardt *et al.*, *Physica* **A 316** 87 (2002).
- [103] Y. X. Zhang, W. Y. Qian and C. B. Yang, *Int. J. Mod. Phys.* **A 23**(18), 2809 (2007).
- [104] X. Wang and C. B. Yang, *Int. J. Mod. Phys.* **E 22**(4), 1350021 (2013).
- [105] M. I. Adamovich *et al.* (EMU01 Collaboration), *J. Phys.* **G 19**, 2035 (1993).
- [106] I. M. Dremin, *Pis'ma Zh. Eksp. Teor. Fiz.* **30**, 152 (1979); *Yad. Fiz.* **33**, 1357 (1981).
- [107] I. M. Dremin *et al.*, *Phys. Lett.* **B 499**, 97 (2001).
- [108] S. Vokál *et al.*, *Phys. Atom. Nucl.* **71**, 1395 (2008).
- [109] S. Vokál *et al.*, *Phys. Atom. Nucl.* **72**, 237 (2009).
- [110] V. V. Uzhinsky *et al.*, *Phys. Atom. Nucl.* **67**, 156 (2004).
- [111] I. Daubechies, *Ten Lectures on Wavelets* (Society for Industrial and Applied Mathematics, Philadelphia, Pennsylvania, 1992).
- [112] P. Carruthers and I. Sarcevic, *Phys. Rev. Lett.* **63**, 1562 (1989).
- [113] S. Hegyi, *Phys. Letts.* **B 274**, 214 (1992); *Phys. Letts.* **B 309**, 443 (1993).

Chapter 2

Experiment and Simulation

2.1 Nuclear Emulsion

In this study we employ the age old nuclear photo-emulsion technique to collect the experimental data. Emulsion experiments involve fixed targets, where the target medium itself acts as the detector. Some excellent reviews and texts [1–3] are available on the details of nuclear emulsion technique. However for the sake of completeness, we summarize here some of the essential features of the nuclear emulsion technique and the data collection method. The first use of photographic emulsion to record charged particle tracks was made in 1891, when α -particles were found to affect silver bromide grains along the paths they traveled [4]. However, during 1940’s due to the efforts of various commercial firms like Ilford Ltd. (London), Kodak Ltd. (New York), and to a great extent due to the contribution of the emulsion research group in the University of Bristol (UK), nuclear emulsion technique became an effective and successful tool in cosmic-ray, nuclear and particle physics research. The usefulness of this technique can be understood from its rich history of being a key detector in discovering several new particles like the charged π and K -mesons, the Σ^+ and $\bar{\Lambda}$ baryons, etc. In spite of a stiff competition offered by the modern sophisticated detectors and dedicated electronic readout technology, even in a not so distant past the emulsion experiments have contributed significantly in the field of high-energy hadron-nucleus and nucleus-nucleus (AB) interactions.

Nuclear photographic emulsion is basically a dispersion of silver halide crystals within a gelatin matrix. The medium is used to record charged particle tracks of silver halide micro-crystals embedded into about equal parts in volume, a matrix material comprising mainly of gelatin and water with a small amount of glycerol and a few other substances. An electrically charged particle while passing through the medium, produces latent image along its track that upon proper chemical treatment appears as trails of black colloidal grains of metallic silver along the trajectory of the particle. Compared to an ordinary photographic plate, nuclear emulsion pellicles have several distinguishing features, Nuclear emulsion pellicles are much thicker (thickness ranging between several hundreds to $\sim 10^3$ microns) as compared to only several microns in case of ordinary photographic plates. The photo-sensitive silver halide material (mostly AgBr molecules) has three to four times more concentration in nuclear emulsion than that in a conventional photographic plate. The AgBr grains in nuclear emulsions are well separated and are much smaller in size (less than a micron in diameter), whereas the AgBr grains in an ordinary photographic plate are interlocked and they can be as large as several microns. The Ilford G5 emulsion pellicles are used in this experiment where the grain diameter is about 0.3 micron. However, the mean crystal grain diameters are different in different types of emulsions. It is observed that the contrast of nuclear emulsion may be improved if the grains are uniform in size, and the sensitivity goes up with increasing grain size. The dimension of each Ilford G5 emulsion pellicle used in the present investigation is 18 cm. \times 7 cm. \times 600 microns. Gelatin being a hygroscopic material emulsion can absorb water from the atmosphere. Therefore, while citing the relative composition of emulsions it is necessary to refer to the real time relative humidity of the surroundings. At a relative humidity of 58% each gram of Ilford nuclear emulsion contains about 0.83 gm. of silver halide and 0.162 gm. of gelatine while the corresponding volume ratio is about 45 : 55. The chemical composition of a standard research emulsion (such as Ilford G5) is given in Table 2.1. In emulsion the total number of atoms per c.c. is 7.898×10^{22} , whereas the total number of electrons is 1.0446×10^{24} per c.c. Taking the nuclear radius parameter $r_0 = 1.2$ fm, the geometrical mean free path of all elements in nuclear emulsion comes out to be approximately 37 cm. However, the actual interaction mean free path is quite different from this geometrical value.

2.1.1 Particle Track Formation

When a charged particle passes through nuclear emulsion it losses energy through electromagnetic interaction. The energy lost by the charged particle is transferred to the electrons of the target atoms present in the emulsion medium, and if the transferred energy is greater than the ionization potential of the target atoms, electrons are liberated and the atoms are ionized. As a result silver specks are formed within the silver halide crystal grains. They

Table 2.1: Chemical composition of standard emulsion.

Element	Atomic weight (A)	No. of atoms per cc $\times 10^{20}$	Moles per cc $\times 10^{-3}$	Concentration at 58% R.H.
H	1.008	321.56	53.571	0.074
C	12.0	138.30	22.698	0.227
N	14.01	31.68	5.147	0.053
O	16.0	94.97	16.050	0.007
S	32.06	1.353	0.216	0.249
Br	79.92	100.41	16.673	1.338
Ag	107.88	101.01	16.764	1.817
I	129.93	0.565	0.094	0.012

serve as ‘latent images’ which when undergo proper chemical treatment become visible. It may be mentioned here that the most important mode of energy loss of a charged particle is the ionization, and it depends on the atomic number and kinetic energy of the incoming particle. In the development process the silver specks act as catalysts for the action of weak reducing agents that deposit additional silver atoms from the same crystal. The deposited silver which appears as black grains under a microscope is permanently embedded into the gelatin through a fixing process. The unexposed silver halide crystals that remain unaffected in the development bath, are removed in the fixing bath. Thus the trail of opaque silver grains form a permanent track structure. To get a good track resolution, the emulsion should have very small grain size and a low density of background grains. It also depends on the emulsion sensitivity and energy of the moving particle as well. Various characteristics of the tracks formed in emulsion are discussed in the next section.

2.1.2 Track Structure

- **Grain Density:** The grain density dn/dx is defined as the number of silver grains deposited per unit (say 100 micron) path length of a track. The grain density is found to be proportional to the rate of energy loss (dE/dx) of the moving particle. However, for high values of dE/dx the proportionality may not always be valid. For an incoming particle of mass m , charge $Z_p e$ and velocity $\beta (= v/c)$ that is large compared to the velocity of the K -shell electrons of the stopping material (in this case emulsion), the average restricted energy loss per unit distance (also called the specific energy loss) is given by [5]

$$-\frac{dE}{dx} = \frac{4\pi Z_p^2 e^4 N Z_t}{mv^2} \left[\ln \left(\frac{2mv^2}{I} \right) - \ln(1 - \beta^2) - \beta^2 \right], \quad (2.1)$$

where N is the number of atoms per c.c. of emulsion material, Z_t and I are respectively, the mean atomic number and ionization potential of the emulsion nuclei. In terms of dE/dx an empirical expression for the grain density is obtained as [6],

$$\frac{dn}{dx} = \kappa \left[1 - \exp \left\{ -bZ_p \left(\frac{dE}{dx} \right)^{\frac{1}{2}} - \sqrt{\alpha} \right\} \right]. \quad (2.2)$$

Here κ and b are experimentally determinable constants that depend on the type of emulsion and the developing material used, and α is the minimum specific energy loss required to ensure that grains are developed. Thus in order to estimate the specific energy loss dE/dx and hence the velocity of the moving charged particles, one can see that the grain density is a useful parameter. It is determined by counting the number of developed grains within a measured length of the track. Sometimes instead of grain density, the blob density B is measured. A blob is a resolvable spot in which more than one grains are present. The estimation of blob number is equivalent to measuring the number of gaps between two blobs. It is observed that the frequency distribution of the gap length follows an exponentially decaying nature [7]. According to [8], the number density of gaps H exceeding a gap length value l is

$$H(l) = B \exp(-g l), \quad (2.3)$$

where the slope parameter g is a measure of the grain density, but cannot be set exactly equal to the true grain density dn/dx . Fowler and Perkins gave another relation for the blob density

$$B = g \exp(-g \alpha'), \quad (2.4)$$

where α' is a parameter determined by the average developed grain size. From these two relations one can determine g as a useful ionizing parameter.

• **Lacunarity and Opacity:** The lacunarity L of a track is defined as the fraction of a track that is made up of gaps. In terms of the grain density g it is expressed as,

$$L = \int_0^\infty -l \left(\frac{dH}{dl} \right) dl = \exp(-g \alpha'). \quad (2.5)$$

From Eq. (2.4) and Eq. (2.5) we get $g = B/L$ and $\alpha' = -(L/B) \ln L$. For particles with low Z and high velocity ($\beta \approx 1$) the specific energy loss is small, and a proportionality like

$$\frac{dE}{dx} \propto \frac{dn}{dx} \quad (2.6)$$

holds. Assuming $g \approx dn/dx$, one may relate Z of the particle with L as, $Z^2 \propto -\ln L$. Opacity O on the other hand, is defined as the fraction of a track that is made up of blobs, and therefore it is related to lacunarity as, $O = 1 - L$. Thus the charge of a particle can be

determined either by measuring its lacunarity or opacity. By default for low charge values ($Z \leq 3$) a high degree of accuracy for the charge measurement can be achieved in this method because

$$\delta Z \propto \frac{1}{Z} \frac{\delta L}{L}. \quad (2.7)$$

Here the error in L measurement, $\delta L = \sigma_L / \sqrt{N_c}$ can arbitrarily be reduced by increasing N_c , the number of cells of equal length over which the measurement of L has been made. $\sigma_L = \sqrt{\langle L^2 \rangle - \langle L \rangle^2}$ is the variance in L .

• **Delta Ray:** For high charge values (usually for $Z \geq 4$) the rate of energy loss of the moving particle is high, and secondary electrons are produced with sufficient kinetic energies, and some of these electrons may have observable tracks within emulsion. Such electron tracks are referred to as delta rays. The number of delta rays (n_δ) is also dependent on dE/dx . Therefore, when lacunarity measurement is not possible, the method of delta ray counting can be utilized to determine the charge of a particle. For a particle of charge Ze the number of delta rays with energies between W and $W + dW$ is given as [9],

$$dn_\delta = \frac{2\pi N Z_p^2 e^4}{m_e v^2} \frac{dW}{W} \left[1 - \beta^2 \frac{W}{W_{\max}} \right]. \quad (2.8)$$

Where m_e is the electron rest mass, and

$$W_{\max} = \frac{2 m_e c^2 \beta^2 \gamma^2}{1 + 2\gamma \left(\frac{m_e}{m} \right) + \left(\frac{m_e}{m} \right)^2} \quad (2.9)$$

being the upper energy limit that the electron may have received, and $\gamma = \sqrt{1 - \beta^2}$ is the Lorentz factor. The lower limit of delta ray energy is found to be more or less 10 KeV. Integrating Eq. (2.8) one obtains, $n_\delta \propto Z^2 / \beta^2$. For particles moving with relativistic speed, $\beta \approx 1$ and hence a relation like, $n_\delta \propto Z^2$ can be utilized to determine the charge of such particles.

• **Particle Range:** Charged particles loose energy through collisions with the atoms present in the medium through which they traverse. When the energy of the moving particle becomes less than the ionization potential of the atoms present in the medium, the particle in motion suffers multiple elastic scattering and ultimately stops within the medium. The track length of the particle is the distance along the trajectory starting from its point of origin to the last developed grain. It is also known as the residual range (R). The true range can then be defined as the distance traveled by the particle before it stops within the emulsion. From the knowledge of specific energy loss dE/dx and initial energy E_0 , the range of a charged particle can be determined,

$$R(E_0) = \int_0^{E_0} \frac{1}{dE/dx} dE. \quad (2.10)$$

Using the expression for dE/dx , the above relation can be written as,

$$R(E_0) = \frac{m}{Z^2} f(v_0) \quad (2.11)$$

where v_0 is the initial velocity. In the nonrelativistic limit ($E_0 < m c^2$) a range-energy relation for any particle is similar to that of a proton, $R_p = K E_p^n$, where R is in microns and the kinetic energy E_p is in MeV. Here K (typical value 0.262) and n (typical value 0.575) are experimentally obtained parameters. For an arbitrary particle of mass m and charge Ze the range-energy relation is derived to be [10]

$$E = K \left(\frac{m}{m_p} \right)^{(1-n)} Z^{2n} R^n, \quad (2.12)$$

where m_p is the proton rest mass. Due to different types of uncertainties and fluctuations, range of even mono-energetic particles exhibit straggling. A straggling parameter may be defined as,

$$\Gamma_R = \frac{\pi}{2} \left[\frac{\sum_{i=1}^N (R_i - \bar{R})^2}{N} \right]^{1/2}. \quad (2.13)$$

The full width at half maximum (ΔR) of the differential distribution curve of ranges is related to Γ_R as, $\Delta R = 0.94 \Gamma_R$.

- **Track Width:** For a highly ionizing particle (usually $Z > 10$) the linear track structure contains little information in terms of grain or blob density, and n_δ becomes too large to be counted. Under such circumstances, the track width has been found to be a useful parameter to identify the charge of the particle [3]. The track width depends on various factors such as, the type of emulsion and the developer used, the particle variables like charge, mass, velocity etc. Experimental data show that the track width increases linearly with particle charge for $Z \geq 10$. As the track caused by a heavy-ion reaches toward its end, a thinning down (tapering) of the track is observed due to electron capture, which reduces the effective charge of the ion. The length of this tapered portion (L_t) of the track may also be used to find out the atomic number of the particle [11]. An empirical relation like $L_t = C Z^\nu$ with $\nu \approx 1$ has been obtained in this connection.

- **Shrinkage Factor:** Since gelatin is a hygroscopic material, the actual equilibrium thickness and index of refraction of both the processed and unprocessed emulsion depend on the surrounding humidity. Consequently, we define the shrinkage factor (S) as,

$$S = \frac{\text{thickness of emulsion plate during exposure}}{\text{thickness of emulsion plate during scanning}}. \quad (2.14)$$

Thus for any quantitative measurement of the track densities in emulsion, the original thickness of the emulsion has to be known.

2.2 The Microscopy

• **Counting and Statistics:** In an emulsion experiment counting is as important as measurement. Tracks belonging to different categories (to be discussed later) should be properly counted, and the target nucleus should be identified accordingly. The ionization of a track may be measured by counting the number of grains or blobs over a particular track length (say 100 micron). To identify the charge of the particle the delta rays over a similar length interval may also be counted. Energy spectra are determined by counting the number of tracks within particular range intervals. Angular distributions are determined by counting the number of tracks in prescribed angular intervals. Therefore, a practical knowledge of counting statistics is essential in order to justify the reliability of the collected data. The Poisson distribution is usually used for this purpose.

• **Dip Angle:** The dip angle (δ) of a linear track segment is given by

$$\tan \delta = \frac{S \Delta z}{L_{xy}}, \quad (2.15)$$

where Δz is the difference in depth between any two points on the track segment under consideration, L_{xy} is the length of the track projected between these two points on the horizontal (x, y) plane, and S is the shrinkage factor. It has been implicitly assumed that the refractive index of the oil employed for oil immersion objective is very close to the refractive index of the developed emulsion and the glass plate. If dry objectives are used, the apparent depth d_a will be less than the true depth d_{true} , which is measured as, $d_{\text{true}} = \mu_e d_a$. Here μ_e is the refractive index of the emulsion.

• **Space Angle:** The space angle also known as the emission angle (θ) between two tracks may be measured by the simple co-ordinate method. If the direction cosines of the tracks are (l_1, m_1, n_1) and (l_2, m_2, n_2) , then θ is given by

$$\cos \theta = l_1 l_2 + m_1 m_2 + n_1 n_2. \quad (2.16)$$

The direction cosines of a track can easily be obtained by taking space coordinates of any two points on the track. If (x_1, y_1, z_1) and (x_2, y_2, z_2) are the space points on the track, the direction cosines are given as

$$(l, m, n) \equiv \left(\frac{x_1 - x_2}{d}, \frac{y_1 - y_2}{d}, \frac{z_1 - z_2}{d} \right) \quad (2.17)$$

with $d = [(x_1 - x_2)^2 + (y_1 - y_2)^2 + (z_1 - z_2)^2]^{1/2}$. The azimuthal plane is defined as a plane perpendicular to the direction of motion of the incoming projectile nucleus. The track direction projected onto the azimuthal plane with respect to some reference direction may

be defined as the azimuthal angle (φ) of the track. If the projectile direction is taken as one of the displacement directions (say x -direction), then the azimuthal angle is given by,

$$\varphi = \tan^{-1} \left(\frac{S \Delta z}{\Delta y} \right). \quad (2.18)$$

If the projectile direction does not completely coincide with the specified x -direction, then φ for a particular track may be measured by setting the corresponding quantity for the projectile track as zero. The track geometry is schematically presented in Fig. 2.1. Due to scattering the track of a charged particle in emulsion may not always be straight. Therefore, it is convenient to break up the track into M number of essentially straight segments, and the residual range of the particle may be determined from the relation,

$$R = \sum_{i=1}^M [(x_i - x_{i-1})^2 + (y_i - y_{i-1})^2 + S^2(z_i - z_{i-1})^2]^{1/2}. \quad (2.19)$$

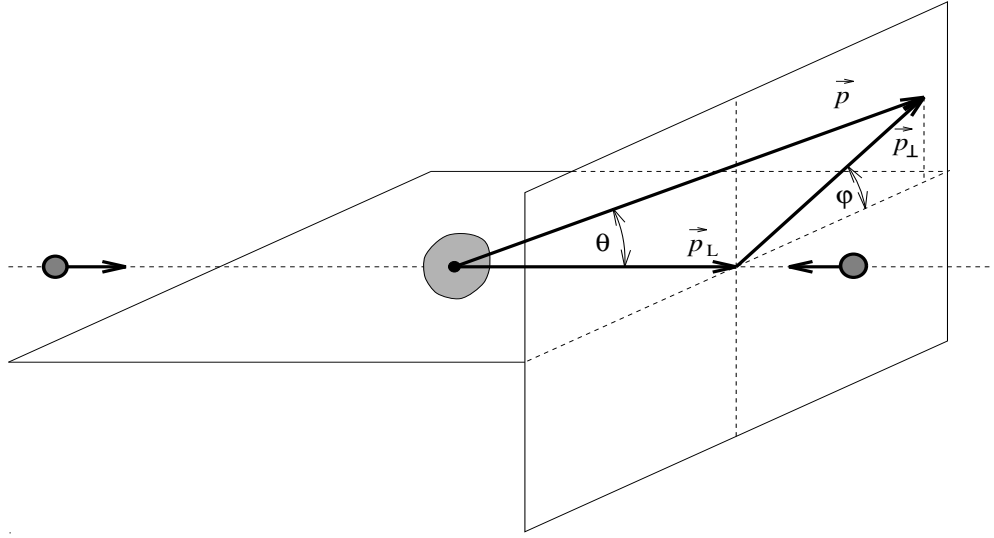


Figure 2.1: Schematic of a secondary track geometry with respect to the projectile.

- **Momentum Measurement:** While passing through emulsion medium, charged particles experience frequent small deflections due to elastic scattering with the Coulomb field of the atomic nuclei present in the medium. The probability for such a deflection having small angular deviations but at high frequency, is governed by Rutherford's scattering formula. A general expression for the projected absolute angle of deviation (ϕ) is theoretically derived by Goudsmit and Sauderson [12] and its mean is given by

$$\bar{\phi} = \frac{\chi Z}{p\beta} \left(\frac{t}{100} \right)^{1/2}. \quad (2.20)$$

Where χ is a constant of scattering, defined as

$$\chi = Z_p e^2 Z_t N^{1/2} \left[\ln \left(\frac{\phi_{\max}}{\phi_{\min}} \right) \right]^{1/2}. \quad (2.21)$$

Here N is the number of atoms per unit volume in emulsion, Z_t is the average atomic number of the atoms presents in the medium, Z_p is the atomic number of the particle moving with velocity β and p being its momentum, ϕ_{\max} (ϕ_{\min}) is the maximum (minimum) value of the projected angle in the plane of the initial particle trajectory, and t is the path length in the scattering medium. It is necessary to determine the value of $\bar{\phi}$ very accurately in order to find out $p\beta$ value of a track. This can be done following a method suggested by Fowler [8]. In Fowler's method the plate is placed on the mechanical stage of the microscope in such a way that the track is (at least approximately) parallel to one of the sides of the stage, say x -axis. The coordinate (x_0, y_0) of an arbitrary point on the track are measured. The plate is then displaced by a distance equal to the cell length t along x -direction, and the ordinate y_1 of the point is determined by means of an eyepiece scale. The measurement should be performed under a very high magnification (e.g., $2500\times$), and the ordinate eyepiece scale is commonly replaced by a flair micrometer, which is capable of reading distances within a few hundreds of micron. Once again the stage is moved through the standard distance t , and the ordinate y_2 is recorded. The operation is repeated several times along the length of the track. The absolute value of the second differences taken irrespective of the sign: $D_k = |y_{k+2} - 2y_{k+1} + y_k|$ of successive such measurements are determined. The mean absolute value between successive chords of length t corrected for stage noise and cell length $\bar{D} = \sum_k^n (D_k/n)$ gives a measure of the scattering parameter through

$$\bar{\phi} = \frac{\bar{D}}{t} (180/\pi). \quad (2.22)$$

From the above relation $p\beta$ (in MeV/c) can be evaluated. In a given cell length t of the track, the energy loss must be negligible if $\bar{\phi}$ is to be a meaningful quantity.

2.2.1 Scanning Emulsion Plates

In a scanning process events (or interactions, also called stars) of a certain types are located in a systematic way. In area (more specifically volume) scanning the focal surface is continually shifted to sweep up and down from the surface of the emulsion to the supporting glass. This is done by rolling the fine focus control while observing the events successively coming into and going out of view. Each field of view is scanned throughout its depth from one surface of the emulsion to the other. For high efficiency the field may be divided into a number of sufficiently small separate areas, so that the entire volume can be covered as

the traverse is made. Generally area scanning is performed under either of the following two circumstances, (i) when events of a certain type within a given volume of emulsion are to be found, and (ii) if the situation demands a representative sample of events. Preliminary volume or line scanning may be performed under a magnification of $300 - 400\times$, but the angle measurement and track identification process may finally be done under a total magnification of $1500\times$. It would be worthwhile to note that volume scanning is not an effective method for finding out single diffractive dissociation events and/or interactions with H-nuclei. Only high multiplicity events easily catch human eyes. Therefore, to get an unbiased sample of events area/volume scanning is not recommended. For that purpose the technique of along the track scanning is preferred. In this technique each projectile track is carefully followed from the leading edge of a plate along its length until the projectile interacts or leaves the plate. Like the area scanning, the preliminary scanning along the track may be performed under $300 - 400\times$ total magnification, though the final selection of events has to be done under a higher magnifications (say at $1500\times$). There can be no denial that the emulsion scanning is a tiresome and time consuming process, and it requires a lot of patience and concentration on the part of a scanner. Accuracy of an emulsion experiment depends largely on the skill of the observer. To avoid individual bias counter checking of the same data sample by independent observers is therefore, recommended. By adopting along the track scanning method in emulsion experiments it is possible to build up a sample of minimum bias events.

2.3 Data Characteristics

Stacks of Ilford G5 nuclear photographic emulsion pellicles of size $18\text{ cm} \times 7\text{ cm} \times 600\text{ }\mu\text{m}$, were horizontally irradiated to a beam of ^{28}Si nuclei at an incident energy of 14.5A GeV (Experiment No. E847) from the Alternating Gradient Synchrotron (AGS) at the Brookhaven National Laboratory (BNL) [13]. The flux of incident ^{28}Si nuclei was 3×10^3 ions per square centimeter. The equivalent nucleon-nucleon (NN) center of mass energy $\sqrt{s_{NN}} = 5.382\text{ GeV}$. If the AB collision is considered as a superposition of many incoherent NN collisions, then for a central collision where all 28 nucleons of the ^{28}Si nucleus participate in the interaction, this amounts to a total center of mass energy $\sqrt{s} \approx 151\text{ GeV}$. On the other hand, if the AB interaction is considered as a coherent collision between an incoming ^{28}Si nucleus and a stationary Ag or Br nucleus (for which the weighted average mass number $A \approx 94$), then the total center of mass energy comes out to be $\sqrt{s} \approx 275\text{ GeV}$. These are two extreme limits, and the actual center of mass energy is perhaps somewhere in between the two extreme cases mentioned. However, the above quoted values of \sqrt{s} give a qualitative idea about the center of mass energy scale of the interactions, and not to determine the exact

degree of coherence. To find out the primary ^{28}Si -emulsion stars Leitz microscopes with a total magnification of $300\times$ were utilized, and the emulsion plates were scanned along individual projectile tracks. According to the emulsion terminology, tracks emitted from a star are classified into four categories namely, the shower tracks, the gray tracks, the black tracks, and the projectile fragments.

- **Shower Tracks:** The shower tracks are caused by singly charged particles moving with relativistic speed ($\beta > 0.7$). This category comprises of particles produced in a high energy interaction, most of which are charged pi-mesons. The ionization of a shower track $I \leq 1.4 I_0$, where I_0 (≈ 20 grains/100 microns) is the minimum ionization due to any track observed within a G5 plate. The total number of such tracks in an event is denoted by n_s .

- **Gray Tracks:** The gray tracks are generally due to the protons that have directly participated in an interaction and are knocked out from the target nuclei. They usually fall within an energy range of 30 – 400 MeV. The ionization limit of gray tracks is $1.4 I_0 < I \leq 6.8 I_0$ and its range is ≥ 3 mm in standard emulsion. A few percent of the gray tracks may also be due to the slow moving mesons. The velocity range of these particles is $0.3c$ to $0.7c$. The number of gray tracks in an event is denoted by n_g .

- **Black Tracks:** Black tracks are predominantly originate from the slowly moving protons and other heavier fragments emitted by the excited target nucleus after an interaction has taken place. Their velocity is $< 0.3c$, and for a black track caused by a proton the kinetic energy < 30 MeV. Ionization of these category of particles is greater than $6.8 I_0$, and range less than 3 mm. in emulsion. The number of black tracks in an event is denoted by n_b .

- **Projectile Fragments:** The projectile fragments are the spectator parts of the incident nucleus that do not directly participate in an interaction. Having almost same energy and/or momentum per nucleon as the incident projectile, these fragments exhibit uniform ionization over a long range and suffer negligible scattering. Their number in an event is denoted by n_{pf} . The projectile fragments are emitted within an extremely narrow forward cone along the beam direction whose semi-vertex angle θ_F is decided by the momentum of the incoming nucleus (p_{inc}). For a given p_{inc} and Fermi momentum (p_F) of the target nucleus, θ_F is defined as,

$$\theta_F = p_F/p_{\text{inc}}. \quad (2.23)$$

According to a simple Fermi gas model the Fermi energy of a nucleus is given by

$$E_F = \frac{\hbar^2}{2m_N} \left(\frac{3}{2}\pi^2 n_N \right)^{2/3}, \quad (2.24)$$

where m_N and n_N are, respectively, the nucleon mass and nucleon number density. The Fermi momentum is calculated from E_F through: $p_F = \sqrt{2m_N E_F}$. Roughly, p_F is estimated

to be 200 MeV/c for the silicon nucleus. For a projectile nucleus having 14.5A GeV of kinetic energy, $\theta_F \approx 0.013$ rad. In an event n_{pf} denotes the number of projectile fragments of charge $z \geq 2$ falling within this cone.

• **Event Selection:** A sample of inelastic events can be classified into two different categories namely, the electromagnetic dissociation (ED) events and the nuclear events. Extremely strong electromagnetic fields offered by the target nuclei causes electromagnetic dissociation of the projectile nuclei. The ED events typically consist only of projectile fragments [14]. Barring the ED events, rest of the events in the sample may be considered as nuclear interactions. Nuclear interactions are subdivided into peripheral (large impact factor) and central (small impact factor) collisions in terms of their shower multiplicities. The target of an interaction, whether a light nucleus (H, C, N, O) or a heavy nucleus (Ag, Br), is decided by the number of heavy tracks (n_h) produced from the event. The total number of heavy tracks of an event is $n_h = n_b + n_g$. By imposing a restriction $n_h \geq 8$ with at least one fragment of charge $Z \geq 2$ per event, it can be ensured that the interaction is either with an Ag nucleus or with a Br nucleus. An event with $n_h < 8$ can either be an Ag/Br or a light nucleus (H, C, N, O) event. A further restriction on the number of spectator projectile fragments in an event $n_{pf} (Z \geq 2) = 0$ enable us to choose only those interactions where total fragmentation of the incident ^{28}Si nucleus has taken place. By following 113.25 mts. of primary track length a total of 1003 events were found, which is equivalent to a mean free path of $\lambda_{tot} = 11.29 \pm 0.36$ cms. for ^{28}Si nuclei in emulsion and which corresponds to a total cross section $\sigma_{tot} = 1121 \pm 34$ mb. Among 1003 primary events, 88 events were due to the ED of the ^{28}Si projectile and the rest were due to inelastic interactions. The experimental value of the mean free path for the latter class of events is $\lambda_{inel} = 12.38 \pm 0.41$ cm., and the corresponding cross-section $\sigma_{inel} = 1023 \pm 34$ mb [13]. From a simple geometric participant-spectator model [15], the AB interaction cross-section is given as

$$\sigma_{th} = \pi r_0^2 \left[A_p^{1/3} + A_t^{1/3} - \delta \right]^2, \quad (2.25)$$

where A_t (A_p) is the target (projectile) mass number. In our case $A_p = 28$, and the weighted average target mass number of emulsion nuclei (Table 2.1) is taken to be $A_t = 29.10$. This gives $\sigma_{th} = 1262.02$ mb, where $r_0 = 1.2$ fm. and $\delta = 0.83$ have been used. In Fig. 2.2 we have shown a plot of reaction cross-section in the framework of the participant-spectator model [16]. Due to intrinsic inefficiency associated with human bias, in particular to detect diffractive dissociation and electromagnetic dissociation events, the present experimental value of σ_{tot} is slightly lower than the universal trend.

After counting measurements are completed, the emission angle (θ) with respect to the

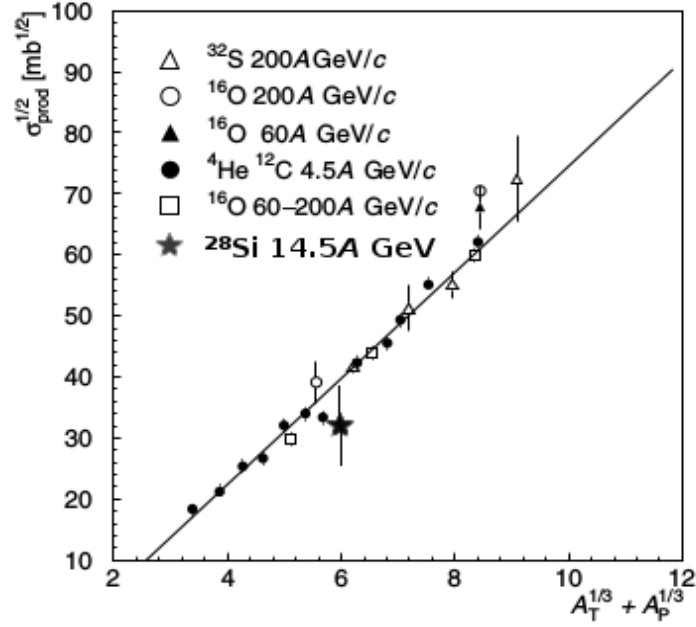


Figure 2.2: Plot of reaction cross-section with $A_p^{1/3} + A_t^{1/3}$ up to SPS energy

projectile nucleus and the azimuthal angle (φ) of each track were measured. The angle measurement are performed by using $100\times$ oil immersion objectives at a total magnification of $1500\times$ with the help of Koristka microscopes. In an emulsion experiment the pseudorapidity (η) together with the azimuthal angle (φ) of a track constitutes a convenient pair of basic variables in terms of which the particle emission data can be analyzed. Knowing θ , the η variable can be determined. As mentioned in Section 1.2, when energy and/or momentum measurements are difficult as it is the case for emulsion experiment, and where in comparison with the total energy the rest mass of a particle can be neglected, as it is the case for most of the charged mesons produced in high energy interactions, the pseudorapidity variable is a convenient replacement of the rapidity variable. The η -resolution is given as

$$\delta\eta = -\frac{1}{\sin\theta}\delta\theta. \quad (2.26)$$

So, at small angles only a small error in θ measurement can ensure a good resolution in η . An accuracy of $\delta\eta = 0.1$ unit of pseudorapidity and $\delta\varphi = 1$ mrad. could be achieved through the reference primary method of angle measurement. Following the criteria mentioned above a sample of ^{28}Si -Ag/Br events of size $N_{ev} = 331$ is considered for further analysis. Our analysis is confined only to the shower tracks having an average shower track multiplicity $\langle n_s \rangle = 52.67 \pm 1.33$. To avoid contamination between the singly charged produced particles and the spectator projectile protons, shower tracks falling within the Fermi cone were excluded from our analysis. Distribution of both η and φ for all the shower tracks in the event sample

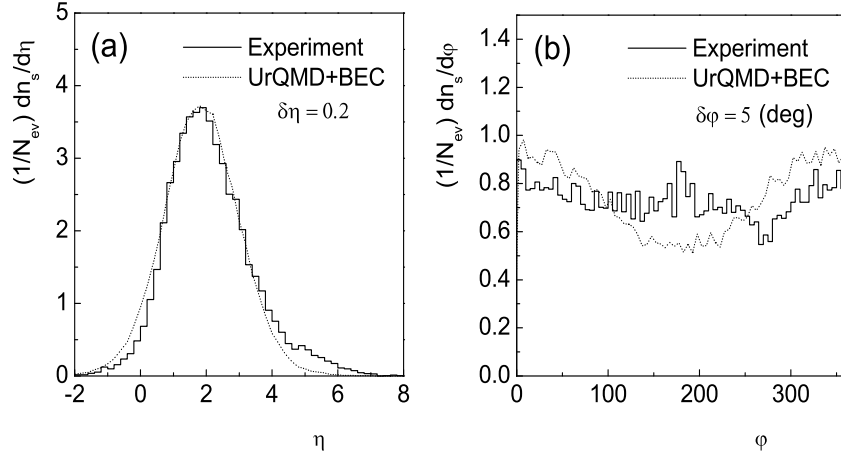


Figure 2.3: Distributions of (a) pseudorapidity and (b) azimuthal angle of shower tracks emitted from ^{28}Si -Ag/Br interaction at 14.5A GeV.

have been obtained in terms of the respective density functions

$$\rho(x) = \frac{1}{N_{ev}} \frac{dn_s}{dx}, \quad (2.27)$$

with $x = \eta$ or φ . The η -distribution of shower tracks can be approximated by a Gaussian function like,

$$\rho(\eta)d\eta = \rho_0 \exp \left[-\frac{(\eta - \eta_0)^2}{2\sigma_\eta^2} \right] d\eta, \quad (2.28)$$

where ρ_0 is the peak density, η_0 is the centroid and σ_η is the width of the distribution. The experimental η and φ -distributions are shown in Fig. 2.3. The η -distribution is fitted to Eq. (2.28). The fit parameters are, $\rho_0 = 17.88$, $\eta_0 = 1.90$ and $\sigma_\eta = 2.17$. The φ -distribution on the other hand, is asymmetric within its accessible range $(0, 2\pi)$. The dips in the φ -distribution near $\varphi \approx 90^\circ$ and 270° may either be due to inefficient recording of shower tracks in the directions vertical to the emulsion plane, exactly toward or away from the direction of vision, or it may be due to a dynamical reason like azimuthal asymmetry (flow), or it may be due to the combination of both.

The energy density in the central η region can be estimated by making use of Bjorken's formula (1.72). While applying the formula two important points have to be kept in mind: (i) that the production of neutral pions in any high energy interaction is as abundant as either of their charge varieties, and (ii) that the overlapping area (\mathcal{A}) between the projectile (^{28}Si nucleus) and target Ag (or Br) is almost equal to the geometrical area of a ^{28}Si nucleus. Therefore, the factor $dN/dy \approx dN/d\eta$ in Bjorken's formula has to be replaced by $1.5 dn_s/d\eta$. Note that dN/dy is the rapidity density of all produced particles in the given sample. Keeping these two factors in mind and putting $\langle m_t \rangle = \sqrt{m^2 + \langle p_t \rangle^2} \approx 0.38$ GeV and $\tau_0 = 1$ fm/c, we obtain $\epsilon \approx 1.5$ GeV/fm³ for a subsample of events with shower track multiplicity $n_s \geq 50$. Note that even for the subsample with a high number of produced particles, the

energy density value is just above the threshold required for the onset of a QGP like state, which according to the lattice QCD is approximately a few GeV/fm³ [17]. In soft processes like multiparticle production, it is even more difficult to extract the signature of such a state, even if it is formed. Therefore, though we do not aspire to conclusively establish a QGP formation in the present colliding system, obviously the multiparticle production phenomenon, which itself is an interesting topic in heavy-ion collision, can be statistically analyzed. Based on the Glauber model following a method prescribed in [18], for a subsample of events falling within a limited shower multiplicity range, one can even obtain a rough estimate of the collision centrality and hence the average impact parameter (\bar{b}), from the number density of shower tracks in the central η region. In this method the peak value of the η density of produced charged particles in AB collision at an impact parameter b is related to the same density for pp interaction at the same energy by the following relation:

$$\left. \frac{dN_{ch}}{d\eta}(b) \right|_{AB} \approx 1.28 \frac{AB}{A^{2/3} + B^{2/3}} \frac{1}{1 + a(A^{1/3} + B^{1/3})} \exp(-b^2/2\beta^2) \left. \frac{dN_{ch}}{d\eta} \right|_{pp}. \quad (2.29)$$

Here a is a parameter obtained by linear fitting of $dN_{ch}/d\eta$ against $A^{1/3}$ for different AB collisions at 14.5A GeV. For our event sample with $n_s \geq 50$ we obtained $\bar{b} = 4.45$ fm.

2.4 Merits and Demerits of Emulsion Experiments

One of the main advantages of nuclear emulsion is that, it can be used as a detector of charged particles as well as a target medium comprising of nuclei of varying mass numbers. As mentioned above, standard emulsions consist of H, C, N, O, Ag and Br nuclei. As far as high-energy interactions are concerned, information regarding target nucleus mass can be obtained from the characteristic appearances of an event. Nuclear emulsion has the ability to detect all charged particles coming out of an event (also called a star) i.e., emulsion as a detector has 4π acceptance. However, the detection efficiency is not equally good in all directions. Particularly along the vertical direction (along the thickness of the plates) the efficiency is not very good. The stopping power of nuclear emulsion is usually very high due to its high medium density, and therefore, the interaction probability between a projectile particle and a target nucleus is also very large. This in other words means an ultra-high energy particle that may easily pass through any other detector even without interacting, has a very small possibility to pass through an emulsion plate without creating any track. As a detector nuclear emulsion is less costly, light weight and very easy to handle. The sensitivity of undeveloped nuclear emulsion pellicle lasts for a few weeks. Hence all charged particles passing through it are able to get their tracks permanently recorded within a long span of time. That makes emulsion a suitable detector for balloon flight and satellite experiments to

study the cosmic-ray events where the projectile / beam is rarely found. In nuclear emulsion neutral particles can also be indirectly detected, as and when they interact with the light nuclei, particularly Hydrogen, and produce tracks of charged particles. The same mechanism is used in the scintillation detectors to detect neutral particles, specially neutrons. Nuclear emulsion can be used from the temperature of liquid Helium up to the boiling point of water. The most striking advantage of nuclear emulsion is its high spatial resolution. For conventional horizontally irradiated stacks of emulsion pellicles, in spite of multiple Coulomb scattering and distortion effects, an accuracy of 0.1 unit of pseudorapidity can be achieved. This unique feature makes the emulsion experiments important to investigate distributions of produced particles in narrow intervals of pseudorapidity space.

There are some difficulties associated with the emulsion experiments too. It is not possible to identify the sign of a charged particle unless a magnetic field is applied. But it is difficult to get the magnetic field penetrate into the emulsion material, hence to produce enough curvature in the track of a relativistic particle to identify its charge. The sensitivity and thickness of emulsion pellicles are affected by temperature, humidity, age etc. Unless special care is taken these factor always introduce some error in the data. The track lengths of most of the produced particles in emulsion are at best a few millimeter long. So high magnification devices such as high power microscopes are required to scan and collect data. Moreover, till date no automated device could be designed for scanning emulsion pellicles, so we totally depend on our eyes. This makes the data acquisition process a tedious and time consuming process. For AB interactions at GeV energy range, where a few hundreds of particles may come out of an event, the time taken to build up even a moderate statistics requires huge effort. The collected data can never be fully free from personal bias and errors. However, such errors can be reduced through counter checking by more than one independent observer. Identification of target fragments often becomes extremely difficult, and sometimes even impossible. Therefore, in the data collection process it is often impossible to exactly identify the target nucleus of the interaction. However, as mentioned in Section 2.3 a gross distinction between the light group (H, C, N, O) and the heavy group (Ag, Br) of target nuclei can be made.

2.5 The Simulation

We know that a complete theoretical description of high-energy AB collisions requires exact QCD calculations. But due to the intrinsic complexities associated with the QCD, non-perturbative effects are treated through model calculations. In our analysis we use the the Ultra-relativistic Quantum Molecular Dynamics (UrQMD) [19] model to simulate the experiment in most of the cases. However, on one occasion (Ring-jet analysis, Chapter 6) we have

also used the RQMD model [20]. Both RQMD and UrQMD are transport models where an AB interaction is considered as a superposition of many elementary NN interactions, and simulates the entire history of the space-time evolution an AB event, starting from its initial pre-equilibrium stage to the final freeze-out. Brief descriptions of both the models are given in Section 1.5. While a provision to accommodate nuclear emulsion as a probable target has been made in the RQMD model, the same in UrQMD cannot be automatically done. The sampling of Ag/Br events generated by UrQMD is described below. Here we describe the salient features of the UrQMD model in details.

The UrQMD model is a microscopic model based on a phase space description of nuclear reactions. It describes the phenomenology of hadronic interactions at low and intermediate energies ($\sqrt{s} < 5$ GeV) in terms of interactions between known hadrons and their resonances. At higher energies ($\sqrt{s} > 5$) GeV, the excitation of color strings and their subsequent fragmentation into hadrons are taken into account. The model was proposed mainly for a microscopic description of AB interactions. Note that up to now there is no unique theoretical description of the underlying hadron-hadron interactions, with their vastly different characteristics at different incident energies and in different kinematic intervals. Perturbative quantum chromodynamics (pQCD) can be applied to describe hard processes, processes with large four-momentum (Q^2) transfer. But pQCD is formally inappropriate for the description of soft processes because of the small Q^2 values. Therefore, low- p_t collisions are described in terms of phenomenological models. With advance computation facilities available now-a-days a vast variety of models for hadronic and nuclear collisions can be implemented. The UrQMD model is one of them which is quite appropriate for the collision energy involved in the present experiment.

The UrQMD model is based on the covariant propagation of all hadrons considered on the (quasi)particle level on classical trajectories in combination with stochastic binary scatterings, color string formation and resonance decay. It represents a Monte Carlo solution of a large set of coupled partial integro-differential equations for the time evolution of the various phase space densities of particle species $i = N, \Delta, \Lambda, \pi$, etc. The main ingredients of the model are the cross sections of binary reactions, the two-body potentials and the decay widths of resonances. Projectile and target are modeled according to a Fermi-gas ansatz. The nucleon are represented by a Gaussian shaped density distribution,

$$\varphi_j(\mathbf{x}_j, t) = \left(\frac{2\alpha}{\pi}\right)^{3/4} \exp \left[-\alpha \{(\mathbf{x}_j - \mathbf{r}_j(t))\}^2 + \frac{i}{\hbar} \mathbf{p}_j(t) \mathbf{x}_j \right]. \quad (2.30)$$

The wave function of the nucleus is defined as the product of single nucleon Gaussian functions without invoking the Slater determinant that is necessary for antisymmetrization.

Therefore, the total N -body wave function is given as

$$\Phi = \prod_i \varphi_i(\mathbf{x}_i, \mathbf{p}_i, t). \quad (2.31)$$

In configuration space the centroids of the Gaussian are distributed at random within a sphere of radius

$$R(A) = r_0 \left(\frac{1}{2} \left[A + (A^{1/3} - 1)^3 \right] \right)^{1/3} : \quad r_0 = \left(\frac{3}{4\pi\rho_0} \right)^{1/3}, \quad (2.32)$$

where ρ_0 is the nuclear matter density in the ground state. The finite widths of these Gaussians result in a diffused surface region beyond the radius of that sphere. The initial momenta of the nucleons are randomly chosen between 0 and the local Thomas-Fermi momentum,

$$p_F^{\max} = \hbar c \left(3\pi^2 \rho \right)^{\frac{1}{3}}, \quad (2.33)$$

ρ is the corresponding local nucleon density. A disadvantage of the initialization mentioned above is that the initialized nuclei are not really in their ground state with respect to the Hamiltonian used for their propagation. However, the parameters of the Hamiltonian are tuned to the equation of state of finite nuclear matter and to properties of finite nuclei, e.g., binding energy, root mean square radius, etc. If however, the energy of the nucleons within the nucleus is minimized according to the Hamiltonian in a self consistent fashion, then the nucleus would collapse to a single point in momentum space because the Pauli principle has not been taken into account in the Hamiltonian. One possible solution to this problem is the inclusion of fermionic properties of the nucleons via the antisymmetrization of the wave function of the nucleus. This ansatz has been implemented in the framework of the Fermionic Molecular Dynamics (FMD) [21]. But the FMD equations of motion are computationally very expensive. To get rid of the problems one can use the so called Pauli potential [22] in the Hamiltonian. Its advantage is that the initialized nuclei remain absolutely stable, whereas in the conventional initialization and propagation without the Pauli potential, the nuclei start evaporating single nucleons after approximately 20–30 fm/c. A drawback of the potential is that the kinetic momenta of the nucleons are not anymore equivalent to their canonical momenta, i.e. the nucleons carry the correct Fermi-momentum, but their velocities are zero. Furthermore, the Pauli potential leads to a wrong specific heat and changes the dynamics of fragment formation.

For AB collisions the interaction potential used in UrQMD is the density dependent Skyrme potential. This potential consists of a sum of two and a three-body interaction term. The two-body term (E^{Sk2}) having a linear density dependence, models the long-range attractive component of the NN interaction, whereas the three-body term (E^{Sk3}) with its quadratic

density dependence is responsible for the short-range repulsive part of the interaction. In addition to the Skyrme potential, Yukawa (E^{Yuk}), Coulomb (E^{Coul}) and Pauli (E^{Pauli}) (optional) potentials are also implemented in the UrQMD model. In finite nuclei the usage of a Yukawa term has the advantage that the parameter can be tuned to the proper surface potential of the nuclei without changing the equation of state. Currently only CASCADE mode or a hard Skyrme equation of state are available in the UrQMD. The default mode is CASCADE, the hard Skyrme equation of state is limited to incident beam energies below 4.0 GeV per nucleon. With these interactions the classical UrQMD Hamiltonian can be written as,

$$\mathcal{H} = \sum_{j=1}^N E_j^{\text{kin}} + \frac{1}{2} \sum_{j,k=1}^N \left(E_{jk}^{\text{Sk2}} + E_{jk}^{\text{Yuk}} + E_{jk}^{\text{Coul}} + E_{jk}^{\text{Pauli}} \right) + \frac{1}{6} \sum_{j,k,l=1}^N E_{jkl}^{\text{Sk3}}. \quad (2.34)$$

The equation of motion of the many-body system is calculated by means of a generalized variational principle. The time evolution of the system is obtained by the requirement that the action is stationary under the allowed variation of the wave function. This yields an Euler-Lagrange equation for each parameter:

$$\dot{\mathbf{p}}_i = -\frac{\partial \langle \mathcal{H} \rangle}{\partial \mathbf{q}_i} = -\nabla_{\mathbf{q}_i} \sum_{j \neq i} \langle V_{ij} \rangle = -\nabla_{\mathbf{q}_i} \langle \mathcal{H} \rangle \quad (2.35a)$$

$$\dot{\mathbf{q}}_i = -\frac{\partial \langle \mathcal{H} \rangle}{\partial \mathbf{p}_i} = \frac{\mathbf{p}_i}{m} + \nabla_{\mathbf{p}_i} \sum_j \langle V_{ij} \rangle = -\nabla_{\mathbf{p}_i} \langle \mathcal{H} \rangle, \quad (2.35b)$$

$$\langle V_{ij} \rangle = \int d^3x_1 d^3x_2 \varphi_i^* \varphi_j^* V(x_1, x_2) \varphi_i \varphi_j. \quad (2.35c)$$

These are the time evolution equations which are solved numerically. The equations have the same structure as the classical Hamilton equations. Impact parameter of a collision is sampled according to the quadratic measure, $dW \sim b db$. Two particles collide if their relative distance d fulfills the relation, $d \leq d_0 = \sqrt{\sigma_{\text{tot}}/\pi}$. In UrQMD the total cross section σ_{tot} depends on the center of mass energy \sqrt{s} , the particle type and its isospin. The neutron-neutron cross section is set equal to the proton-proton cross section (i.e., isospin-symmetry). In the high-energy limit ($\sqrt{s} \geq 5$ GeV) the CERN/HERA parametrization for the proton-proton cross section is used [23]. Since the functional dependence of σ_{tot} on \sqrt{s} at low energies shows a complicated shape, UrQMD uses a table-lookup for those cross sections. For momenta $p_{\text{lab}} < 5$ GeV/c, UrQMD uses the following parametrization to obtain a good fit to the data,

$$\sigma_{\text{tot}}(p) = \begin{cases} 75.0 + 34.1p^{-1} + 2.6p^{-2} - 3.9p & \text{for } 0.3 < p < 5 \\ 271.6 \exp(-1.1p^2) & \text{for } p < 0.3. \end{cases} \quad (2.36)$$

Particle production in UrQMD either takes place via the decay of a meson or baryon resonance or via a string excitation and fragmentation. Up to incident beam energies of 8-10 GeV/nucleon particle production is dominated by resonance decays. Production cross sections for the excitation of individual resonances can be calculated in the framework of the one-pion exchange (OPE) or one-boson exchange (OBE) models [24]. Regarding the number of implemented resonances in UrQMD and considering the limited applicable energy range for cross sections calculated within OPE and OBE models, the calculation of all implemented resonance excitation cross sections in the framework of these models is not practical. Therefore, an effective parametrization based on simple phase space considerations has been employed in UrQMD, and free parameters are tuned to experimental measurements. After the fragmentation, decay of the resonances proceeds according to the branching ratios compiled by the Particle Data Group [23]. The resonance decay products have isotropic distributions in the rest frame of the resonance. If a resonance is among the outgoing particles, its mass must first be determined according to a Breit-Wigner mass distribution. If the resonance decays into $N > 2$ particles, then the corresponding N -body phase space is used to calculate their N momenta stochastically. The Pauli principle is applied to hadronic collisions or decays by blocking the final state, if the outgoing phase space is occupied. The collision term in the UrQMD model includes more than fifty baryon species (including nucleon, delta and hyperon resonances with masses up to 2.25 GeV) and five meson nonets (including strange meson resonances), which are supplemented by their corresponding anti-particles and all isospin-projected states. The states can either be produced in string decays, s -channel collisions or resonance decays. For excitations with higher masses e.g., more than 2 GeV, a string picture is used. Full baryon/antibaryon symmetry is included. Therefore the number of implemented baryons defines the number of antibaryons in the model and the antibaryon-antibaryon interaction is defined via the baryon-baryon interaction cross sections. The framework allows to bridge within one concise model, the entire available range of energies, from the Bevalac region ($\sqrt{s_{NN}} \sim$ a few GeV) to the RHIC ($\sqrt{s_{NN}} = 200$ GeV).

2.5.1 Modeling Bose-Einstein Correlation

The Bose-Einstein correlation (or equivalently, the Hanbury-Brown-Twiss effect) is one of the primary reasons of particle correlation in relativistic nuclear collisions. Even though the phenomena in nuclear and particle physics was introduced more than thirty years ago, several basic questions concerning the form of the correlation function remain unanswered. With the modernization of computational facility, the level of sophistication both in the theoretical description and in the experimental studies has increased very much, in particular in the field of heavy-ion physics [25]. The Bose-Einstein correlation (BEC) between identical

particles is a quantum statistical effect which is usually not embedded in a classical Monte-Carlo model like the UrQMD model. We know that intensity correlations appear due to the symmetrization of the two-particle states. Suppose that a pair of particles is observed with respective momenta q_1 and q_2 . If final state interactions can be neglected, the amplitude of such a final state is proportional to

$$\mathcal{A} \propto \frac{1}{\sqrt{2}} \left[e^{i(q_1 x_1 + q_2 x_2)} + e^{i(q_1 x_2 + q_2 x_1)} \right], \quad (2.37)$$

where x_i ($i = 1, 2$) is the emission point of the i -th particle. If the particles are emitted incoherently, the observed two-particle spectrum is given by

$$\rho_2(q_1, q_2) \propto \int dx_1 \rho_1(x_1) \int dx_2 \rho_1(x_2) |\mathcal{A}(q_1, q_2)|^2, \quad (2.38)$$

and the two-particle intensity correlation function is defined as,

$$D_2(q_1, q_2) = \frac{\rho_2(q_1, q_2)}{\rho_1(q_1)\rho_1(q_2)} = 1 + |d_1(q_1 - q_2)|^2. \quad (2.39)$$

This function carries information about the Fourier-transformed space-time distribution of the particle emission:

$$d_1(q) = d_1(q_1 - q_2) = \int dx e^{iqx} d_1(x) \quad (2.40)$$

as a function of the relative momentum q . As compared to the unsymmetrized case, BECs modify the momentum distribution of the pair of particles in the final state by a weight factor:

$$f_{BEC}(q, x) = \langle 1 + \cos[(q_1 - q_2) \cdot (x_1 - x_2)] \rangle. \quad (2.41)$$

A large amount of data exists on the two-particle correlation function. It has been seen that like-charge particle correlations are much stronger than those between unlike-charge particles [26]. These means that the two and many-particle correlations are mainly due to the Bose-Einstein interference.

Since the model code (UrQMD) employed here to simulate the interactions is a classical Monte-Carlo model, and hence the quantum statistical effects like the Bose-Einstein correlation (BEC) between identical bosons are not embedded into the code. We make an attempt to include the BEC effect numerically in the form of the so called ‘after burner’ algorithm [27] by making use of the output of the event generator. The particle information are contained in the UrQMD output file ‘`test.f19`’ which is written in accordance with the OSCAR format. Only the (even-wise) pi-mesons are chosen from the output file. Each particle entry in an event contains a serial number, the particle ID, the particle 4-momentum (p_x, p_y, p_z, E) , the particle mass m , and the final freeze-out 4-coordinates (x, y, z, t) . The

algorithm of the procedure is as follows:

- (i) Randomly choose a meson from an event, call it the i th one, and assign a charge ‘*sign*’ i.e., $+$, $-$ or 0 to it, irrespective of its original charge with weight factors respectively, given by $p_+ = n_+/n$, $p_- = n_-/n$ and $p_0 = n_0/n$. Here n_+ , n_- , n_0 are respectively, the number of $+$ ve, $-$ ve and neutral mesons in the event, and $n (= n_+ + n_- + n_0)$ is obviously the total number of mesons in that event. This meson, say the i th one, defines a new phase space cell.
- (ii) Calculate the distances in the 4-momenta $\delta_{ij}(p) = |p_i - p_j|$ and 4-coordinates $\delta_{ij}(x) = |x_i - x_j|$ between the already chosen meson (i.e., the i th one) and all other mesons (indexed by j) that are not yet assigned any charge ‘*sign*’.

- (iii) Assign a weight factor

$$P_{ij} = \exp \left[-\frac{1}{2} \delta_{ij}^2(x) \delta_{ij}^2(p) \right] \quad (2.42)$$

to each j -th particle. The weight factor actually characterizes the bunching probability of the particles in a given cell.

- (iv) Then start generating uniformly distributed random numbers $r \in (0, +1)$. If $r < P_{ij}$, reassign to the j -th meson the same charge ‘*sign*’ as the i -th one. Continue the process until either r exceeds P_{ij} , or until all mesons in the event having the same charge ‘*sign*’ as the i -th one are exhausted.
- (v) Repeat the whole set of operations for all other mesons for which the charge reassignment has not yet been done. Obviously, the weight factors $p_{\pm,0}$ will now be modified, as some of the particles present in the event are already used up. The algorithm is repeated until mesons belonging to all charge varieties in the event are used up.

The UrQMD model provides all pion pairs with $-Q = (p_i - p_j)^2 = (\Delta E)^2 - (\Delta p)^2 < 0$. In order to keep the value of the factor (2.42) below unity, only the pion pairs having space-like separation: $-R^2 = (x_i - x_j)^2 = (\Delta t)^2 - (\Delta x)^2 < 0$ are accepted [28]. Without changing the overall set of 4-momenta, 4-coordinates, or total meson charge of the system, we can in this way generate clusters of identical charge states of mesons. A schematic of such clustering is illustrated in Fig. 2.4.

2.5.2 Sampling $^{28}\text{Si-Ag/Br}$ Simulated Events

Two sets of minimum bias $^{28}\text{Si} + \text{Ag}$ and $^{28}\text{Si} + \text{Br}$ events at $E_{\text{lab}} = 14.5\text{A GeV}$ are generated separately using UrQMD (the UrQMD input parameter `CToption(27) = 1`). In order to

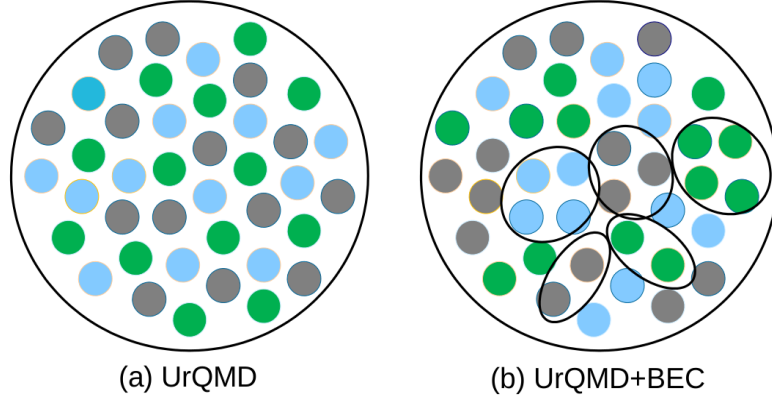


Figure 2.4: An illustration of the effect of the Bose-Einstein correlation algorithm. The phase space distribution of pi-mesons produced in the event generator (UrQMD) is modified by the after burner algorithm of BEC (UrQMD+BEC). Three color varieties represent the members of the pion family.

accommodate the Bose-Einstein correlation into UrQMD, the output files of UrQMD are supplemented by the algorithm mentioned in Section 2.5.1. After that only charged mesons have been retained for subsequent analyses. The event samples corresponding to different target nuclei are then mixed up to produce a new (say) ‘hybrid’ sample. While doing so, the proportional abundance of Ag and Br nuclei in G5 emulsion is maintained [3]. From the hybrid samples we select events in such a way as to match the experimental s -particle multiplicity distributions. The simulated sample is five times as large as the experimental one. Since the simulated event sample possesses identical multiplicity distribution, the average charged meson multiplicity $\langle n_{ch} \rangle$ is obviously same as the experimental $\langle n_s \rangle$. The η and φ distributions for the simulated sample are overlaid onto their respective experimental distribution, shown in Fig. 2.3. One can see that the simulated event sample possesses more or less similar η -distribution as the experiment. The peak density, centroid and the width of the best Gaussian fit to the simulated η -distribution are also very close to their respective experimental values. The values obtained here are: $\rho_0 = 18.18$, $\eta_0 = 1.80$ and $\sigma_\eta = 2.22$. The φ distribution on the other hand possesses a dip at around 180° . This once again is due to a preferential emission of charged secondaries in the direction of the reaction plane, or equivalently due to an ‘elliptic flow’ ($v_2 > 0$) in UrQMD [29].

For error calculation we have generated event samples based on random numbers, where a pair of random numbers representing the η and φ values has been associated with each track. For the pseudorapidity variables we have generated a set of random numbers following Gaussian distribution with the mean and variance as extracted from the experimental sample, and for the azimuthal angle another set of uniformly distributed random numbers with

appropriate limits are generated. The generated sample also possesses identical multiplicity distribution, same η -distribution (actually the best Gaussian fitted distribution) as the experimental sample and uniform φ -distribution. An inverse of integral method is used to generate the Gaussian distributed random numbers, whereas the linear congruential method is used to generate the uniformly distributed random numbers [30]. While generating the random numbers, no correlation has been assumed, and hence these data sets correspond to independent emission of particles. The random number generated sample size is five times larger than the experimental one.

Bibliography

- [1] A. Beiser, *Rev. Mod. Phys.* **24**, 273 (1952).
- [2] C. F. Powell, P. H. Fowler and D. H. Perkins, *The study of elementary particles by photographic method* (Pergamon, Oxford, 1959).
- [3] W. H. Barkas, *Nuclear research emulsions Vol. I and II* (Academic Press, NY, 1963).
- [4] M. Reingamum, *Z, Physik* **12**, 1076 (1911).
- [5] M. S. Livingstone and H. A. Bethe, *Rev. Mod. Phys.* **9**, 245 (1937).
- [6] M. Balu, *Phys. Rev.* **75**, 279 (1949).
- [7] C. O’Ceallaigh, *Nuov. Cim. Suppl.* **12**, 412 (1954).
- [8] P. H. Fowler and D. H. Perkins, *Phil. Mag.* **46**, 587 (1955).
- [9] N. F. Mott, *Proc. Roy. Soc. (London)* **124**, 425 (1929).
- [10] C. M. G. Lattes *et al.*, *Proc. Roy. Soc. (London)* **61**, 173 (1948).
- [11] P. Freier, E. J. Lofgren, E. P. Ney and F. Oppenheimer, *Phys. Rev.* **74**, 1818 (1948).
- [12] S. Goudsmit and J. L. Saunderson, *Phys. Rev.* **58**, 36 (1940).
- [13] G. Singh, A. Z. M. Ismail and P. L. Jain, *Phys. Rev. C* **43**, 2417 (1991).
- [14] G. Singh, K. Sengupta and P. L. Jain, *Phys. Rev. C* **41**, 999 (1990).
- [15] G. D. Westfall *et al.*, *Phys. Rev. C* **19**, 1309 (1979).
- [16] J. Letessier and J. Rafelski, *Hadrons and Quark-Gluon Plasma*, (Cambridge University Press, Cambridge, UK, 2004).
- [17] F. Karsch, *Nucl. Phys. A* **698**, 199c (2002).
- [18] C. Y. Wong, *Introduction to High-Energy Heavy-Ion Collisions* (World Scientific, 1994).
- [19] S. A. Bass *et al.*, *Prog. Nucl. Part. Phys.* **41**, 255 (1998);
M. Bleicher *et al.*, *J. Phys. G* **25**, 1859 (1999).

- [20] H. Sorge, *Phys. Rev. C* **52**, 3291 (1995);
H. Sorge, H. Stocker and W. Greiner, *Ann. Phys.* **192**, 266 (1989).
- [21] H. Feldmeier, *Nucl. Phys. A* **515**, 147 (1990).
- [22] L. Wilets *et al.*, *Nucl. Phys. A* **282**, 341 (1977).
- [23] R. Barnett *et al.*, *Phys. Rev. D* **54**, 1 (1996).
- [24] M. Berenguer, *Thesis*, Goethe University, Frankfurt am Main, Germany (1993).
- [25] W. A. Zajc, *Nucl. Phys. A* **525**, 315c (1991).
- [26] A. D. Angelis, *Mod. Phys. Lett. A* **5**, 2395 (1990).
- [27] O. V. Utyuzh, G. Wilk and Z. Wlodarczyk, *Phys. Lett. B* **522**, 273 (2001).
- [28] M. Bystersky, *Nucleonica Supplement* **49**, s37 (2004).
- [29] P. P. Bhaduri and S. Chattopadhyay, *Phys. Rev. C* **81**, 034906 (2010);
Md. Nasim *et al.*, *Phys. Rev. C* **83**, 054902 (2011).
- [30] P. R. Bevington and D. K. Robinson, *Data Reduction and Error Analysis for Physical Sciences* (McGraw-Hill, New York, 2003).

Chapter 3

Intermittency in $^{28}\text{Si-Ag/Br}$ Interaction at 14.5A GeV

3.1 Introduction

The single particle density distributions of charged particles produced in high-energy collisions exhibit rapid fluctuations having sharp peaks and deep valleys. The origin of such fluctuations might be, (i) a statistical noise arising out of the finiteness of an event multiplicity, (ii) one or more kinematic conservation rules of energy, momentum etc., and (iii) some nontrivial and hitherto unknown dynamical reason. By averaging over a large number of events the effect of statistical component (noise) of these fluctuations can be substantially reduced, but at the same time the nonstatistical (dynamical) components are also averaged out leaving behind a smooth distribution. One way to study the nonstatistical (dynamical) component of fluctuations is to use the technique of scaled factorial moments (SFM) first introduced in [1, 2], and first applied to the JACEE events induced by ultra-high energy cosmic ray nuclei [3]. In [1, 2] the SFM (F_q) of integer order q , was shown to depend on the phase space resolution size (say, δX) obeying a power-law type scaling behavior such as

$$F_q \sim (\delta X)^{-\phi_q} \quad : \quad \delta X \rightarrow 0. \quad (3.1)$$

In high-energy physics the above dependence of F_q on δX is known as ‘intermittency’, a term that usually is used to describe turbulence in fluid dynamics. The positive valued exponent ϕ_q known as the intermittency index represents the strength of intermittency, and it should be a scale-invariant quantity down to the experimental resolution. Several speculative measures, some conventional and a few other exotic, are adopted to interpret the intermittency phenomenon observed in high-energy interactions. As for example, to a large extent intermittency can be explained in terms of the ordinary Bose-Einstein type of correlation (BEC) [4, 5] arising out of an enhanced yield in the like charge sign mesons within narrow phase space intervals. While incorporating the BEC into a numerical modeling certainly reduces the mismatch between the observation and corresponding Monte-Carlo (MC) simulation [6], the experimental results as we shall later see, still cannot always be fully accounted for. Large particle densities within narrow phase space region may also occur due to collective effects [7, 8] like the Cerenkov gluon emission [9]. The intermittency may as well be due to a QCD parton shower cascading process of particle emission [10], or it may be due to a nonthermal phase transition [11] similar to that observed in a spin glass system. Last but not the least, large fluctuations in the final state particle density particularly in the nucleus-nucleus (AB) collisions may be an outcome of a transition from the exotic state QGP to an ordinary hadronic state [12, 13].

While the SFM accounts for local fluctuations in the particles densities, the correlations among particles at different phase space points that are located at a distance larger than the scale size at which the correlations are being examined, generated by the intermittency type of fluctuation, are usually characterized by the two-fold factorial moment or the factorial correlator (FC) [2]. Therefore, the FC corresponds to the bin-to-bin correlation. Both the SFM and the FC are actually integrals of the same underlying correlation function, but they differ from each other only with respect to the respective domains of integration. This close relationship between the two can be traced into the sum rules involving the SFM and the FC, an issue that we shall discuss later. Both moments are sensitive to the projection (dimensional reduction) effects and both contain contributions from the corresponding lower-order moments. In order to study the genuine multiparticle correlation, all lower-order correlations must therefore be appropriately taken care of. To serve this purpose one can study the phase space dependence of another set of moments known as the normalized cumulant moments (NCM) [14]. The ratio of NCM and SFM of a particular order known as the oscillatory moment (OM), can also provide some more insight of the multiparticle dynamics [15, 16] e.g., the gluon-dynamical equation predicts a minimum of OM at rank $q \approx 5$. One should keep in mind though that the OM is effective only to the partonic multiparticle dynamics [16].

The presence of dynamical components in particle density fluctuations has been confirmed

in many high-energy experiments. There are some excellent compilations on the subject, see ref. [17, 18]. The overall picture till date however is neither complete nor very clear. There still exist plenty of unresolved issues related to this phenomenon that need to be further scrutinized. To understand the dynamics of correlated particle emission, the SFM analysis has to be complimented by other types of correlation analysis for the same set of data. Moreover, it is also necessary to simulate experiments by using various computer codes on high-energy AB interactions including all possible sources of correlations in multiparticle production mechanism.

In this chapter we present some results on the SFM and other short-range correlation analysis of singly charged particles produced in $^{28}\text{Si-Ag/Br}$ interaction at an incident energy of 14.5A GeV. We compare the experimental results with those obtained from the UrQMD model and with the UrQMD data modified by the Bose-Einstein correlation (UrQMD+BEC). Whenever felt necessary, the findings of this analysis are compared with similar other heavy-ion induced experiments. The motivations of this analysis are: (i) to study intermittency and various other short-range correlations in $^{28}\text{Si-Ag/Br}$ interaction at 14.5A GeV, (ii) to compare the experimental results with the UrQMD model and to check whether or not the BEC implemented in the UrQMD output (discussed in Section 2.5.1) can account for the experiment. However, before going into the detailed discussion on intermittency and correlation analysis of our data, we provide below a section that shows the nature of the multiplicity fluctuation and the local density fluctuation of the experimental events studied here. A brief but general discussion on multiplicity moments is also incorporated in this section.

3.2 Fluctuation of Particle Densities

Consider a collision between particles a and b yielding exactly n particles falling within a subspace Ω of the total phase space Ω_{tot} . We consider y as the basic variable which specifies the position of each particle in Ω (e.g., y can be the rapidity variable of each particle and Ω an interval of length δy). The distribution of n particles in Ω can be represented by continuous probability densities $P_n(y_1, y_2, \dots, y_n)$, $n = 1, 2, \dots$ etc. Now if all the final state particles are of the same type, P_n is said to be an *exclusive* distribution of n particles which describes the distribution in Ω when the multiplicity is exactly n . The *inclusive* distribution for q particles in variable y is defined as,

$$\rho_q(y_1, y_2, \dots, y_q) = \frac{1}{\sigma_{\text{incl}}} \frac{d^q \sigma_{\text{incl}}}{dy_1 dy_2 \dots dy_q}, \quad (3.2)$$

with σ_{inel} and σ_{incl} the total inelastic and inclusive cross sections. For $q = 1, 2, \dots$ the inclusive distribution can also be written in terms of P_n as,

$$\rho_q(y_1, \dots, y_q) = P_q(y_1, \dots, y_q) + \sum_{l=1}^{\infty} \frac{1}{l!} \int_{\Omega} P_{q+l}(y_1, \dots, y_q, y'_1, \dots, y'_l) \prod_{i=1}^l dy'_i, \quad (3.3)$$

where $\rho_q(y_1, y_2, \dots, y_q)$ is the symmetrized number density for q points (particles) to be at y_1, y_2, \dots, y_q irrespective of the presence and location of any other particle. The inverse of the above formula is

$$P_q(y_1, \dots, y_q) = \rho_q(y_1, \dots, y_q) + \sum_{l=1}^{\infty} (-1)^l \frac{1}{l!} \int_{\Omega} P_{q+l}(y_1, \dots, y_q, y'_1, \dots, y'_l) \prod_{i=1}^l dy'_i. \quad (3.4)$$

The m th order moment of the distribution function is

$$\rho_q^m|_P = \int_{\Omega} \dots \int_{\Omega} P(y_1, \dots, y_q) \rho_q^m dy_1 \dots dy_q \quad (3.5)$$

and it can be generated from the moment generating function as given in the next section. Integrating Eq. (3.3) over Ω in y yields

$$\begin{aligned} \int_{\Omega} dy \rho_1(y) &= \langle n \rangle \rightarrow \text{average event multiplicity,} \\ \int_{\Omega} dy_1 \int_{\Omega} dy_2 \rho_2(y_1, y_2) &= \langle n(n-1) \rangle \rightarrow \text{average number of particle pairs,} \\ \int_{\Omega} dy_1 \dots \int_{\Omega} dy_q \rho_q(y_1, y_2, \dots, y_q) &= \langle n(n-1) \dots (n-q+1) \rangle \rightarrow q\text{th order FM.} \end{aligned} \quad (3.6)$$

Here the angular brackets stand for the average over the event ensemble and n is the event multiplicity in Ω .

3.2.1 Multiplicity Moments

Any statistical distribution can be characterized by its moments. Given a count probability distribution P_n ($n = 1, 2, \dots$) the ordinary q -th order moment is defined as,

$$m_q \equiv \langle n^q \rangle = \sum_{n=0}^{\infty} n^q P_n : \quad q = 0, 1, 2, \dots \quad (3.7)$$

Corresponding moment generating function $\mathcal{G}(z)$ is given by

$$\mathcal{G}(z) \equiv \sum_{n=0}^{\infty} e^{nz} P_n = \sum_q \frac{m_q}{q!} z^q. \quad (3.8)$$

Since P_n is a probability distribution, $\mathcal{G}(0) = 1$, and one gets the ordinary moments from the derivatives of \mathcal{G} :

$$\langle n^q \rangle = \left. \frac{\partial^q \mathcal{G}(z)}{\partial z^q} \right|_{z=0}. \quad (3.9)$$

The reduced moments r_q are obtained by normalizing the ordinary moments by the average count as,

$$r_q = \frac{\langle n^q \rangle}{\langle n \rangle^q}. \quad (3.10)$$

They characterize a particular distribution in terms of the standard deviation, skewness, kurtosis etc.. If the parameter z is assumed to be a constant, the generating functions $\mathcal{G}(z)$ reduce to the generating functions $G(z)$ for the multiplicity distribution (say, P_n). Then one can write

$$\begin{aligned} G(z) &= \sum_{n=0}^{\infty} (1+z)^n P_n \\ &= 1 + \sum_{q=1}^{\infty} \frac{z^q}{q!} \int_{\Omega} dy_1 \dots dy_q \rho_q(y_1, \dots, y_q) \\ &= 1 + \sum_{q=1}^{\infty} \frac{z^q}{q!} \langle f_q \rangle. \end{aligned} \quad (3.11)$$

Here

$$\langle f_q \rangle = \langle n^{[q]} \rangle \equiv \langle n(n-1) \dots (n-q+1) \rangle \quad (3.12)$$

is the unnormalized q th order (a positive integer) factorial (or binomial) moment averaged over many events [Eq. (3.6)], n is the number of particles falling within an arbitrary phase space interval. The multiplicity distribution in terms of $G(z)$ is given by

$$P_n = \frac{1}{n!} \left. \frac{d^n G}{dz^n} \right|_{z=-1}. \quad (3.13)$$

The normalized factorial moments can be derived from the generating function $G(z)$ as,

$$\begin{aligned} F_q &= \frac{1}{\langle n \rangle^q} \left. \frac{d^q G}{dz^q} \right|_{z=0} \\ &= \frac{\sum_{n=0}^{\infty} n(n-1) \dots (n-q+1) P_n}{\langle n \rangle^q} \end{aligned} \quad (3.14)$$

with $F_1 = 1$, while the cumulant moments are given by

$$K_q = \frac{1}{\langle n \rangle^q} \left. \frac{d^q \ln G}{dz^q} \right|_{z=0}. \quad (3.15)$$

Note that the generating function can be expressed in terms of the moments F_q and K_q as,

$$G(z) = 1 + \sum_{q=1}^{\infty} z^q \langle n \rangle F_q / q!, \quad (3.16a)$$

$$\ln G(z) = \langle n \rangle z + \sum_{q=2}^{\infty} z^q \langle n \rangle K_q / q!. \quad (3.16b)$$

Using $dG/dz = G (d \ln G / dz)$ we see that for $q \geq 2$

$$F_q = \sum_{l=0}^{q-1} \binom{q-1}{l} K_{q-l} F_l. \quad (3.17)$$

However, normalized or not, the ordinary moments cannot address the issue of noise elimination, but the factorial moment can do so. As for example, for a Poisson distributed noise

$$P_n = \int_0^{\infty} \frac{t^n}{n!} e^{-t} D(t) dt, \quad (3.18)$$

where $D(t)$ is the dynamical component of the distribution in the same bin. The critical point here is that, for a large event sample the bin-multiplicity n can run from zero to a very large value. Therefore,

$$\begin{aligned} \langle f_q \rangle &= \sum_{n=0}^{\infty} n(n-1) \cdots (n-q+1) P_n = \sum_{n=q}^{\infty} \frac{n!}{(n-q)!} P_n \\ &= \sum_{n=q}^{\infty} \int_0^{\infty} \frac{t^n}{(n-q)!} e^{-t} D(t) dt \\ &= \int_0^{\infty} t^q D(t) dt \quad (\text{summing over } n). \end{aligned} \quad (3.19)$$

This shows that $\langle f_q \rangle$ is identical to the ordinary q th order moment of the dynamical component of the distribution P_n . The normalization property of the Poisson distribution is used in the above derivation. This shows that the statistical fluctuations have been successfully eliminated by averaging over the event sample. A detailed discussion on multiplicity moments especially related to the hadronic physics can be found in refs. [18, 19].

3.2.2 Fluctuation in η -space

As mentioned in Section 3.1, a high energy AB collision can have highly fluctuating density distribution that gets smoothed out when the distribution is averaged over many events. To have an idea about the nature of the fluctuation, the η distributions of the shower tracks

emerging from two high multiplicity $^{28}\text{Si-Ag/Br}$ events at 14.5A GeV are shown in Fig. 3.1. For each event the shower track multiplicity n_s is given in the corresponding figure and each distribution is drawn at two different scales: $\delta\eta = 0.2$ (left panel) and 0.1 (right panel). Presence of high particle densities (spikes) as well as empty bins (dips) can be seen in η -

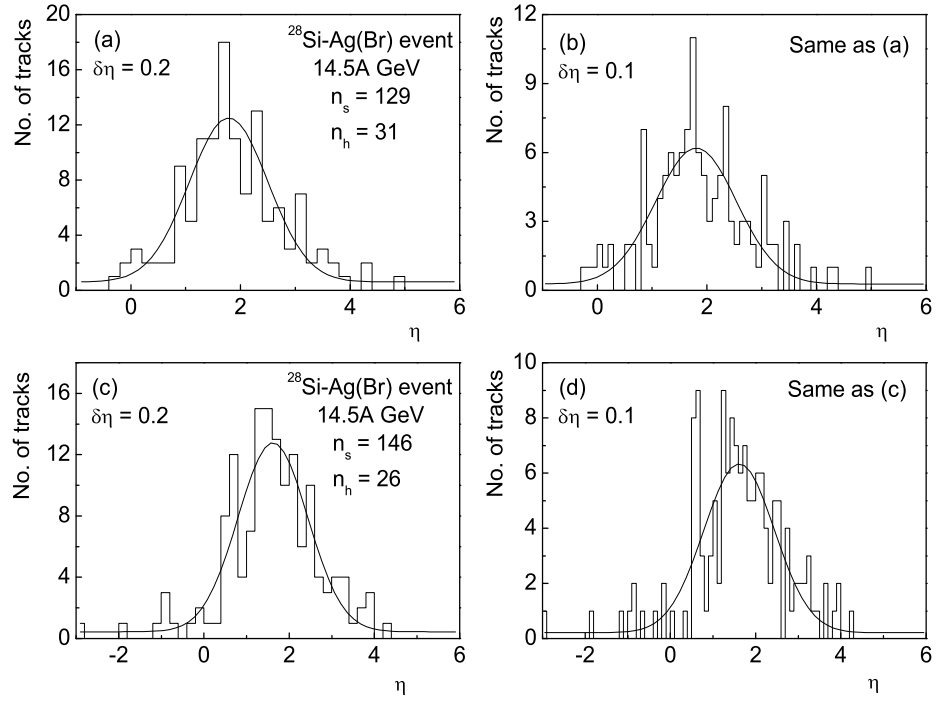


Figure 3.1: Pseudorapidity distribution of shower tracks of two high multiplicity events in $^{28}\text{Si-Ag/Br}$ interactions at 14.5A GeV. Note how the fluctuation increases with decreasing bin size from $\delta\eta = 0.2$ to $\delta\eta = 0.1$. n_s and n_h represent respectively the number of s -tracks and heavy fragments of the event. Gaussian fits to the distributions are shown.

space. One can also see that the local particle density ($\rho = \delta n_s / \delta\eta$) can shoot up to 110, which is about 6 times the average density ($\rho \sim 18$). The peak ρ value in one of the JACEE events was found to be ~ 300 at $\delta\eta = 0.1$ [3], and one NA22 event showed a rapidity spike of $\rho \sim 100$ at a resolution $\delta y = 0.1$ [20] – the latter corresponds to 60 times the average density. When the same distribution is made for many events, the local fluctuations disappear as illustrated in Fig. 2.3(a) for our $^{28}\text{Si-Ag/Br}$ event sample.

Distributions of the local densities around the central η -region obtained from individual events are shown in Fig. 3.2: (a) for $\eta_0 - 1 < \eta < \eta_0$ and (b) for $\eta_0 < \eta < \eta_0 + 1$, where $\eta_0 = 1.9$ is the centroid of the η -distribution, and the density values are obtained for $\delta\eta = 0.2$. These diagrams provide a qualitative idea of the density fluctuation in and around the central particle producing region in $^{28}\text{Si-Ag/Br}$ interaction at 14.5A GeV.

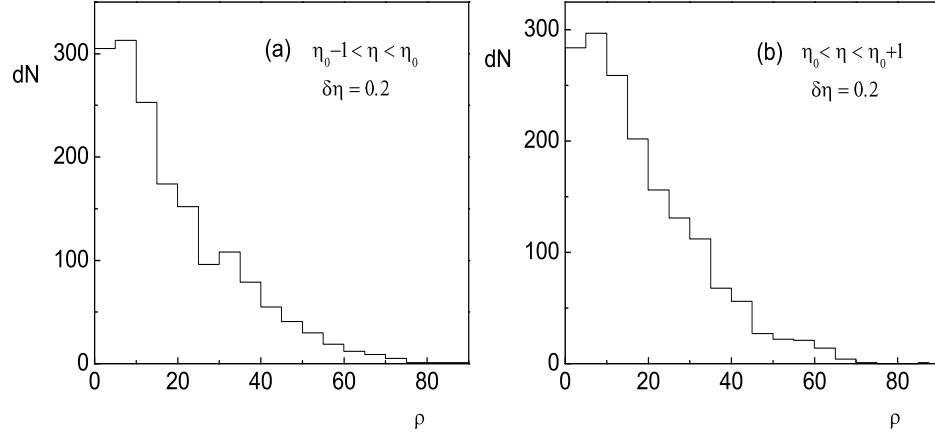


Figure 3.2: Distributions of local pseudorapidity density of shower tracks in $^{28}\text{Si-Ag/Br}$ interactions at 14.5A GeV.

3.3 Scaled Factorial Moments

The normalized or scaled factorial moment (SFM) [2] can be defined in two distinct ways, and based on the normalization method adopted, it is customary to call them either a *horizontally averaged* or a *vertically averaged* factorial moment. In terms of the inclusive distribution $\rho_q(\eta)$ the horizontally averaged SFM is defined as,

$$\begin{aligned} \langle F_q^H(\eta) \rangle &= \frac{1}{M} \sum_{m=1}^M \frac{\int_{\delta\eta} \rho_q(\eta_1, \dots, \eta_q) \prod_{i=1}^q d\eta_i}{\left(\int_{\delta\eta} \rho(\eta) d\eta / M \right)^q} \\ &= \frac{1}{M} \sum_{m=1}^M \frac{\langle n_m^{[q]} \rangle}{\langle \bar{n}_m \rangle^q}, \end{aligned} \quad (3.20)$$

where $\langle \bar{n}_m \rangle = \langle n \rangle / M$, $n = \sum_m n_m$ is the total number of particles in an event. Here we consider that a large phase space interval Δ is divided into M smaller non-overlapping bins of equal size $\delta = \Delta / M$. The symbol $\langle \rangle$ represents an average over all events of our sample. Note that, in the above expression δ can be any phase space variable such as the rapidity (y), pseudorapidity (η), azimuthal angle (φ), transverse momentum (p_t), or even a suitable combination of any two (or three) of them. In emulsion experiments we consider either η or φ as our phase space variable, and in two-dimension (2d) it is the (η, φ) -plane that serves our purpose. On the other hand the vertically averaged SFM is defined as,

$$\begin{aligned} \langle F_q^V(\eta) \rangle &= \frac{1}{M} \sum_{m=1}^M \frac{\int_{\delta\eta} \rho_q(\eta_1, \dots, \eta_q) \prod_{i=1}^q d\eta_i}{\left(\int_{\delta\eta} \rho(\eta) d\eta \right)^q} \\ &= \frac{1}{M} \sum_{m=1}^M \frac{\langle n_m^{[q]} \rangle}{\langle n_m \rangle^q}. \end{aligned} \quad (3.21)$$

In Eq. (3.21) $\langle n_m \rangle$ is the average number of particles in the m th bin in the event sample. Irrespective of the averaging techniques, the SFMs are capable of suppressing the Poisson type statistical noise, which the ordinary moments cannot. The vertically averaged SFMs are more sensitive to the bin-to-bin density variations within events but they become unstable at small bin sizes, whereas the horizontally averaged SFMs are sensitive only to the local fluctuations of the particle densities and they remain stable over a large range. It should be pointed out here that both the moments are equal for $M = 1$ and also when $\langle n_m \rangle = \langle n \rangle / M$ for all m , i.e. the underlying distribution in the particular phase space variable is flat. To satisfy the latter criterion one can use a cumulative variable [21]

$$X_\eta = \int_{\eta_{\min}}^{\eta} \rho(\eta) d\eta / \int_{\eta_{\min}}^{\eta_{\max}} \rho(\eta) d\eta, \quad (3.22)$$

where $\eta_{\min}(\eta_{\max})$ is the minimum(maximum) value of η , and $\rho(\eta) = N_{ev}^{-1}(dn/d\eta)$ is the single particle inclusive density in terms of η . Irrespective of its original form, density distribution in terms of X_η is always uniform $\in (0, 1)$. The present analysis is based on the cumulative variables corresponding to the η and/or φ variables, though we shall continue to call the corresponding space either the η or the φ -space.

3.3.1 Intermittency in 1d

In 1d intermittency analysis the data have been analyzed in terms of η and φ variables. Figure 3.3 shows the log-log plot of the horizontally averaged SFM $\langle F_q \rangle$ against the phase space partition number M in η -space for $q = 2, \dots, 6$. Note that the superscripts h or v is omitted from the subsequent text, though a horizontal averaging used here. We have noticed that there is little deviation in the horizontally averaged SFM from the corresponding vertically averaged moment. The experimentally obtained, the UrQMD generated and the UrQMD+BEC generated results have been plotted side by side in the same figure. A similar set of plots in the φ -space is shown in Fig. 3.4. In both diagrams one can see that for each q there is a definite linear rise in the experimental $\ln \langle F_q \rangle$ values with $\ln M$ that confirms a power-law behavior like

$$\ln \langle F_q \rangle = \phi_q \ln M + c_q, \quad (3.23)$$

as is also suggested in Eq. (3.1). The UrQMD simulated $\ln \langle F_q \rangle$ values remain practically uniform with varying $\ln M$ over its entire range that indicates almost no intermittency in the UrQMD events. On the other hand, the UrQMD+BEC sample shows moderate rise in the $\ln \langle F_q \rangle$ values and thereby in comparison with the experiment a weaker intermittency. All these observations are true in the φ -space as well. At this point one may remember that the string fragmentation model FRITIOF [22] also did not show any intermittency for

AB interactions at 200A GeV [23]. The values of the intermittency index along with the

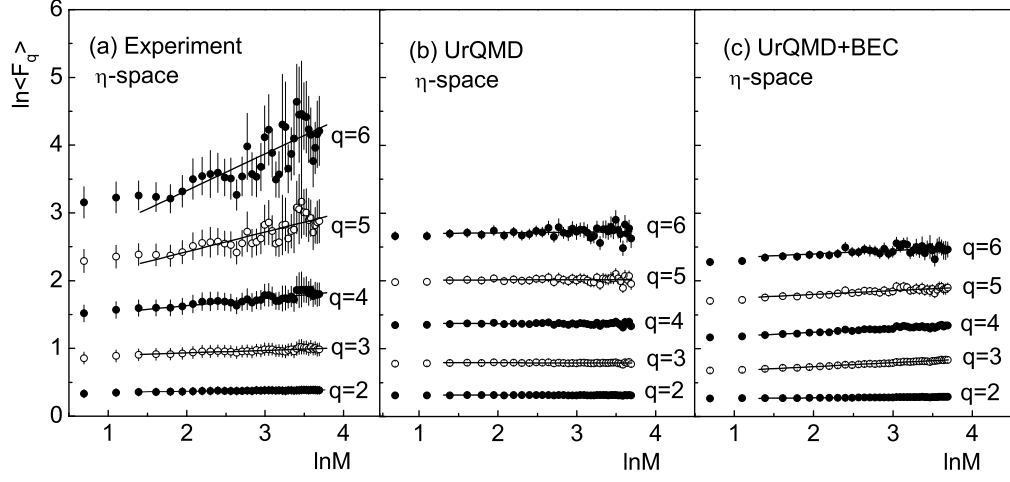


Figure 3.3: Variation of the event averaged SFM of shower tracks with phase space resolution in η -space. Straight lines best fitted to the data points are shown.

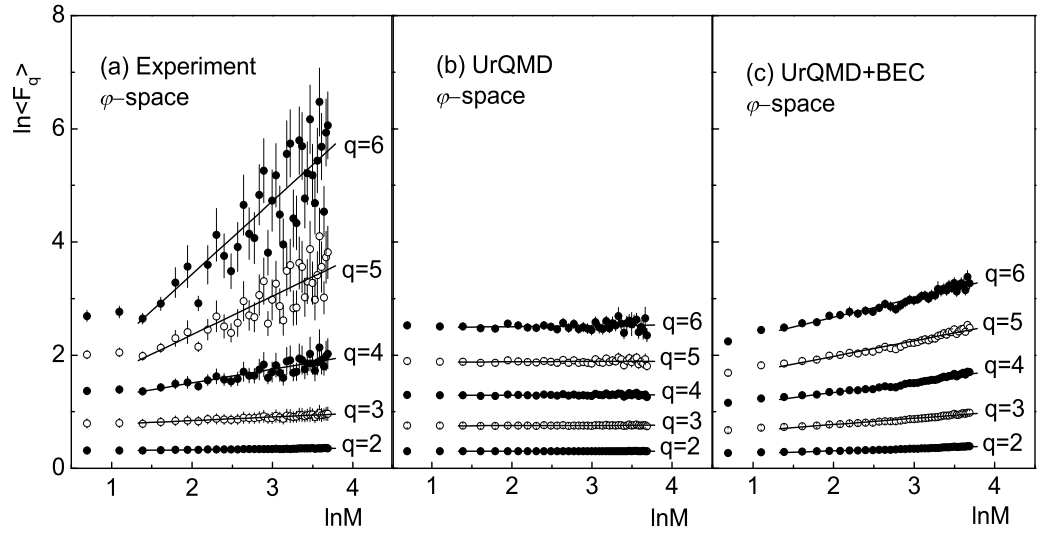


Figure 3.4: Same as Fig. 3.3 but in ϕ -space.

Pearson's R^2 coefficients, indicating the goodness of fit, are shown in Table 3.1. For each q , a linear fit of $\ln \langle F_q \rangle$ against $\ln M$ has been performed by excluding the very small M (or large δX) region (first two points in each diagram), so that the effects of kinematic conservation rules are minimized. The errors associated with $\langle F_q \rangle$ as shown in the figures, and those associated with ϕ_q as quoted in the table, are only of statistical origin. For each event the F_q is assumed to be an error free quantity, and the standard error of the mean $\langle F_q \rangle$ over event space is calculated and shown in the diagrams. On the other hand, as the data points in $\langle F_q \rangle$ versus M plots are highly correlated, the errors in ϕ_q are nontrivially estimated [24] by generating several event samples based on random numbers that have same statistics

Table 3.1: The values of $1d$ intermittency exponent (ϕ_q) for order $q = 2 - 6$ in $^{28}\text{Si-Ag/Br}$ interaction at 14.5A GeV. The errors are of statistical origin only.

	Order	η -space		φ -space	
		ϕ_q	R^2	ϕ_q	R^2
Experiment	$q = 2$	0.011 ± 0.001	0.989	0.016 ± 0.001	0.955
	$q = 3$	0.039 ± 0.003	0.972	0.065 ± 0.002	0.940
	$q = 4$	0.112 ± 0.007	0.949	0.214 ± 0.005	0.911
	$q = 5$	0.255 ± 0.013	0.941	0.600 ± 0.011	0.908
	$q = 6$	0.477 ± 0.023	0.938	1.941 ± 0.029	0.934
UrQMD	$q = 2$	-0.0001 ± 0.0006	0.971	0.002 ± 0.001	0.982
	$q = 3$	0.0001 ± 0.0018	0.963	0.004 ± 0.002	0.985
	$q = 4$	0.006 ± 0.005	0.960	0.005 ± 0.002	0.951
	$q = 5$	0.028 ± 0.011	0.951	0.008 ± 0.003	0.943
	$q = 6$	0.075 ± 0.048	0.943	0.018 ± 0.011	0.927
UrQMD+BEC	$q = 2$	0.001 ± 0.0005	0.991	0.0045 ± 0.0015	0.982
	$q = 3$	0.003 ± 0.0017	0.972	0.041 ± 0.004	0.981
	$q = 4$	0.013 ± 0.006	0.963	0.099 ± 0.007	0.980
	$q = 5$	0.045 ± 0.013	0.987	0.219 ± 0.010	0.978
	$q = 6$	0.091 ± 0.024	0.983	0.352 ± 0.015	0.970

as the experimental one. Following the same scaling-law as the data points follow, the ϕ_q values for each individual random event sample is determined, and then the statistical spread about the mean $\langle \phi_q \rangle$ are quoted as errors in Table 3.1. Since in the process the nonstatistical component is not taken into account the errors are certainly underestimated. One can see that the ϕ_q values are consistently larger in the φ -space than in the η -space. To conserve transverse momentum, probably the particles experience extra correlation in the azimuthal plane. However, such differences in the ϕ_q values are more prominent in interactions induced by nuclei with higher mass number e.g., ^{28}Si or ^{32}S , and are not so much when the interaction is induced by a comparatively lighter (^{16}O) nucleus [23]. Results of the present investigation are also significantly different from what was previously obtained from the analysis of another set of $^{28}\text{Si-Ag/Br}$ data at the same incident energy [25, 26]. This discrepancy is probably due to the non-conversion of the phase space variables (η , φ) to their respective cumulant variables. Hence, the intermittency phenomenon depends more on the colliding system and less on the collision energy. It is also dependent on the choice of the phase space variable, which is in contradiction to the observation of ref. [24], but consistent with our previous observation on AB interactions [23].

One can now put the ϕ_q values to further tests and try to look for the underlying physical processes (e.g., phase-transition or no phase-transition) that probably have resulted in the

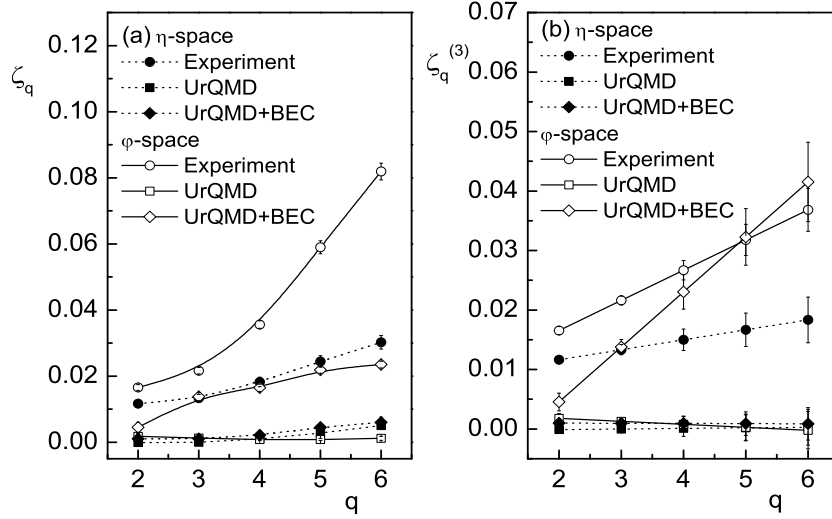


Figure 3.5: Normalized intermittency exponents as a function of order number q . Lines joining points are drawn to guide the eye.

observed intermittency pattern. In order to check to what extent the particle correlation embedded within a higher order SFM is influenced by the contribution from lower order (two or three-particle) correlation(s), one can introduce the normalized exponents ζ_q and the true three-particle correlation function $\zeta_q^{(3)}$, and can then study their dependence on q . These exponents are defined as [24],

$$\zeta_q = \phi_q / \binom{q}{2}, \quad (3.24a)$$

$$\zeta_q^{(3)} = (q-2)\zeta_3 - (q-3)\zeta_2. \quad (3.24b)$$

In Fig. 3.5 the normalized exponents for the experiment, for the UrQMD and for the UrQMD+BEC simulated data have been plotted against q . Results in η -space and in φ -space are shown together in the same diagram. We see that the experimental ζ_q value increases with increasing q , and the rate of increase is much higher in the φ -space than what it is in the η -space. The observation also confirms a linear relationship between $\zeta_q^{(3)}$ and q as prescribed in Eq. (3.24b). Expectedly, the experimental and the simulated results behave in quite different ways and within statistical errors the UrQMD simulated values exhibit little intermittency and thereby no correlation. The effect of incorporating BEC into the UrQMD simulation can be clearly seen in these diagrams. However, one has to note that the shower tracks are caused by all kinds of charged mesons. Therefore, due to intermixing of different charge and particle states, the usual BE type correlation arising out of the symmetrization of the wave function of a system of identical bosons is significantly weakened. The results on normalized exponents suggest that to a large extent higher order ($q \geq 4$) correlations may be understood in terms of two and three-particle correlations.

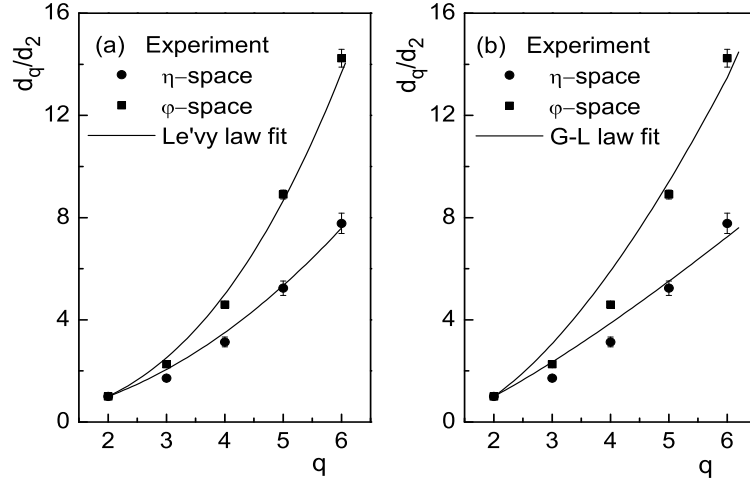


Figure 3.6: Plots of d_q/d_2 as a function of order number q for the experiment—(a) curves represent the best fitted log-Lévy law, Eq. (3.27) and (b) curves represent the Ginzburg-Landau model, Eq. (3.28).

A power-law behavior of the $1d$ SFMs characterizes some kind of scale invariance of the dynamics of multiparticle production. This can be realized either in terms of the self-similar random cascading models [27], or in the statistical systems at critical temperature for a second-order phase transition [28] (for a review see ref. [17]). The dependence of ϕ_q on q would be different in these two cases that can be examined by establishing a connection between intermittency and (multi)fractality [29]. The generalized Rényi dimensions of multifractality D_q , a direct measure of multifractality, are directly related to the intermittency exponents ϕ_q through the relation:

$$D_q = D_T - \frac{\phi_q}{q-1}, \quad (3.25)$$

where D_T is the topological dimension of the supporting space, $D_T = 1$ in $1d$ and $D_T = 2$ in $2d$ analysis. On the other hand, the anomalous dimension d_q is defined as

$$d_q = D_T - D_q. \quad (3.26)$$

For a system at the critical temperature of a second-order phase transition, the multifractal behavior reduces to a monofractal behavior for which the SFM of a single cluster will have the same structure as the NCMs of all events. Based on a linked pair approximation, it has been shown that under such a circumstance a scaling relation like Eq. 3.23 would imply the presence of Poisson distributed monofractal clusters characterized by a unique anomalous dimension i.e., $d_q/d_2 = 1$ [30]. A plot of d_q/d_2 against q presented in Fig. 3.6 shows that our results are certainly not indicating a monofractal structure of the density function, and therefore, not toward a second-order phase transition either. For multiplicative cascade mechanisms like the α -model [2], where the final state particle density is given as a product

of random numbers, the density function can be approximated by a long-tailed log-Lévy distribution. Under this approximation, the following relation holds:

$$\frac{d_q}{d_2} = \frac{1}{(q-1)} \frac{q^\mu - q}{2^\mu - 2}, \quad (3.27)$$

where $\mu(0 \leq \mu \leq 2)$ is called the Lévy stable index [27]. The Lévy-law approximation allows a simple description of multifractal properties of random cascade models using only one free parameter μ . Under this scheme $\mu < 1$ is indicative of a second-order (thermal) phase transition, while $\mu > 1$ indicates a nonthermal phase transition. Moreover, a monofractal behavior is characterized by $\mu = 0$ and $d_q = 0$ for $q > 2$. On the other hand, in the limit of the log-normal approximation $\mu = 2$, $d_q = d_2$ and all bunching parameters follow the same power-law. A fit of our experimental data points to Eq. (3.27), shown in Fig. 3.6(a), results $\mu = 3.15 \pm 0.03$ in η -space, and $\mu = 3.70 \pm 0.03$ in φ -space. Both these values far exceed the allowed limit of the stability index, thereby showing that the (dynamical) density function in the present case cannot exactly be represented by a log-Lévy type of distribution. Similar observation was also made in the 1d intermittency analysis in $^{12}\text{C}-(\text{Cu}, \text{Ne})$ interactions at 4.5A GeV/c [31], where a second-order phase transition was ruled out as a probable mechanism of hadronization. Note that an incident energy of 14.5 GeV/nucleon is not very much different either. The reason may as well be due to the ‘projection’ effect as is usually found in the lower dimensional intermittency analysis. In Section 3.3.2 where the results on 2d analysis have been presented, we would expect a better estimate of d_2 . The stability index can also be obtained through other approaches, e.g. using the multifractal spectrum as discussed in Chapter 5. Though the present μ -values ($>$ unity) indicate a nonthermal phase transition during the particle emission process, the issue needs further scrutiny before arriving at a definite conclusion. Intermittency can also be studied in the framework of the Ginzburg-Landau (G-L) model. According to which the ratio d_q/d_2 should obey a relation:

$$\frac{d_q}{d_2} = (q-1)^{\nu-1}, \quad (3.28)$$

where $\nu(= 1.304)$ is a dimension independent universal parameter, as suggested in ref. [32]. For our $^{28}\text{Si-Ag/Br}$ data we found $\nu = 2.30 \pm 0.02$ in η -space and $\nu = 2.65 \pm 0.03$ in φ -space. A graphical representation of the Ginzburg-Landau prediction has also been shown in Fig. 3.6(b). Thus, our intermittency results cannot be explained in terms of the Ginzburg-Landau theory either.

A more direct measure of the intermittency strength can be obtained from its connection with (multi)fractality, at first in the framework of the α -model [2], and subsequently in a model independent way irrespective of any particular hypothesized mechanism of particle production [33]. According to the α -model, the strength parameter α_q is related to D_q by

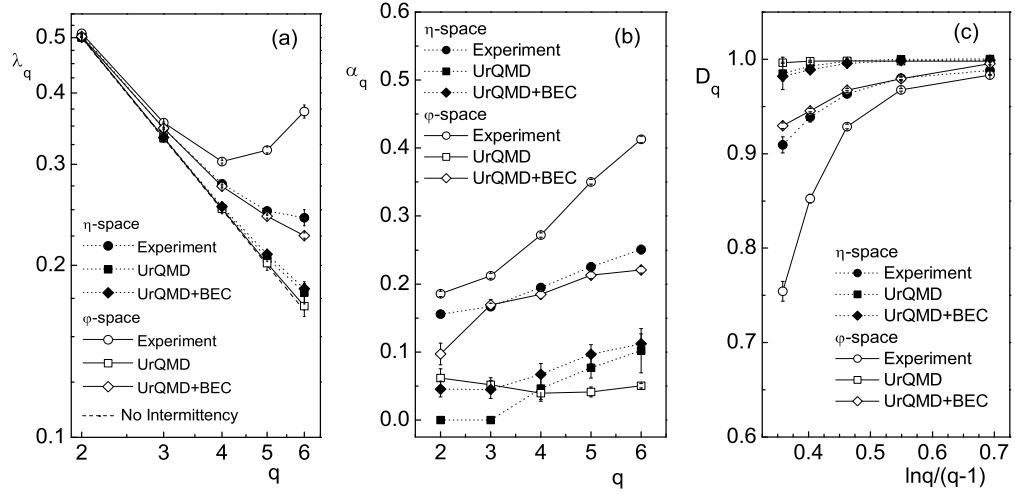


Figure 3.7: (a) Plot of λ_q with order number q . (b) Plot of intermittency strength α_q with q . (c) Plot of generalized Rényi dimension D_q with $\ln q/(q-1)$. The curves are drawn to guide the eye.

a simple relation:

$$\alpha_q = \sqrt{\frac{6 \ln 2}{q} (D_T - D_q)}. \quad (3.29)$$

The α_q values in 1d have been calculated for all three data sets, one experimental and two simulated, and their variation with q has been schematically presented in Fig. 3.7(b). One can see that for the experiment the strength parameter linearly increases with increasing order, whereas for the simulation it hovers around a very small value (≈ 0.05) except the UrQMD+BEC generated plot in φ -space. From the above discussion it cannot be claimed in clear terms as to which process (i.e., second-order phase transition or random cascading) is actually responsible for the observed intermittency. For an arbitrary underlying dynamics it is possible to define an effective fluctuation strength $\alpha_{\text{eff}} = \sqrt{2\phi_2}$ [33]. We found that $\alpha_{\text{eff}} = 0.15 \pm 0.003$ in η -space and $\alpha_{\text{eff}} = 0.18 \pm 0.003$ in φ -space for the present set of experimental data. These values are about 1/6 times the maximum fluctuation strength ($\alpha = 1.0$) allowed in the α -model. Comparing with our previous results, we find that the present values are even less than what we observed in $^{16}\text{O-Ag/Br}$ interaction at 200A GeV (about one fourth the maximum value), but within error they are of same magnitude as the $^{32}\text{S-Ag/Br}$ interactions at 200A GeV [23]. Thus, it appears that for same target the intermittency strength depends more on the projectile mass number than on the energy of interaction.

A thermodynamic interpretation of multifractality has also been given in terms of a constant specific heat C that is related to the Rényi dimensions as [34],

$$D_q = D_\infty + \frac{C \ln q}{q-1}. \quad (3.30)$$

Table 3.2: The values of multifractal specific heat C calculated from the SFM analysis. The C values evaluated at different q -regions are specified.

	Fit region	η -space	φ -space
Experiment	$2 \leq q \leq 4$	0.103 ± 0.035	0.224 ± 0.089
	$2 \leq q \leq 5$	0.158 ± 0.049	0.047 ± 0.156
	$3 \leq q \leq 5$	0.273 ± 0.061	0.758 ± 0.229
UrQMD	$2 \leq q \leq 4$	0.009 ± 0.006	-0.001 ± 0.0010
	$2 \leq q \leq 5$	0.022 ± 0.011	0.0001 ± 0.0013
	$3 \leq q \leq 5$	0.046 ± 0.017	0.0006 ± 0.0004
UrQMD+BEC	$2 \leq q \leq 4$	0.013 ± 0.007	0.120 ± 0.011
	$2 \leq q \leq 5$	0.013 ± 0.005	0.149 ± 0.008
	$3 \leq q \leq 5$	0.052 ± 0.018	0.214 ± 0.021

While deriving the relation (3.30) it has been assumed that only *Bernoulli* type of fluctuations are responsible for a transition from monofractality to multifractality. A monofractal to multifractal transition corresponds to a jump in the value of C from zero to a nonzero positive finite value. By examining the variation of D_q with q one can obtain the value of C . A plot of D_q can be found in Fig. 3.7(c) for all the data sets used in this analysis. Whereas the simulated D_q values are always very close to the dimension of the supporting space ($D_T = 1$), the experimental values are consistently different from unity. Over the full range ($q = 2, \dots, 6$) the experimental D_q varies nonlinearly with $\ln q/(q-1)$, and the nonlinearity is more prominent in the φ -space than in the η -space. The C value will obviously depend on the range of q over which the data are fitted. In Table 3.2, the fit results in different q ranges are given, which always show nonzero positive C . The simulated values are within error, either zero or about an order less than the corresponding experimental values. One can also see that contrary to what is found in $^{32}\text{S-Ag/Br}$ interaction at 200A GeV [35], in the present case the C value in φ -space is always higher than that in η -space. However, the values of C are not consistent with the universality of the parameter as claimed in ref. [34].

The phase transition, if there is any, may not necessarily always be a thermal one, as the new phase is not essentially defined by a (set of) thermodynamic parameter(s). Simultaneous existence of two nonthermal phases (like those in a spin-glass system) is a possibility that can be investigated by the intermittency parameter [36]

$$\lambda_q = \frac{\phi_q + 1}{q}. \quad (3.31)$$

In the α -model λ_q exhibits a minimum at a critical point $q = q_c$, where the regions $q < q_c$ and $q > q_c$ are respectively, dominated by a large number of small fluctuations (liquid phase), and

a small number of large fluctuations (dust phase). The variation of λ_q has been schematically presented in Fig. 3.7(a) for the experiment as well as for the simulations. In η -space there is a hint of a probable minimum beyond our region of investigation ($q > 6$). Whereas, in φ -space a clear minimum at $q_c = 4$ can be seen. The UrQMD and the UrQMD+BEC simulated values do not follow such pattern. The present experimental results are similar to what was observed in $^{12}\text{C-Cu}$ interaction at 4.5A GeV/c [37].

3.3.2 Intermittency in 2d

As mentioned above to a great extent the projection effect influences the intermittency results. We therefore, extend our analysis to the two dimensional (η, φ) plane. Since our analysis is based on the cumulative variables, the (η, φ) plane is effectively a (X_η, X_φ) square of unit area. As mentioned before, we continue to call it the (η, φ) plane. Setting the partition numbers along each direction equal i.e., $M_\eta = M_\varphi$, the phase space is first symmetrically (or self-similarly) partitioned to result in $M (= M_\eta^2)$ smaller non-overlapping squares of equal size. The q th order two-dimensional SFM $F_q^{(2)}$ is now defined in the similar way as in Eq. (3.20), and n_m is now the number of particles falling within the m th sub-cell (a smaller square) of size $1/(M_\eta \cdot M_\varphi)$. Figure 3.8 shows the plot of $\ln \langle F_q^{(2)} \rangle$ against $\ln M$ which we shall later refer to as the 2d-SFM plot, and where (a) is for the experiment, (b) is for the UrQMD simulation and (c) is for the UrQMD+BEC simulation. The experimental

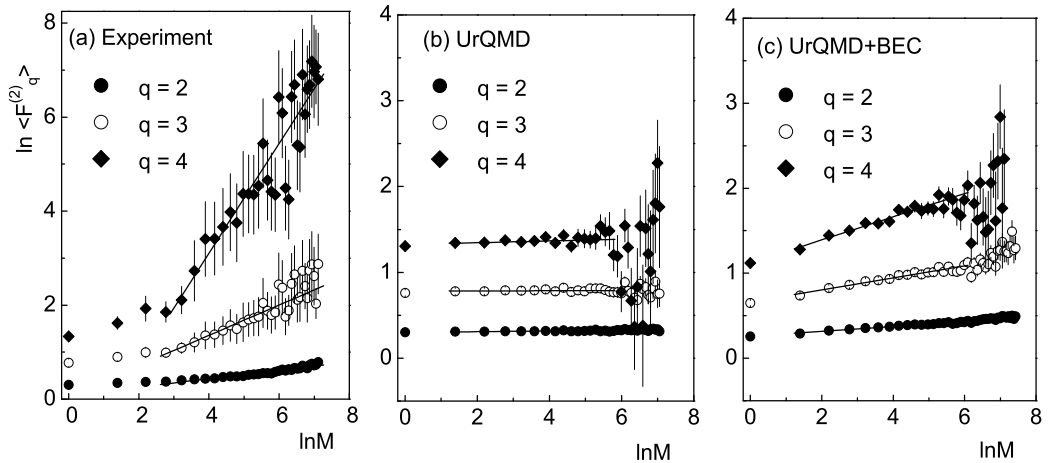


Figure 3.8: Plot of 2d-SFM for a self-similar partitioning of the (η, φ) plane. The lines represent linear regressions to the data points.

points show a nonlinear dependence of $\ln \langle F_q^{(2)} \rangle$ on $\ln M$. In contrast, the UrQMD simulated 2d-SFMs are almost independent of M . For $q > 2$ only at large M they exhibit an irregularly fluctuating pattern. On the other hand, the UrQMD+BEC data points follow more or less a self-similar power-law like Eq. (3.23). We denote the corresponding exponents by β_q (similar

Table 3.3: The values of $2d$ intermittency exponent β_q of order $q = 2 - 4$ for self-similar partitioning of the (η, φ) space in $^{28}\text{Si-Ag/Br}$ interaction at 14.5A GeV.

	Order	β_q	$\chi^2(dof)$
Experiment	$q = 2$	0.086 ± 0.005	18.92(32)
	$q = 3$	0.322 ± 0.036	28.98(32)
	$q = 4$	1.124 ± 0.074	44.88(32)
UrQMD	$q = 2$	0.0043 ± 0.0027	04.27(14)
	$q = 3$	0.0002 ± 0.0046	10.28(14)
	$q = 4$	0.0103 ± 0.0092	26.45(14)
UrQMD+BEC	$q = 2$	0.028 ± 0.002	04.38(16)
	$q = 3$	0.067 ± 0.003	16.35(16)
	$q = 4$	0.122 ± 0.006	34.04(16)

to ϕ_q in $1d$) and calculate them by fitting straight lines to the data points. For a nonlinear variation obviously the slope will depend on the region of fit. Hence, we have done so in a region where the variations are visibly linear as shown in the diagrams. The β_q values obtained from the linear fits are given in Table 3.3. As a measure of the goodness of the fits the χ^2 values along with the number of degrees of freedom (dof) are also quoted in the table. However, we insist that the β_q values only represent a qualitative estimate of the rise in $2d$ -SFMs with diminishing phase space partition size. When the rise is nonlinear, these indices are in no way connected to the power-law scaling, or for that matter to intermittency. The UrQMD generated graphs are always almost uniformly distributed showing very little or no intermittency. Correlation of any type, either due to the symmetry property of the underlying field(s) and/or due to any dynamical reason, is virtually non-existing. When the BEC is numerically modeled into the UrQMD data to some extent we can retrieve the power-law type of scaling. Corresponding β_q values also indicate that by accommodating the BEC into the simulated data, one can to a certain degree account for the intermittent behavior. However, as mentioned above, the experimental values are still several times larger than the UrQMD+BEC values, and the experiment still cannot be fully accounted for. The observation here supports our results on $1d$ analysis. We have checked that there is hardly any nonlinearity in the variation of $\ln \langle F_q^{(2)} \rangle$ with $\ln M$ in the UrQMD+BEC simulation. As the simulated data do not exhibit any anisotropy in the (η, φ) plane we did not extend our self-affine analysis for them. We notice that the experimental β_q values are several times larger than the $1d$ intermittency indices ϕ_q obtained for the same sets of data [Table 3.1].

The distribution of particles in the (η, φ) plane is anisotropic [38], while the allowed η range depends on the collision energy, the φ range irrespective of all kinematic conditions is bound within $(0 - 2\pi)$. Similarly depending on the kinematic conditions, the longitudinal momenta

(p_t) of produced particles can vary over a wide range, whereas the average transverse momenta p_\perp of these particles, irrespective of the nature of interactions and for a reason that is still unknown to us, are limited within a relatively small range of 0.3 – 0.5 GeV/c. As a direct consequence of this anisotropy, an equal bin partitioning of the 2d distribution results in an upward bending in the corresponding log-log plot of SFM. It is suggested that in the 2d SFM analysis, the phase space should be partitioned differently in a self-affine way as said in the fractal theory, taking the anisotropy of the phase space into account [39]. One way to implement this is to introduce a ‘roughness’ parameter called the *Hurst exponent* (H). The anomalous scaling of the 2d-SFM that characterizes intermittency, can then be retrieved only with a proper choice of the H value. Then the phase space scale factors in the longitudinal (η) and transverse (φ) directions can be related as,

$$M_\eta = M_\phi^H, \quad \text{for } H \leq 1.0; \quad M_\phi = 1, 2, \dots, M_\phi^{\max}; \quad (3.32a)$$

$$M_\phi = M_\eta^{1/H}, \quad \text{for } H > 1.0; \quad M_\eta = 1, 2, \dots, M_\eta^{\max}. \quad (3.32b)$$

Here we choose $M_\phi^{\max} = M_\eta^{\max} = 50$. For $H < 1.0$ the φ -direction is partitioned into finer intervals than the η -direction, whereas for $H > 1.0$ the reverse is true. It is obvious that, both M_η and M_φ simultaneously cannot always be integers. After dividing the η (φ) direction by a non-integer partition number, only the integer part is retained. As for example, if $\delta X_i = \Delta X_i / M_i$ and $M_i = N_i + a_i$: $i = \eta$ or φ , where N_i is integer and a_i is a positive fraction (< 1) that one can do away with. In effect, contribution from a smaller strip of width $a_i \Delta X_i / M_i$ is discarded while summing (or averaging) over bins, which is done either by placing the smaller strip at the beginning or at the end of all other equal sized strips of width δX_i . In doing so no error should in principle be incurred, as the translational invariance of both the particle density and the SFM is ensured by choosing the cumulant variables. We have calculated the second order 2d-SFM $F_2^{(2)}$ as a function of M over a wide range of H ($= 0.4 - 3.0$ in steps of 0.1) values. The variation of some of the $F_2^{(2)}$ values are graphically represented in Fig. 3.9. Once again the errors associated with the data points are of statistical origin. The solid curves in each case represent a quadratic function like

$$f(\zeta) = a\zeta^2 + b\zeta + c, \quad (3.33)$$

where $\zeta \equiv \ln M$ and $f(\zeta) \equiv \ln \langle F_2^{(2)} \rangle$. The first two points are always excluded from the fitting process. By doing so one can get rid of the effects arising out of kinematic constraints. From Fig. 3.9 it can be seen that the strong upward bending of $\ln \langle F_2^{(2)} \rangle$ with $\ln M$, as it is observed for $H = 1$ in Fig. 3.9(a), gets systematically weakened as H deviates from unity. For $H < 1$ we find the weakest bending at $H = 0.5$ and for $H > 1$ at $H = 2.5$. The SFM plots corresponding to these values of H are almost linear as demanded by the theory of intermittency. A quantitative description of the above observation is provided by the

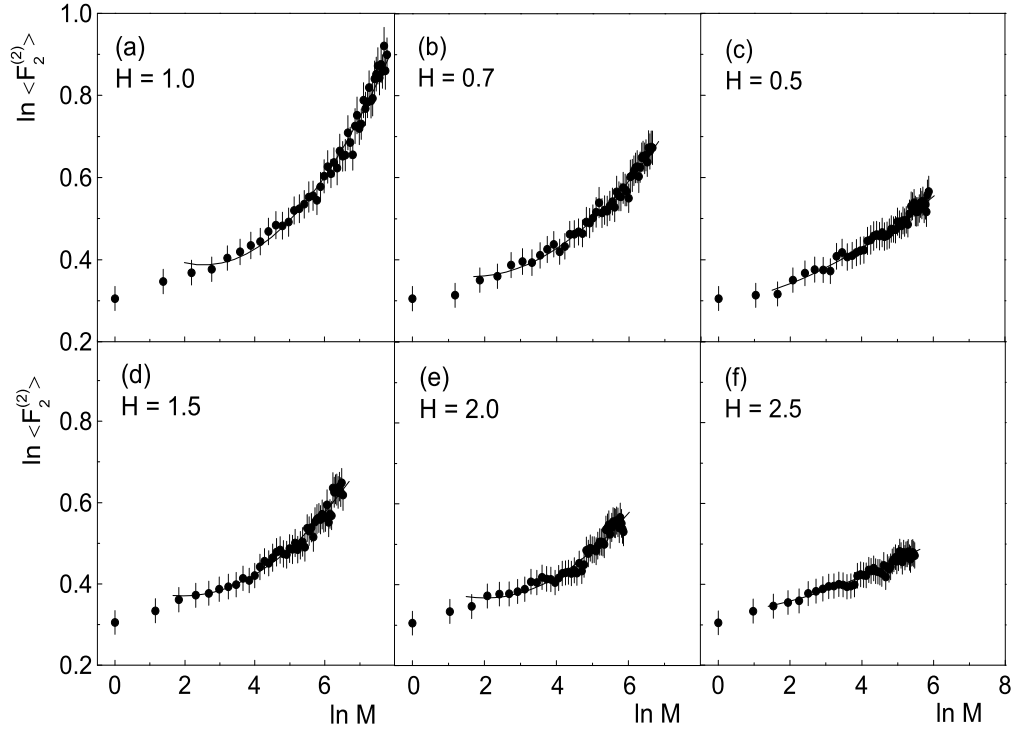


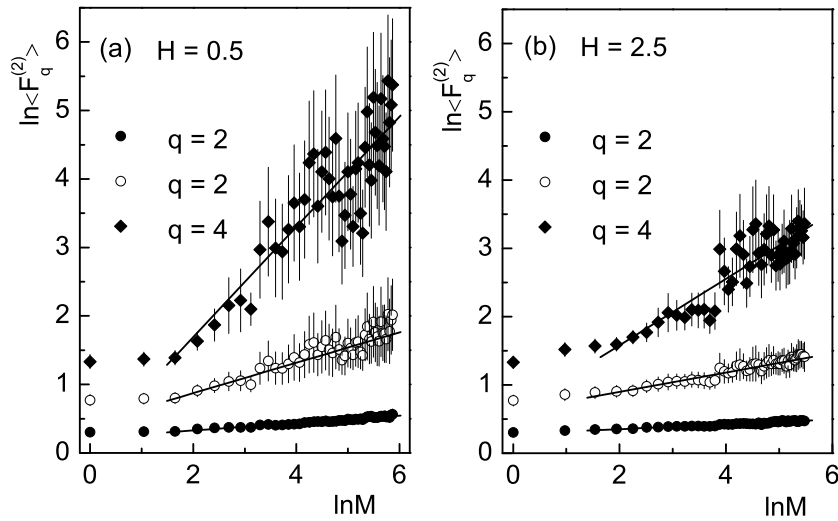
Figure 3.9: Plot of 2d-SFM of order $q = 2$ against (η, φ) -space resolution for several different values of H . The lines represent the quadratic function Eq. (3.33) with best fitted parameter set given in Table 3.4. First two data points are excluded from the fits.

quadratic fit of the data points in terms of Eq. (3.33) along with the $\chi^2(dof)$ values listed in Table 3.4. We see that for the $H \leq 1.0$ category ‘a’ is minimum and ‘b’ is maximum at $H = 0.5$, while for the $H > 1.0$ category similar values are obtained at $H = 2.5$. The fit quality as seen from the $\chi^2(dof)$ values are always reasonably good. Our observation shows that the power-law scaling of the 2d-SFM can be recovered through an asymmetric partition of the (η, φ) space.

The self-affine analysis of the NA22 [40] data on pp interaction and of the NA27 [41] data on hp interactions show that the power-law characterizing intermittency is obtained for $H < 1.0$, which suggests that the transverse direction has to be partitioned finer than the longitudinal one. In these experiments the appropriate Hurst exponent is calculated by fitting the 1d SFM with Ochs’ formula [10]. In contrast, the EMU01 experiment on AB collisions [24] finds that the power-law is valid for $H > 1.0$ i.e., the longitudinal direction has to be partitioned finer than the transverse direction. An AB interaction can be viewed as a superposition effect of many elementary NN interactions, as a result of which the effective Hurst exponent $H^{\text{eff}} \gg H$. On the other hand, in all of our AB experiments, previous and the present one, we consistently find that the power-law of intermittency is obtained only if $H \neq 1$. It does not matter which direction (i.e., longitudinal or transverse) is partitioned finer. We have also calculated the event averaged $F_q^{(2)}$ for $q = 2, 3$ and 4

Table 3.4: The parameters of the quadratic Eq. (3.33) fit to the experimental data for various H values. The $\chi^2(dof)$ values showing the goodness of the fits are given.

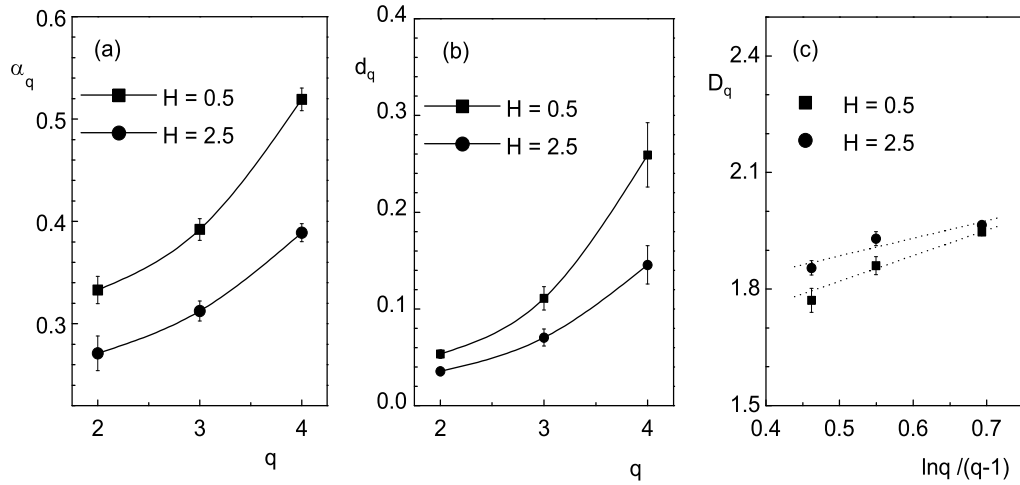
H	a	b	c	$\chi^2(dof)$
0.4	0.0051 ± 0.0033	0.0098 ± 0.0321	0.0298 ± 0.0579	6.17(45)
0.5	0.0047 ± 0.0026	0.0155 ± 0.0300	0.2919 ± 0.0584	4.79(45)
0.6	0.0066 ± 0.0032	0.0062 ± 0.0281	0.2988 ± 0.0581	5.72(45)
0.7	0.0121 ± 0.0030	-0.0393 ± 0.0274	0.3904 ± 0.0598	6.68(45)
0.8	0.0140 ± 0.0027	-0.0530 ± 0.0262	0.4154 ± 0.0602	8.57(45)
0.9	0.0145 ± 0.0025	-0.0562 ± 0.0252	0.4202 ± 0.0608	8.27(45)
1.0	0.0180 ± 0.0023	-0.0918 ± 0.0242	0.5036 ± 0.0615	13.5(45)
1.2	0.0152 ± 0.0026	-0.0675 ± 0.0258	0.4523 ± 0.0605	7.36(45)
1.5	0.0126 ± 0.0030	-0.0492 ± 0.0275	0.4123 ± 0.0591	8.45(45)
2.0	0.0132 ± 0.0036	-0.0533 ± 0.0295	0.4205 ± 0.0575	8.56(45)
2.4	0.0051 ± 0.0039	-0.0019 ± 0.0308	0.3427 ± 0.0570	5.18(45)
2.5	0.0032 ± 0.0021	0.0104 ± 0.0310	0.3246 ± 0.0568	3.60(45)
2.6	0.0041 ± 0.0035	0.0053 ± 0.0313	0.3303 ± 0.0567	3.69(45)
3.0	0.0057 ± 0.0044	-0.0064 ± 0.0325	0.3485 ± 0.0566	5.49(45)

**Figure 3.10:** 2d-SFM of order $q = 2 - 4$ against (η, φ) space resolution with two optimized values of H for which the power-law scaling of $F_2^{(2)}$ can be recovered at its best: (a) for $H = 0.5$ and (b) for $H = 2.5$.

using the optimized values of H obtained from $F_2^{(2)}(M)$ analysis. Figure 3.10 represents such plots, where $\ln \langle F_q^{(2)} \rangle$ is plotted against $\ln M$, (a) for $H = 0.5$ and (b) for $H = 2.5$. The solid curves in either of these plots represent the linear fit to the data points, leaving first two points in each case for the same reason as mentioned earlier. The intermittency index $\phi_q^{(2)}$ is nothing but the slope of these linear fits, which indirectly is related with the intermittency strength. Table 3.5 shows the values of $\phi_q^{(2)}$ along with $\chi^2(dof)$. One can

Table 3.5: The values of $2d$ intermittency exponents $\phi_q^{(2)}$ of order $q = 2 - 4$ for self-affine partitioning of the (η, φ) space in $^{28}\text{Si-Ag/Br}$ interaction at 14.5A GeV.

Order	H = 0.5		H = 2.5	
	$\phi_q^{(2)}$	$\chi^2(dof)$	$\phi_q^{(2)}$	$\chi^2(dof)$
$q = 2$	0.053 ± 0.004	06.39(46)	0.035 ± 0.004	04.27(46)
$q = 3$	0.222 ± 0.012	27.06(46)	0.141 ± 0.008	16.82(46)
$q = 4$	0.778 ± 0.033	46.23(46)	0.436 ± 0.022	59.63(46)

**Figure 3.11:** (a) $2d$ intermittency strength α_q in (η, φ) space with order q . (b) Anomalous fractal dimension d_q with order q . (c) The generalized dimension of (multi)fractality D_q with $\ln q/(q-1)$. The lines in (a) and (b) are drawn joining the data points, whereas those in (c) are linear regressions.

see that the $\phi_q^{(2)}$ indices obtained for a symmetric partitioning are much larger than the corresponding values for $H = 0.5$ and 2.5 . Moreover, the $H = 0.5$ scaling reproduces larger $\phi_q^{(2)}$ than those obtained for the $H = 2.5$ scaling. Comparing with our previous works we find that the present set of self-affine $\phi_2^{(2)}$ values [42] are of the same order of magnitude as those obtained in $^{32}\text{S-Ag/Br}$ and $^{16}\text{O-Ag/Br}$ interactions at 200A GeV [43].

In Fig. 3.11(a) the intermittency strength α_q values are plotted against the order number q for both the H values. It can be seen that the strength parameter nonlinearly increases with increasing order, though the values obtained for $H = 0.5$ are consistently higher than those for $H = 2.5$. In view of our observation mentioned above regarding the intermittency index, it is not surprising that the $2d$ intermittency strength in $^{28}\text{Si-Ag/Br}$ interactions at 14.5A GeV is of the same order of magnitude as those obtained in the $^{32}\text{S-Ag/Br}$ and $^{16}\text{O-Ag/Br}$ interactions at 200A GeV [43]. The generalized dimension of (multi)fractality D_q is related to the anomalous fractal dimension d_q by $D_q = D_T - d_q$, where d_q can be expressed in terms

of the intermittency exponents as [44],

$$d_q = \frac{\phi_q}{q-1}. \quad (3.34)$$

The direct relationship between intermittency and (multi)fractality is not yet fully understood. But it has been argued that, if a second-order phase transition from QGP to hadron phase takes place, then the particle density distribution would show such intermittency that the anomalous dimension d_q becomes independent of q [45]. On the other hand, hadronization through a cascading process will lead to d_q linearly increasing with q . The dependence of d_q on q is shown in Fig. 3.11(b) for $H = 0.5$ and 2.5. The plot shows that the anomalous fractal dimension increases approximately linearly with increasing order q in both cases and the rate of increase for $H = 0.5$ is greater than that for $H = 2.5$. Hence the observation is in agreement with the prediction of the cascade model. Similar to the $1d$ analysis, we make an attempt to interpret the observed multifractality in terms of the constant specific heat C , defined through Eq. (3.30). In Fig. 3.11(c), plots of D_q with $\ln q/(q-1)$ are given for $H = 0.5$ and 2.5. The multifractal specific heat is extracted by fitting straight line to the data points, shown in the figure. For $H = 0.5$, $C = 0.657 \pm 0.083$ and for $H = 2.5$, $C = 0.453 \pm 0.064$, are found. The C values in $2d$ are larger than the universal value of $C = (1/4)$ suggested in ref. [34], they are larger than the $1d$ values of C in $^{32}\text{S-Ag/Br}$ and $^{16}\text{O-Ag/Br}$ interactions at 200A GeV [43], and they are very close to the $1d$ values obtained in a similar ^{28}Si -induced experiment [46].

3.4 Factorial Correlators

The dynamics of particle correlation beyond that obtained from the single particle inclusive spectra, can be investigated by studying the two-fold factorial moment or the factorial correlator (FC). As mentioned, whereas the SFM can be used to measure the local density fluctuations, the FC can extract additional information on the bin-to-bin correlation between such fluctuations within an event. The FC in terms of single particle factorial moment $n_m^{[q]}$ [see Eq. (3.12)] is defined as [2],

$$\tilde{f}_{pq} = \left\langle n_m^{[p]} n_{m'}^{[q]} \right\rangle, \quad (3.35)$$

where $n_m(n_{m'})$ is the number of particles falling within the $m(m')$ th bin. The FCs are calculated at a fixed resolution (say, δX) and for each combination of nonoverlapping pair of intervals (e.g., mm') that are separated by a distance D along the considered phase space variable. As mentioned above, using cumulant variables [see Eq. (3.22)] we ensure the translational invariance of particle density, and for the sake of statistics the FCs are averaged over all such combinations of bins as well as over the entire event sample. The

multivariate correlator \tilde{f}_{pq} is then normalized as

$$\tilde{F}_{pq} = \frac{\tilde{f}_{pq}}{\tilde{f}_p \tilde{f}_q}, \quad (3.36)$$

where $\tilde{f}_q = \langle n_m^{[q]} \rangle$ is the single-variate factorial moment averaged over many non-overlapping equal sized phase space intervals belonging to different events. Hence, factorial moments and factorial correlators are intimately related quantities. In terms of inclusive densities one has

$$\tilde{F}_{pq} = \int_{\Omega_1} d\eta_1 \dots d\eta_p \int_{\Omega_2} d\eta_{p+1} \dots d\eta_{p+q} \rho_{p+q}(\eta_1, \dots, \eta_p; \eta_{p+1}, \dots, \eta_{p+q}), \quad (3.37)$$

where ρ_{p+q} is the inclusive densities of order $p+q$. The integrations are performed over two arbitrary phase space cells Ω_1 and Ω_2 , separated by D . Factorial moment and factorial correlators of the same order are thus seen to differ only in the choice of the integration domains. It should be noted that the above definition is more general than Eq. (3.35). For $\Omega_1 = \Omega_2$ or $D = 0$, Eq. (3.37) reduces to the correct definition of f_2 Eq. (3.12), whereas Eq. (3.35) equals to $\langle n^2 \rangle$ and misses the so called ‘short-noise’ term, $-\langle n \rangle$.

Since $p \neq q$, the normalized FCs \tilde{F}_{pq} as defined in Eq. (3.36) are not symmetric under the $p \leftrightarrow q$ interchange. For analysis purpose the symmetrized correlators

$$F_{pq} = (\tilde{F}_{pq} + \tilde{F}_{qp})/2 \quad (3.38)$$

are often used. According to the α -model, F_{pq} should depend on the correlation distance D but not on the phase space interval size δX_η , and as D approaches a small value the FC should follow a power-law type of dependence like,

$$\langle F_{pq} \rangle \propto (\Delta X_\eta / D)^{\phi_{pq}}. \quad (3.39)$$

Figure 3.12 depicts how $\ln \langle F_{pq} \rangle$ depends on $-\ln D$ for (a) the experiment, (b) the UrQMD simulation and (c) the UrQMD+BEC simulation for various combinations of (p, q) . In the experimental case for each such combination with increasing $-\ln D$ one can see a rapid growth in the $\ln \langle F_{pq} \rangle$ value at the beginning, a saturation next, followed by a moderate but systematic linear rise near the end. Over the entire range of $-\ln D$ this variation may not be linear. But at the end when $1/D$ is large, an approximately linear variation can be observed over a limited range. The exponents ϕ_{pq} are obtained by fitting straight lines to the data points only in the large $-\ln D$ region (the last five/six data points), a region that corresponds to short range correlation. Once again the errors either in $\langle F_{pq} \rangle$ or in ϕ_{pq} are of statistical origin and they are estimated by using data sets generated by random numbers. For the

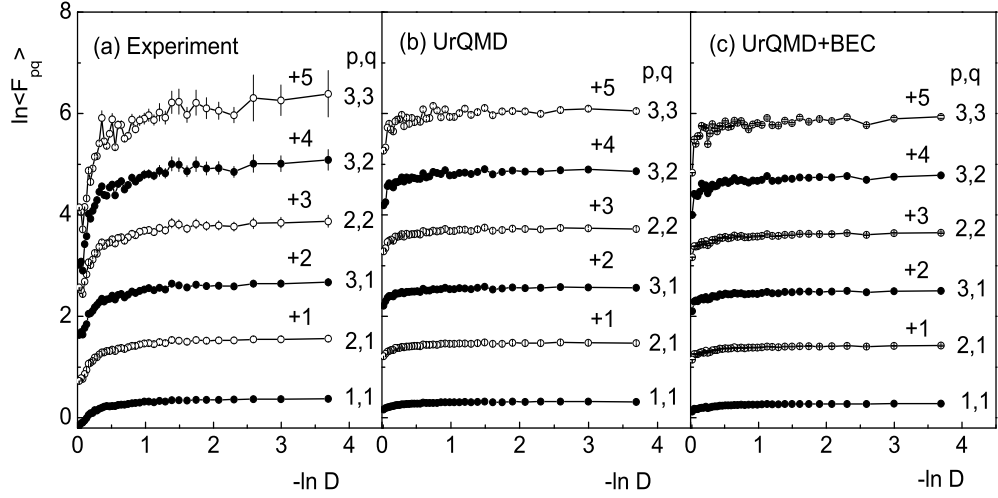


Figure 3.12: Factorial correlators with correlation length in η -space. The error bars are only of statistical origin. For clarity successive orders are shifted by one unit along the vertical axis as shown in the diagram. Lines joining points are drawn to guide the eye.

UrQMD and the UrQMD+BEC events one can hardly see any variation in the $\ln \langle F_{pq} \rangle$ values with varying $-\ln D$. The FC exponents ϕ_{pq} and the R^2 values corresponding to the best linear fit are presented in Table 3.6 for all three data samples employed in this analysis. As expected, negligibly small values of ϕ_{pq} in the simulated data shows that the UrQMD as well as the UrQMD+BEC simulation cannot reproduce the experimentally observed correlation effects among the final state charged mesons. Moreover, the ϕ_{pq} values obtained from the UrQMD+BEC simulation always underestimate the corresponding UrQMD values, though in case of intermittency indices the reverse is observed. According to the α -model, under a log-normal approximation, the exponents ϕ_{pq} should follow a sum rule, like

$$\phi_{pq} = \phi_{p+q} - \phi_p - \phi_q = (p \cdot q) \phi_{11}. \quad (3.40)$$

Table 3.6: The ϕ_{pq} exponents of the FC scaling relation Eq. (3.39) for several different combinations of (p, q) .

(p, q)	Experiment		UrQMD		UrQMD+BEC	
	ϕ_{pq}	R^2	ϕ_{pq}	R^2	ϕ_{pq}	R^2
(1,1)	0.012 ± 0.002	0.959	0.006 ± 0.006	0.964	0.003 ± 0.001	0.985
(2,1)	0.024 ± 0.004	0.958	0.011 ± 0.009	0.932	0.007 ± 0.003	0.910
(3,1)	0.045 ± 0.009	0.923	0.013 ± 0.011	0.971	0.011 ± 0.007	0.967
(2,2)	0.057 ± 0.013	0.911	0.021 ± 0.015	0.893	0.014 ± 0.005	0.820
(3,2)	0.089 ± 0.017	0.933	0.033 ± 0.021	0.887	0.021 ± 0.020	0.821
(3,3)	0.203 ± 0.025	0.979	0.041 ± 0.032	0.851	0.028 ± 0.043	0.830

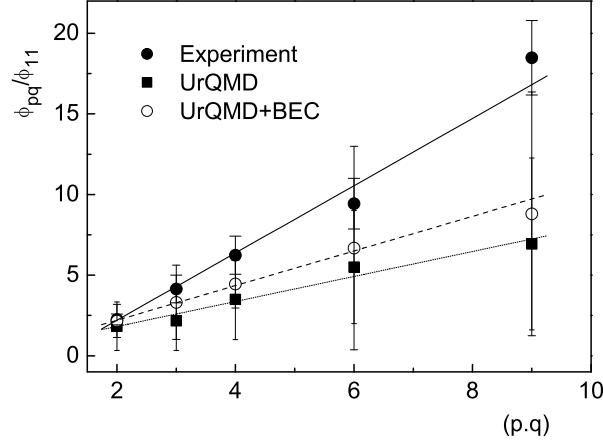


Figure 3.13: Variation of $\phi_{p,q}/\phi_{1,1}$ against the product $p \cdot q$ for various combinations of p and q . The lines represent linear fit to the respective data points which confirm the validity of the α -model.

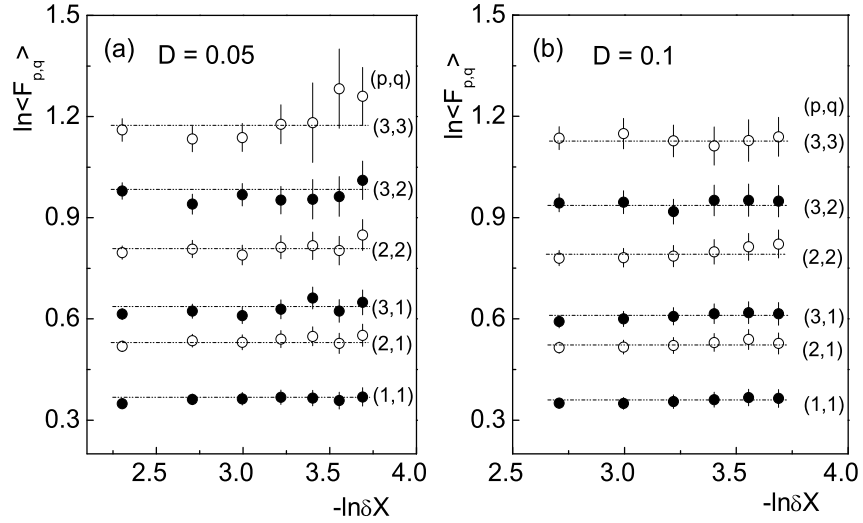


Figure 3.14: Factorial correlators with phase space resolution for two different values of correlation length $D = 0.05$ and 0.1 . The plots are for the experiment. The dashed lines are the best fitted horizontal lines to the data points.

Therefore, the ϕ_{pq}/ϕ_{11} value should linearly rise with the product $(p \cdot q)$, which can be used as a consistency check between the experimental data and the α -model. Such a plot for the experiment together with the UrQMD and the UrQMD+BEC simulated data is given in Fig. 3.13. The expected linear variation is satisfactorily ascertained in this plot. One also notices that the UrQMD line is well short of reproducing the experiment, and the UrQMD+BEC line falls in between these two. Though the experiment and both the simulations are consistent with this prediction of the intermittency model, there exists a certain quantitative difference between them. Another prediction of the α -model is that, for a fixed D the correlators should be independent of δX_η . This aspect has been verified

in Fig. 3.14, where graphical plots of $\ln \langle F_{pq} \rangle$ at fixed $D (= 0.1, \text{ and } 0.2)$ and for several different values of $\ln \delta X_\eta$ are shown for the experiment. Within errors the δX_η independence of F_{pq} is established. It should be pointed out here that, such a property does not hold for the α -model only, but is a feature of any model that takes short range correlation into consideration.

3.4.1 Sum Rules

Suppose the initial interval ΔX_η is divided into M subintervals of size $\delta X_\eta = \Delta X_\eta / M$ for the calculation of the bivariate factorial moments $\langle n_m^{[p]}(\delta X_\eta) n_{m'}^{[q]}(\delta X_\eta) \rangle$, while the same interval is divided into $L = M/2$ bins of size $2\delta X_\eta$ for the determination of the single variate factorial moments $\langle n_l^{[p]}(2\delta X_\eta) \rangle$. Between the two types of factorial moments the following relation should hold:

$$\begin{aligned} \langle n_l^{[p]}(2\delta X_\eta) \rangle &= \langle (n_m(\delta X_\eta) + n_{m+1}(\delta X_\eta))^{[p]} \rangle \\ &= \sum_{q=0}^p \binom{p}{q} \langle n_m^{[p]}(\delta X_\eta) n_{m+1}^{[p-q]}(\delta X_\eta) \rangle, \end{aligned} \quad (3.41)$$

with $m = 2l - 1$ for $l = 1, 2, \dots, L$. The relation is obtained by application of the binomial theorem generalized to factorial powers [47]. In case of translational invariance, the above equation can be used to derive a relation between F_{11} and F_2 . For $p = 2$, after a division by $\langle n_m \rangle \langle n_{m+1} \rangle$ Eq. (3.41) becomes

$$\frac{\langle (n_m + n_{m+1})^{[2]} \rangle}{\langle n_m \rangle \langle n_{m+1} \rangle} = \frac{\langle n_m^{[2]} \rangle}{\langle n_m \rangle \langle n_{m+1} \rangle} + \frac{\langle n_{m+1}^{[2]} \rangle}{\langle n_m \rangle \langle n_{m+1} \rangle} + 2 \frac{\langle n_m n_{m+1} \rangle}{\langle n_m \rangle \langle n_{m+1} \rangle}. \quad (3.42)$$

Since translational invariance is assumed,

$$\langle n_m \rangle \langle n_{m+1} \rangle = \langle n_m \rangle^2 = \langle n_{m+1} \rangle^2 = \frac{1}{4} \langle (n_m + n_{m+1})^2 \rangle. \quad (3.43)$$

After averaging over m , one can obtain [48]

$$\langle F_{11}(D) \rangle = 2 \langle F_2(2D) \rangle - \langle F_2(D) \rangle. \quad (3.44)$$

Here $F_{11}(D)$ denotes the FC calculated for a distance D between the bins of size δX_η . Guided by the predictions of the α -model, one can state that the relationship (3.44) holds for all bin sizes δX_η for which $F_{11}(D)$ is effectively independent of δX_η in the range $\delta X_\eta \leq D \leq D_0$. Relation (3.44), known as the ‘sum-rule’, can be trivially extended to more than two cells. They allow to measure high-order correlations by varying the distances between the cells. In Fig. 3.15 we have shown such a plot of $\ln \langle F_{11}(D) \rangle$ and $\ln [2 \langle F_2(2D) \rangle - \langle F_2(D) \rangle]$ as functions

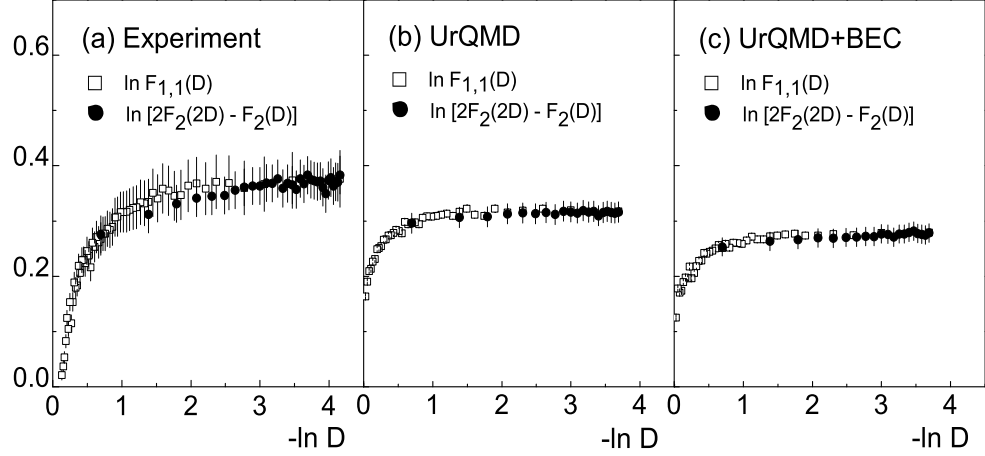


Figure 3.15: The validity of the scaling relation Eq. (3.44) for (a) the experiment, (b) the UrQMD and (c) the UrQMD+BEC.

of $-\ln D$ for (a) the experiment, (b) the UrQMD simulation and (c) the UrQMD+BEC simulation. One can see that the data points corresponding to either side of Eq. (3.44) fall almost over each other for the experiment as well as for both the simulations, thereby proving the validity of the scaling relation. Overall, our study on FC shows the presence of a short range correlation in the $^{28}\text{Si-Ag/Br}$ data, and gross features of the experiment are consistent with the predictions of the α -model. Due to intermixing of many sources of particle production in AB interaction most of the long range correlations are probably smeared out. The present set of observations on factorial correlator is qualitatively consistent with those of similar such studies in high energy AB interactions [49, 50].

3.5 Factorial Cumulant Moments

The inclusive q -particle densities $\rho_q(\eta_1, \dots, \eta_q)$ in general contains ‘trivial’ contributions from the lower-order densities. Under certain conditions it is advantageous to consider a new sequence of correlation functions $C_q(\eta_1, \dots, \eta_q)$ which vanish whenever one of the arguments becomes statistically independent of the others. The quantities with such properties are called the cumulant functions defined via the sequence,

$$C_1(1) = \rho_1(1), \quad (3.45a)$$

$$C_2(1, 2) = \rho_2(1, 2) + \rho_1(1)\rho_1(2), \quad (3.45b)$$

$$C_3(1, 2, 3) = \rho_3(1, 2, 3) - \sum_{(3)} \rho_1(1)\rho_2(2, 3) + 2\rho_1(1)\rho_1(2)\rho_1(3), \quad (3.45c)$$

and so on ...

Likewise, the higher order expressions can be derived from the related formulae. With the help of the cumulant functions the cell averaged normalized factorial cumulant moments are defined as,

$$K_q(\delta\eta) = \frac{1}{M(\delta\eta)^q} \sum_{m=1}^M \int_{\delta\eta} \prod_i d\eta_i \frac{C_q(\eta_1, \dots, \eta_q)}{(\bar{\rho}_m)^q}. \quad (3.46)$$

The cumulants provide a measure of genuine higher order correlation beyond the contribution(s) coming from the lower order. The inter-relationship between the cumulant moments and the factorial moments is guided by Eq. (3.17)

$$F_q = \sum_{j=1}^{q-1} \binom{q-1}{j-1} F_{q-j} K_j + K_q; \quad q = 2, 3, \dots, \quad (3.47)$$

with $F_0 = F_1 = K_1 = 1$, and $K_0 = 0$. Successive terms in the expansion correspond to contributions coming from genuine 2, 3 \dots , q -particle correlation present in the local particle densities. In order to calculate the cumulant moment, one needs to calculate F_q first following Eq. (3.20), and then the corresponding cumulants are obtained from the following set of explicit relations (for $q = 2 - 5$):

$$F_2 = 1 + K_2, \quad (3.48a)$$

$$F_3 = 1 + 3K_2 + K_3, \quad (3.48b)$$

$$F_4 = 1 + 6K_2 + 3\overline{K_2^2} + 4K_3 + K_4, \quad (3.48c)$$

$$F_5 = 1 + 10K_2 + 15\overline{K_2^2} + 10\overline{K_3 K_2} + 10K_3 + 5K_4 + K_5. \quad (3.48d)$$

The bar average is defined as $\overline{AB} = (1/M) \sum_m A^{(m)} B^{(m)}$. For a Poisson distribution $K_q = 0$ for $q > 1$. Nonzero K_q values ($q > 1$) should therefore, indicate an existence of nontrivial correlation in the inclusive density distribution of produced particles. In Fig. 3.16 we graphically present the variation of $\ln \langle K_q \rangle$ for ($q = 2, \dots, 5$) with $\ln M$ for the present $^{28}\text{Si-Ag/Br}$ data. The errors shown in these diagrams are calculated by making use of the random number generated data sets, and hence they are of statistical origin only [51]. The cumulants increase with diminishing phase space interval size. There are obvious statistically significant contributions coming from two and three-particle correlation(s). However, the same is not true for K_4 or K_5 , which are either vanishingly small within errors (at wide δX_η), or the cumulant values are associated with large statistical uncertainties (in narrow δX_η interval), and it is difficult to draw any definite conclusion from the data. We do not attach much significance to the observation that at $\eta \sim 3.5$ a few points suddenly rise above the neighboring points. The UrQMD and UrQMD+BEC generated points are almost uniform over the entire $\ln M$ range, and both simulations underestimate the corresponding experimental result on K_2 , K_3 and K_4 . The same is however not true for K_5 . In the

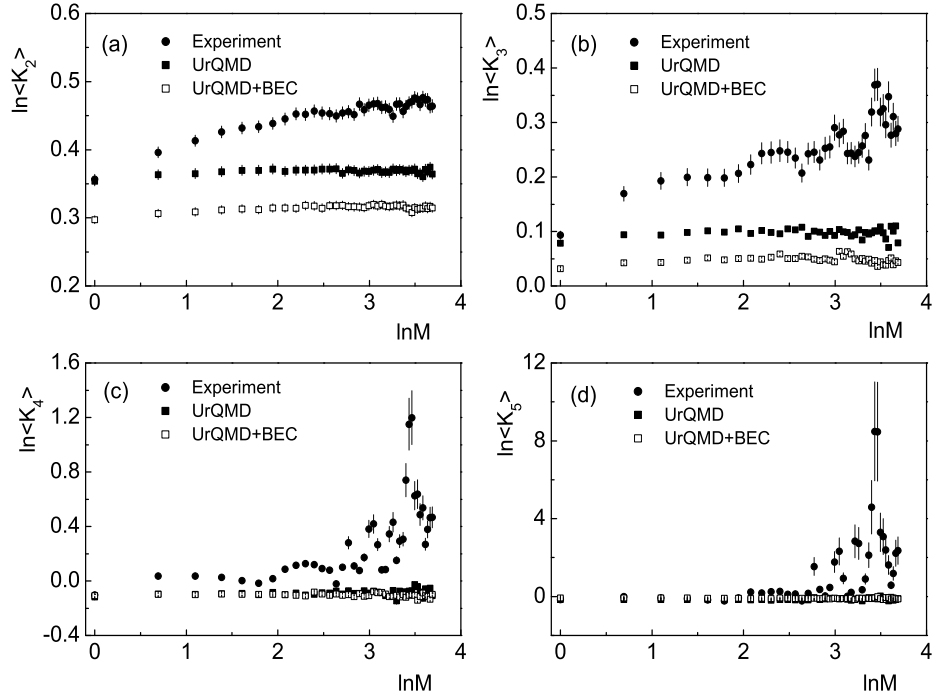


Figure 3.16: The normalized cumulant moments plotted against the phase space partition number in $^{28}\text{Si-Ag/Br}$ interaction at 14.5A GeV.

latter case there is hardly any difference between the experiment and the UrQMD or the UrQMD+BEC simulated points where statistical errors are small. The errors attached correspond to one standard deviation and any conclusion regarding a systematic behavior will be only at the $\sim 68\%$ confidence level. While the present observation is consistent with one previously obtained AB result [52], it is in contradiction with a few similar other experiments [53, 54].

3.6 Oscillatory Moment

By a parton shower cascade model based on the QCD it has been predicted that the K_q moments should oscillate irregularly around the zero value with increasing order q [15, 16]. Both F_q and K_q have strong energy and order dependence, and due to finite multiplicity in an event the high rank moments are difficult to measure at high phase space resolution. To overcome the deficiency a new set of moments is introduced that are defined as,

$$H_q = K_q/F_q. \quad (3.49)$$

The H_q moment also known as the oscillatory moment, shows a very interesting oscillatory behavior with q , which even at large q is also much more regular than F_q or K_q . The ratio reflects genuine q -particle correlation integral relative to the global correlation integral,

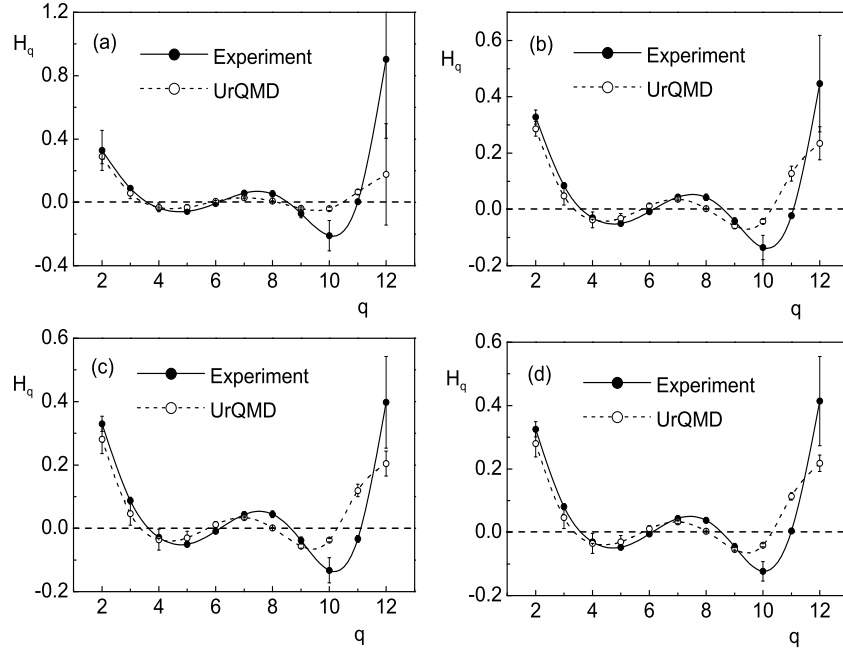


Figure 3.17: The oscillatory moments H_q plotted with its rank q for the experiment (solid circle) and for the UrQMD (empty circle). The lines joining points are shown to guide the eye. The pseudorapidity cuts taken as (a) $\eta_0 - 0.25 \leq \eta \leq \eta_0 + 0.25$, (b) $\eta_0 - 0.5 \leq \eta \leq \eta_0 + 0.5$, (c) $\eta_0 - 0.75 \leq \eta \leq \eta_0 + 0.75$ and (d) $\eta_0 - 1.0 \leq \eta \leq \eta_0 + 1.0$.

and it is very sensitive to the tail of the multiplicity distribution. In the cases of high energy e^+e^- , hh and hA interactions oscillatory behavior of H_q with increasing q around the zero value has been experimentally confirmed. Whereas, for e^+e^- and hh interactions the oscillatory behavior has been attributed to the multicomponent structure of the particle production process [16], in the hA case [55] the result has been explained in terms of a leading particle cascade model. In all cases, for each participating particle/nucleon either a negative binomial distribution, or a modified negative binomial multiplicity distribution, or both have been successfully used.

In the present case of $^{28}\text{Si-Ag/Br}$ interaction at 14.5A GeV of energy, the variation of H_q moments with order q is graphically presented in Fig. 3.17, for the experiment as well as for the UrQMD model simulation. The BEC effect introduced into the UrQMD output does not make any measurable deviation in H_q from its original values, and hence are not adopted in the diagrams. The jet structure has been examined in the central particle-producing region with four different η windows selected as: (a) $\eta_0 - 0.25 \leq \eta \leq \eta_0 + 0.25$, (b) $\eta_0 - 0.5 \leq \eta \leq \eta_0 + 0.5$, (c) $\eta_0 - 0.75 \leq \eta \leq \eta_0 + 0.75$ and (d) $\eta_0 - 1.0 \leq \eta \leq \eta_0 + 1.0$, where η_0 is the mean of the η -distribution. One can see that after an initial fall the H_q values oscillate about the $H_q = 0$ line. In the considered η -intervals there are always a marginal difference between the experiment and the UrQMD. However, the differences are not statistically significant. The extent of oscillation is large in the high q region where

H_q values have large statistical errors (once again calculated from random number based data sets). As the η window is increased beyond $\eta_{cut} = 1.0$, probably due to intermixing from different particle producing sources the correlation effects are washed out, and the experiment and simulation start to coincide, showing only a small or no oscillation. We observe that the H_q moment though oscillating, is not a very sensitive parameter that can filter out the correlation effects of the experiment from the simulation which is otherwise lacking any significant correlation.

3.7 Discussion

Multiplicity moments related to intermittency and short-range particle correlation phenomena have been studied in $^{28}\text{Si-Ag/Br}$ interaction at 14.5A GeV. The experimental results are compared with the prediction of the microscopic transport model UrQMD, and with the UrQMD output supplemented by the Bose-Einstein type of correlation included as an after-burner. In general we observe a nonstatistical component present in the final state charged particle density distribution. On most occasions neither the UrQMD nor the UrQMD+BEC model can replicate the experimental pattern well. The following specific observations can be made from the analysis.

The $1d$ intermittency analysis shows that in AB interaction the phenomenon is dependent more on the colliding objects than on the collision energy involved. The $1d$ intermittency also depends on the choice of the underlying phase space variable. It is slightly stronger in φ -space than in the η -space. The higher order intermittency exponents can be explained in terms of two- and three-particle correlations. The shower tracks are caused by non-identical mesons (both positive and negative charge). Hence, the observed correlations are not entirely due to the usual Bose-Einstein type which is being reflected from the comparison of our experiment with the UrQMD+BEC results. The order dependence of the intermittency indexes is neither in conformity with a second-order thermal phase transition, nor with a multiplicative cascade mechanism. Instead, our intermittency results indicate that there may be a nonthermal phase transition and (or) simultaneous coexistence of two different states of hadronic matter. Using the generalized Rényi dimensions, the multifractal specific heat C has also been obtained for the interactions. However, no universality is found to be associated with this parameter.

The $2d$ intermittency is several times stronger than the $1d$ one. Like in the $1d$ case, due to the absence of any correlation between particles in the input, the UrQMD model alone cannot produce significant intermittency, but definite improvement in this regard is observed when BEC is incorporated into the UrQMD output. The experimental slope values however, still

remain several times larger than the UrQMD+BEC simulation, and the upward bending that is so typical of the anisotropy in two dimensional density distribution, is absent in both the UrQMD and UrQMD+BEC simulated plots. As reflected from the upward bending in the variation of the 2d-SFM, there is a strong anisotropy in the (η, φ) space. This anisotropy is taken care of by introducing the Hurst exponent H , which in the present case comes out to be 0.5 and 2.5. With the above choice of H values we can retrieve the anomalous scaling of the 2d-SFM, and obtain the actual intermittency strength. As the anomalous scaling is obtained both for $H < 1$ and $H > 1$, in our case it is not mandatory that one particular direction (e.g., longitudinal η or transverse φ) has to be partitioned finer with respect to the other. This in a sense contradicts the observations of similar AB experiments [56, 57], and an interpretation of AB results in terms of the superposition of many elementary NN collisions seems inadequate [58]. Using the appropriate H values we have determined the intermittency strength, the generalized multifractal dimension, and the multifractal specific heat in (η, φ) -plane. The 2d intermittency strength is of the same order of magnitude as obtained from similar AB experiments at a much higher incident energy (200 GeV per nucleon). This in a sense indicates that the intermittency phenomenon in nucleus-nucleus experiments is less sensitive to the variation in collision energy. The general nature of the fractal parameters obtained here tells us that a multifractal structure is present in the underlying dynamical fluctuation of the particle density function, which probably is an outcome of a random cascading process of particle production.

The short-range particle correlation study on the other hand demands, besides local fluctuations bin-to-bin correlations should also be present in the experimental data. However, such correlation effects cease to exist beyond a small length in η -space. The experimental results on FC are in conformity with the sum rules and the scaling-laws suggested by the α -model. That the observed intermittency effects primarily result from two and three-particle correlation is verified from our results on the factorial cumulants. As expected, these correlations grow with diminishing phase space interval size as it narrows down to the experimental resolution. There is an indication that small amount of higher order ($q > 3$) correlations may also be present in the experiment. Due to large statistical errors however, the observation cannot be considered very seriously. All these correlation effects could not be reproduced either by the UrQMD model or by the BEC effect implemented over the same model. The oscillatory nature of H_q has been confirmed for the present data on $^{28}\text{Si-Ag/Br}$ interactions. However, in this case the difference between the experimental and the simulated (UrQMD or UrQMD+BEC) results is not very significant. Note that the Bose-Einstein correlation has been accommodated into the UrQMD output as an after-burner without any check on the two-particle correlations, and not directly at the real correlation level. Hence, the method adopted cannot be considered as a fully convincing way of taking the BEC effect into account as a probable cause of the intermittency in the $^{28}\text{Si-Ag/Br}$ data analyzed here.

Bibliography

- [1] A. Bialas and R. Peschanski, *Nucl. Phys.* **B 273**, 703 (1986).
- [2] A. Bialas and R. Peschanski, *Nucl. Phys.* **B 308**, 857 (1988).
- [3] T. Burnett *et al.* (JACEE Collaboration), *Phys. Rev. Lett.* **50**, 2062 (1983).
- [4] P. Carruthers *et al.*, *Phys. Lett.* **B 222**, 487 (1989).
- [5] M. Gyulassy and L. van Hove, in: *Multiparticle Dynamics*, Eds. A. Giovannini and W. Kittel (World Scientific, Singapore, 1990).
- [6] K. Kadiza and P. Seyboth, *Phys. Lett.* **B 287**, 363 (1992).
- [7] I. M. Dremin, *Pisma Zh. Eksp. Teor. Fiz.* **30**, 152 (1979).
- [8] I. M. Dremin, *JETP Lett.* **45**, 643 (1987); *Nucl. Phys.* **A 467**, 233 (2006).
- [9] I. M. Dremin, *Sov. J. Nucl. Phys.* **30**, 726 (1981).
- [10] W. Ochs, *Phys. Lett.* **B 247**, 101 (1990).
- [11] A. Bialas, K. Zalewski, *Phys. Lett.* **B 238**, 413 (1990).
- [12] L. van Hove, *Z. Phys.* **C 21**, 93 (1983).
- [13] E. Shuryak, *Phys. Lett.* **B 423**, 9 (1988).
- [14] P. Carruthers, H. C. Eggers and I. Sarcevic, *Phys. Lett.* **B 254**, 258 (1991).
- [15] I. M. Dremin, *Phys. Lett.* **B 313**, 209 (1993).
- [16] I. M. Dremin *et al.*, *Phys. Lett.* **B 336**, 119 (1994).
- [17] E. A. De Wolf, I. M. Dremin and W. Kittel, *Phys. Rep.* **270**, 1 (1996).
- [18] W. Kittel and E. A. De Wolf, *Soft Multihadron Dynamics* (World Scientific, 2005).
- [19] R. Botet and M. Ploszajczak, *The Phenomenology of Hadronic Matter*, World Scientific Lecture Notes in Physics Vol. 65 (World Scientific, 2002).
- [20] M. Adamus *et al.* (NA22 Collaboration), *Phys. Lett.* **B 185**, 200 (1987).
- [21] A. Bialas and M. Gazdzicki, *Phys. Lett.* **B 252**, 483 (1990).
- [22] B. Andersson, G. Gustafson and B. Nilsson-Almqvist, *Nucl. Phys.* **B 281**, 289 (1987).
- [23] M. K. Ghosh, A. Mukhopadhyay and G. Singh, *J. Phys.* **G 34**, 177 (2007).
- [24] M. I. Adamovich *et al.* (EMU01 Collaboration), *Nucl. Phys.* **B 388**, 3 (1992).
- [25] S. Vokál and J. Vrláková, *JINR Preprint*, **E1**, 188 (2009).
- [26] M. I. Adamovich *et al.* (EMU01 Collaboration), *Phys. Rev.* **D 47**, 3726 (1993).
- [27] Ph. Brax and R. Peschanski, *Phys. Lett.* **B 253**, 225 (1991);
I. Sarcevic and H. Satz, *Phys. Lett.* **B 233**, 251 (1989).

- [28] R. C. Hwa and M. T. Nazirov, *Phys. Rev. Lett.* **69**, 741 (1992).
- [29] R. C. Hwa and J. Pan, *Phys. Rev.* **D 45**, 1476 (1992).
- [30] S. Hegyi and T. Csörgő, *Phys. Lett.* **B 296**, 256 (1992).
- [31] E. K. Sarkisyan, *et al.*, *Phys. Lett.* **B 318**, 568 (1993).
- [32] H. Satz, *Nucl. Phys.* **B 326**, 613 (1989).
- [33] L. Lianshou, F. Jinghua and W. Yuanfang, *Phys. Lett.* **B 444**, 563 (1998).
- [34] A. Bershadski, *Phys. Rev.* **C 59**, 364 (1999).
- [35] M. K. Ghosh, A. Mukhopadhyay and G. Singh, *J. Phys.* **G 32**, 2293 (2006).
- [36] R. Peschanski and Ph. Brax, *Nucl. Phys.* **B 346**, 65 (1990).
- [37] E. K. Sarkisyan *et al.*, *Phys. Lett.* **B 347**, 439 (1995).
- [38] L. Van Hove, *Phys. Lett.* **B 28**, 429 (1969); *Nucl. Phys.* **B 9**, 331 (1969).
- [39] L. Liu, Y. Zhang and Y. Wu, *Z. Phys.* **C 69**, 323 (1996).
- [40] N. M. Agababyan *et al.* (NA22 Collaboration), *Phys. Lett.* **B 382**, 305 (1996).
- [41] S. Wang, Z. Wang and C. Wu, *Phys. Lett.* **B 410**, 323 (1997).
- [42] P. Mali, A. Mukhopadhyay and G. Singh, *Acta Phys. Pol.* **B 43**(3), 463 (2012).
- [43] M. K. Ghosh, *et al.*, *Can. J. Phys.* **88**, 575 (2010).
- [44] G. Paladin and A. Vulpiani, *Phys. Rep.* **156**, 147 (1987).
- [45] W. Ochs, *Z. Phys.* **C 50**, 339 (1991).
- [46] M. Mohsin Khan *et al.*, *Act. Phys. Pol.* **B 38**, 2653 (2007).
- [47] H. Eggers *et al.*, *Phys. Rev.* **D 44**, 1975 (1991).
- [48] R. Peschanski and J. Seixas, *CERN preprint*, CERN-TH-5903/90 (1990).
- [49] S. Islam and R. Hasan, *J. Phys.* **G 34**, 779 (2007).
- [50] D. Ghosh *et al.*, *Phys. Rev.* **C 52**, 2092 (1995).
- [51] W. Shaoshun, Z. Jie, W. Zhaomin and S. Ming, *Phys. Rev.* **D 56**, 1668 (1997).
- [52] P. L. Jain, A. Mukhopadhyay and G. Singh, *Z. Phys.* **C 58**, 1 (1993).
- [53] M. I. Adamovich *et al.* (EMU01 Collaboration), *Heavy Ion Physics* **13**, 213 (2001).
- [54] P. Carruthers, H. C. Eggers and I. Sarcevic, *Phys. Rev.* **C 44**, 1629 (1991).
- [55] N. Suzuki *et al.*, *Phys. Rev.* **C 58**, 1720 (1998).
- [56] M. I. Adamovich *et al.* (EMU01 Collaboration), *Z. Phys.* **C 76**, 659 (1997).
- [57] M. M. Haq, S. Islam and R. Hasan, *J. Phys.* **G 30**, 1959 (2004).
- [58] L. Lianshou (EMU01 Collaboration), *Nucl. Phys. Proc. Suppl.* **B 71**, 341 (1999).

Chapter 4

Erraticity in $^{28}\text{Si-Ag/Br}$ Interaction at 14.5A GeV

4.1 Introduction

In Chapter 3 we have presented our results on the scaled factorial moment (SFM) analysis for the $^{28}\text{Si-Ag/Br}$ collision events at an incident energy of 14.5A GeV. It is found that the SFM (F_q) of integer order q anomalously scales with diminishing phase space resolution size, which is technically termed as intermittency. The factorial moments are capable of filtering out the dynamical component of fluctuation from the statistical noise if the latter is Poisson distributed. However the moments are incapable of locating the position of a spike or a sharp void in an event, and also while averaging over a large event sample, the event space fluctuations of the factorial moments are smoothed out. In case a factorial moment analysis is made over a narrow region of phase space, so that due to finite event multiplicity only a few phase space sub-intervals contribute to the moment calculation, very little information about the dynamical fluctuation present in that event can be retrieved. Moreover, the averaging of SFM over a limited number of bins does not completely satisfy the criterion of disentangling the statistical noise. Therefore, a simple intermittency analysis cannot fully account for all kind of fluctuations. To investigate the nature of event-to-event

fluctuations beyond intermittency, it therefore, becomes essential to introduce a new set of moments.

The *erraticity* moment ($C_{p,q}$) is free from some of the limitations of the factorial moment as described above and is a useful tool for investigating the event-space fluctuation of multiparticle emission data [1, 2]. The $C_{p,q}$ moment is defined for any positive value of p but only for integer positive q . The idea of erraticity was originally introduced to understand the possible chaotic behavior in quark and gluon (parton) jet formation (or branching processes) [2]. The parameters extracted from the $C_{p,q}$ moment analysis can on one hand quantify the chaotic nature of spatial fluctuation in event space and on the other it is capable of characterizing the degree of fluctuation of the parton multiplicity that initiates the QCD branching processes. It is claimed that in order to describe the chaoticity of multiparticle production in high-energy interactions, the ‘entropy index’ (μ_q) (to be defined later) is as effective as the *Lyapunov exponent* for describing a classical deterministic nonlinear system [2], and nonvanishing positive values of μ_q can be used as a criterion for this purpose. Moreover, from the magnitude of μ_q one can distinguish a branching process initiated by a quark from one that is initiated by a gluon. A quark triggered branching process will result in a high value of entropy index than one triggered by a gluon, though there is not yet any quantitative measure for how large or small that value would be. The scaling behavior of erraticity moments has so far been verified in several high-energy experiments and in all cases nonvanishing values of erraticity parameters confirm the existence of a chaotic nature of particle production data that may vary from event-to-event [3–9]. However, the physics behind such a chaotic nature of fluctuation could not yet be explained. In the recent past it has been observed that the FRITIOF and VENUS model calculations also reproduce considerable amount of erraticity in central AB collisions [7], where the produced particle multiplicities are as high as $10^2 - 10^3$ per event. In other words this means that within the framework of these models the statistical fluctuations still dominate the erraticity behavior. On the other hand, some previous works of our group showed that the FRITIOF prediction of erraticity parameters like $\tilde{\mu}_q$ are about 100 – 50 times smaller than those obtained from the experiment (^{32}S and ^{16}O -induced collisions at an incident energy of 200A GeV), and the model estimated values of $\tilde{\mu}_q$ are close to the corresponding values obtained from ordinary random number generated data samples [8, 9]. Therefore, a systematic comparison between experiment and model simulation(s) using various computer codes is necessary to understand the chaotic nature of multiparticle production in high-energy AB collisions.

In this chapter we present the erraticity related results of our data on $^{28}\text{Si-Ag/Br}$ interaction at an incident energy of 14.5A GeV. For the sake of completeness the erraticity analysis methodology is also briefly outlined. The objectives of the present investigation are: (i) to investigate comprehensively the erraticity characteristics of multiparticle production in

$^{28}\text{Si-Ag/Br}$ interaction at 14.5A GeV, (ii) to compare the experimental values of erraticity parameters with those obtained from the simulated data sets, and (iii) to investigate the influence of the Bose-Einstein type of correlation (BEC) between identical meson pairs on the erraticity parameters. The UrQMD simulation technique and the numerical algorithm of inducting BEC into the UrQMD generated events have been described in Section 2.5.

4.2 Methodology and Results

The erraticity moment deals with the event space fluctuation of factorial moments. The single event factorial moment F_q^e of order q is defined as,

$$F_q^e = \frac{\frac{1}{M} \sum_{m=1}^M n_m(n_m - 1) \dots (n_m - q + 1)}{\left(\frac{1}{M} \sum_{m=1}^M n_m \right)^q}, \quad (4.1)$$

in the same way as we did it for the intermittency analysis, where M is the number of non-overlapping equal sized sub-intervals (bins) into which the entire accessible phase space (here η space), say of size $\Delta\eta$, is divided. Note that, instead of the η variable here we have used the corresponding cumulative variables X_η [defined in Eq. (3.22)], though we continue to call the underlying space as the η -space. The moment F_q^e does not fully describe the structure of an event, since at any fixed q it is insensitive to the rearrangement of the bins. However, it does capture some aspect of the fluctuations from bin-to-bin that is adequate for the intermittency analysis. As for instance, in Fig. 4.1 we have shown the F_q^e distribution for the experimental events along with the corresponding UrQMD simulated events for two different values of phase space partition number $M = 5$ and $M = 10$. It can be seen that majority of the F_q^e values are concentrated within an initial small range, but a long tail that corresponds to unusually large F_q^e values is also visible in each distribution. It is our objective to quantify these large fluctuations of F_q^e in terms of the erraticity moments and associated scaling parameters. The method of analysis starts by introducing a normalized moment Φ_q defined for an individual event as, $\Phi_q = F_q^e / \langle F_q^e \rangle$, and then by defining a pair of erraticity moments expressed in terms of Φ_q . On one hand, we have the $C_{p,q}$ moments defined as the vertically averaged p th order moment of Φ_q , $C_{p,q} = \langle \Phi_q^p \rangle$ and on the other, we have an entropy like quantity Σ_q defined as, $\Sigma_q = \langle \Phi_q \ln \Phi_q \rangle$. In the $p > 1$ region, $C_{p,q}$ characterizes the large F_q^e behavior of the corresponding distribution $P(F_q^e)$ and is sensitive only to the spikes in the η -distribution. Conversely for $p < 1$, $C_{p,q}$ measures the low F_q^e behavior of the distribution $P(F_q^e)$, which is influenced mainly by bins with low multiplicities, including the empty ones i.e., the valleys present in the underlying space.

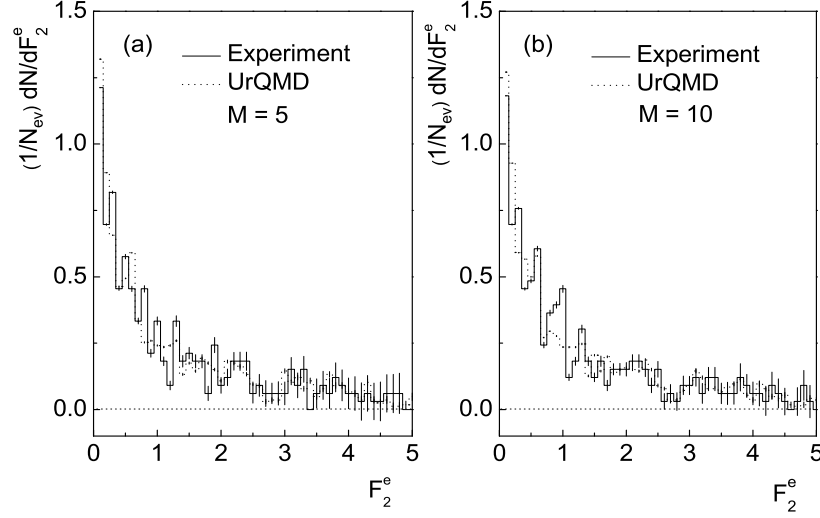


Figure 4.1: Distributions of F_2^e in $^{28}\text{Si-Ag/Br}$ interaction at 14.5A GeV for two different values of η -space partition number $M = 5$ (a) and 10 (b).

The domain of analysis ($0 < p < 2$) reveals enough information about the properties of $P(F_q^e)$, probably beyond those probed by intermittency. We are particularly interested in studying the erraticity behavior in the region $p \approx 1$. In multiparticle dynamics the erraticity moments $C_{p,q}$ are found to follow a scaling-law with phase space partition number M (or equivalently with the resolution size $\delta\eta$) as

$$C_{p,q} \propto M^{\psi(p,q)} \quad : \quad M \rightarrow \infty. \quad (4.2)$$

This behavior is referred to as the ‘erraticity’ and the exponent $\psi(p,q)$ is called the ‘erraticity index’. If the spatial pattern of particle density function does not change from one event to the other, one would expect the distribution $P(F_q^e)$ to behave like a delta function. Correspondingly, both Φ_q and C_{pq} would reduce to unity and $\psi(p,q)$ to zero. Hence, any deviation of $\psi(p,q)$ from zero can be considered as a measure of erraticity. The slope $\mu_q = (d/dp)\psi_q(p)|_{p=1}$ is the entropy index mentioned above. In high-energy AB interactions however, $C_{p,q}$ may not exhibit as strict a scaling-law as prescribed in Eq.(4.2), but would rather follow a more generalized form like,

$$C_{p,q} \propto f(M)^{\tilde{\psi}(p,q)}, \quad (4.3)$$

where $f(M)$ is some well behaved function of M . Similar to Eq.(4.3) one would expect a generalized scaling-law for the Σ_q moments as well,

$$\Sigma_q \propto \tilde{\mu}_q \ln f(M). \quad (4.4)$$

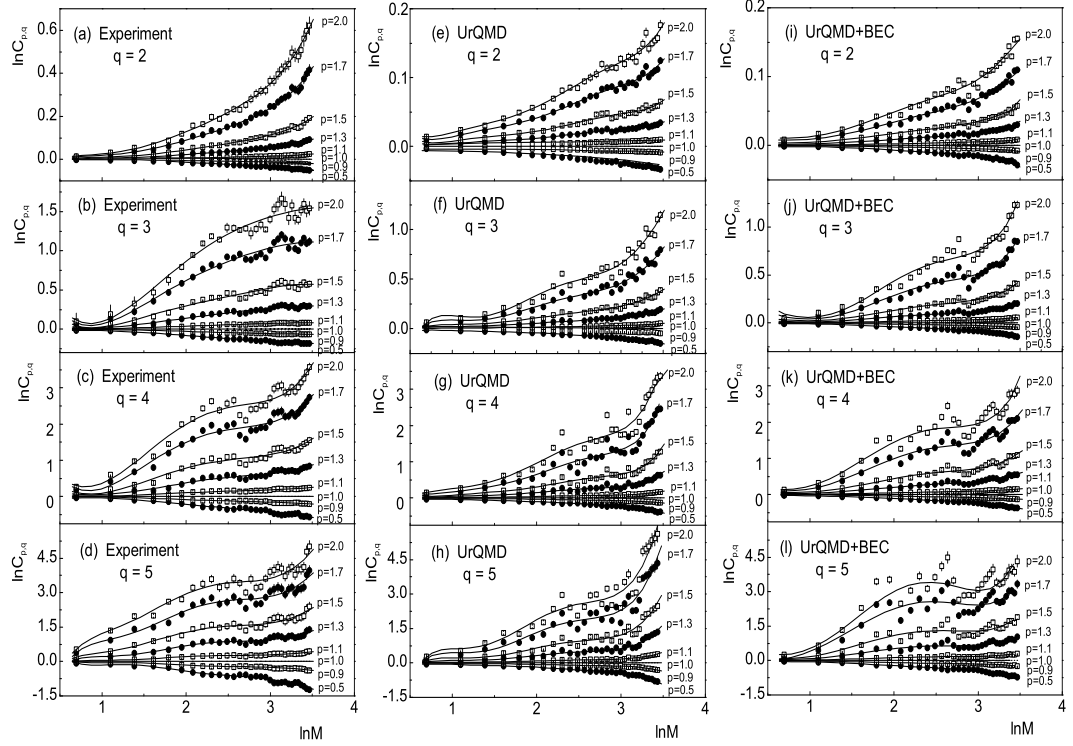


Figure 4.2: Erraticity moments $C_{p,q}$ plotted as functions of phase space partition number M . The solid curves are drawn to guide the eye.

From the definitions of $C_{p,q}$ and Σ_q it follows that the slope

$$\tilde{\mu}_q = \left. \frac{d}{dp} \tilde{\psi}(p, q) \right|_{p=1}. \quad (4.5)$$

The parameter $\tilde{\mu}_q$ is quite different from the entropy index μ_q related to the simple scaling-law of Eq. (4.2), and should therefore, not be compared with each other. However, this parameter is again a measure of the erratic behavior of event-to-event fluctuation and a chaotic behavior in the QCD branching processes [2]. Whereas a small $\tilde{\mu}_q$ value corresponds to a large Σ_q and hence to a less chaotic system, a large $\tilde{\mu}_q$ value corresponds to a small entropy and therefore, to a highly chaotic system.

In Fig. 4.2 the $C_{p,q}$ moments for $q = 2 - 5$ over a wide range of p values are plotted with the phase space partition number M . For better comparison the experimental results and those obtained from the UrQMD and the UrQMD+BEC simulations are shown side by side. From these graphs one can see that the experimental $C_{p,q}$ values vary over a wider range than the corresponding UrQMD and UrQMD+BEC generated values. A smooth but nonlinear variation of $\ln C_{p,2}$ with $\ln M$ can be seen over its entire range, which indicates the justification of invoking a generalized power law like Eq. (4.3). For $q = 3, 4$ and 5 the variation patterns are more or less similar to those for $q = 2$. However, several kinks (or discontinuities) at large M are observed for all three sets of plots, which may be a

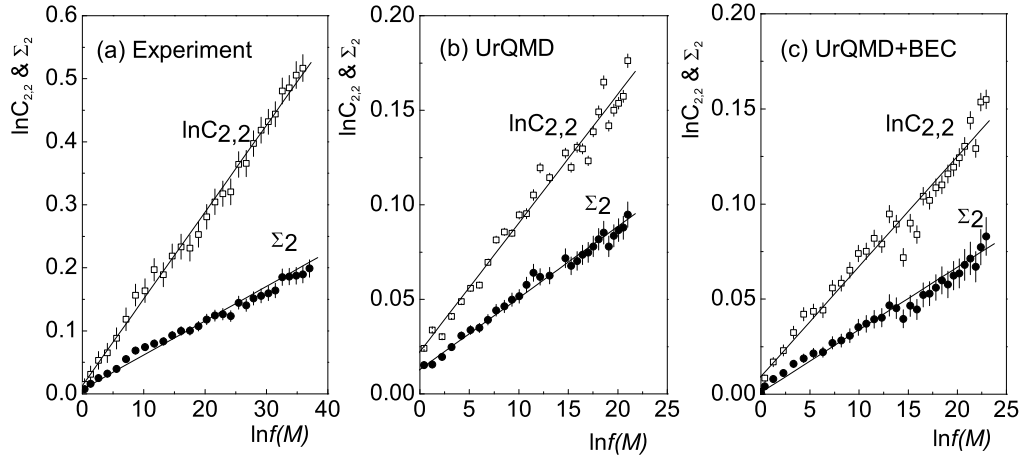


Figure 4.3: Plot of $\ln C_{2,2}$ and Σ_2 with $\ln f(M) = (\ln M)^b$. The lines represent best linear fits to the data points.

Table 4.1: Values of b , $\tilde{\psi}(2,2)$ and $\tilde{\mu}_2$ for the experiment, the UrQMD, the UrQMD+BEC and for a random number generated sample.

Data set	b	$\tilde{\psi}(2,2)$	$\tilde{\mu}_2$
Experiment	2.95	0.0138 ± 0.0006	0.0049 ± 0.0001
UrQMD	2.45	0.0068 ± 0.0003	0.0037 ± 0.0001
UrQMD+BEC	2.52	0.0063 ± 0.0005	0.0031 ± 0.0001
Random	2.70	0.0082 ± 0.0004	0.0037 ± 0.0008

result of finite event multiplicity, or limited statistics, or both. As the present $^{28}\text{Si-Ag/Br}$ event sample does not possess a very high multiplicity ($\langle n_s \rangle \approx 52$), with increasing q more events become susceptible to the empty bin effect and a kind of saturating trend beyond $M = 10$ can be seen with growing fluctuation in the data points. To establish a generalized scaling-law as suggested by Cao and Hwa [2], we have assumed $\ln f(M) = (\ln M)^b$, where b is a free parameter that has to be adjusted from the linear fit of $\ln C_{2,2}$ against $\ln f(M)$. Such plots can be found in Fig. 4.3 for (a) the experiment, (b) the UrQMD and (c) the UrQMD+BEC with the respective best fitted straight lines represented by solid lines. The values of b obtained are given in the first column of Table 4.1. One can compare these values with $b = 3.23$ and $b = 2.08$ (experiment), respectively for the $^{16}\text{O-Ag/Br}$ and $^{32}\text{S-Ag/Br}$ interactions at $200A$ GeV/c [8, 9]. In all cases Pearson's coefficient (R^2) which decides the goodness of fit, are found to be > 0.98 . The slope of $\ln f(M)$ versus $\ln C_{2,2}$ straight line gives us another erraticity parameter $\tilde{\psi}(2,2)$. The calculated $\tilde{\psi}(2,2)$ values are also quoted in the second column of the Table 4.1. The indices $\tilde{\mu}_2$ can now be obtained from the linear relationship between Σ_2 and $\ln f(M) = (\ln M)^b$ from the estimated values of b . These plots are also included in Fig. 4.3 and the $\tilde{\mu}_2$ values as shown in the third column of the Table 4.1, are nothing but the slopes of the $\ln f(M)$ versus Σ_2 straight lines of the respective data

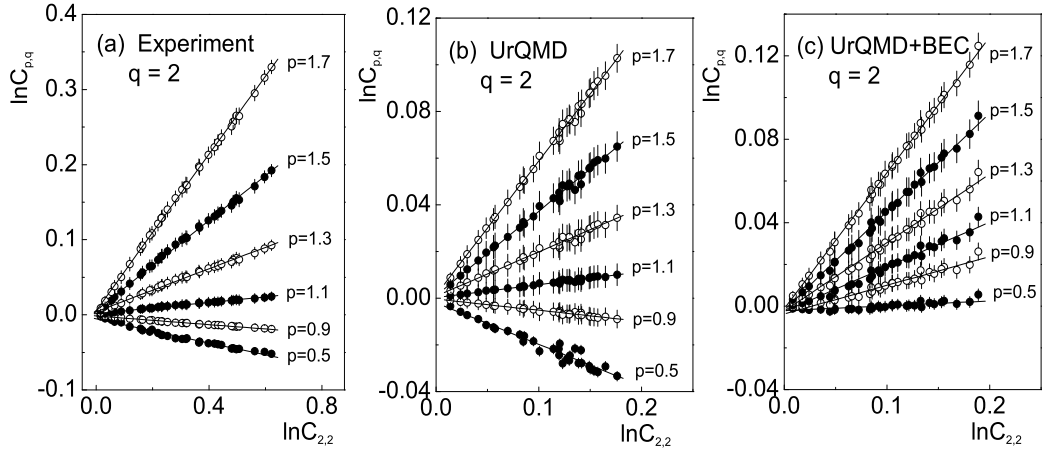


Figure 4.4: Plot of $\ln C_{p,2}$ with $\ln C_{2,2}$. The best fitted straight lines are shown.

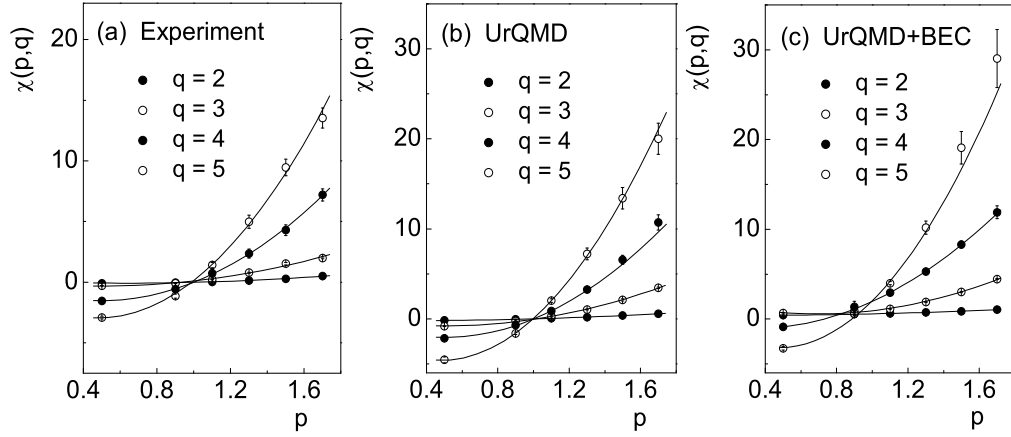


Figure 4.5: Variation of $\chi(p, q)$ with p . The curves represent the best quadratic fits.

sample. Note that all the $C_{p,q}$ moments depend almost similarly on $\ln M$. Therefore, one can also use $\ln C_{2,2}$ in place of $\ln g(M)$ to evaluate the erraticity parameters. The scaling relation (4.3) can thus be converted to

$$C_{p,q} \propto (C_{2,2})^{\chi(p,q)}. \quad (4.6)$$

We have found that for $q = 2$ the expected linear dependence of $\ln C_{p,q}$ on $\ln C_{2,2}$ is almost exact and for different values of p the results are graphically presented in Fig. 4.4. For $q > 2$ the linear dependence is only approximate, in the sense that it is valid in the low M region, and effects of finite multiplicity (saturation) and limited statistics (scattered points) are visible at high M . For $q > 2$ we have however, obtained $\chi(p, q)$ through linear fit of the approximate linear dependence of $\ln C_{p,q}$ on $\ln C_{2,2}$ within a limited region ($M \leq 12$), where $\ln C_{p,q}$ is found to behave systematically. In Fig. 4.5 the $\chi(p, q)$ values so obtained for the experiment, UrQMD and UrQMD+BEC are plotted against p for different q values.

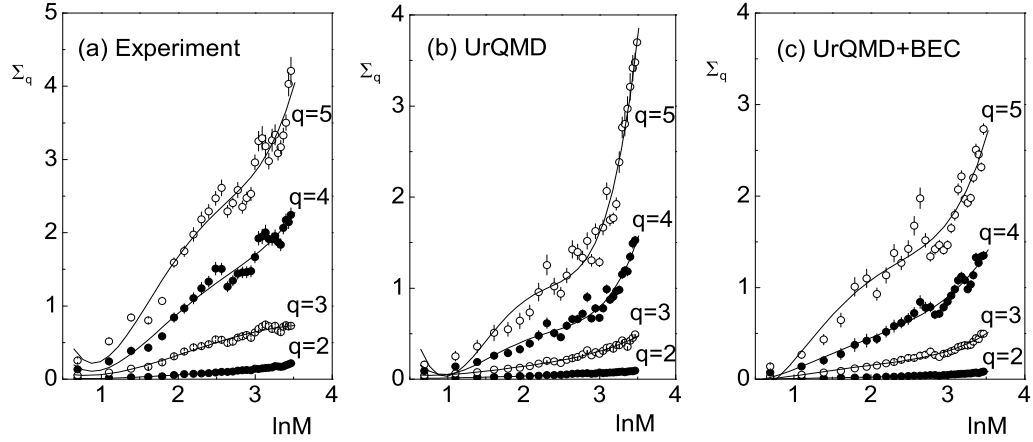


Figure 4.6: Plot of Σ_q with $\ln M$. The lines joining points are drawn to guide the eye.

For each q the data points are fitted to a quadratic function like

$$\chi(p, q) = a_2 p^2 + a_1 p + a_0. \quad (4.7)$$

The solid curves in the diagrams represent this quadratic function. The first order derivatives of $\chi(p, q)$ at $p = 1$,

$$\chi'_q = \left. \frac{\partial}{\partial p} \chi(p, q) \right|_{p=1} \quad (4.8)$$

can now be obtained by using this diagram and/or the corresponding quadratic fit parameters, and can further be utilized to determine the $\tilde{\mu}_q$ index from the following relation:

$$\tilde{\mu}_q = \tilde{\psi}_{2,2} \chi'_q. \quad (4.9)$$

The entropy-like moments Σ_q for different q are also plotted against $\ln M$ in Fig. 4.6. As expected, one can see that these moments are also not linearly varying with $\ln M$ over its entire range. However, for all q the variation patterns look similar. Hence, in place of $g(M)$ one can as well use Σ_2 and make a plot of Σ_q against Σ_2 , which is given in Fig. 4.7. In both these figures the UrQMD and the UrQMD+BEC prediction are incorporated along with the experimental. In each case the slope parameters

$$\omega_q = \frac{\partial}{\partial \Sigma_2} \Sigma_q \quad (4.10)$$

are obtained by making a linear fit of the Σ_2 versus Σ_q data point within a limited M (≤ 12) region, as shown in Fig. 4.7. Subsequently, following a different relationship

$$\tilde{\mu}_q = \tilde{\mu}_2 \omega_q, \quad (4.11)$$

once gain we can derive the $\tilde{\mu}_q$ index. All the erraticity parameters pertaining to this

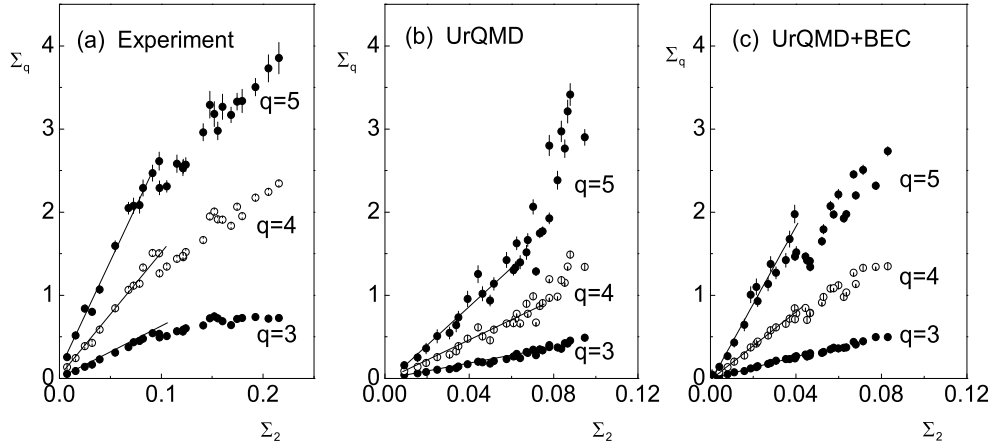
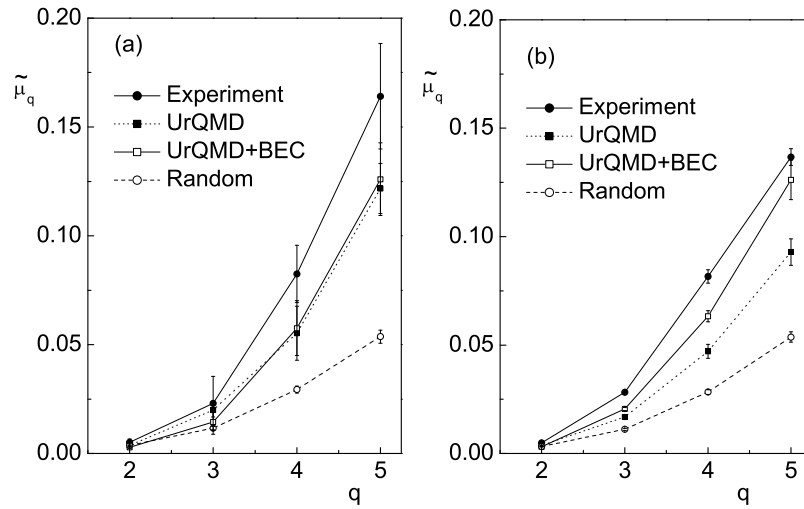


Figure 4.7: Plot of Σ_q against Σ_2 . The lines represent the best linear fits to the data points for $M \leq 12$.

analysis of $^{28}\text{Si-Ag/Br}$ data, namely χ'_q , ω_q and two sets of $\tilde{\mu}_q$ using Eq. (4.9) and Eq. (4.11), have been presented in Table 4.2 for $q = 2-5$. The parameters obtained from the experiment as well as from the simulations are presented together. Several observations can now be made regarding the erraticity behavior of our $^{28}\text{Si-Ag/Br}$ event sample. First of all, in general the erraticity of particle distribution is observed for all four data sets. With increasing q while the experimental χ'_q parameter increases at a slower rate, the ω_q parameter increases at a faster rate than the corresponding UrQMD and UrQMD+BEC generated values. Both parameters for the random number generated sample change at a slower rate than both the experiment and model simulations. For the $^{16}\text{O-Ag/Br}$ interaction at 14.5A GeV both χ'_q and ω_q are found to increase at a much slower rate than what was observed previously in AB interactions at 200A GeV/c [8, 9]. The index ($\tilde{\mu}_q$) obtained by using two different formulae [i.e., Eq. (4.9) and Eq. (4.11)], within their statistical uncertainties, are very close to each other. For a better understanding the parameter $\tilde{\mu}_q$ is plotted with q in Fig. 4.8 for all four data sets used in this analysis. Fig. 4.8(a) is drawn following Eq. (4.9) and Fig. 4.8(b) follows Eq. (4.11). In either of these diagrams the experimental data show a rapid increase with increasing q . The experimental values are always larger than the corresponding simulated values. The experimental $\tilde{\mu}_q$ values in $^{28}\text{Si-Ag/Br}$ interaction at 14.5A GeV are almost of the same order of magnitude as the $\tilde{\mu}_q$ values obtained in $^{32}\text{S-Ag/Br}$ interaction at 200A GeV [8], but are slightly larger than the corresponding values found in $^{16}\text{O-Ag/Br}$ interaction at 200A GeV [9]. So the dependence on the projectile mass number seems to dominate the erraticity behavior over the collision energy involved in an AB experiment. We note that the $\tilde{\mu}_q$ parameter characterizes the event space entropy and hence the chaoticity of the interacting system. An increase in the entropy index signals the augmentation of a possible quark-hadron phase transition [10]. This feature has indeed been observed for a possible nonthermal phase transition [11], where it is shown that the μ_q

Table 4.2: Erraticity parameters in $^{28}\text{Si-Ag/Br}$ interaction at 14.5A GeV.

Data set	Order	χ'_q	ω_q	$\tilde{\mu}_q$ [Eq. (4.9)]	$\tilde{\mu}_q$ [Eq. (4.11)]
Experiment	$q = 2$	0.368 ± 0.111	—	0.0051 ± 0.0015	0.0049 ± 0.0001
	$q = 3$	1.671 ± 0.904	5.272 ± 0.132	0.0230 ± 0.0124	0.0282 ± 0.0008
	$q = 4$	5.995 ± 0.922	16.554 ± 0.536	0.0825 ± 0.0132	0.0816 ± 0.0031
	$q = 5$	11.918 ± 1.672	27.729 ± 0.588	0.1641 ± 0.0242	0.1367 ± 0.0039
UrQMD	$q = 2$	0.546 ± 0.033	—	0.0037 ± 0.0003	0.0037 ± 0.0001
	$q = 3$	2.929 ± 0.463	4.452 ± 0.227	0.0199 ± 0.0032	0.0168 ± 0.0009
	$q = 4$	8.138 ± 1.808	12.487 ± 0.803	0.0553 ± 0.0124	0.0471 ± 0.0032
	$q = 5$	17.908 ± 1.537	24.638 ± 1.536	0.1217 ± 0.0115	0.0929 ± 0.0061
UrQMD +BEC	$q = 2$	0.449 ± 0.061	—	0.0028 ± 0.0004	0.0031 ± 0.0001
	$q = 3$	2.308 ± 0.883	6.609 ± 0.142	0.0145 ± 0.0057	0.0205 ± 0.0007
	$q = 4$	9.135 ± 1.865	20.438 ± 0.577	0.0576 ± 0.0126	0.0633 ± 0.0026
	$q = 5$	19.997 ± 2.115	40.719 ± 2.618	0.1260 ± 0.0167	0.1262 ± 0.0091
Random	$q = 2$	0.441 ± 0.094	—	0.0037 ± 0.0001	0.0032 ± 0.0001
	$q = 3$	1.367 ± 0.077	3.431 ± 0.104	0.0116 ± 0.0001	0.0111 ± 0.0005
	$q = 4$	3.451 ± 0.127	8.709 ± 0.249	0.0294 ± 0.0016	0.0283 ± 0.0011
	$q = 5$	6.308 ± 0.226	16.529 ± 0.599	0.0537 ± 0.0030	0.0537 ± 0.0024

**Figure 4.8:** Plot of the entropy index $\tilde{\mu}_q$ against order number q calculated from (a) Eq. (4.9) and (b) Eq. (4.11). The lines joining the data points are shown.

index increases fast with q in case of a ‘critical’ M interval. We can find a similar increasing trend of our $\tilde{\mu}_q$ parameter for the present set of $^{28}\text{Si-Ag/Br}$ data, which is consistent with the nonthermal phase transition as indicated our intermittency analysis [Fig. 3.7(a)].

The $\tilde{\mu}_2$ values of the present analysis are significantly (by approximately two-order) smaller

than what was obtained in a similar experiment on $^{28}\text{Si-Ag/Br}$ interaction at 14.6A GeV [5]. In ref. [5] $\tilde{\mu}_2$ is calculated as a function of average event multiplicity $\langle n_s \rangle$ and it is found that the parameter μ_2 decreases monotonically with increasing $\langle n_s \rangle$. Note that the average event multiplicity of our sample is greater than the highest multiplicity of the subsample used in ref. [5]. Also it may be noted here that in ref. [5] the erraticity moments were plotted against $\ln M$, not against $\ln f(M)$. Hence as already mentioned above, the entropy index μ_2 obtained thereby is altogether a different parameter than the $\tilde{\mu}_2$ parameter obtained in the present investigation. We have checked that a similar linear fit of the $\ln C_{p,q}$ versus $\ln M$ data in the region $11 \leq M \leq 25$ for the present event sample results in $\mu_2 = 0.092 \pm 0.009$, and the value is very close to the μ_2 values of ref. [5] within a similar M -range. We observe that the UrQMD as well as the UrQMD+BEC simulation fail to replicate any of the intermittency predictions of our $^{28}\text{Si-Ag/Br}$ data, whereas both the model simulated samples and the random number generated sample exhibit reasonable amount (well below the experiment though) of erraticity. Similarly we earlier found that the FRITIOF also reproduced erraticity behavior to a lesser extent than the experiment [9]. Either the FRITIOF or the UrQMD has nothing to do with the dynamics of erraticity of particle production, as no particle correlation is embedded into these models. The erraticity behavior comes merely as a statistical effect in these models, as is also confirmed from the random number generated values. The effect of BEC in $\tilde{\mu}_q$ almost vanishes when the parameter is calculated following Eq. (4.9), but it is quite prominent in case of the second formalism adopted i.e., Eq. (4.11). The UrQMD+BEC values of $\tilde{\mu}_q$ calculated by using Eq. (4.11) are always well above the corresponding UrQMD values, and are always very close to their experimental counterparts. Similar observation regarding the statistical contribution to erraticity behavior has been highlighted in other experiments as well [12]. As for example, in ref. [13] it was demonstrated that the erraticity behavior of a set of low multiplicity data of the NA27 experiment, could be reproduced by considering purely statistical fluctuations. Fuming *et al.* [7] showed that the FRITIOF and the VENUS simulations on AB interactions fit very well with the expected form of the $3d$ pure statistical fluctuation model. The results are independent of the event generator, the colliding nuclei, the incident energy, the particle species and even the phase space variables used in the analysis. Thus one can say, in the framework of the FRITIOF and/or VENUS event generators, even in the central collision of heavy nuclei at energies up to 200A GeV, the statistical fluctuations dominate the erraticity behavior. The erraticity analysis of hadronic interaction at 250 GeV/c [6] also confirms the dominance of statistical fluctuation in the experimental measurement. However, in emulsion experiments [4, 5] the experimental results of s -particles are found to be far apart from the corresponding random number generated results. In this regard our observation supports the previous records of AB experiments based on the emulsion technique.

4.3 Discussion

In this chapter the erraticity analysis of charged mesons produced in $^{28}\text{Si-Ag/Br}$ interaction at 14.5A GeV is presented. Various parameters related to chaoticity in event space fluctuation are estimated. The experimental results are compared with the prediction from two sets of simulated data, one by using the microscopic transport model UrQMD, and another set of UrQMD data which is supplemented by the Bose-Einstein type of correlation (UrQMD+BEC). To check whether the erraticity parameters are sensitive enough to the statistical fluctuation, we also perform the same analysis for a purely random number generated data sample. To summarize, the event-to-event fluctuation in the experiment, as well as in the models are found to be of chaotic nature. The following critical observation can be made from the analysis.

The erraticity moments are found to abide by a less stringent generalized scaling-law than the scaled factorial moment (see the intermittency analysis in Chapter 3). Quantitatively, this observation is true for the experimental, the UrQMD as well as for the UrQMD+BEC simulated data. Unlike the intermittency, the UrQMD and the UrQMD+BEC generated results on $^{28}\text{Si-Ag/Br}$ interactions also exhibit erratic nature, and the simulated system appears to be almost as chaotic as the experimental one. Also the effect of BEC in this analysis is not as prominent as it was observed in the intermittency analysis. It may be noted that as found earlier, the string fragmentation model FRITIOF does not fully reproduce either the intermittency results or the erraticity results at a similar or higher energies in AB or in hadronic interactions. The erratic behavior present in the transport models UrQMD as well as in the pure statistical fluctuations is signaling the dominance of the statistical fluctuation in UrQMD.

The present sample of $^{28}\text{Si-Ag/Br}$ events at 14.5A GeV seems to be almost as chaotic as the $^{16}\text{O-Ag/Br}$ and the $^{32}\text{S-Ag/Br}$ interactions at 200A GeV/c [9]. A comparison of our results with those obtained from the random number generated events, as well as the results from other experiments on hadron-nucleon (hN), nucleon-nucleon (NN) and AB interactions [3, 4, 6] show that, in the present case the $\tilde{\mu}_q$ indices are significantly smaller than the entropy indices μ_q obtained in other analyses. A high value of $\langle n_s \rangle$ and correspondingly a lower statistical fluctuation in bin-to-bin multiplicity might have contributed to a smaller entropy index. The geometry of collisions might be another important factor of concern, as it has been observed that the factorial moment increases with decreasing particle multiplicity [6]. Similar observation is also made in ref. [14] for the $^{28}\text{Si-Ag/Br}$ interactions at 4.5A and 14.5A GeV, where μ_q for $q = 2$ and 3 are found to decrease with increasing $\sqrt{\langle n_s \rangle}$. In emulsion experiments usually the sample statistic is not too large, and being a fixed target

experiment the event-to-event multiplicity fluctuates to a large extent, which in other words contributes a large fraction to the statistical noise.

Bibliography

- [1] Z. Cao and R. C. Hwa, *Phys. Rev. Lett.* **75**, 1268 (1995).
- [2] Z. Cao and R. C. Hwa, *Phys. Rev.* **D 53**, 6608 (1996);
Z. Cao and R. C. Hwa, *Phys. Rev.* **D 61**, 074011 (2000).
- [3] W. Shaoshun and W. Zhaomin. *Phys. Rev.* **D 57**, 3036 (1998).
- [4] D. Ghosh, A. Deb, M. Mondal and J. Ghosh, *Phys. Lett.* **B 540**, 52 (2002).
- [5] R. Hasan, M. Mohib-ul Haq and S. Islam, *J. Phys.* **G 28**, 2939 (2002).
- [6] M. R. Atayan *et al.* (EHS/NA22 Collaboration), *HEN* **450** (2003);
Phys. Lett. **B 558**, 22 (2003); *Phys. Lett.* **B 588**, 29 (2003).
- [7] L. Fuming *et al.*, *Phys. Lett.* **B 516**, 293 (2001).
- [8] M. K. Ghosh and A. Mukhopadhyay, *Phys. Rev.* **C 68**, 034907 (2003).
- [9] D. Chanda *et al.*, *Phys. Rev.* **C 71**, 034904 (2005).
- [10] R. C. Hwa, *Proc. VII International Workshop on Multiparticle Production*, p.303 (World Scientific, Singapore 1997).
- [11] L. K. Gelovani, G. L. Gogiberidze and E. K. Sarkisyan, *Proc. VIII International Workshop on Multiparticle Production*, p.334 (Matrahaza, Hungary, 1998).
- [12] E. A. De Wolf, I. M. Dremin and W. Kittel, *Phys. Rep.* **270**, 1 (1996).
- [13] Jinghua Fu, Yuanfang Wu, Lianshou Liu, *Phys. Lett.* **B 472**, 161 (2000).
- [14] S. Ahmad, M. M. Khan and A. Ahmad, *J. Phys.* **G 30**, 1145 (2004).

Chapter 5

Multifractality in $^{28}\text{Si-Ag/Br}$ Interaction at 14.5A GeV

5.1 Introduction

It is known that the theory of fractals has the ability to explain deterministic chaos in nonlinear physics [1]. Studies of intermittent behavior in turbulent fluids have also been well explained in terms of the fractal dimensions [2]. This observation has prompted the fractal formalism to be adopted to explain multiparticle emission data in high-energy collisions, which subsequently leads to the study of intermittency from the perspective of (multi)fractality. Several techniques based on the fractal theory are available to analyze the multiparticle emission data [2–4]. The most popular one has been the frequency moment method [5, 6] followed by a similar technique introduced in ref. [7]. In this chapter we use both of these methods to analyze shower track emission data of $^{28}\text{Si-Ag/Br}$ interaction at an incident energy of 14.5A GeV, along with a couple of detrended techniques, namely the multifractal detrended fluctuation analysis (MF-DFA) method [8] and the multifractal detrended moving average (MF-DMA) method [9].

The single particle density distribution of particles produced in a high-energy collision exhibits random fluctuations consisting of sharp peaks and deep valleys, which are apparently

devoid of any regular pattern. In the intermittency analysis we have characterized these fluctuations in terms of a set of regularly behaving parameters. The power law scaling behavior of SFM as elucidated in Eq. (3.23) indicates that some kind of scale invariant dynamics is involved in the particle production process that may have a connection with the theory of fractals [5, 10–13]. Efforts have been made to interpret the intermittency parameters and the self-similarity observed in the particle density distribution, in terms of several conventional as well as exotic speculative processes, but each with a limited degree of success. Both the experimental and phenomenological development of the subject has been comprehensively reviewed in ref. [14].

For a self-similar process, the multifractal G_q moment (also called the frequency moment) introduced in ref. [5, 6] exhibits a power-law dependence on the phase space resolution size in a way similar to Eq. (3.23). Over intermittency the G_q moment technique has an added advantage in the sense that, by using the G_q moments one can study not only the spikes (for $q > 0$) but also the non-empty valleys (for $q < 0$), while the F_q moments are useful only for the spikes of the density distribution. Unlike the F_q moments, the G_q moments can be defined for fractional as well as for negative q values, and hence one can enjoy the freedom of computing a continuous spectrum of moments. However, in low multiplicity events as the empty bin effects dominate the G_q moments saturate with $\delta X \rightarrow 0$, and the statistical noise present in the density function cannot be automatically accounted for. The limiting condition $\delta X \rightarrow 0$ is again a mathematical idealization, and the only achievable limit is up to the phase space resolution allowed by the detector granularity. In G_q technique the noise has to be eliminated by using an equivalent uncorrelated event sample generated by the random numbers. Takagi's T_q moments on the other hand, are defined only for positive integer order q , and are not particularly affected by the finiteness of the event multiplicity [7]. Takagi used his technique to determine several multifractal parameters by analyzing $p\bar{p}$ and e^-e^+ annihilation data. However, a proper method of eliminating the statistical noise from the T_q moments has not yet been formulated. In the recent past both Hwa's and Takagi's methods have been applied to analyze high-energy nucleus-nucleus (AB) collision data at different collision energies involving different colliding systems [5, 6, 15, 16].

The multifractal detrended fluctuation analysis (MF-DFA) [8] method is a very useful tool for the multifractal characterization of noisy and nonstationary time series data. As a robust and powerful technique for capturing the long-range correlations in time series data, the method has so far been applied to various fields of stochastic analysis e.g., in stock markets, foreign exchange, geophysical time series, medicine and many more. To illustrate the applicability of the MF-DFA method we cite a few recent articles in ref. [17], certainly the list is not a complete one. In the recent past Zhang et al. [18] have applied the method probably for the first time to analyze the multiparticle data on Au+Au interaction at

$\sqrt{s_{NN}}=200$ GeV. The multifractal detrended moving average analysis (MF-DMA) technique [9] on the other hand, is a comparatively new method adopted in time series analysis. The MF-DMA analysis method is also an efficient tool for the detection and characterization of multifractal scaling and long-range correlation properties of noisy and non-stationary time series data [19, 20]. It is obvious that like other multifractal techniques, MF-DMA technique can also be used to investigate the scale invariance property of the particle density in high-energy collisions, though to the best of our knowledge it has not so far been applied to any such multiparticle distribution.

As mentioned above, the intermittency analysis of our AB data signals towards the possibility of some kind of scale invariant dynamics that ultimately leads to a self-similar density distribution in one dimensional density distribution [21], and a self-affine distribution in the two-dimensional (η, φ) plane [22]. These observations encouraged us to perform a multifractal analysis of the $^{28}\text{Si-Ag/Br}$ data. Therefore, in this chapter we examine the scaling behavior of various multifractal moments and derive several parameters related to multifractality. We adopt four different techniques, namely Hwa's moment [5, 6, 11], Takagi's moment [7], the MF-DFA moment [8] and the MF-DMA moment [9]. Moreover, the results obtained from the experimental data sample are systematically compared with the predictions of the UrQMD and UrQMD+BEC simulations.

5.2 Hwa's Moment

The frequency moment or the q th order multifractal moment G_q averaged over many events as well as over many non-overlapping phase space intervals of equal size say $\delta X_\eta = \Delta X/M$, is defined as [5],

$$\langle G_q \rangle = \frac{1}{N_{ev}} \sum_{e=1}^{N_{ev}} \sum_{m=1}^M \left[\frac{n_m^e}{n_s^e} \right]^q. \quad (5.1)$$

In the above definition of G_q , the order q can be any real number, M represents the total number of equal size intervals into which the entire accessible phase space ΔX is partitioned, n_m^e is the number of shower tracks falling within the m th such interval of the e th event, n_s^e is the total number of shower tracks in the e th event (i.e., $n_s^e = \sum_{m=1}^M n_m^e$). For finite n_s^e the single event G_q moments are subjected to large statistical fluctuations that can be minimized through event averaging. To get rid of the saturation problem mentioned above, Hwa and Pan [6] introduced a step function $\Theta(n_m^e - q)$ into the definition of G_q which acts like a filter for the empty bin. With this modification the $\langle G_q \rangle$ moment is redefined as,

$$\langle G_q \rangle = \frac{1}{N_{ev}} \sum_{e=1}^{N_{ev}} \sum_{m=1}^M \left[\frac{n_m^e}{n_s^e} \right]^q \Theta(n_m^e - q). \quad (5.2)$$

The Θ function equals to 1 if $n_m^e > q$, and vanishes otherwise. According to the theory of fractals, if the single particle density distribution possesses multifractal structure, then $\langle G_q \rangle$ like the SFM should also exhibit a scaling relation,

$$\langle G_q \rangle \propto (\delta X_\eta)^{\tau(q)} \quad : \text{ as } \delta X_\eta \rightarrow 0. \quad (5.3)$$

The exponent $\tau(q)$ is called the ‘multifractal mass exponent’ or simply the ‘fractal exponent’ that can be related to the generalized Renyi (fractal) dimensions D_q through the relation: $\tau(q) = (q-1) D_q$. The phase space variable used here is nothing but the cumulative variable X_η defined in Eq. (3.22) corresponding to the pseudorapidity (η). We have calculated the G_q moments as functions of phase space partition number M over a wide range of q values. Fig. 5.1 shows the corresponding schematic representations, where $\ln \langle G_q \rangle$ has been plotted against $\ln M$ (a) for the experiment, (b) for the UrQMD, and (c) for the UrQMD+BEC. The diagrams show that the phase space dependence of G_q is more or less similar for all the three data samples e.g., $\ln \langle G_q \rangle$ increases for $q < 0$ and decreases for $q > 1$, $\ln \langle G_q \rangle$ tends to saturate at large $\ln M$, and the saturation effect that might simply be an outcome of the finiteness of $\langle n_s \rangle$, is more prominent for the higher positive values of $q (\geq 4)$. The mass exponent $\tau(q)$ is calculated from the linear dependence of $\ln \langle G_q \rangle$ on $\ln \delta X_\eta$ (see Eq. (5.3)) through

$$\tau(q) = \lim_{\Delta \rightarrow 0} \frac{\Delta \ln \langle G_q \rangle}{\Delta \ln \delta X_\eta}. \quad (5.4)$$

For each q , $\tau(q)$ is extracted from the best linear fit to the $\ln \langle G_q \rangle$ versus $\ln M$ data. While fitting a straight line we did not take into account the points falling in the saturation region. From the knowledge of $\tau(q)$ one can now establish a connection between intermittency and multifractality, can evaluate the fractal dimensions, and can also construct the most

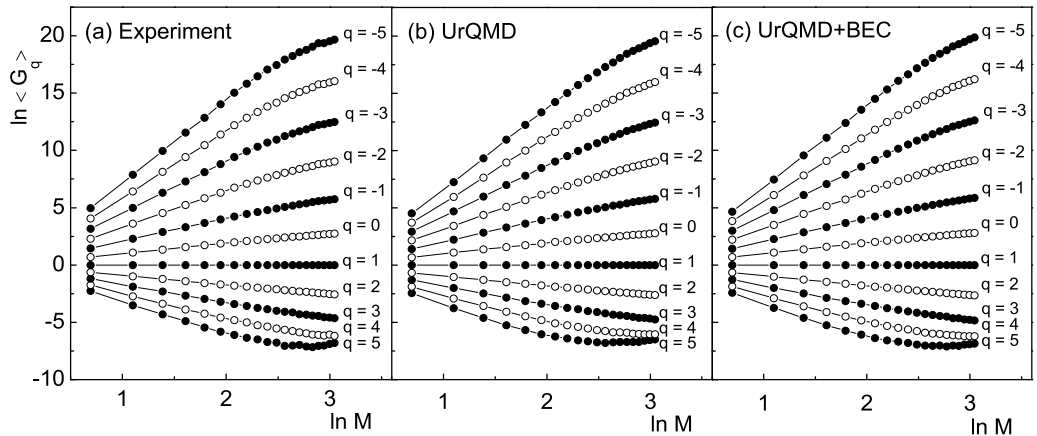


Figure 5.1: Multifractal G_q moment plotted with phase space partition number in $^{28}\text{Si-Ag/Br}$ interaction at 14.5A GeV. Lines joining points are drawn to guide the eye.

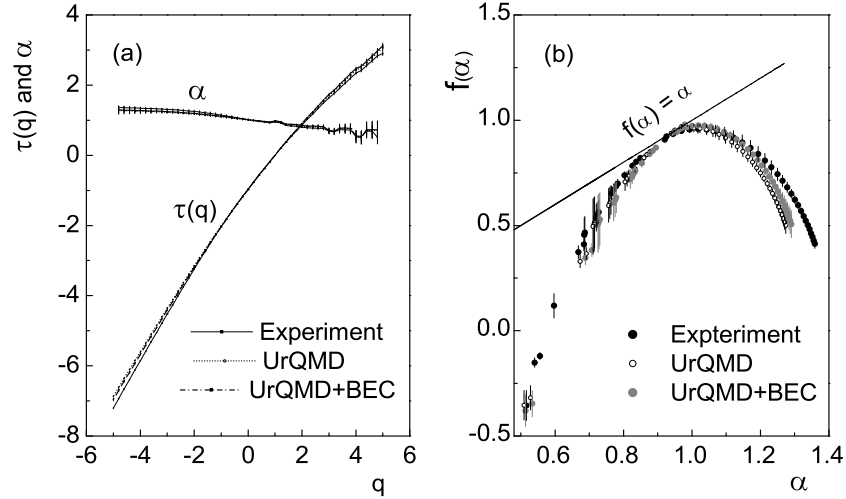


Figure 5.2: (a) The event average mass exponent $\tau(q)$ and the Lipschitz-Hölder exponent α plotted against q . Note that the experiment (solid line), the UrQMD (dotted line) and the UrQMD+BEC (dashed line) are very close to each other. (b) The multifractal spectral function for the experiment (solid circles), the UrQMD (open circles) and the UrQMD+BEC (shaded circles).

important multifractal singularity spectral function [23],

$$f(\alpha) = q\alpha(q) - \tau(q). \quad (5.5)$$

Here the Lipschitz-Hölder exponent α is defined as $\alpha(q) = \partial\tau(q)/\partial q$. The importance of the singularity spectrum in the theory of multifractals is that, the width of the spectrum is a direct measure of the degree of multifractality present in the data, which for a monofractal object should reduce to a delta function centered around a particular $\alpha(q) = \alpha(0)$. A finite width of $f(\alpha)$ distribution on the other hand would suggest that, the quantitative nature of the singularities of particle density, as the scaling law (5.1) suggests, may be different at different phase space points, and not guided by any universal exponent. In Fig. 5.2(a) we have shown a plot of $\tau(q)$ against q for the experiment and the simulations. Corresponding α values are also presented in the same diagram. One can notice that the experimental and the simulated results behave almost identically. It can also be seen that (i) there exists a small but definite non-linearity in the variation of $\tau(q)$ with q , and (ii) a decreasing trend of α with increasing q . In the phenomenology of multifractality both the observations indicate the presence of multifractality in the actual density distribution [5, 6]. The multifractal spectral functions $f(\alpha)$, obtained for the experiment, for the UrQMD simulation with and without BEC are plotted in Fig. 5.2(b). All the spectra are found to be very stable, smooth and concave downwards having peaks at $\alpha(q = 0)$. The straight line $f(\alpha) = \alpha$ shown in the diagram, tangentially touches all the spectra at around $\alpha \approx 1.0$. The maxima of $f(\alpha)$ is very close to unity, indicating that the empty bin effect, especially within the scale region of analysis, has properly been taken care of. A wide $f(\alpha)$ spectrum for all the data

samples is strengthening the proposition of multifractality. The important issue is that the experimental spectrum is wider than both the UrQMD and UrQMD+BEC generated spectra, and the UrQMD+BEC spectrum falls in between the experimental and the UrQMD generated spectra. This is an indication of the fact that multifractality in the experimental data is greater than the UrQMD simulation, and inclusion of BEC actually enhances the multifractal character of the UrQMD data. Similar effect has also been observed in our intermittency analysis as well [21]. The spectral functions obtained in our analysis exhibit similar features that are observed in the $p\bar{p}$ collisions of the UA1 collaboration [12], or in the AB collisions of the EMU01 [15] experiments. It is to be noted that the UA1 results were compared with the GENCL and the PYTHIA(v4.8) predictions, whereas a stochastic model was used to compare the EMU01 results. As mentioned, in addition to the dynamical component of fluctuation (if any), the G_q moment calculated through Eq. (5.2) is contaminated by the statistical noise. While the dynamical component in the particle density fluctuation can automatically be filtered in the intermittency technique, the same is not true for multifractality. Therefore, it would be a useful exercise to estimate the nontrivial dynamical component of the G_q moment, and to see whether it can match the same obtained from our intermittency analysis. In order to find out the statistical contribution, we have calculated the G_q moments over an uncorrelated event sample (call it G_q^{sta}) generated by (pseudo)random numbers as discussed in Chapter 2. For each q corresponding mass exponents $\tau^{\text{sta}}(q)$ are also calculated from the best fitted straight lines to the data points. It has been shown in ref. [6] that the dynamical component of $\tau(q)$, denoted by $\tau^{\text{dyn}}(q)$ is related to the statistical one $\tau^{\text{sta}}(q)$ by the following relation,

$$\tau^{\text{dyn}}(q) = \tau(q) - \tau^{\text{sta}}(q) + q - 1. \quad (5.6)$$

In deriving the above relation, it has been assumed that G_q^{dyn} obeys the same scaling-law as G_q i.e., $\langle G_q^{\text{dyn}} \rangle \propto (\delta X_\eta)^{\tau^{\text{dyn}}(q)}$ as $\delta X_\eta \rightarrow 0$. It then follows from Eq. (5.6) that for a trivial dynamics $\tau^{\text{dyn}}(q)$ should be equal to $(q-1)$. Therefore, any deviation in $\tau^{\text{dyn}}(q)$ from $(q-1)$ may be considered as an outcome of the nontrivial dynamics. A phenomenological relation between the intermittency exponent ϕ_q and the dynamical component of mass exponent $\tau^{\text{dyn}}(q)$ after Hwa [6] is given by,

$$\tau^{\text{dyn}}(q) - q + 1 \approx \phi_q. \quad (5.7)$$

The effect of eliminating the statistical contribution to the G_q moments can be readily seen from Fig. 5.3, where the $q-1-\tau(q)$, the $q-1-\tau^{\text{dyn}}(q)$, along with the ϕ_q values taken from ref. [21] are plotted together against q . The results obtained from the experiment, the UrQMD and UrQMD+BEC simulation are shown separately to avoid mutual overlapping of the points. Both in the experiment and in the simulations (with and without BEC) the

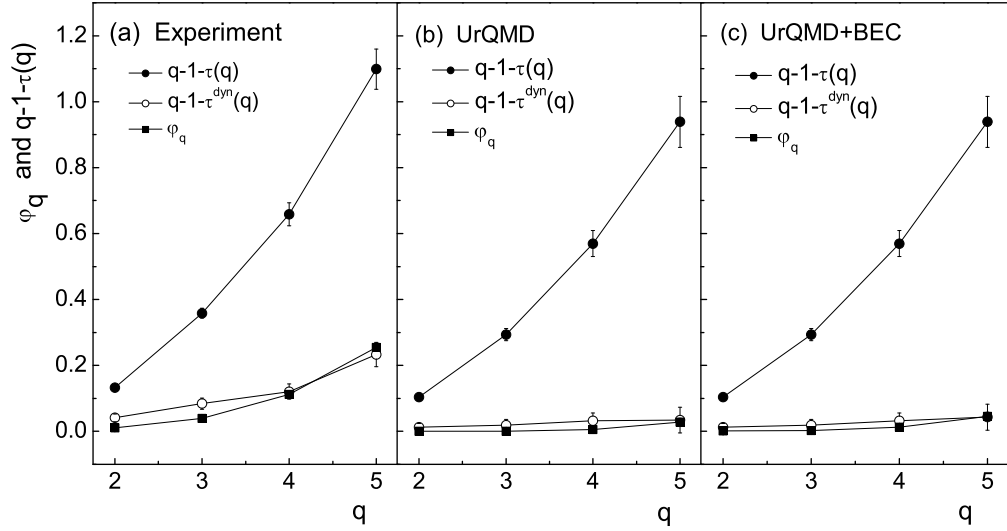


Figure 5.3: Plots of $q - 1 - \tau^{\text{dyn}}(q)$, $q - 1 - \tau(q)$ and the intermittency exponent ϕ_q [21] versus order number q . In all diagrams lines joining points are drawn to guide the eye.

$q - 1 - \tau(q)$ values are far above the corresponding ϕ_q values. As soon as the statistical contribution is subtracted, the respective $q - 1 - \tau^{\text{dyn}}(q)$ values come down very close to the intermittency index. It is to be noted that, very little evidence of dynamical fluctuation has been observed in the intermittency analysis ($\phi_q \approx 0$) of the UrQMD data [21, 22], and the UrQMD+BEC estimation of ϕ_q is about 5 – 10 times larger than the respective UrQMD values. The UrQMD and the UrQMD+BEC predictions of $q - 1 - \tau^{\text{dyn}}(q)$ also match their respective ϕ_q values. In spite of the fact that the model produces only statistical fluctuations, the UrQMD shows multifractality and the Bose-Einstein correlation included by the prescribed afterburner technique enhances the degree of multifractality. Since the multifractal character is also found in the random number generated sample, the scaling behavior of G_q cannot be taken as the characteristic of the dynamical fluctuation, rather the dynamical signature of the data has to be scrutinized at the level of scaling exponents and derivatives obtained thereof.

A fractal system can also be characterized by a parameter called the Lévy stable index (μ) which has a stability range, $0 \leq \mu \leq 2$ [24, 25], though occasionally the index is found outside the specified stability range [26]. The upper limit $\mu = 2$ corresponds to minimum fluctuation for a self-similar branching process, whereas the lower limit $\mu = 0$ corresponds to maximum fluctuation i.e., monofractals that may be a signal of a second order phase transition. For the α -model [27], where the final state particle density is given as a product of random numbers, the density function can be approximated by a log-Lévy type of distribution. Under this approximation the Lévy index μ can be determined using the following relation [25, 28]:

$$\frac{D_T - D_q}{D_T - D_2} = \frac{1}{q-1} \frac{q^\mu - q}{2^\mu - 2}, \quad (5.8)$$

where D_T is the topological dimension of the supporting space, which is 1 in the present case, and D_q is the generalized Renyi dimension of integer order q defined in terms of the intermittency exponents ϕ_q as,

$$D_q = D_T - \frac{\phi_q}{q-1}. \quad (5.9)$$

Following Eq. (5.7) one can also set

$$D_q \approx \frac{\tau^{\text{dyn}}(q)}{q-1}. \quad (5.10)$$

We shall discuss more about D_q in the next section. In practice only a few D_q values are obtained from the intermittency and/or multifractal analysis. Therefore, the μ value extracted by fitting Eq. (5.8) to a small set of data points is likely to be unreliable. Hence we follow an alternative method of calculating μ using the multifractal spectral function $f(\alpha)$, as described by Hu *et al.* [29]. According to [29], $f(\alpha)$ is related to μ by the following relation,

$$1 - f(\alpha) \propto (B - \alpha)^{\mu/(\mu-1)} \quad \text{for } \alpha < B, \quad (5.11)$$

where with $B = 1 + (1 - D_2)/(2^\mu - 2)$. Note that for any q , positive or negative, $f(\alpha)$ is a smooth and continuous function of $\alpha(q)$. Therefore, the index μ can be extracted from the slope $\mathcal{C} = \mu/(\mu - 1)$ of the $\ln(1 - f(\alpha))$ versus $\ln(B - \alpha)$ straight line in the $\alpha < B$ region. As it follows from Eq. (5.11), the only criterion that has to be satisfied here is $f(B) = 1$. Fig. 5.4 shows the results of such calculations. In either of these plots, it is clear that a single straight line cannot reproduce the data well and hence the μ value is found to depend on the region of fitting the straight lines. The best fitted straight lines in two different q -regions are shown in the diagrams. In the positive and low- q region the straight line fit is

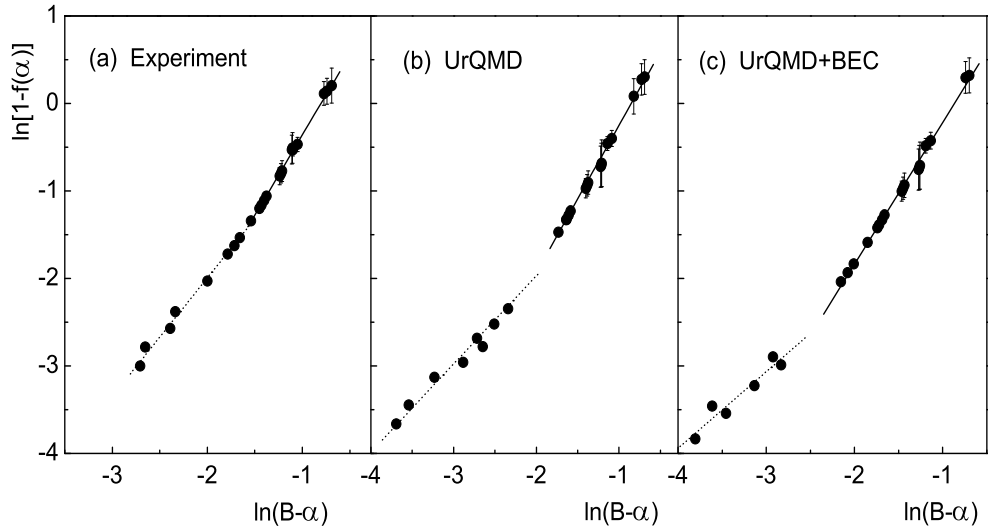


Figure 5.4: Plot of $\ln[B - \alpha]$ versus $\ln[1 - f(\alpha)]$. In all diagrams the dotted(solid) lines represent linear fits to the data points in the low(high)- q region.

shown by the dotted line and the solid line represents the linear fit in the positive and high- q region. The values of μ obtained from these fittings are listed in Table 5.1. The experiment and the UrQMD simulation provide somewhat reasonable values of μ in the high- q region, otherwise the index is either diverging or far from the admissible limits. Therefore, one may conclude that the (dynamical) density fluctuations present in our data are not compatible to the log-Lévy type of distributions.

Table 5.1: The values of the Lévy stable index (μ) obtained at two different regions of q in $^{28}\text{Si-Ag/Br}$ interaction at 14.5A GeV.

Fit region	Experiment	UrQMD	UrQMD+BEC
Low- q region	3.843 ± 0.089	$\rightarrow \infty$	6.880 ± 0.0124
High- q region	2.199 ± 0.164	2.466 ± 0.152	-2.6129 ± 0.0801

5.3 Takagi's Moment

In order to study the multifractal structure of particle density distributions, Takagi proposed a new set of moments called the T_q moments [7]. Takagi's method is based on two assumptions: (i) the density distribution ρ is uniform all over the phase space interval and (ii) the multiplicity distribution P_n does not depend on the location of the phase space interval. Both these criteria are found to be more or less valid when the cumulative variables are used in place of the basic phase space variable like η or φ . The T_q moment for positive integer order q is defined as,

$$T_q(\delta X_\eta) = \ln \sum_{i=1}^{N_{ev}} \sum_{j=1}^M (p_{ij})^q, \quad (5.12)$$

where $p_{ij} = n_{ij}/K$, K being the total number of tracks present in all N_{ev} events, and n_{ij} is the number of tracks in the j th bin of the i th event. Unlike the G_q moments, the T_q moments so defined are not very much affected by the finiteness of an event multiplicity $\langle n_s \rangle$. According to Takagi [7], $T_q(\delta X_\eta)$ should be a linear function of $\ln(\delta X_\eta)$, i.e.

$$T_q(\delta X_\eta) = A_q + B_q \ln(\delta X_\eta), \quad (5.13)$$

where A_q and B_q are two constants independent of the phase space resolution size. When a linear relation like Eq. (5.13) is observed over a considerable range of δX_η , the generalized

dimension D_q can be obtained in terms of the fit parameter B_q as

$$D_q = \frac{B_q}{q-1}, \quad \text{for } q \geq 2. \quad (5.14)$$

For a sufficiently large N_{ev} one can set

$$\sum_{i=1}^{N_{ev}} \sum_{j=1}^M (p_{ij})^q = \frac{\langle n^q \rangle}{K^{q-1} \langle n \rangle}, \quad (5.15)$$

where $\langle n \rangle$ represents the average bin multiplicity. From Eq. (5.12)–(5.15) and replacing δX_η by $\langle n \rangle$ one can derive an expression for the generalized dimension for $q \geq 2$ through the following relation:

$$\ln \langle n^q \rangle = A_q + \{(q-1)D_q + 1\} \ln \langle n \rangle. \quad (5.16)$$

For $q = 1$ the parameter D_1 is known as the information dimension, which provides the information of how much of a phase space interval is filled up with the distributed tracks. D_1 is obtained by taking an appropriate limit to Eq. (5.14) [30]. This is equivalent to considering an entropy like function

$$\mathcal{S}(\delta X_\eta) = - \sum_{i=1}^{N_{ev}} \sum_{j=1}^M p_{ij} \ln p_{ij}, \quad (5.17)$$

and to looking for its linear dependence on $\ln(\delta X_\eta)$,

$$\mathcal{S}(\delta X_\eta) = -D_1 \ln(\delta X_\eta) + \text{constant}. \quad (5.18)$$

Using Eq. (5.15) one can now easily obtain an expression for D_1 as,

$$\langle n \ln n \rangle / \langle n \rangle = C_1 + D_1 \ln \langle n \rangle. \quad (5.19)$$

Following the prescription of Takagi [7], we have calculated $\langle n \ln n \rangle$ and $\ln \langle n^q \rangle$ (for $q = 1 - 7$) with increasing phase space interval δX_η taken symmetrically about the centroid of the η -distribution. The results are shown graphically in Fig. 5.5 for all the data sets employed in this analysis. The information dimension D_1 is evaluated from the best fitted straight lines to the $\langle n \ln n \rangle / \langle n \rangle$ versus $\ln \langle n \rangle$ plot and is shown in the upper panel of the Fig. 5.5. The generalized dimensions D_q are evaluated from the best linear fits to the $\ln \langle n^q \rangle$ versus $\ln \langle n \rangle$ graph for $q = 2 - 7$. It turns out that $D_1 = 0.933 \pm 0.037$ for the experiment, $D_1 = 0.926 \pm 0.005$ for the UrQMD, $D_1 = 0.935 \pm 0.005$ for the UrQMD+BEC and $D_1 = 0.934 \pm 0.005$ for the random number generated event sample. All these values are slightly less than the phase space dimension, which according to the theory of fractals, is a signature of fractal density distribution function. The generalized dimensions D_q obtained

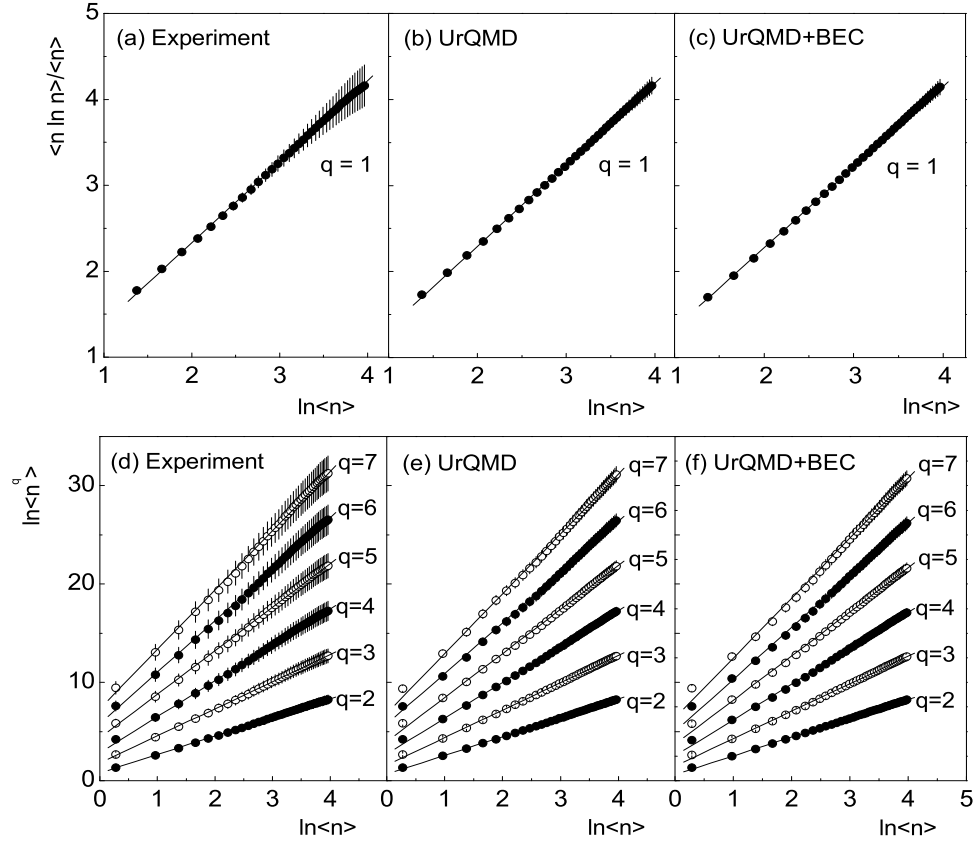


Figure 5.5: Multifractal T_q moment as a function of number of counts in the phase space interval. The best fitted straight lines are shown in all diagrams.

from Takagi's moments [Eq. (5.16)], and those obtained from Hwa's moments [Eq. (5.10)] are plotted together against q in Fig. 5.6. On the same figure we have included the D_q values obtained from the SFM analysis [21]. A general decreasing trend of D_q with increasing q has been observed for all three data samples, which again indicates multifractality. In the case of experiment the D_q values obtained from the SFM fall at a much faster rate than those obtained from the G_q moment, whereas for UrQMD the D_q values calculated either from the SFM or from the G_q moment, within the errors are very close to unity, which is the dimension of the supporting space. The UrQMD+BEC data, on the other hand, shows a rapid fall in D_q when calculated from the SFM but the rate of fall is not as high as the experimental one. The D_q values obtained from the T_q moment for all the data sets are significantly and consistently lower than those obtained from the SFMs and the G_q moments. Such a large and systematic deviation might reflect the fact that the T_q moments are not corrected from the statistical contamination, the technique of which is still unknown to us. Moreover, the moments are defined in different ways, which might be another source of such inconsistencies. Note that for a simple Poissonian type of multiplicity distribution within a given interval δX_η , the generalized dimensions would all be equal to the topological dimension of the supporting space. Any deviation from unity, as it is observed in

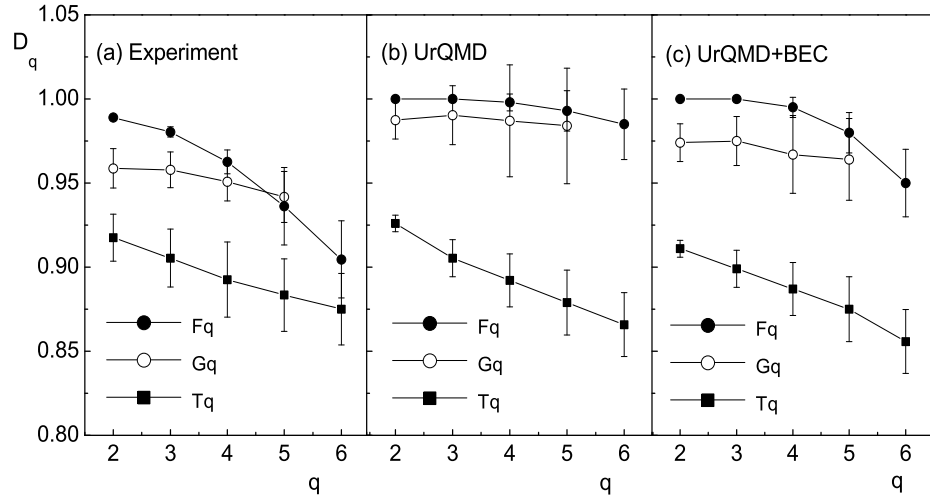


Figure 5.6: Generalized dimensions D_q with order number q calculated from the SFM (solid circles) [21], G_q moment (open circles) and T_q moment (solid square) analysis. The lines joining points are shown to guide the eye.

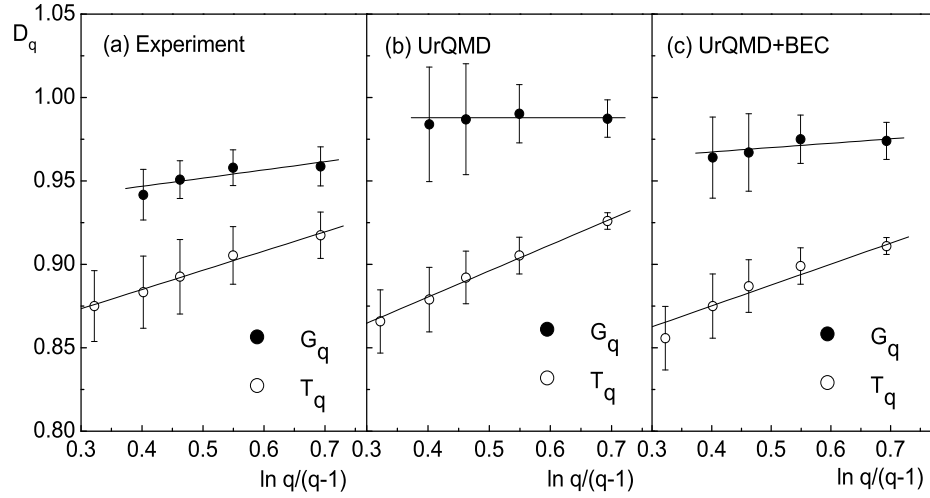


Figure 5.7: Plot of D_q with $\ln q/(q-1)$. The solid (open) circles are the results of the $G_q(T_q)$ moment analysis. The lines are the best linear fits to the data points.

our analysis, should therefore be considered as a signature of nonstatistical elements present in the particle distribution.

The thermodynamic interpretation of fractals in terms of the multifractal specific heat, has been given by Bershadski [31]. If the monofractal to the multifractal transition is governed by a Bernoulli type of fluctuation only, then the multifractal specific heat C can be derived from the relation [31]:

$$D_q = D_\infty + \frac{C \ln q}{q-1}. \quad (5.20)$$

A monofractal to multifractal transition corresponds to a jump from $C = 0$ to a nonzero

finite value. In Fig. 5.7 we have plotted D_q against $\ln q/(q-1)$ for (a) the experiment, (b) the UrQMD and (c) the UrQMD+BEC data, and the values obtained from both Hwa's moments and Takagi's moments are shown together. An approximately linear dependence of D_q on $\ln q/(q-1)$ is observed for all three data samples, indicating the relevance of Bershadski's interpretation of multifractality [31] in the context of a phase transition in the present case. The C values are extracted from the best linear fits to the data points shown in the diagrams. The values of C are quoted in Table 5.2. The effect of eliminating the statistical noise using the random number generated event sample is manifested once again in the C value obtained from Hwa's method, which produces almost null value of C for the simulated events. On the other hand, in Takagi's method no distinction is possible between the experiment and the UrQMD predictions, but for some reason that cannot be clarified at this point, inclusion of BEC lowers the value of C by about ten times the experiment/UrQMD prediction. The present set of C values are not consistent with the universality as it was claimed in ref. [31].

Table 5.2: The values of multifractal specific heat C calculated from the G_q and T_q moment analysis of the $^{28}\text{Si-Ag/Br}$ data at 14.5A GeV.

Method employed	Experiment	UrQMD	UrQMD+BEC
Hwa's moments	0.0493±0.0076	0.00004±0.09055	0.0261±0.0074
Takagi's moments	0.1154±0.0598	0.1566±0.0371	0.0125±0.0371

5.4 Multifractal Detrended Fluctuation Analysis

The details of the multifractal detrended fluctuation analysis (MF-DFA) method is given in ref. [8], however for the sake of completeness we provide a brief description of this method in the following section.

Let $\{x_k : k = 1, 2, \dots, N\}$ be a fluctuating signal of length N . In our case x_k is nothing but the single particle η -density values in an event. The MF-DFA procedure consists of the following steps:

- (i) Determine a profile series through

$$Y(i) = \sum_{k=1}^i [x_k - \langle x \rangle], \quad i = 1, 2, \dots, N, \quad (5.21)$$

where $\langle x \rangle = (1/N) \sum_{i=1}^N x_i$ is the mean value of the signal to be analyzed.

- (ii) Divide the profile $Y(i)$ into $N_M = \text{int}(N/M)$ non-overlapping segments of equal length M . One has to choose the M value depending upon the signal length. If the length N is not a multiple of the considered scale M , then the same dividing procedure is repeated starting from the opposite end of the series. Hence, in order not to disregard any part of the signal, usually altogether $2N_M$ segments of equal length are obtained.
- (iii) Calculate the local trend for each of the $2N_M$ segments. This is done by least-square fits of the segments (or subseries). Linear, quadratic, cubic or even a higher order polynomial may be used to detrend the series, and accordingly the procedure is said to be the MF-DFA1, MF-DFA2, MF-DFA3, \dots analysis. Here we use a linear fit, and hence the detrended method is denoted as MF-DFA1. Let, y_ν be the best fitted polynomial to an arbitrary segment ν of the signal. Then determine the variance

$$F^2(\nu, M) = \frac{1}{M} \sum_{i=1}^M \{Y[(\nu-1)M + i] - y_\nu(i)\}^2 \quad (5.22)$$

for $\nu = 1, \dots, N_M$, and the same for $\nu = N_M + 1, \dots, 2N_M$ is given as

$$F^2(\nu, M) = \frac{1}{M} \sum_{i=1}^M \{Y[N - (\nu - N_M)M + i] - y_\nu(i)\}^2. \quad (5.23)$$

- (iv) The MF-DFA fluctuation function (moment) F_q is defined by averaging the variance $F^2(\nu, M)$ over all the $2N_M$ segments as,

$$F_q(M) = \left\{ \frac{1}{2N_M} \sum_{\nu=1}^{2N_M} [F^2(\nu, M)]^{q/2} \right\}^{1/q} \quad \forall q \neq 0, \quad (5.24a)$$

$$F_q(M) = \exp \left\{ \frac{1}{4N_M} \sum_{\nu=1}^{2N_M} \ln[F^2(\nu, M)] \right\} \quad \text{for } q = 0. \quad (5.24b)$$

In general, the order parameter q can take any real value.

- (v) Finally varying the scale parameter M , i.e. the phase space partition number, one can study the scaling behavior of the detrended fluctuation functions.

If the series $\{x_k\}$ possesses long-range correlation, $F_q(M)$ for large values of M would follow a power-law type of scaling relation, such as

$$F_q(M)|_{M \rightarrow \infty} \propto M^{h(q)} \quad \forall q. \quad (5.25)$$

The exponent $h(q)$, in general a function of q , is said to be the generalized Hurst exponent [8]. It follows that $h(2) = H$, the well known Hurst exponent. The series $\{x_k\}$ is considered

as long-range anti-correlated if $0 < H < 0.5$, uncorrelated if $H = 0.5$ and long-range correlated if $H > 0.5$. Although such a classification is based on the consideration that the signal $\{x_i\}$ is a stationary one, such as the fractional Gaussian noise (fGn) [32]. For non-stationary signals e.g., the fractional Brownian motion (fBm), H is related to $h(2)$ through $H = h(2) - 1$ and $h(2) > 1.0$ [33]. For a monofractal series $h(q)$ is independent of q since the variance $F^2(\nu, M)$ is identical for all the subseries, and hence Eq. (5.24) yields identical values for all q . Note that the function F_q can be defined only for $M \geq m + 2$, where m is the order of the detrending polynomial. Moreover, F_q is statistically unstable for very large M ($\geq N/4$). If small and large fluctuations scale differently, there will be a significant dependence of $h(q)$ on q . Whereas for positive values of q , F_q will be dominated by the large variance which corresponds to the large deviations from the detrending polynomial, for negative values of q major contributions of F_q arise from small fluctuations from the detrending polynomial. Thus, for positive (negative) values of q , $h(q)$ describes the scaling behavior of the segment with large (small) fluctuations. Note that the MF-DFA method is a kind of generalization of the detrended fluctuation analysis (DFA) [33], introduced to study the scaling properties of DNA sequences [33, 34]. For $q = 2$ the function defined in Eq. (5.24)(a) reduces to the ordinary DFA fluctuation function.

5.4.1 Relation with Standard Multifractal Variables

One can easily relate the $h(q)$ exponent with the standard multifractal exponent, such as the multifractal (mass) exponent $\tau(q)$. Suppose the series $\{x_k\}$ is stationary and normalized. Then the detrending procedure in step (iii) of the above methodology is not required. The variance of such a series is given by

$$F_N^2(\nu, M) = \{Y(\nu M) - Y[(\nu - 1)M]\}^2, \quad (5.26)$$

and the fluctuation function and its scaling-law would be

$$F_q(M) = \left\{ \frac{1}{2N_M} \sum_{\nu=1}^{2N_M} |Y(\nu M) - Y[(\nu - 1)M]|^q \right\}^{1/q} \sim M^{h(q)}, \quad \forall q. \quad (5.27)$$

Now if we assume that the length of the series N is an integer multiple of the partition number M , then the above relation can be rewritten as

$$\sum_{\nu=1}^{N/M} |Y(\nu M) - Y[(\nu - 1)M]|^q \sim M^{qh(q)-1}. \quad (5.28)$$

In the above relation the term under $|\cdot|$ is nothing but the sum of $\{x_k\}$ within an arbitrary ν th segment of length M . In the standard theory of multifractals it is known as the box probability $p(M, \nu)$ for the series $\{x_k\}$. Hence,

$$p(M, \nu) \equiv \sum_{k=(\nu-1)M+1}^{\nu M} x_k = Y(\nu M) - Y((\nu-1)M). \quad (5.29)$$

The multifractal scaling exponent $\tau(q)$ is defined through the partition function $Z_p(M)$ as

$$Z_p(M) \equiv \sum_{\nu=1}^{N/M} |p(M, \nu)|^q \sim M^{\tau(q)}, \quad (5.30)$$

where q is a real parameter. From Eq. (5.28) to Eq. (5.30) it is clear that the multifractal exponent $\tau(q)$ is related to $h(q)$ through the following relation

$$\tau(q) = q h(q) - 1. \quad (5.31)$$

After knowing $\tau(q)$ once again we can calculate the multifractal singularity spectrum: $f(\alpha) = q\alpha - \tau(q)$ and the generalized fractal dimension $D_q = \tau(q)/(q-1)$. Here $\alpha = \partial\tau/\partial q$ is the Lipschitz-Hölder exponent also known as the singularity strength parameter [23].

5.4.2 Results of Multifractal Detrended Fluctuation Analysis

As mentioned, the detrended method has been originally developed for the (multi)fractal characterization of the time series data of effectively infinite length. Here we apply the methods to the single event η distributions of particles produced in $^{28}\text{Si-Ag/Br}$ collision at 14.5A GeV. In our event sample the event-to-event multiplicity varies over a wide range, and there exists a large number of low multiplicity events where the detrended technique cannot be applied. Therefore, we impose a shower multiplicity cut of $n_s > 50$ that makes the average shower multiplicity $\langle n_s \rangle \sim 80$. Further, we have as many signals as the number of events present in the sample. Therefore we take an average of the single event MF-DMA fluctuation function $F_q^{(e)}$ over the event sample. In this way we actually study the average behavior of the detrended fluctuation functions i.e., $\langle F_q \rangle = (1/N_{ev}) \sum F_q^{(e)}$, and the scaling relation (5.25) reads as

$$\langle F_q \rangle|_{M \rightarrow \infty} \propto M^{h(q)} \quad \forall q. \quad (5.32)$$

Accordingly, the exponent $h(q)$ and other multifractal variables derived thereof are none other than their event space averaged values. We show the event averaged DFA fluctuation functions $\langle F \rangle = \langle F_{q=2} \rangle$ with phase space partition number M in Fig. 5.8 for (a) the experiment, (b) the UrQMD and (c) the UrQMD+BEC. In this analysis we vary M from

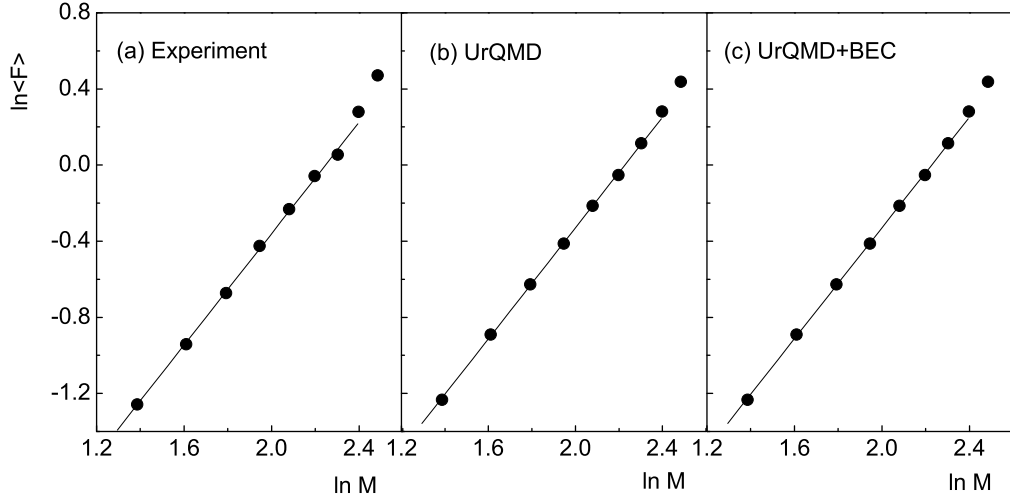


Figure 5.8: Event averaged DFA fluctuation functions $\langle F_{q=2} \rangle$ plotted with phase space partition number. The lines represent the best linear fits to the data points in the linear region.

Table 5.3: The values of the Hurst exponent H and the fractal dimension D_F calculated from the MF-DFA method for the $^{28}\text{Si-Ag/Br}$ interaction data at 14.5A GeV.

Parameter	Experiment	UrQMD	UrQMD+BEC	Random
H	1.463 ± 0.021	1.456 ± 0.019	1.450 ± 0.018	1.446 ± 0.017
D_F	0.537 ± 0.021	0.544 ± 0.019	0.550 ± 0.018	0.554 ± 0.017

4 to $n_s^{\min}/4$, where n_s^{\min} is the least multiplicity of the event sample (here $n_s \geq 50$). It is noticed that the data points are nicely reproduced by the scaling-law (5.32). The Hurst exponent H is evaluated from a straight line fit to the $\ln \langle F \rangle$ versus $\ln M$ data points in the region $4 \leq M \leq 10$, since a couple of points at large- M side slightly deviate from the initial linear trend. The H values are given in Table 5.3 for all the data sets. We repeat the analysis for a random number generated event sample, and the corresponding value of H is also put in the table. As mentioned earlier, the exponent H allows us to identify the type of correlation present in the signals. Accordingly, we argue that a long-range correlation may exist in all the cases studied. The values of fractal dimension (D_F) calculated from the H values are given in the same table. We know that for a fractal object $D_F < D_T$, the topological dimension of the supporting space (here unity), and the deviation of D_F from D_T is a measure of the degree of fractality. The results of the DFA analysis therefore, demand that the η -distribution for the $^{28}\text{Si-Ag/Br}$ interaction is highly fractal in nature.

We compute the event averaged MF-DFA1 fluctuation function $\langle F_q \rangle$ for $q = -5$ to 5 with an incremental step of 0.25. Some of them (for integer q only) are plotted against M in Fig. 5.9 for the experiment, UrQMD and UrQMD+BEC samples. Apparently we do not

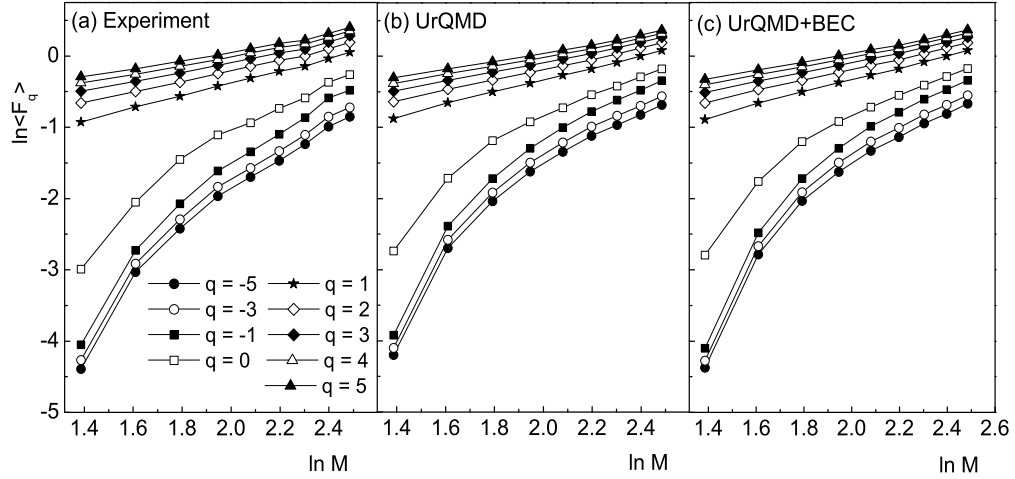


Figure 5.9: Event averaged MF-DFA1 fluctuation functions plotted with phase space partition number for integer $q \in [-5, +5]$ in $^{28}\text{Si-Ag/Br}$ interaction at 14.5A GeV. Lines joining points are drawn to guide the eye.

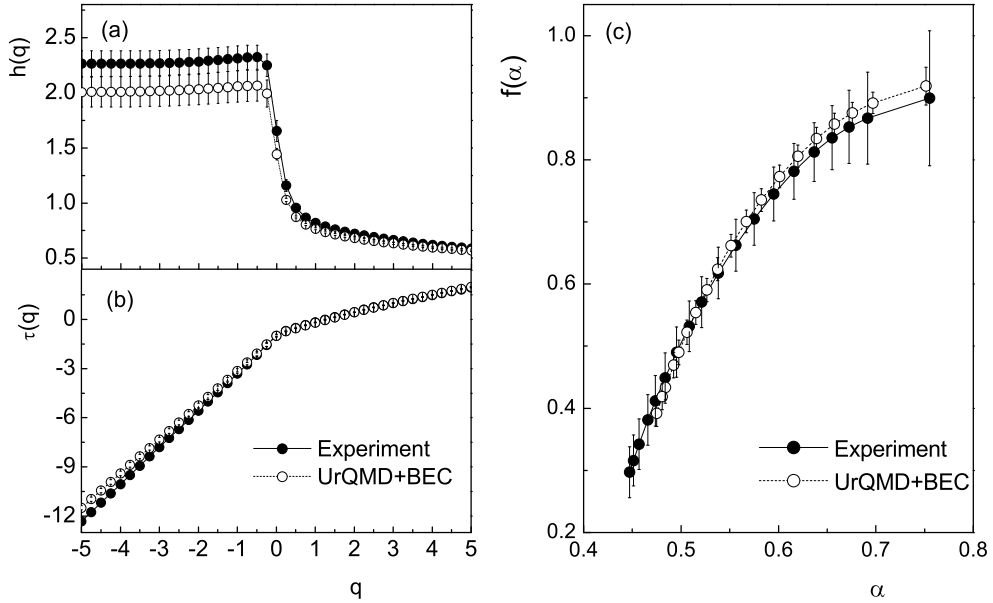


Figure 5.10: (a) Plot of $h(q)$ versus q , (b) $\tau(q)$ versus q , and (c) the singularity spectra $f(\alpha)$ obtained from the MF-DFA1 method. Lines joining points are shown.

find any difference between the experimental and the model simulated values of F_q . The scaling behavior of the $\langle F_q \rangle$ -functions are not linear over the entire scale range, especially for the $F_{q \leq 0}$ functions which are nonlinear in the low- M region. Therefore we compute $h(q)$ in the large- M region ($6 \leq M \leq 12$), where the scaling relation (5.25) holds satisfactorily. This is not a surprising phenomenon and the reason of which is already mentioned and also specified in Eq. (5.25). It is to be noted that unlike the G_q moments [Section 5.2] the detrended moments of this analysis are not influenced by the finiteness of the event multiplicity. The multifractal parameters, namely (a) the generalized Hurst exponents $h(q)$,

(b) the multifractal mass exponents $\tau(q)$ and (c) the singularity spectra $f(\alpha)$, measured from the MF-DFA1 fluctuation functions are shown in Fig. 5.10. We have dropped the UrQMD generated spectrum from this diagram since it almost coincides with the UrQMD+BEC plot. A number of observations can be made from this figure, which are: (i) $h(q)$ for $q \leq -1$ is approximately constant at ~ 2 , then it falls rapidly in the $q = -1$ to 1 region and tends to saturate at $h(q) \sim 0.5$ for $q \geq 1$, (ii) the $\tau(q)$ spectra are nonlinear, especially in the $q \approx 0$ region, (iii) the singularity spectra are smooth and nonlinear function of α and (iv) the difference between the experiment and UrQMD+BEC (and also UrQMD) simulation is insignificant. Since the $h(q < 0)$ values are approximately constant, all the $f(\alpha)$ values for $q < 0$ are assemble together around a fixed point that results in an unstable singularity spectrum for $q < 0$. A similar observation has also been made for a set of high multiplicity $^{32}\text{S-Ag/Br}$ event sample at 200A GeV [35]. Till date the MF-DFA technique has not been widely used in multiparticle data analysis, and therefore, we are not in a position to make a direct comparison of our results with similar other such analysis. In ref. [18] also the singularity spectrum for $q < 0$ has been found to be unstable. The MF-DFA method D_q values are compared with all the other methods of this analysis in Section 5.5.1.

5.5 Multifractal Detrended Moving Average Analysis

The multifractal detrended moving average (MF-DMA) analysis technique shares many ideas with the detrended fluctuation analysis, but an added advantage in the former method probably makes it more sophisticated over the latter one. The advantage in MF-DMA analysis is that it gives us the freedom to chose the location of the detrending window with respect to the measurement to be detrended. On the other hand, while in MF-DFA one can detrend the signal under consideration by a polynomial of desired order, in MF-DMA the signal has to be detrended only by the average value of the series. The MF-DMA analysis method is nicely described in ref. [9]. In the following subsection a brief outline of the method is itemized below. Like in the MF-DFA case let $\{x_i : i = 1, 2, \dots, N\}$ be a fluctuating signal of length N , which in our case is the single particle η -distribution function in an event. The MF-DMA procedure consists of the following steps.

- (i) Construct an integrated sequence

$$Y(i) = \sum_{k=1}^i [x_k - \langle x \rangle], \quad i = 1, 2, \dots, N \quad (5.33)$$

with respect to the mean $\langle x \rangle = (1/N) \sum_i x_i$. In the subsequent steps the above sequence is considered as the signal.

- (ii) Calculate the moving average function $\tilde{y}(i)$ in a moving window of size M through

$$\tilde{Y}(i) = \frac{1}{n} \sum_{k=-\lfloor (M-1)\theta \rfloor}^{\lceil (M-1)(1-\theta) \rceil} Y(i-k), \quad (5.34)$$

where $\lfloor \xi \rfloor$ is the largest integer not larger than ξ and $\lceil \xi \rceil$ is the smallest integer not smaller than ξ . Here θ is a parameter $\in [0, 1]$ that specifies the position of the moving window and it is said to be the window parameter. In general the moving average function includes $\lceil (M-1)(1-\theta) \rceil$ data points in the past and $\lfloor (M-1)\theta \rfloor$ data points in the future with respect to the point/variable to be detrended (say x_λ). Here we consider $\theta = 0.5$ for which the moving average function $\tilde{Y}(i)$ is equally extended on both sides of x_λ , and hence the moving window is said to be the ‘central moving’ window. Note that for $\theta = 0$ the moving average function $\tilde{Y}(i)$ is calculated over all the n data points in the past ($x_{k<\lambda}$), while for $\theta = 1$ the function is calculated over all the n data points in the future ($x_{k>\lambda}$), and accordingly the detrending windows are said to be the ‘backward moving’ and ‘forward moving’ windows, respectively.

- (iii) Detrend the sequence $Y(i)$ by subtracting $\tilde{Y}(i)$ and obtain the residue series,

$$e(i) = Y(i) - \tilde{Y}(i), \quad (5.35)$$

where i satisfies the criterion: $M - \lfloor (M-1)\theta \rfloor \leq i \leq N - \lfloor (M-1)\theta \rfloor$.

- (iv) Divide the series $e(i)$ into $N_n = \lfloor N/M - 1 \rfloor$ non-overlapping segments of equal length M . Let the segments are denoted by e_v so that $e_v(i) = e(l+i)$ for $1 \leq i \leq M$ and $l = (v-1)M$. For an arbitrary segment v the mean-square fluctuation function $\mathcal{F}_v^2(M)$ is calculated as a function of M ,

$$\mathcal{F}_v^2(M) = \frac{1}{M} \sum_{i=1}^M \{e_v(i)\}^2. \quad (5.36)$$

- (v) The overall q th order MF-DMA fluctuation function $\mathcal{F}_q(M)$ is then defined as,

$$\mathcal{F}_q(M) = \left\{ \frac{1}{N_n} \sum_{v=1}^{N_n} [\mathcal{F}_v^2(M)]^{q/2} \right\}^{1/q} \quad \forall q \neq 0, \quad (5.37a)$$

$$\mathcal{F}_q(M) = \exp \left\{ \frac{1}{2N_n} \sum_{v=1}^{N_n} \ln[\mathcal{F}_v^2(M)] \right\} \quad \text{for } q = 0. \quad (5.37b)$$

- (vi) The scaling behavior of $\mathcal{F}_q(M)$ is examined for a set of q exponents. If the signal $\{x_i\}$ contains multifractality (long-range correlation), $\mathcal{F}_q(M)$ for large values of M would

follow a power-law type of scaling relation, such as

$$\mathcal{F}_q(M)|_{M \rightarrow \infty} \propto M^{h(q)}, \quad (5.38)$$

and the exponent $h(q)$ known as the generalized Hurst exponent, would be a nonlinear function of q .

Knowing $h(q)$ once again we can calculate the multifractal scaling exponent $\tau(q)$, the multifractal singularity spectrum $f(\alpha)$, and the generalized multifractal dimensions D_q . The formulae are given in sub-section 5.4.1. Needless to mention that similar to the MF-DFA method here also we study the average behavior of the fluctuation function $\mathcal{F}_q(M)$, and the above scaling-law becomes

$$\langle \mathcal{F}_q \rangle |_{M \rightarrow \infty} \propto M^{h(q)}. \quad (5.39)$$

5.5.1 Results of Multifractal Detrended Moving Average Analysis

In Fig. 5.11 the event averaged MF-DMA ($\theta = 0.5$) fluctuation functions $\langle \mathcal{F}_q \rangle$ are plotted for $q = 0, \pm 2, \pm 5$ versus the phase space partition number M . Actually we have calculated the function $\langle \mathcal{F}_q(M) \rangle$ for all q values between -5 and $+5$ with an incremental step of 0.25 , but all of them are not shown in the diagram to maintain clarity. One can see that the scaling behavior of $\langle \mathcal{F}_q(M) \rangle$ is not linear over the entire region, especially not at low M , although the nonlinearity is not as prominent as it is in the case of the MF-DFA functions. Like the MF-DFA methods the MF-DMA method with $\theta = 0.5$ also produces visually identical variation of \mathcal{F}_q in both the simulated samples as the experiment, and therefore, we again drop the UrQMD results from the diagrams of our subsequent MF-DMA analysis. For a given q the exponent $h(q)$ is calculated from the log-log plot of the fluctuation function $\langle \mathcal{F}_q(M) \rangle$ in the large- M region. Here we take $8 \leq M \leq 18$, since the best linear behavior of the functions $\langle \mathcal{F}_q(M) \rangle$ is found in this region. The $h(q)$ values so obtained are plotted against q in Fig. 5.12(a), while the corresponding multifractal exponents $\tau(q) = qh(q) - 1$ are plotted in Fig. 5.12(b). It is seen that in the experiment the q dependence of both $h(q)$ and $\tau(q)$ values are stronger than the UrQMD+BEC (and also the UrQMD) generated values. Unlike the $h(q) - q$ plot of the MF-DFA method [see Fig. 5.10], here we obtain a smoothly varying $h(q)$ values for the experiment as well as for the simulations. The existence of a multifractal pattern in the particle density function can be conjectured for all the data samples studied. The calculated $h(q = 2)$ values are 0.619 ± 0.047 (Experiment) and 0.878 ± 0.039 (UrQMD+BEC). The parameter $h(2)$ indicates that the η -distributions are similar to the stationary time series signal for which $h(2) = H$, the ordinary Hurst exponent, and that the η -distribution functions have long-range correlation ($H > 0.5$). In

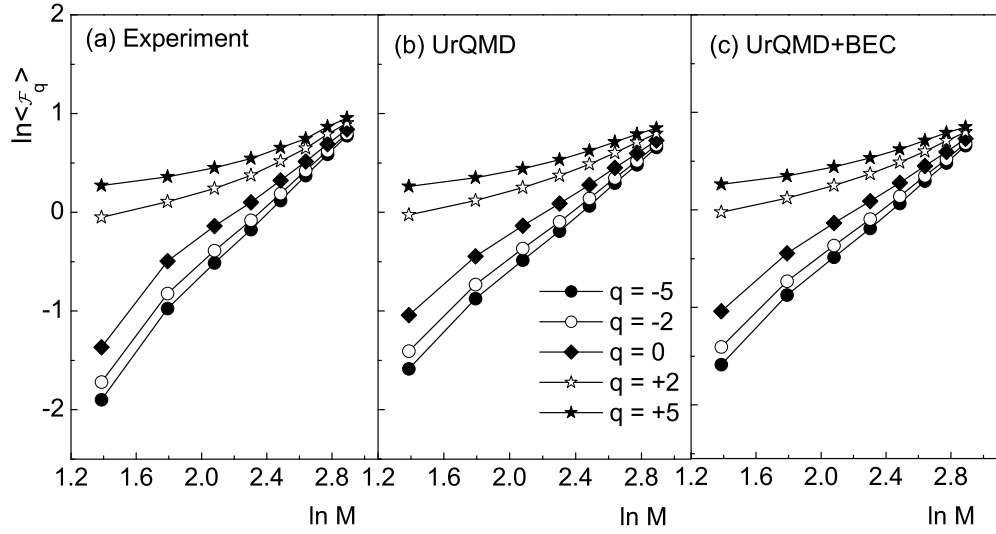


Figure 5.11: Event averaged MF-DMA ($\theta = 0.5$) fluctuation functions for the window parameter $\theta = 0.5$. Lines joining points are drawn to guide the eye.

diagram 5.12(c) we present the singularity spectra obtained from the MF-DMA technique. The $f(\alpha)$ spectra have a similar look as those obtained from the G_q moment analysis for the same set of data, but without any multiplicity cut as imposed in the detrended analysis. It is worth mentioning that the $f(\alpha)$ spectra of the MF-DFA technique are found to be unstable for $q < 0$. In contrast, the singularity spectra obtained in this method are smooth and bell-shaped functions of the Lipschitz-Hölder exponent α . A mismatch between the experiment and the UrQMD+BEC simulation, mainly at the low- α side of the spectra, is prominent. The difference originates from a mismatch between the corresponding $h(q)$ values. Another important observation of the diagram is that, the experimental spectrum is slightly right-skewed (skewness ≈ 0.052). Such an asymmetric $f(\alpha)$ spectrum implies that the pronounced multifractality appears from a small scale (noise like) fluctuation, while the dynamics of large scale fluctuation is much weaker in this respect [36]. This is not an unusual phenomenon in multiparticle data, since the coarse fluctuation pattern arises from a small scale statistical noise, whereas a small number of events may contribute with very large scale fluctuations due to one or more dynamical effects. As we know, the degree of multifractality is usually quantified by the width of the spectrum $W = \alpha_{\max} - \alpha_{\min}$ at $f(\alpha_{\max}) = f(\alpha_{\min}) = 0$. If the calculated $f(\alpha)$ spectrum does not extend up to $f(\alpha) = 0$, as it is the case here, then the spectrum is extrapolated by an appropriate function to obtain the values of α for which $f(\alpha) = 0$. From this analysis we find $W = 1.55$ (experiment) and 1.31 (UrQMD+BEC). This is a direct evidence that the multifractality present in the experiment is stronger than that of the simulation. One can mention here that the MF-DMA method has been adopted here in multiparticle data analysis probably for the first time, therefore we could not compare the results of this analysis with similar other analysis for different colliding nuclei and/or energy involved. However the MF-DMA results presented here show a gross similarity with

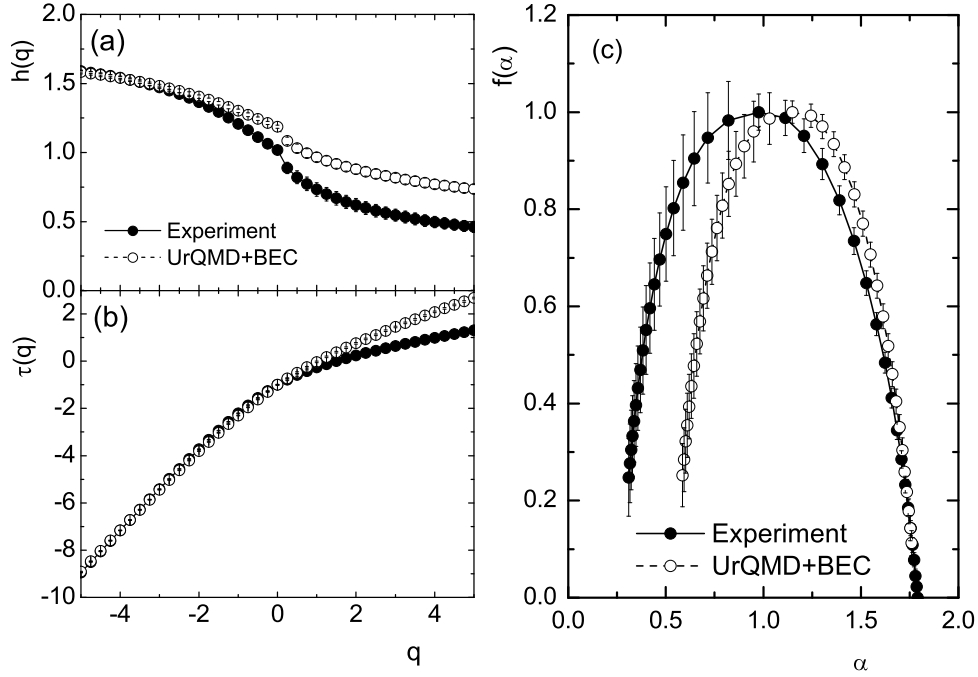


Figure 5.12: (a) Plot of $h(q)$ versus q , (b) $\tau(q)$ versus q , and (c) the singularity spectra obtained from the MF-DMA analysis with the window parameter $\theta = 0.5$. Line joining points are shown to guide the eye.

those obtained for a set of high multiplicity ($n_s \geq 150$) $^{32}\text{S-Ag/Br}$ events at 200A GeV [37]. In Fig. 5.13 the generalized fractal dimensions D_q are plotted against q . Following the trend we draw two separate diagrams, one for the experiment and another for the simulation. The D_q values obtained from all the other methods (G_q , T_q , SFM and MF-DFA) are included in the diagrams for an easy comparison. The D_q values measured from the conventional methods like G_q , T_q and SFM are all very close to the topological dimension of the supporting space. For the experiment all the D_q values decrease very slowly with increasing q , thereby indicating multifractality, whereas for the simulation the values are almost q independent. The detrended methods yield much smaller values of D_q over the interval $2 \leq q \leq 5$. According to the theory of fractals, the conventional G_q , T_q and SFM methods indicate the presence of a very low degree of multifractality in the data. The detrended methods contradict this observation and imply the existence of a strong multifractal structure of the data. Note that the SFM, G_q and T_q moment techniques are formulated particularly for the multiparticle data analysis, whereas the detrended method is formulated for the nonstationary time series data analysis. Therefore, the observed inconsistency between the detrended method and other conventional methods might be an outcome of the definitions of their moment generating functions, or it may so happen that the detrended method is not sensitive enough to the nature of fluctuation present in the multiparticle emission data, or the statistical component dominates the distribution to such an extent that in the detrended method it eventually suppresses the actual signal.

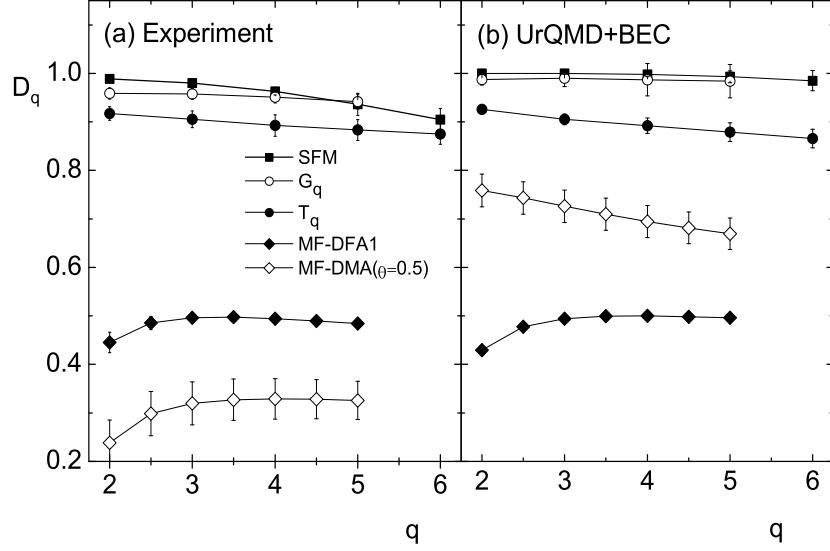


Figure 5.13: Generalized multifractal dimensions. The results of the MF-DMA (with $\theta = 0.5$) method are compared with those of the other methods. Lines joining points are drawn to guide the eye.

As mentioned, we have studied the event averaged values of the detrended multifractal variables. One can also extract the generalized Hurst exponent $h^{(e)}(q)$ from the single event detrended fluctuation function on an event-by-event basis, and can then take the average over the event sample [18], i.e.

$$\langle h(q) \rangle = \frac{1}{N_{ev}} \sum_{N_{ev}} h^{(e)}(q). \quad (5.40)$$

In this context we also study the difference between these two kinds of averaging of the $h(q)$ exponent, and find that the difference $\delta h(q) = h(q) - \langle h(q) \rangle$ marginally deviates from zero. That means, the detrended multifractal results presented here are not affected by one or the other averaging process adopted.

In the detrended analysis we select only the high multiplicity events with a multiplicity cut of $n_s \geq 50$. So the statistics of the samples reduce significantly, and it might influence the multifractal results. Therefore, we study the effects of the sample size on the results presented here. To do that, we consider a random number generated sample of 10,000 events. The multiplicity and pseudorapidity distributions of this sample are identical to those of the experiment (with a multiplicity cut $n_s > 50$). We calculate the generalized Hurst exponent $h^{\text{rand}}(q)$ for the random number generated sample. The big sample is thereafter divided into ten smaller equal sized subsamples (1000 events in each) and the analysis is repeated for each of them. It is found that for the smaller subsamples the $h^{\text{rand}}(q)$ values do not differ significantly (less than 6%) from each other as well as from the estimated value of the overall sample. In addition we have verified the sample size effect in the UrQMD+BEC generated

events. For this we divide the UrQMD+BEC sample, which is five times the experimental one, into five equal sized subsamples and redo the analysis individually for each of them. From this analysis also we have not noticed any substantial difference in the individual $h(q)$ values from those of the original UrQMD+BEC event sample. The entire exercise implies that the detrended multifractal results presented here are not significantly affected by the size of the sample statistics. Probably the key operation acting behind such a sample size independence of the multifractal exponent $h(q)$ is the averaging over the event sample. It is worth noting that in the case of time series data analysis the detrended multifractal results are quite sensitive to the length of the signal to be analyzed [8, 20].

5.6 Discussion

To summarize, we have presented some results on multifractal analysis of singly charged particles produced in $^{28}\text{Si-Ag/Br}$ interactions at 14.5A GeV. Specifically, we provide a multifractal characteristics of the pseudorapidity distribution of produced singly charged particles. Following the trend of our analysis the experimental results are systematically compared with a set of model simulation. The data behave expectedly and the results are consistent with those obtained from similar other experiments on AB interactions. The observations of this analysis can be summarized in the following way.

The multifractal moments introduced by Hwa [5] follow a scale invariant power-law and scale with diminishing phase space resolution size. The trend of the UrQMD+BEC (or UrQMD) simulated results are almost identical to the experiment. The intermittency results on the same sets of data, however, behave differently for the experiment and the simulations. Whereas, the self-similar nature of the $1d$ intermittency of the density fluctuation observed previously [21] is the primary motivation of the present work, where we have observed that the differences between experiment and simulations lie not in the scaling pattern of the multifractal moments, but in the quantitative aspects of the scaling parameters and in the derivatives thereof. The nature of multifractal mass exponent $\tau(q)$ or the Lipschitz-Hölder exponent α for the experiment cannot be distinguished from the simulations. The parameters themselves are probably not very sensitive to the nature of the fluctuation (statistical or dynamical) present in the data. However, when the statistical contribution is properly taken care of, we observe that within experimental uncertainties, the intermittency exponents ϕ_q overlap with the corresponding multifractal parameter (i.e., $q - 1 - \tau^{\text{dyn}}(q)$). A small but definite departure from the simulations can be traced into the experiment, and the deviation slightly diminishes when BEC is incorporated into the UrQMD data. The multifractal spectrum, consistent in all aspects with its expected behavior, has a slightly smaller width in the UrQMD generated curve than that of the experiment and of the UrQMD+BEC. Therefore,

the multifractal spectrum might be considered as a sensitive variable that can distinguish the dynamical contribution from the statistical noise in the density fluctuation.

The stability index μ associated with the log-Lévy distribution is an important parameter that needs to be mentioned separately. Our intermittency analysis for the same sets of data resulted in a μ value that is way beyond its stability limit. In this analysis we have adopted a method based on the multifractal spectral function and, irrespective of the data set used, we have obtained different μ values in different q -regions. The estimated values of μ in the low- q region are consistent with the observation of our intermittency analysis, though the values are far above the upper acceptable limit $\mu = 2$ [24, 25]. However, in the high- q region the experimental μ value within errors is very close to the upper limit of the parameter. In any case the simulated values of μ deviate the experimental values to a large extent. Hence in the present case a log-Lévy distribution can not appropriately describe the multiplicity fluctuation.

Takagi's multifractal moments also exhibit expected power-law type of scaling behavior. Though Takagi's technique has a few advantages over Hwa's technique of analysis, the T_q moments are contaminated by statistical noise. This limitation is reflected in the multifractal parameters derived by using this method. The experimental D_q values obtained from the T_q moments are not significantly different from the corresponding simulated values. This is not true either for the factorial moment or for Hwa's moments, where the statistical noise has been taken care of at some level of analysis. However, a systematic deviation in D_q from the topological dimension which increases with order number, is an indication of the presence of multifractality in the single particle density distribution. The parameter D_q , unlike $\tau(q)$ and α , is found to be sensitive to the nature of fluctuation. The variation of D_q with $\ln q/(q-1)$ is consistent with the thermodynamic interpretation of the monofractal to multifractal phase transition, though the magnitude of specific heat does not corroborate any kind of universality as claimed in [31].

The detrended fluctuation functions for all the analyzed data also scale in a manner as expected from a multifractal system. The $h(q)$, $\tau(q)$ and $f(\alpha)$ obtained from the MF-DFA and MF-DMA analysis also confirm the presence of multifractality both in the experiment as well as in the simulations. The nature of these spectra and the estimated values of the Hurst exponent demand that the origin of fractality may be two, three or higher order particle correlation. The MF-DFA/MF-DMA prediction of the generalized fractal dimensions are consistently lower than that of the SFM method, Hwa's method and Takagi's method, the discrepancies being $\sim 50\%$. We also notice that except for the singularity spectrum and to a small extent the D_q values, within the error margins the experimental detrended multifractal parameters are not significantly different from the simulated values. The observations signify that the detrended technique like the other previously used techniques, is either probably

not sufficiently sensitive to the self-similar nature of fluctuation present in the data, or they lack an appropriate noise elimination technique. A reliable method of filtering out the statistical noise from the detrended fluctuation moments should therefore, be formulated to make the technique more effective.

Bibliography

- [1] B. B. Mandelbrot, *The Fractal Geometry of Nature* (New York, Freeman, 1977).
- [2] G. Paladin and A. Vulpiani, *Phys. Rep.* **156**, 147 (1987).
- [3] P. Grassberger, I. Procaccia, *Physica* **D 13**, 34 (1984).
- [4] T. C. Halsey *et al.*, *Phys. Rev.* **A 33**, 1141 (1986).
- [5] R. C. Hwa, *Phys. Rev.* **D 41**, 1456 (1990); *Phys. Rev.* **D 51**, 3323 (1995).
- [6] R. C. Hwa and J. Pan, *Phys. Rev.* **D 45**, 1476 (1992).
- [7] F. Takagi, *Phys. Rev. Lett.* **72**, 32 (1994).
- [8] J. W. Kantelhardt *et al.*, *Physica* **A 316**, 87 (2002).
- [9] G.-F. Gu and W.X. Zhou, *Phys. Rev.* **E 82**, 011136 (2010).
- [10] W. Florkowski and R. C. Hwa, *Phys. Rev.* **D 43**, 1548 (1991).
- [11] C. B. Chiu and R. C. Hwa, *Phys. Rev.* **D 43**, 100 (1991).
- [12] C. Albajar *et al.* (UA1 Collaboration), *Z. Phys.* **C 56**, 37 (1992).
- [13] I. Derado, R. C. Hwa G. Jansco and N. Schmitz, *Phys. Lett.* **B 283**, 151 (1991).
- [14] E. A. De Wolf, I. M. Dremin and W. Kittel, *Phys. Rep.* **270**, 1 (1996);
W. Kittel and E. A. De Wolf *Soft Multihadron Dynamics* (World Scientific, 2005).
- [15] M. I. Adamovich *et.al.* (EMU01 Collaboration), *Europhys. Lett.* **44**, 571 (1998).
- [16] D. Ghosh *et. al.*, *Phys. Rev.* **C 70**, 054903 (2004);
M. K. Ghosh, A. Mukhopadhyay and G. Singh, *J. Phys.* **G 32**, 2293 (2006);
S. Ahmad *et al.*, *J. Phys.* **G 32**, 1279 (2006); *Nucl. Phys.* **A 780**, 206 (2006).
- [17] J. Kwapień, P. Oświecimka and S. Drózdź, *Physica* **A 350**, 466 (2005);
E. Koscielny-Bunde *et al.* *J. Hydrology* **322**, 120 (2006);
S. Drożdź *et al.*, *New Journal of Physics* **12**, 105003 (2010);
N. Cardenas, S. Kumar and S. Mohanty, *Appl. Phys. Lett.* **101**, 203702 (2012);
P. Mali, A. Mukhopadhyay, *Physica* **A 413**, 361 (2013); *Phys. Scr.* **90**, 035209 (2015);
P. Mali, *Theor. Appl. Climatol.*, **121**, 641 (2015).
- [18] Y. X. Zhang, W. Y. Qian and C. B. Yang, *Int. J. Mod. Phys.* **A 23**(18), 2809 (2008).
- [19] Y. Wang, C. Wu and Z. Pan, *Physica* **A 390**, 3512 (2011);
F. Wang, L. Wang and R.-B. Zou, *Chaos* **24**(3), 033127 (2014).

- [20] P. Mali, *J. Stat. Mech.* 013201 (in press, 2016).
- [21] P. Mali, A. Mukhopadhyay and G. Singh, *Can. J. Phys.* **89**, 949 (2011).
- [22] P. Mali, A. Mukhopadhyay and G. Singh, *Acta Phy. Pol.* **B 43**, 463 (2012).
- [23] J. Feder, *Fractals* (Plenum Press, New York, 1988).
- [24] Ph. Brax and R. Peschanski, *Phys. Lett.* **B 253**, 255 (1991).
- [25] W. Ochs, *Z. Phys.* **C 50**, 339 (1991).
- [26] S. Hegyi, *Phys. Lett.* **B 318**, 642 (1993).
- [27] A. Bialas and R. Peschanski, *Nucl. Phys.* **B 308**, 857 (1988).
- [28] W. Ochs, *Phys. Lett.* **B 247**, 101 (1990).
- [29] Y. Hu, M. Yu and L. Liu, *Chin. Phys. Lett.* **16**, 553 (1999).
- [30] H. G. E. Hentschel and I. Proccacia, *Physica* **D 8**, 435 (1983).
- [31] A. Bershadski, *Phys. Rev.* **C 59**, 364 (1999).
- [32] C. V. Chianca, A. Ticona and T.J.P. Penna, *Physica* **A 357**, 447 (2005).
- [33] C. -K. Peng *et al.*, *Phys. Rev.* **E 49**, 1685 (1994).
- [34] S. M. Ossadnik *et al.*, *Biophys. J.* **67**, 64 (1994).
- [35] P. Mali, S. Sarkar, S. Ghosh, A. Mukhopadhyay, G. Singh, *Physica* **A 424**, 25 (2015).
- [36] S. Drożdż, P. Oświęcimka, *Phys. Rev.* **E 91**, 030902(R) (2015).
- [37] P. Mali, A. Mukhopadhyay and G. Sing, *Physica* **A** (in press, 2016).

Chapter 6

Azimuthal Structure of Particle Distribution in Relativistic Nucleus-Nucleus Collisions

6.1 Introduction

It is now confirmed that the experimental data on $^{28}\text{Si-Ag/Br}$ interaction at 14.5A GeV contain rapid fluctuations of produced particle multiplicity in the pseudorapidity space, which goes beyond the trivial statistical noise. The most important reason of the observed fluctuation as advocated in refs. [1–3], is the Bose-Einstein Correlation (BEC) between identical bosons. Another probable reason that has recently drawn the interest of several heavy-ion research groups is the emission of Cherenkov gluons [4, 5], or the formation of Mach shock waves [6–8] within the partonic/nuclear medium. In either case the resulting wavefront bears a conical structure, which is characterized by a semi-vertex angle α given by

$$\cos \alpha = \frac{v_{\text{med}}}{v} = \frac{v_0}{\mu v}. \quad (6.1)$$

Depending upon the case as it may be, $v_{\text{med}} = v_0/\mu$ is either the velocity of the gluons or that of the shock wave in the nuclear/partonic medium, v_0 is the velocity of the gluons or the

velocity of the elastic wave in free space, μ is the refractive index of the medium concerned and v is the velocity of the partonic jet that triggers the Cherenkov gluon emission or the shock wave in the nuclear/partonic medium. In this formalism an impinging nucleus is treated as a bunch of confined partons, each of which is capable of emitting the Cherenkov gluons while traversing through a target medium. Under favorable circumstances if the conical structure of the Cherenkov wavefront can withstand the impact of collision, the consequence will be reflected in the azimuthal distribution of the final state particles [5, 9]. In this process if the number of emitted gluons is large, and if each of them generates a minijet, then a ‘ring-like’ structure of final state mesons distributed over the entire target azimuth may appear. On the other hand for a moderate number of emitted gluons, only a few jets are expected and the corresponding pattern is said to be a ‘jet-like’ structure. Similar azimuthal structures may also result due to the formation of nuclear shock waves as the impinging projectile nucleons travel with a speed greater than that of the elastic waves through the nuclear medium. Whatever may be the reason, the phenomenon still largely speculative in nature, and so far it is investigated without taking the BEC effect into consideration [5, 10–17].

In the recent past we have reported an analysis on the azimuthal structure of charged particles in AB collisions at 200A GeV [18]. In ref. [18] two different data sets [$^{32}\text{S-Ag/Br}$ and $^{16}\text{O-Ag/Br}$] are used and the experiment is compared merely with a random number based simulation. Jet-like structures are found in the experimental data. In the present work we present similar analyses for the $^{28}\text{Si-Ag/Br}$ interaction at 14.5A GeV. The analysis also encompasses $^{32}\text{S-Ag/Br}$ data at 200A GeV for a ready reference and systematic comparison. Following the trend of our analysis, the experiments are compared with the UrQMD. In addition to UrQMD we also consider the Relativistic Quantum Molecular Dynamics (RQMD) models [19] for comparison. In both simulations Bose-Einstein correlation is incorporated as an after burner. The simulation technique is elaborated in Section 2.5 of Chapter 2. The primary motivation of this analysis is to eliminate the known cause(s) of particle cluster formation so that any discrepancy between the experiment and the simulation can be regarded as a genuine signal of some nontrivial dynamics. For $E_{\text{lab}} = 14.5\text{A GeV}$ the equivalent nucleon-nucleon (NN) center of mass energy is $\sqrt{s_{NN}} = 5.39\text{ GeV}$ and $E_{\text{lab}} = 200\text{A GeV}$ corresponds to $\sqrt{s_{NN}} = 19.4\text{ GeV}$. Thus, in our data sets the target-projectile combinations are almost of same geometrical size, but the collision energy involved ($\sqrt{s_{NN}}$) differs almost by a factor of four. We therefore, get a chance to examine the energy dependence of the effects to be investigated. The number of participating nucleons in the central collisions is more and therefore it is more likely that unnatural angular structures (if any) will be observed in central collisions.

6.2 Methodology

Without claiming any originality whatsoever, we furnish below the methodology adopted in the present analysis as elaborated in ref. [11]. Accordingly, an event with a shower track multiplicity n_s is first divided into several subgroups (or clusters) each containing a fixed number of shower tracks, say n_d . Each n_d -tuple of particles (tracks) are thereafter consecutively placed along the η -axis in increasing order of their η values. A cluster is characterized by the following quantities,

$$(i) \quad \text{a size } \Delta\eta = \eta_{\max} - \eta_{\min}, \quad (6.2a)$$

$$(ii) \quad \text{a density } \rho = n_d / \Delta\eta, \quad (6.2b)$$

$$(iii) \quad \text{a mean } \eta_m = \sum_{i=1}^{n_d} \eta_i / n_d. \quad (6.2c)$$

Here, η_{\max} (η_{\min}) is the largest (smallest) η value in the particle subgroup (cluster). Since all clusters characterized by the above parameters pertain to same multiplicity n_d , they are statistically comparable with each other. For a similar analysis Gogiberidze *et al.* [20] used a different approach where instead of fixed cluster multiplicity, fixed cluster size $\Delta\eta$ was used. Two other parameters expressed in terms of the azimuthal angle φ of the shower tracks are also used to identify the jet/ring-like structures. They are,

$$S_1 = - \sum_{i=1}^{n_d} \ln(\Delta\varphi_i) \quad \text{and} \quad S_2 = \sum_{i=1}^{n_d} (\Delta\varphi_i)^2, \quad (6.3)$$

where $\Delta\varphi_i = \varphi_{i+1} - \varphi_i$ is the azimuthal gap between successive particles in the target diagram belonging to a particular cluster/subgroup, starting from the first and second, followed by second and third \dots , so on, ultimately ending at the last and the first. For simplicity one can measure $\Delta\varphi_i$ in the unit of a full revolution (2π) of φ . For an ideal ring-like structure the tracks will be concentrated within a narrow η interval but isotropically distributed over the whole azimuth, while for an ideal jet-like structure the tracks will be concentrated into small dense groups within a narrow region of both η and φ . To make things clear a schematic representation of the target azimuth of an ideal ring/jet-like structure is given in Fig. 6.1. The ‘ S -parameters’ and the cluster density ρ will decide whether the structures are ring-like or jet-like. On the other hand, the cluster mean η_m and the cluster size $\Delta\eta$ help us to identify respectively, the location and the size (a measure of correlation length) of the clusters. From the definition of the S -parameters it is clear that while S_1 is sensitive to small gaps, S_2 is sensitive to large ones. In that respect S_1 and S_2 are complementary to each other. For an ideal jet-like emission $S_1 \rightarrow \infty$ and $S_2 \rightarrow 1$, and for an ideal ring-like distribution $S_1 \rightarrow n_d \ln n_d$ and $S_2 \rightarrow 1/n_d$. For a purely stochastic emission

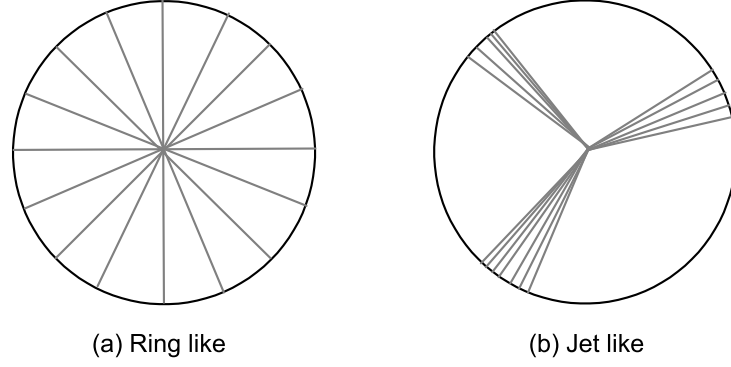


Figure 6.1: Schematic diagrams of an ideal (a) ring-like and (b) jet-like structure in the target azimuth.

of particles the $\Delta\varphi$ -distribution is expected to be

$$f(\Delta\varphi) = (n_d - 1)(1 - \Delta\varphi)^{(n_d-2)}, \quad (6.4)$$

and under such a circumstance the expectation values of the S -parameters evaluated analytically are

$$\langle S_1 \rangle = n_d \sum_{k=1}^{n_d-1} \frac{1}{k} \quad \text{and} \quad \langle S_2 \rangle = \frac{2}{n_d + 1}. \quad (6.5)$$

Distributions of S_1 and S_2 parameters would be peaked around their respective stochastic expectation values. Presence of ring-like structures are reflected as an excess observed in the experiment over the respective stochastic distribution in a region left to the stochastic mean. On the other hand, for jet-like structures such excess counts would occur in a region right to the stochastic mean. A schematic of the normalized S_2 distributions of Gaussian form expected from three different processes are illustrated in Fig. 6.2. In this figure the distributions marked by 1, 2 and 3 represent, respectively the ring-like, the stochastic and the jet-like effects. The solid curve is the combined distribution of all the three individuals. Therefore, in order to extract information about the unusual azimuthal structure(s), one needs to subtract the contribution coming out of the stochastic phenomena. In this analysis the stochastic process is mimicked by using two sets of Monte-Carlo simulations, namely the RQMD and the UrQMD, both supplemented by BEC in the form of an after burner.

6.3 Results

We examine the average as well as the event-wise behavior of both S -parameters introduced above. However, in ref. [11] it is argued that to identify a jet/ring-like structure S_2 is a

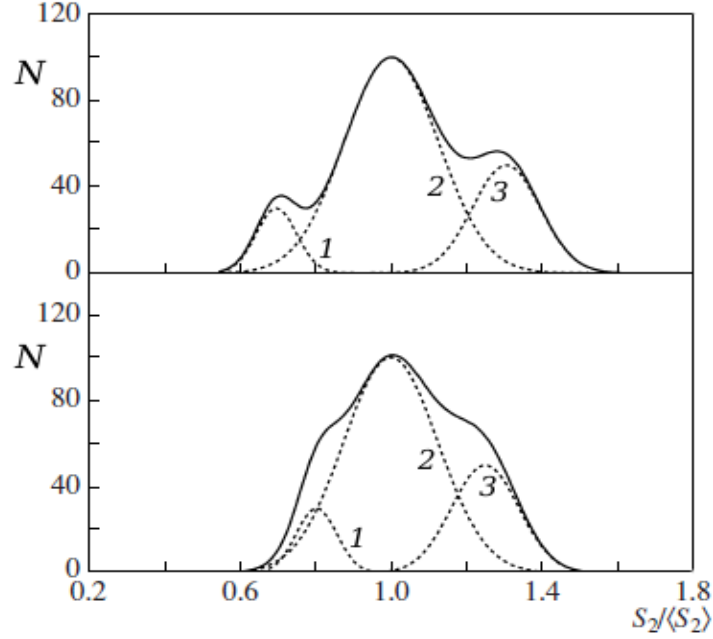


Figure 6.2: A schematic of $S_2/\langle S_2 \rangle$ distributions from three effects, namely (1) ring-like effect distribution, (2) stochastic distribution and (3) jet-like effect distribution. The solid curve represents the resultant distribution.

better choice than S_1 . An analysis on the cluster properties similar to that of ours, was performed by Vokál *et al.* in Pb-Ag/Br interaction at 158A GeV [16]. They found that for the high multiplicity events the effects of any unusual azimuthal structure is almost independent of the choice of the n_d value, while for the low multiplicity events such effects diminish with increasing n_d . The result of Vokál *et al.* [16] in this regard is shown in Fig. 6.3. In the present study only high multiplicity events are chosen, the multiplicity cuts taken are $n_s > 50$ for the ^{28}Si data and $n_s > 200$ for the ^{32}S data. We have checked that within the range, $10 \leq n_d \leq 25$ for the ^{28}Si -Ag/Br interaction and $25 \leq n_d \leq 50$ for the ^{32}S -Ag/Br interaction, our results depend only insignificantly on the choice of n_d . Therefore, throughout our ‘ring-jet’ analysis we set the subgroup multiplicity n_d to 15 for the ^{28}Si -Ag/Br interaction and to 40 for the ^{32}S -Ag/Br interaction. For this choice of the n_d values, the stochastic expectation values for the ^{28}Si -events are $\langle S_1 \rangle = 48.773$ and $\langle S_2 \rangle = 0.125$, while those for the ^{32}S -events are, respectively $= 170.142$ and $= 0.049$ [see Eq. (6.5)]. As a first test, we normalize the S parameters by their respective stochastic values ($\langle S_1 \rangle$ and $\langle S_2 \rangle$) and plot the histograms for two different AB interactions under consideration. Fig. 6.4 is drawn for the ^{28}Si -induced events, whereas Fig. 6.5 is for the ^{32}S -induced events. For comparison the corresponding RQMD+BEC and UrQMD+BEC predictions on the S -parameters are also schematically presented along with the experiment. The S -parameter distributions of ^{28}Si -Ag/Br interaction are slightly right skewed with respect to the corresponding stochastic mean values. As expected we find that the RQMD+BEC and the UrQMD+BEC

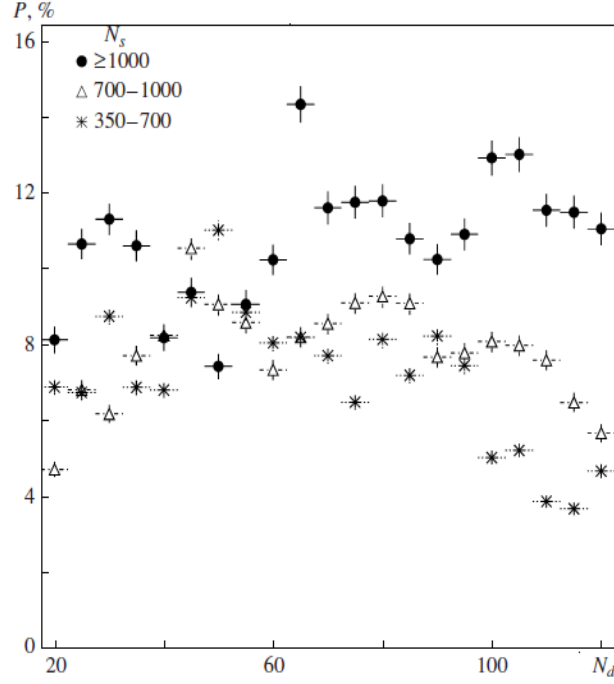


Figure 6.3: Contribution of the ring-like effect to the experimental data on $^{208}\text{Pb-Ag/Br}$ interaction at 158A GeV/c as a function of the number of particles in a subgroup (N_d) for three different multiplicity groups [16].

distributions are marginally different from their experimental counterparts. In each case the difference between the experiment and the simulation is shown in the respective diagram with the help of shaded histograms drawn around the S -axis. We notice that in both cases there exist small experimental excesses in the left to the stochastic mean, i.e., to the jet side. In comparison with experiment the differences are larger in RQMD+BEC simulation. For the $^{32}\text{S-Ag/Br}$ interaction the S -distributions once again are right skewed. The skewness however, is less in this case than the $^{28}\text{Si-Ag/Br}$ interaction. For $^{32}\text{S-Ag/Br}$ interaction the difference between experiment and simulation, once again shown by shaded histograms, lack any definite pattern and their magnitudes are smaller than the $^{28}\text{Si-Ag/Br}$ case. Beyond statistical uncertainties such differences are of little significance. It is to be remembered that an experimental excess in $S_i/\langle S_i \rangle < 1$ (> 1) : $i = 1, 2$ region indicates ring (jet) like structures. Based on the S -parameter distributions we can therefore, say that in the $^{32}\text{S-Ag/Br}$ data there is hardly any indication of an unusual structure, whereas in $^{28}\text{Si-Ag/Br}$ data there is a small signal of ring-like structures. In a similar analysis of the Pb+Ag/Br data at 158A GeV and Au-Ag/Br data at 11.6A GeV [16, 17], experimental excesses over their respective FRITIOF model [21] predictions were obtained in the S_2 -distributions on either side of $S_2/\langle S_2 \rangle = 1$. It is to be remembered that for overlapping η -intervals strong correlations between particles belonging to different sub-groups will be present, and this will certainly influence the statistical errors. One way to estimate the statistical uncertainties

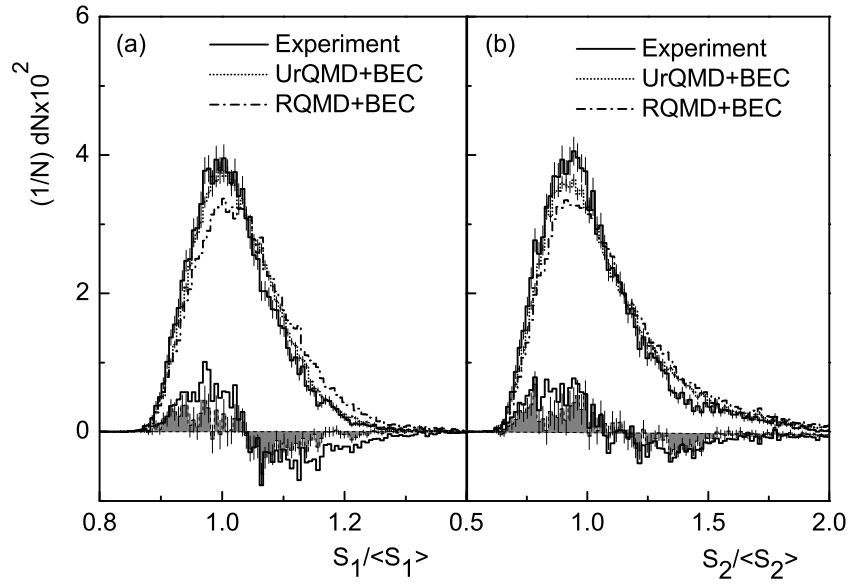


Figure 6.4: Distributions of (a) the S_1 and (b) the S_2 parameters normalized by their respective stochastic values in $^{28}\text{Si-Ag/Br}$ interaction at 14.5A GeV.

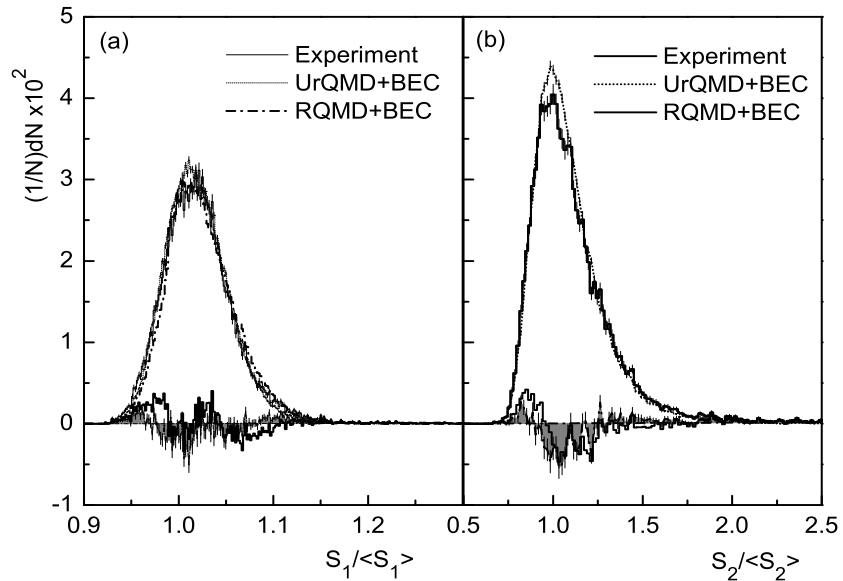


Figure 6.5: Same as Fig. 6.4 but in $^{32}\text{S-Ag/Br}$ interaction at 200A GeV.

in such cases is to generate several independent sets of data based on random numbers that are similar in size, multiplicity, η and φ distributions as the experiment. One can then determine the dispersion or the standard deviation of the parameter/quantity under consideration over the number of generated data sets. The statistical errors obtained in this way can be made free from the influence of such correlations. It may also be mentioned that the problem of γ -conversion and the resulting e^+e^- tracks getting mixed up with the pion tracks can influence our observation. However, this effect is more acute in vertically exposed emulsion chambers. In horizontally exposed emulsion experiments such as the present one,

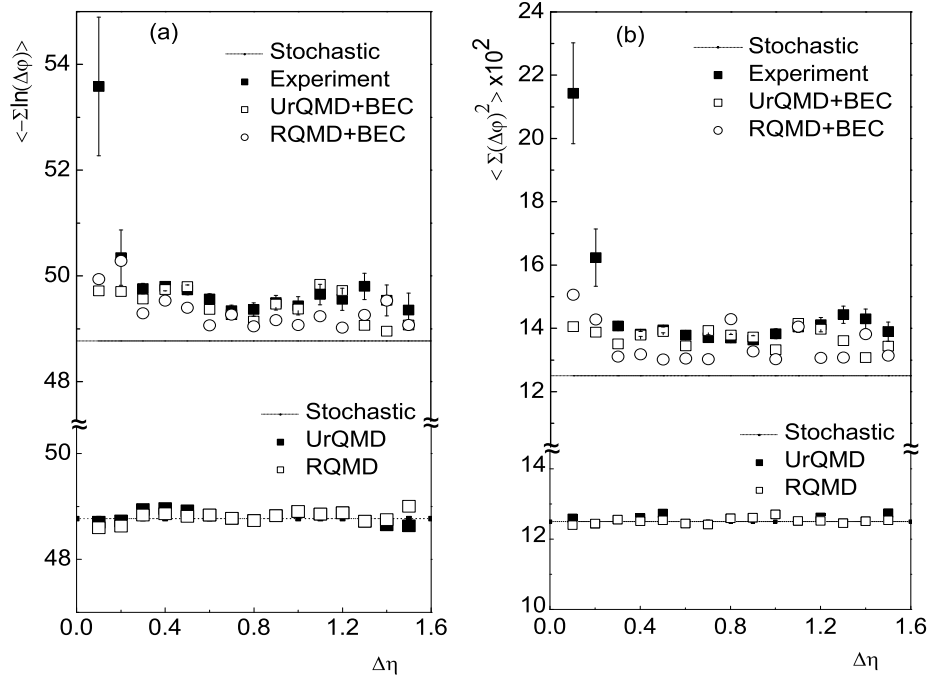


Figure 6.6: Average behavior of (a) the S_1 parameter and (b) the S_2 parameter in ^{28}Si -Ag/Br interaction at 14.5A GeV. Horizontal dashed lines follow Eq. (6.5). The effect of the BEC algorithm is shown in the bottom panel.

it is possible to follow every track back to its production point. Hence the e^+e^- pairs arising out of γ -conversion (if there is any) can easily be traced back to their point of origin which will certainly be different from the primary interaction vertex. Moreover, production of direct gamma is less in the energy range considered. The contamination by e^+e^- pairs is therefore, insignificant in the present investigation.

Following ref. [11] we also study the average behavior of the S -parameters over a small η -interval ($\Delta\eta$). The average values are given by,

$$\bar{S}_1 = \left\langle -\sum \ln(\Delta\varphi_i) \right\rangle \quad \text{and} \quad \bar{S}_2 = \left\langle \sum (\Delta\varphi_i)^2 \right\rangle, \quad (6.6)$$

where $\langle \dots \rangle$ indicates event averaging. These average values are graphically presented as functions of $\Delta\eta$ in Fig. 6.6 and Fig. 6.7, respectively, for the ^{28}Si -Ag/Br and ^{32}S -Ag/Br events. In both figures panel (a) represents \bar{S}_1 while panel (b) represents \bar{S}_2 . In each diagram the dashed lines correspond to the respective stochastic averages obtained from Eq. (6.5). The RQMD+BEC and UrQMD+BEC predictions are also incorporated in these diagrams. From these figures it is seen that the RQMD+BEC and UrQMD+BEC predictions are systematically but consistently a little above the corresponding stochastic line, indicating a positive effect of incorporating BEC into the code. If we do not incorporate BEC then both the RQMD and the UrQMD points overlap with the stochastic lines. This feature is graphically shown at the bottom of each of the diagrams (Fig. 6.6 and Fig. 6.7), indicating thereby

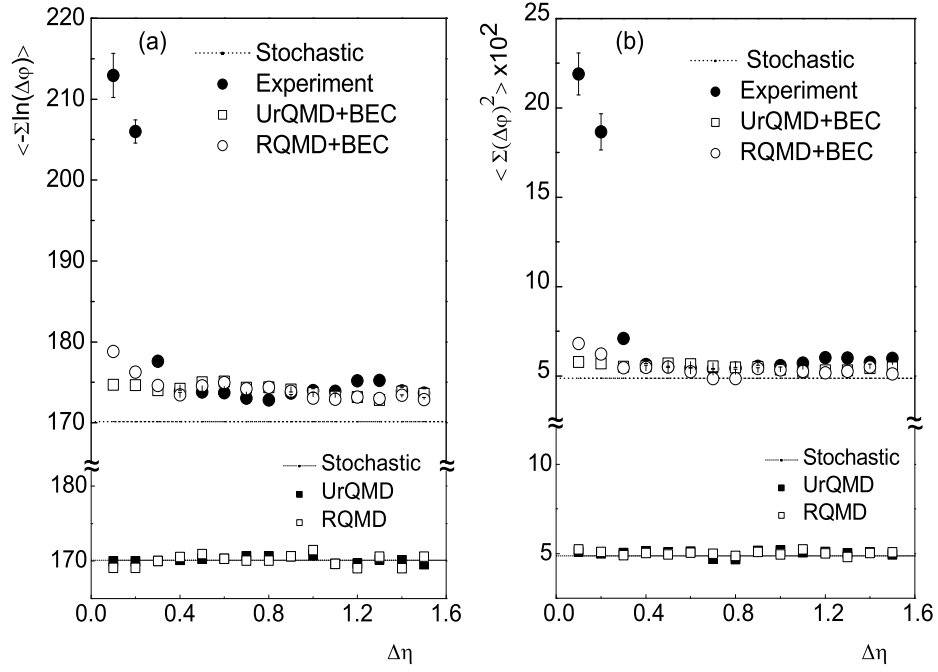


Figure 6.7: Same as Fig. 6.6 but in $^{32}\text{S-Ag/Br}$ interaction at 200A GeV.

absence of any correlation whatsoever among the emitted mesons. The important aspect of these diagrams is that the first one or two experimental points (up to $\Delta\eta \approx 0.2 - 0.3$) are significantly way above all the other values, and beyond $\Delta\eta \approx 0.2 - 0.3$ the experiments are always very close to the respective simulated values. In the $^{32}\text{S-Ag/Br}$ interaction the simulated results beyond $\Delta\eta \approx 0.3$ are almost always overlapping with each other, and both are closer to the stochastic line than what they are in the $^{28}\text{Si-Ag/Br}$ case. The first two or three experimental points (up to $\Delta\eta \approx 0.2 - 0.3$) also show significant deviation from the RQMD, RQMD+BEC, UrQMD, UrQMD+BEC, and the stochastic prediction. The observation confirms that short range particle correlations other than the Bose-Einstein type, are present in both the experiments. We further examine whether the contributions to the experimental excesses in the average S values within a small $\Delta\eta$ ($\approx 0.1 - 0.3$), are coming from a small η region or they are distributed over the entire η space under consideration. For this purpose the average S - parameters are now plotted as functions of both $\Delta\eta$ and η_m . Only the experimental distributions are shown in Fig. 6.8 and Fig. 6.9, respectively, for the $^{28}\text{Si-Ag/Br}$ and $^{32}\text{S-Ag/Br}$ interactions. To our surprise, we notice that while the average S_1 values are more or less uniformly distributed over a wide η range, there are very prominent peaks in the average S_2 distributions. The peaks are located within $1.0 \leq \eta_m \leq 2.0$ in the $^{28}\text{Si-Ag/Br}$ case and within $3.0 \leq \eta_m \leq 4.0$ in the $^{32}\text{S-Ag/Br}$ one. Both sets of data behave similarly, and the peaks in both cases are more or less located around the central particle producing regions. Whatever may be the reason, the results suggest that to detect any unusual structure, S_2 is indeed a better parameter than S_1 [11]. In Fig. 6.10 we

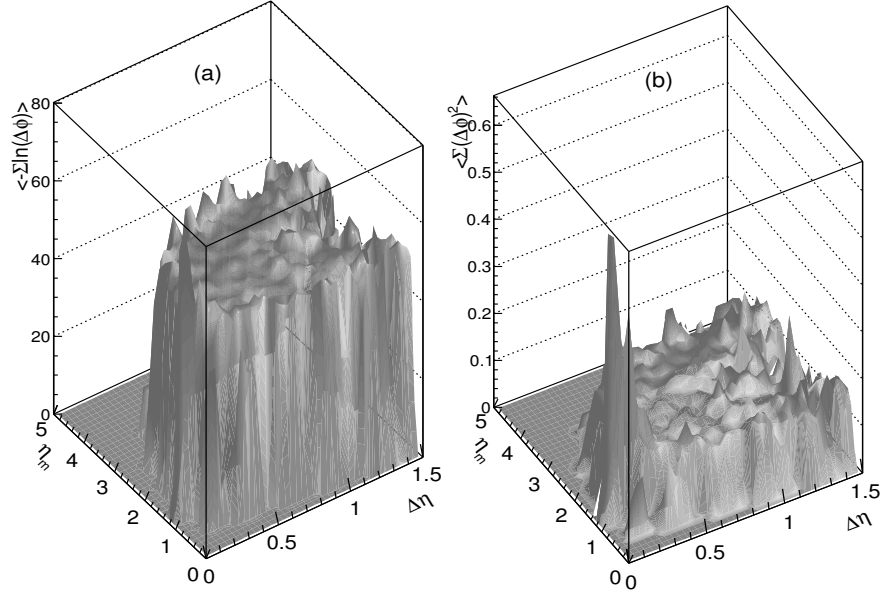


Figure 6.8: Plot of (a) $\langle -\sum \ln(\Delta\varphi) \rangle$ and (b) $\langle \sum (\Delta\varphi)^2 \rangle$ as a function of $\Delta\eta$ and η_m in $^{28}\text{Si-Ag/Br}$ interaction at 14.5A GeV.

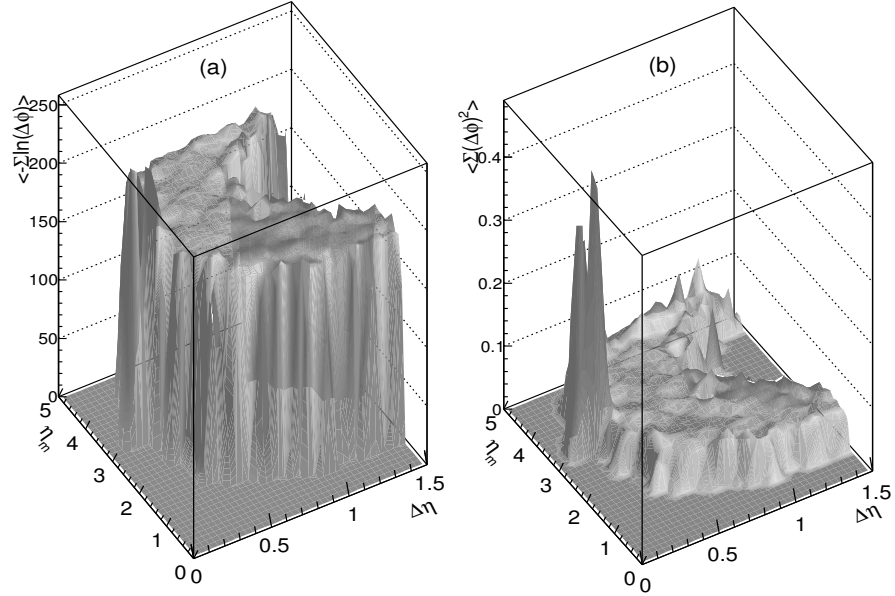


Figure 6.9: Same as Fig. 6.8 but in $^{32}\text{S-Ag/Br}$ interaction at 200A GeV.

plot the cluster density distributions for the $^{28}\text{Si-Ag/Br}$ events, like before for the experiment as well as for the simulated data. Fig. 6.10(a) represents the regions which should be dominated by the ring-like structure, $S_2/\langle S_2 \rangle < 1$, and Fig. 6.10(b) represents the regions which should be dominated by the jet-like structures, $S_2/\langle S_2 \rangle > 1$. Similar plots for the $^{32}\text{S-Ag/Br}$ events are shown in Fig. 6.11. While both the $^{28}\text{Si-Ag/Br}$ diagrams are slightly

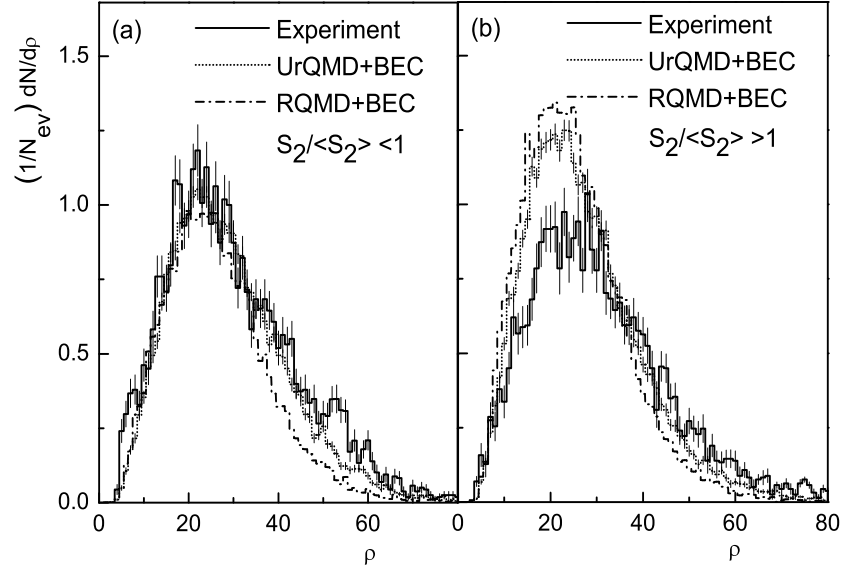


Figure 6.10: Cluster density distributions for (a) the ring-like region, $S_2/\langle S_2 \rangle < 1$ and (b) the jet-like region, $S_2/\langle S_2 \rangle > 1$ in $^{28}\text{Si-Ag/Br}$ interaction at 14.5A GeV.

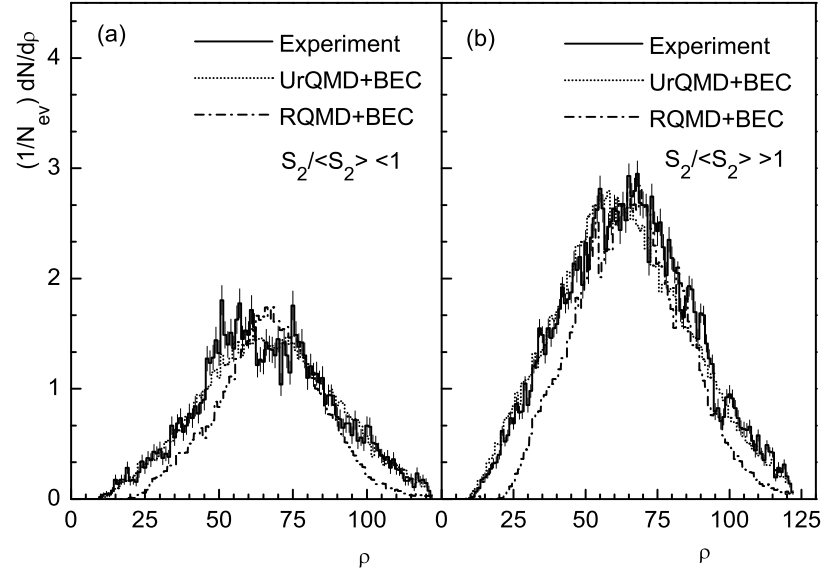


Figure 6.11: Same as Fig. 6.10 but in $^{32}\text{S-Ag/Br}$ interaction at 200A GeV.

right skewed, the $^{32}\text{S-Ag/Br}$ diagrams are more symmetric. If dense groups of particles are present in these data samples, then an excess experimental count over the background noise should have appeared. Occasional differences between the experiment and the simulation are seen in all diagrams. In Fig. 6.10(a) these differences are statistically not very significant. Even in Fig. 6.11(a) the experimental excesses over the simulation are not too large. Differences between experiment and RQMD+BEC are more than those between the

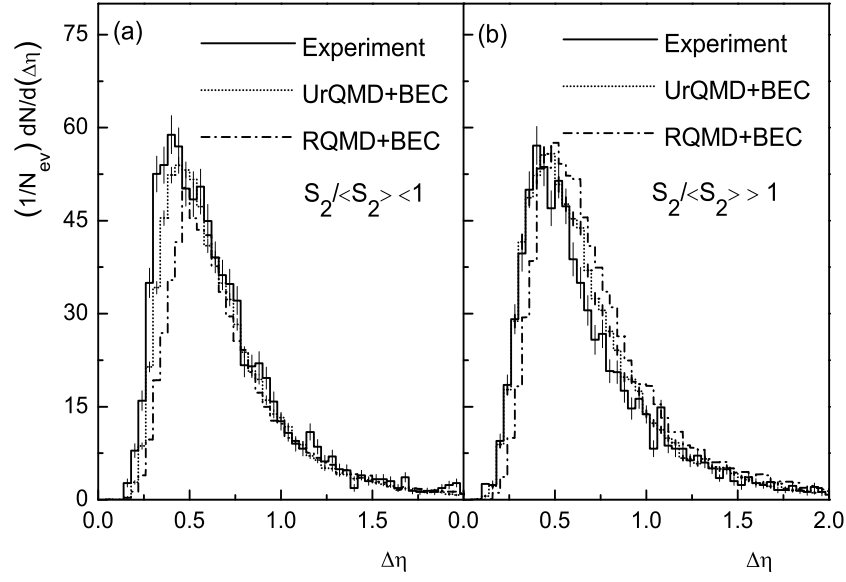


Figure 6.12: Cluster size distributions for (a) the ring-like region, $S_2/\langle S_2 \rangle < 1$ and (b) the jet-like region, $S_2/\langle S_2 \rangle > 1$ in $^{28}\text{Si-Ag/Br}$ interaction at 14.5A GeV.

experiment and the UrQMD+BEC. The results are consistent with our previous observations [18]. To have an idea about the cluster size, we plot the $\Delta\eta$ distributions in Fig. 6.12 and Fig. 6.13, respectively, for the $^{28}\text{Si-Ag/Br}$ and the $^{32}\text{S-Ag/Br}$ data samples. As usual, separate graphs are plotted for regions that should be dominated by the ring-like and the jet-like structures. We notice that all these distributions are asymmetric (right skewed). In the ^{28}Si -induced experiment significant excesses over the simulation are seen in the region that should be dominated by ring-like structures ($S_2/\langle S_2 \rangle < 1$) particularly in the left to the peak (small $\Delta\eta < 0.5$) of the distribution. For $S_2/\langle S_2 \rangle > 1$ the experiment is either well reproduced or the UrQMD+BEC simulation exceeds the experiment. In $^{32}\text{S-Ag/Br}$ events a very narrow and sharp experimental excess is observed in the distribution at $\Delta\eta \approx 0.5$ for $S_2/\langle S_2 \rangle < 1$. While in the probable jet-like region ($S_2/\langle S_2 \rangle > 1$) there is a broader and significant experimental excess over the simulation in and around the peak of the distribution ($0.5 \leq \Delta\eta \leq 0.7$). Barring a very narrow and sharp structure around $\Delta\eta \approx 0.5$ observed in Fig. 6.12(a), all other observations are consistent with our previous results which are, (i) mild effects due to ring-like structure in the $^{28}\text{Si-Ag/Br}$ interaction at 14.5A GeV, (ii) effects due to jet-like structures in $^{32}\text{S-Ag/Br}$ interaction at 200A GeV, and (iii) differences between the experiment and RQMD+BEC are consistently larger than those between the experiment and the UrQMD+BEC. The cluster position on the η -axis is investigated by plotting the η_m -distributions. For the $^{28}\text{Si-Ag/Br}$ interaction, these distributions are shown in Fig. 6.14, and similar plots for the $^{32}\text{S-Ag/Br}$ interactions are given in Fig. 6.15. The experimental distributions are more or less consistently symmetric about a mean value $\eta_m \approx 2$

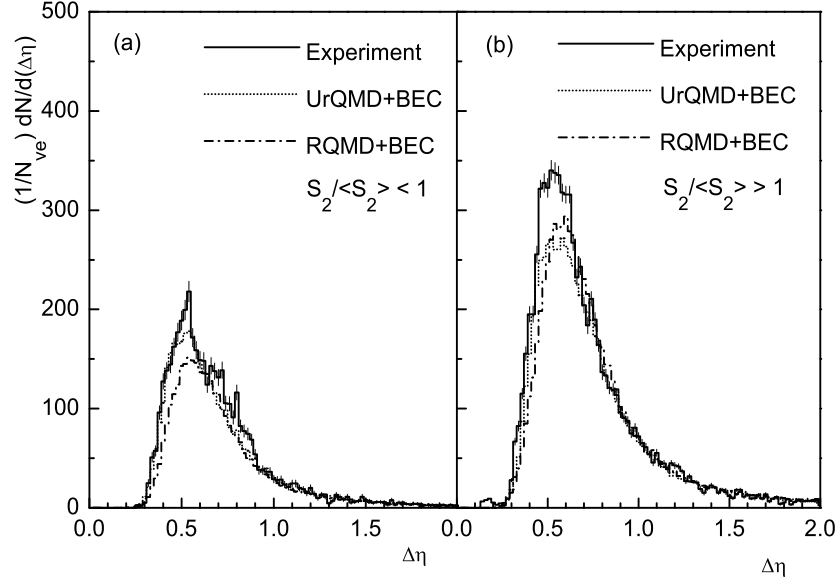


Figure 6.13: Same as Fig. 6.12 but in ^{32}S -Ag/Br interaction at 200A GeV.

for the ^{28}Si -Ag/Br events and about $\eta_m \approx 3.25$ for the ^{32}S -Ag/Br events. To separate azimuthal structure(s) originating due to different reasons, following ref. [16] we use a little more stringent conditions e.g., (i) $S_2/\langle S_2 \rangle < 0.9$ due only to the ring-like structures, (ii) $0.9 < S_2/\langle S_2 \rangle < 1.1$ due to the statistical effects, and (iii) $S_2/\langle S_2 \rangle > 1.1$ due only to the jet-like structures. For ^{28}Si -Ag/Br events we see that (i) in the η_m -distribution the region that should be dominated by ring-like structures ($S_2/\langle S_2 \rangle < 0.9$) at a couple of places e.g., at $\eta_m \approx 1.5$ and 2.2 , the experiment significantly exceeds the UrQMD+BEC simulation. For $0.9 < S_2/\langle S_2 \rangle < 1.1$ the experiment and the simulation more or less match each other within statistical uncertainties. On the other hand, for $S_2/\langle S_2 \rangle > 1.1$ except at the extreme right hand side tail ($\eta_m > 3.6$) the simulation either matches or dominates over the corresponding experimental values. For the ^{32}S -Ag/Br interaction in $S_2/\langle S_2 \rangle < 0.9$ region small experiment-simulation mismatch can be seen at several places. They are however, statistically not very significant. In the $0.9 < S_2/\langle S_2 \rangle < 1.1$ region there are experimental excesses over the simulation in the central η_m -region, the reason of which may probably be attributed to the limited statistics of the experiment. In the $S_2/\langle S_2 \rangle > 1.1$ region there are however significant experimental surplus over the simulation at several places, which indicate presence of jet-like structures at different η_m -locations. We notice that in this case also the RQMD+BEC results either underestimate the experiment, or they behave similarly as the UrQMD+BEC results.

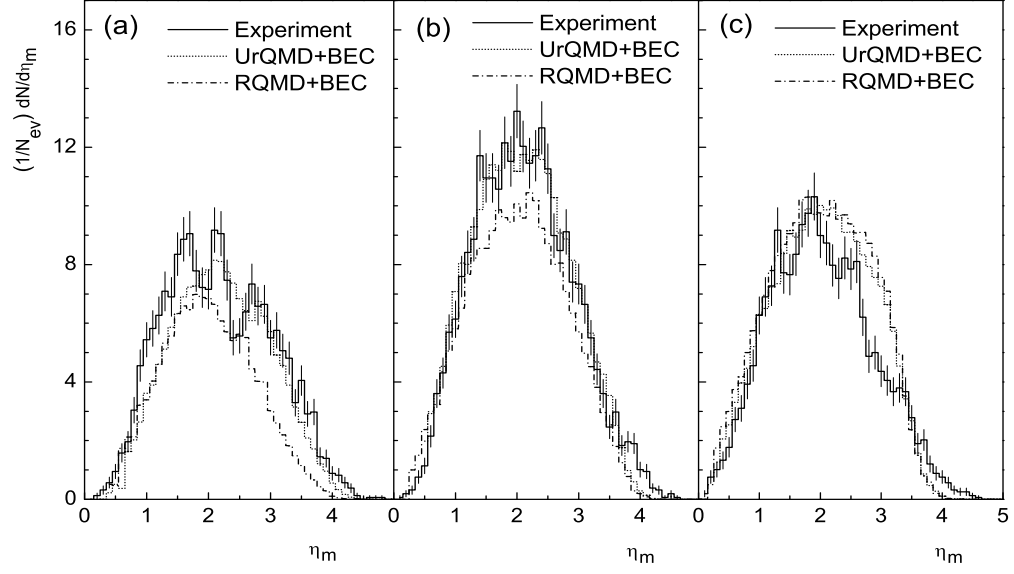


Figure 6.14: Cluster mean η_m distributions for (a) $S_2/\langle S_2 \rangle < 0.9$, (b) $0.9 < S_2/\langle S_2 \rangle < 1.1$ and (c) $S_2/\langle S_2 \rangle > 1.1$ in $^{28}\text{Si-Ag/Br}$ interaction at 14.5A GeV.

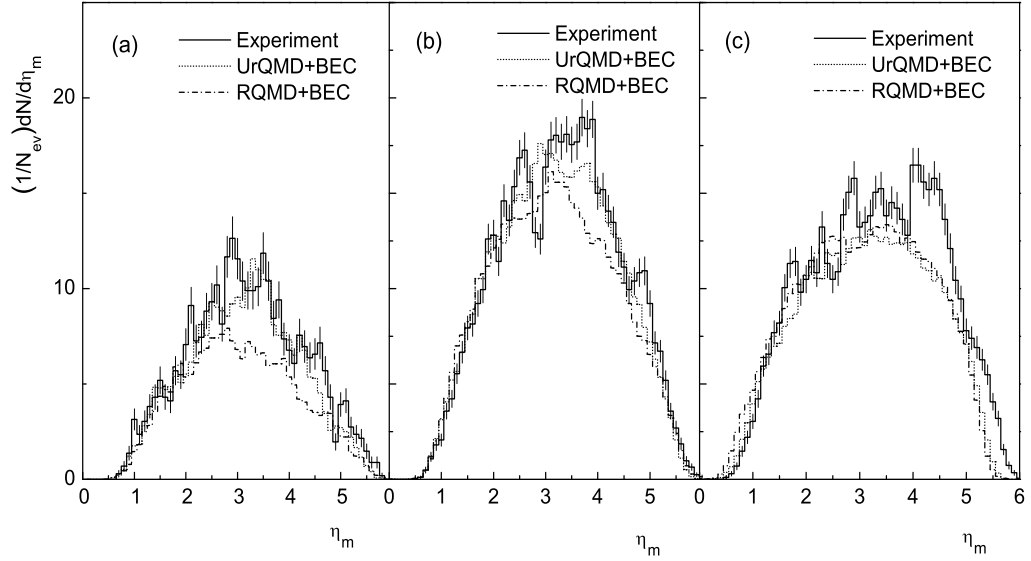


Figure 6.15: Same as Fig. 6.14 but in $^{32}\text{S-Ag/Br}$ interaction at 200A GeV.

6.4 Discussion

The azimuthal substructures of shower track emission from $^{28}\text{Si-Ag/Br}$ interaction at 14.5A GeV and from $^{32}\text{S-Ag/Br}$ interaction at 200A GeV are investigated under the framework of the Cherenkov gluon emission and/or the Mach shock wave formation. The experimental results are compared with the RQMD and the UrQMD models where the Bose-Einstein correlation effect has also been taken into account as an after burner. In general we find

that there are occasional but statistically significant differences between the experiment and the simulation. In comparison with the experiment, the RQMD model differs more than the UrQMD. A brief discussion on our results obtained from the present analysis is given below.

We conjecture that at $E_{\text{lab}} \sim 10^1 - 10^2$ GeV/nucleon, the probability of formation of ring and/or jet-like clusters is small. At this energy scale the phenomenon is not very much energy dependent, rather it depends more on the colliding objects [11, 16–18]. In $^{28}\text{Si-Ag/Br}$ interaction at 14.5A GeV an indication of, however small it may be, ring-like structure is observed. The feature may be attributed to the comparatively lower incident energy, where the conical structure if formed during the initial stage of the collision, has probably survived the impact of collision. On the contrary in $^{32}\text{S-Ag/Br}$ interaction at 200A GeV there are indications of augmentation of jet-like structures, which is not very unusual. From our analysis we can at least claim that, whatever may be the reason (nuclear or partonic) behind the signals that we see in our experiments, they are beyond any known dynamics such as the Bose-Einstein correlation. In particular the prominent short range structures in the average S parameter values that we find in the central particle producing region (Fig. 6.8 and 6.9), are certainly due to some nontrivial reasons. With all probability at incident energies $E_{\text{lab}} \sim 10 - 200\text{A}$ GeV nuclear phenomenon like formation of Mach shock waves, rather than partonic effects (e.g., Cherenkov gluon emission) dominates. In our $^{28}\text{Si-Ag/Br}$ data we see small peaks at certain η_m values in the ring-like region ($\eta_m \approx 1.5$ and 2.2). Similarly in the $^{32}\text{S-Ag/Br}$ data significant excesses in the η_m distribution are seen in the jet region, at $\eta_m \approx 3.0$ and 4.5 . With the knowledge of the velocity distribution of the nucleon/partonic jet in the nuclear/partonic medium, it would be a worthwhile exercise to estimate the speed of sound wave/refractive index in nuclear/partonic matter, either of which can serve significant purpose to constrain the nuclear equations of state.

Bibliography

- [1] P. Carruthers *et al.*, *Phys. Lett.* **B 222**, 487 (1989).
- [2] K. Kadiza and P. Seyboth, *Phys. Lett.* **B 287**, 363 (1992).
- [3] M. Gyulassy and L. van Hove, in *Multiparticle Dynamics*, Eds. A. Giovannini and W. Kittel (World Scientific, Singapore, 1990).
- [4] I. M. Dremin, *Pis'ma Zh. Eksp. Teor. Fiz.* **30**, 152 (1979) [*JETP Lett.* **30**, 140 (1979)].
- [5] I. M. Dremin, *Yad. Fiz.* **33**, 1357 (1981) [*Sov. J. Nucl. Phys.* **33**, 726 (1981)].
- [6] J. Hofmann *et al.*, *Phys. Rev. Lett.* **36**, 88 (1976).
- [7] A. E. Glassgold, W. Heckrotte, and K. M. Watson, *Ann. Phys.* **6**, 1 (1959).

- [8] J. G. Ulery, *J. Phys.* **G 35**, 104032 (2008).
- [9] I. M. Dremin, *Pis'ma Zh. Eksp. Teor. Fiz.* **34**, 594 (1981).
- [10] A. B. Apanasenko *et al.*, *Pis'ma Zh. Eksp. Teor. Fiz.* **30**, 157 (1979) [*JETP Lett.* **30**, 145 (1979)].
- [11] M. I. Adamovich *et al.* (EMU01 Collaboration), *J. Phys.* **G 19**, 2035 (1993).
- [12] A. El-Naghy and K. S. Abdel-Khalek, *Phys. Lett.* **B 299**, 370 (1993).
- [13] N. M. Agababyan *et al.* (NA22 Collaboration), *Phys. Lett.* **B 389**, 397 (1996).
- [14] S. Wang *et al.*, *Phys. Lett.* **B 427**, 385 (1998).
- [15] I. M. Dremin *et al.*, *Phys. Lett.* **B 499**, 97 (2001).
- [16] S. Vokál *et al.*, *Proceedings of the Hadronic Structure* (Slovakia, 2004);
S. Vokál *et al.*, *Phys. Atom. Nucl.* **71**, 1395 (2008).
- [17] S. Vokál, G. I. Orlova, and S. Lehocká, *Phys. Atom. Nucl.* **72**, 237 (2009).
- [18] M. K. Ghosh *et al.*, *Nucl. Phys.* **A 858**, 67 (2011).
- [19] H. Sorge, *Phys. Rev.* **C 52**, 3291 (1995);
H. Sorge *et al.*, *Ann. Phys.* **192**, 266 (1989); *Nucl. Phys.* **A 498**, 567c (1989).
- [20] G. L. Gogiberidze *et al.*, *Phys. Atom. Nucl.* **64**, 143 (2001);
G. L. Gogiberidze, E. K. Sarkisyan, and L. K. Gelovani, *Nucl. Phys.*, **B 92**, 75 (2001).
- [21] B. Nilsson-Almqvist and E. Stenlund, *Comp. Phys. Commun.* **43**, 387 (1987).

Chapter 7

Wavelet Analysis in Relativistic Nucleus-Nucleus Collisions

7.1 Introduction

The fundamental idea behind the wavelets is to analyze a distribution according to scale. Wavelets are functions that satisfy certain mathematical requirements and are used to represent data or other functions. Approximation methods using superposition of functions has existed since the early 1800's, when Joseph Fourier discovered that he could superpose sines and cosines to represent other functions. However, in wavelet analysis the scale that we use to analyze data plays a special role. Wavelet algorithms process data at different scales or resolutions. If we look at a signal with a large 'window' we would notice only its gross features, while if we look at the signal with a small window, we would notice its finer structures. Thus, while using wavelets, one is actually adopting an entirely new mindset or perspective in processing data. The result in wavelet analysis is to see both the forest and the trees, so to speak. This makes wavelets interesting and useful. In order to approximate choppy signals for many years scientists have wanted more appropriate functions than the sines and cosines, which comprise the bases of Fourier analysis [1]. By their definition, the sine and cosine functions are non-local. Therefore, Fourier transform does not seem to be a good approximation for a choppy (sharp spiky) signal. But wavelets are well-suited for approximating data

with sharp discontinuities. With wavelet analysis we can use approximating functions that are contained neatly in finite domains. The wavelet analysis procedure is to adopt a wavelet prototype function, called an *analyzing wavelet* or *mother wavelet*. Temporal analysis is performed with a contracted–high-frequency version of the prototype wavelet, while frequency analysis is performed with a dilated–low-frequency version of the same wavelet. Because the original signal/function can be represented in terms of a wavelet expansion using coefficients in a linear combination of the wavelet functions, while data operations can be performed using just the corresponding wavelet coefficients. If one further chooses the best (mother) wavelet to analyze the data, or truncates the expansion coefficients below a threshold, the data are sparsely represented [2]. This sparse coding makes wavelet analysis an excellent tool in the field of data compression. As for an example, we show in Fig. 7.1 the goodness of the wavelet denoising technique, where a pair of ‘before’ and ‘after’ illustrations of a nuclear magnetic resonance (NMR) signal are shown. The technique works in the following way. When you decompose a data set using wavelets, you use filters that act as *averaging* filters and others that produce *details*. Some of the resulting wavelet coefficients correspond to details in the data set. If the details are small, they might be omitted without substantially affecting the main features of the data set. Then the idea of thresholding is to set to zero all coefficients that are less than a particular threshold. These coefficients are used in an inverse

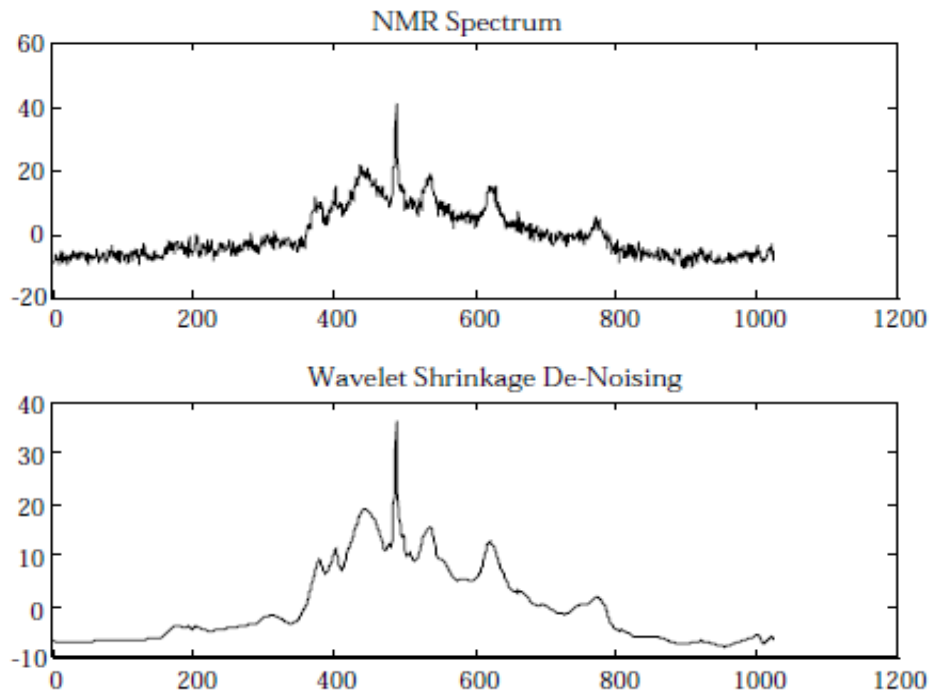


Figure 7.1: ‘Before’ and ‘after’ illustrations of a nuclear magnetic resonance signal. The original signal is at the top and the denoised signal is at the bottom. (Images courtesy David Donoho, Stanford University, NMR data courtesy Adrian Maudsley, VA Medical Center, San Francisco).

wavelet transformation to reconstruct the data set. The signal is transformed, thresholded and inverse-transformed. The technique is a significant step forward in handling noisy data because the denoising is carried out without smoothing out the sharp structures. The result is a cleaned-up signal that still shows important details. Wavelet analysis technique is used in astronomy, acoustics, nuclear engineering, signal and image processing, neurophysiology, magnetic resonance imaging, speech discrimination, optics, fractals, turbulence, human vision, pure mathematics applications such as solving partial differential equations, and many more. For a detail review on the applications of wavelets one can follow the refs. [1–4].

In the present investigation we report some results on the wavelet analysis of the angular distribution of shower tracks coming out of ^{28}Si -Ag/Br interaction at 14.5A GeV and systematically compare them with those obtained from ^{32}S -Ag/Br interaction at 200A GeV [5]. Several works on the wavelet analysis of multiparticle production at $E_{\text{lab}} = 10 - 10^3$ GeV/nucleon have so far been reported [6–11]. However, in this regard there has hardly been any comparison between the experiment and a proper simulation on AB interaction. Hence it is difficult to conclude whether the experimental observations are significant or they are merely consequences of statistical artifacts. Therefore, in both cases the experimental results are compared with the Ultra-relativistic Quantum Molecular Dynamics (UrQMD) model simulation and the UrQMD combined with an additional Bose-Einstein correlation effect (UrQMD+BEC) [see Section 2.5]. Any discrepancy between the experiment and the simulation should now be recognized as a genuine collective behavior of the final state particle emission, that has to be interpreted in terms of some nontrivial dynamics. Thus the present analysis on one hand allows us to compare experiments induced by very close projectile masses while the corresponding E_{lab} values differ by an order of magnitude, on the other it provides an opportunity to compare the experiment with such simulated data where the known dominant source of cluster formation (BEC) is taken into account.

7.2 Methodology

The wavelet method is used to analyze nonstationary as well as inhomogeneous signals that can be any ordered set of numerically recorded information on some processes, objects, functions etc.. A wavelet construction is based on a dilation (a) and a translation (b) parameter. By changing a the local characteristics of a signal are distinguished, while by doing the same with b the whole range of a spectrum can be analyzed. Unlike the Fourier transformation method which uses only two basis functions, the wavelet transformation method can in principle use an infinite set of discrete or continuous functions as the basis. However, a suitable choice of the basic wavelet is made only after looking at the basic features of the signal to be processed. In the present case we use a continuous wavelet

method to find out the strongest fluctuations on an event-by-event basis that may exceed the expected statistical noise at a particular scale and at a particular point of the underlying phase space variable (in this case pseudorapidity η). The wavelet transform of a function $f(x)$ is its decomposition into an orthogonal functional family (Ψ) like

$$W_{\Psi}(a, b) f = \frac{1}{\sqrt{C_{\Psi}}} \int_{-\infty}^{+\infty} f(x) \Psi_{a,b}(x) dx, \quad (7.1)$$

where

$$\Psi_{a,b} \equiv \frac{1}{\sqrt{a}} \Psi \left(\frac{x-b}{a} \right) \quad (7.2)$$

is the mother wavelet characterized by a and b as mentioned above,

$$C_{\Psi} = 2\pi \int_{-\infty}^{+\infty} \frac{|\tilde{\Psi}(\omega)|^2}{|\omega|} d\omega \quad (7.3)$$

is a normalization constant and $\tilde{\Psi}(\omega)$ is the Fourier transform of $\Psi(x)$. Thus, wavelet transforms comprise an infinite set. The different wavelet families make different trade-offs between how compactly the basis functions are localized in space and how smooth they are. There are a lot of wavelet basis functions (family of wavelets) used in reality according to the need. Within each family of wavelets (such as the *Daubechies* family) there are wavelet subclasses distinguished by the number of coefficients and by the level of iteration. Wavelets are classified within a family most often by the number of vanishing moments. There exist an extra set of mathematical relationships for the coefficients that must be satisfied, and they are directly related to the number of coefficients [1]. For example, within the *Coiflet* wavelet family, Coiflets with two vanishing moments and Coiflets with three vanishing moments are found. Even a wavelet basis might be of fractal structure, such as the *Daubechies* wavelet family. In Fig. 7.2 several different wavelet families are illustrated. Derivatives of the Gaussian function

$$\Psi(x) \equiv g_n(x) = (-1)^{n+1} \frac{d^n}{dx^n} e^{-x^2/2} \quad (7.4)$$

are also often used as mother wavelets. In particular the second derivative,

$$g_2(x) = (1 - x^2) e^{-x^2/2} \quad (7.5)$$

popularly known as the Mexican hat (MHAT) wavelet, because of its localized character, is customarily used to analyze multiparticle emission data in η space. In Fig. 7.3 we show the plots of $g_1(x)$ and $g_2(x)$. In the present case the phase space is spanned by the η variables of

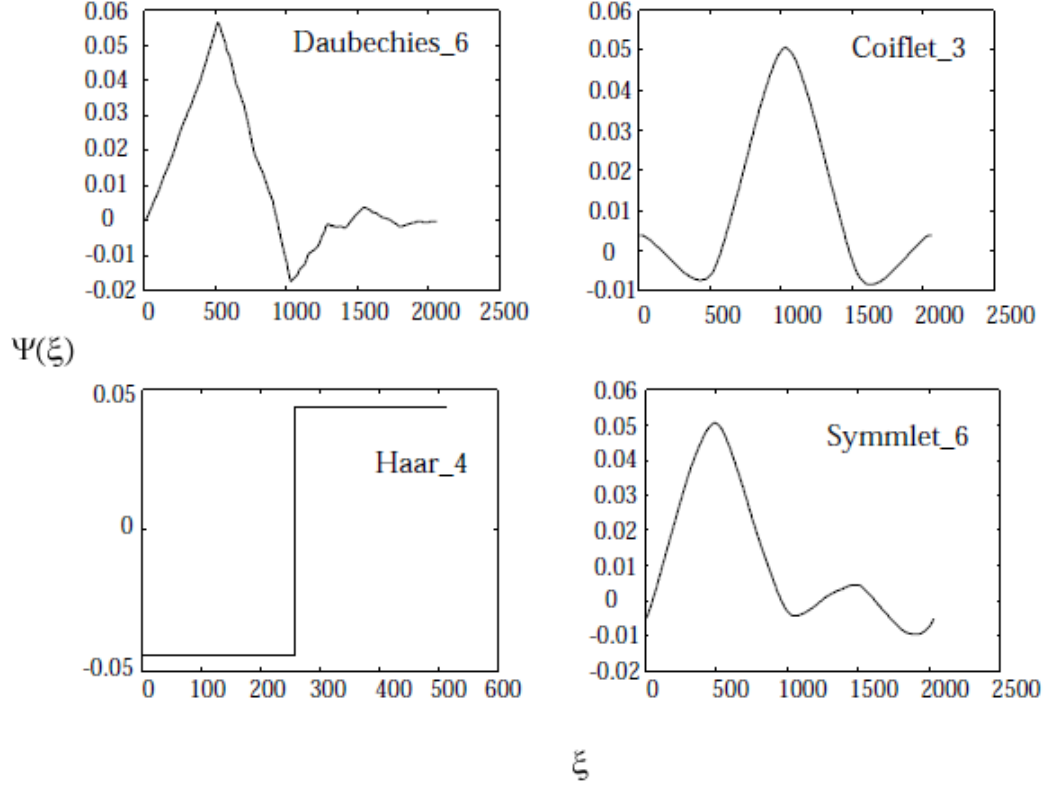


Figure 7.2: Several different families of wavelets. The number next to the wavelet name represents the number of vanishing moments (A stringent mathematical definition related to the number of wavelet coefficients) for the subclass of wavelet.

all the s -particles present in the sample and the signal to be analyzed is the density function

$$f(\eta) = \frac{dn}{d\eta} = \sum_{i=1}^N \delta(\eta - \eta_i), \quad (7.6)$$

where N is the number of shower tracks in the event sample considered, and η_i is the pseudorapidity of the i -th particle. N may either be the n_s value of a single event, or it may be the total number of shower tracks present in the entire event sample/sub-sample within the η interval considered. The wavelet transform of $f(\eta)$ therefore, becomes

$$W_{\Psi}(a, b) f = \frac{1}{N} \sum_{i=1}^N \frac{1}{\sqrt{a}} \Psi\left(\frac{\eta_i - b}{a}\right). \quad (7.7)$$

$W_{\Psi}(a, b)$ is the contribution of $\Psi(a, b)$ to the spectrum $f(\eta)$ in the sense that it represents the probability to find out a particle at some position $b = \eta_i$ at the scale a . A wavelet image at large scale shows only the coarse features, while the same at small a reveals the more detailed and finer structures of the underlying distribution.

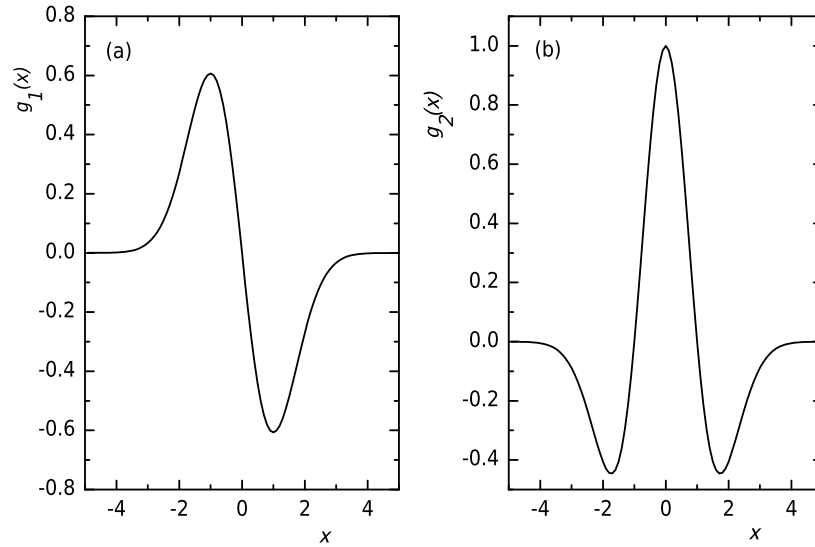


Figure 7.3: (a) First derivative and (b) second derivative (Mexican hat wavelet) of the Gaussian function.

7.3 Results

In Fig. 7.4 we have presented the g_2 pseudorapidity spectra of the shower tracks coming out of all 331 ^{28}Si -Ag/Br events at an incident energy of 14.5A GeV at different scales (four different a values). For comparison, the UrQMD and the UrQMD+BEC predicted graphs are plotted along with those of the experiment. Though the overall multiplicity and the η distributions of the simulated and experimental event samples are identical, we observe that the g_2 spectra of the experiment are quite different from those of the simulations. The fluctuations are more rapid in the experiment. In Fig. 7.4(a) we can see peaks at $b \approx 1.0, 2.0$ and 3.0 in the experimental distribution. These are the preferred η values where particle clusters are formed, and one can relate them respectively, to the target fragmentation, the central particle producing and the projectile fragmentation regions. However, we also notice that the central particle producing peak around $b \approx 2.0$ is well reproduced also by the UrQMD+BEC plot. As expected, with increasing a the fluctuations are smoothed out, and the distributions gradually converge to the mother wavelet g_2 . Needless to say that such plots do not reflect any unique structure of particle distribution in individual events. They would rather correspond to a systematic collective behavior of the particle emission of the entire sample. Similar plots for the entire ^{32}S -Ag/Br event sample at 200A GeV are presented in Fig. 7.5. While the general features of Fig. 7.4 and Fig. 7.5 are more or less similar, we notice that more peaks are present in the ^{32}S -sample than in the ^{28}Si -sample. There are at least 6 prominent peaks within $b \approx 1.0 - 5.0$ in the experiment, out of which two very prominent peaks are lying within the central particle producing region ($b \approx 3.0 - 4.0$), and the simulations cannot replicate them. Even at a large scale $a (= 0.5)$ we find a hump

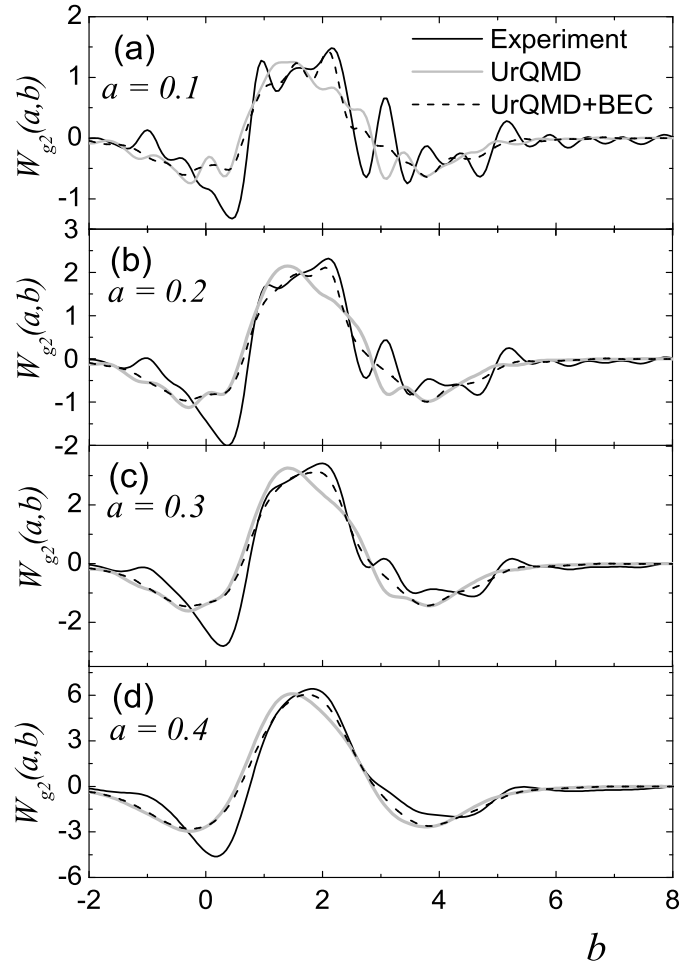


Figure 7.4: g_2 wavelet pseudorapidity spectra in ^{28}Si -Ag/Br interaction at 14.5A GeV for different values of the scale parameter a .

to the left of the peak of the experimental distribution that refuses to be smoothed out, a feature that is absent in the ^{28}Si case. The other peaks, one to the right and three to the left side of the central region, can be related respectively, to the projectile and the target fragmentations.

The wavelet spectra can be generated for individual events at many different scales that can be used to simultaneously study the location and the scale dependence of $W_\Psi(a, b)$. We have obtained such distributions for two high multiplicity events, one for a ^{28}Si -Ag/Br event ($n_s = 146$) and the other for a ^{32}S -Ag/Br one ($n_s = 379$). We have schematically presented the $W_\Psi(a, b)$ distributions respectively, in Fig. 7.6(a) and (b). The dark (white) regions in the graphs correspond to the low (high) values of $W_\Psi(a, b)$. As mentioned before, at the finest scales ($a < 0.05$) we only get information about individual particles, while at large a particles loose their individual identities to coalesce into a big cluster. It is therefore, pointless to study an event under either of these two extreme but trivial scales. We see that in both diagrams several small and large clusters are present at $a > 0.1$. Looking at the

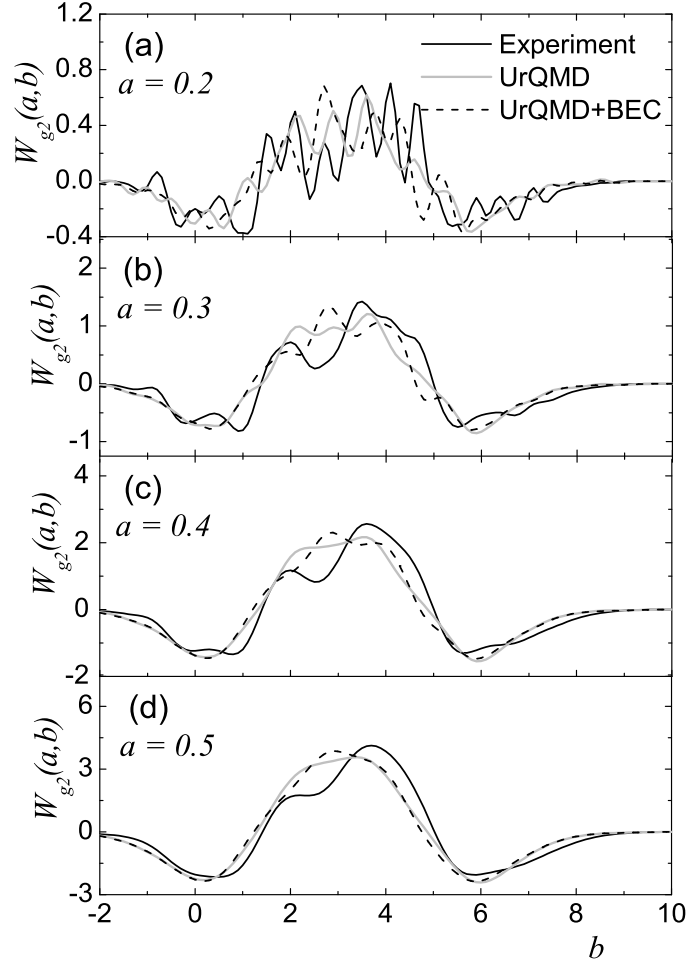


Figure 7.5: g_2 wavelet pseudorapidity spectra in ^{32}S -Ag/Br interaction at 200A GeV for different values of the scale parameter a .

^{28}Si -Ag/Br diagram we recognize that two large groups of particles are present, one centered around $\eta \approx 0.7$ and the other around $\eta \approx 1.4$. Similarly in the ^{32}S -Ag/Br diagram again there are two large groups, one at $\eta \approx 3.0$ and the other at $\eta \approx 4.6$. Beside them several other smaller groups of particles are present, all belonging to the fragmentation regions.

Identification of the peculiarities in particle distribution in individual events from the two-dimensional energy spectrum $\{W_\Psi(a, b)\}^2$ is a difficult proposition. Instead we may concentrate on the scalogram $E_W(a)$ defined as

$$E_W(a) = \int \{W_\Psi(a, b)\}^2 db, \quad (7.8)$$

which represents the one-dimensional energy distribution with respect to the scale a . A scalogram reflects some of the characteristic features of an event. As for example, a minimum on it represents the average distance between the particle clusters, while a maximum represents the most compact group of particles present in the event. Two such scalograms,

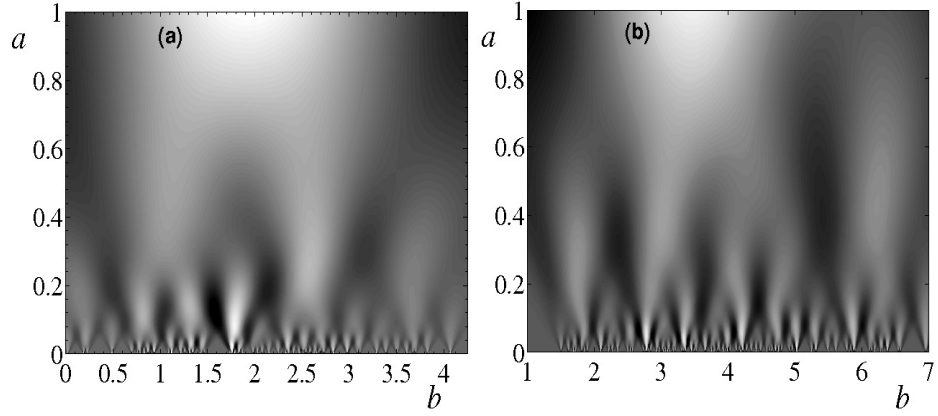


Figure 7.6: Wavelet pseudorapidity spectra for a high-multiplicity event in (a) $^{28}\text{Si-Ag/Br}$ interaction at 14.5A GeV and (b) $^{32}\text{S-Ag/Br}$ interaction at 200A GeV, the event multiplicities are respectively 146 and 379.

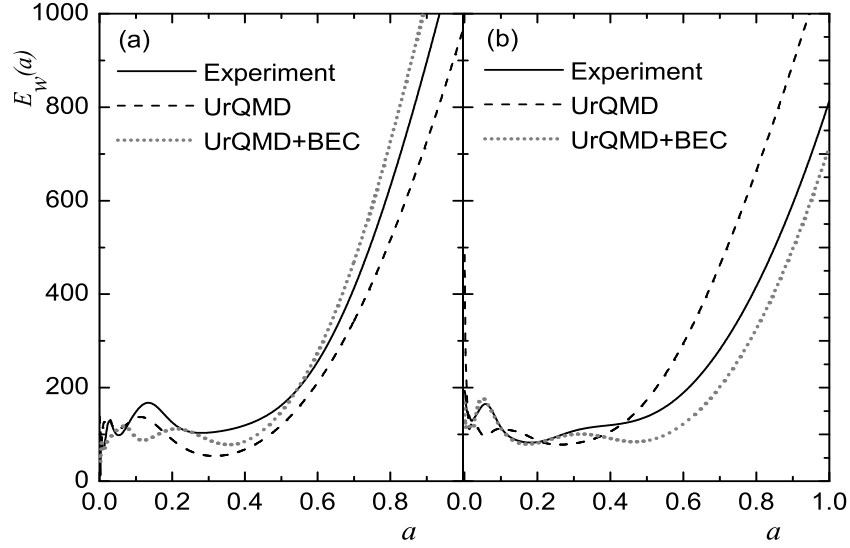


Figure 7.7: Scalograms of the events for which the wavelet pseudorapidity spectra are shown in Fig. 7.6.

one for the $^{28}\text{Si-Ag/Br}$ event and the other for the $^{32}\text{S-Ag/Br}$ event considered above, are shown in Fig. 7.7. In each diagram a peak or a small rise seen at the lowest scale that represents individual particles, and they are of little significance. In the scalogram of the $^{28}\text{Si-Ag/Br}$ event a local peak at $a \approx 0.2$ and a minimum at $a \approx 0.3$ are seen. On the other hand, in the $^{32}\text{S-Ag/Br}$ event there are a couple of local maxima and minima. The maxima are located at $a \approx 0.1$ and 0.2 , while the minima are located at $a \approx 0.15$ and 0.35 . The simulation, either with or without BEC, fails to reproduce the experiment at the significant scales. It is now amply clear that the scales and the η values at which the clusters are formed will vary from one event to the other. Most of the local maxima (minima) are found within $a \approx 0.1-0.5$, and in most of the events only a few such maxima (minima) are found. To check

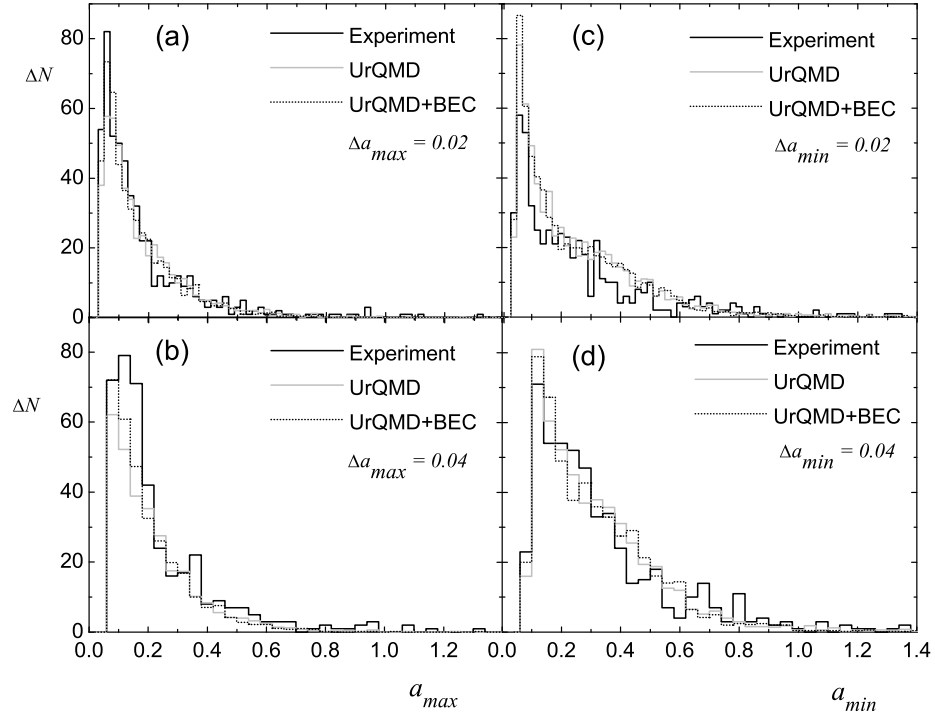


Figure 7.8: Distributions of the local maxima (left panel) and minima (right panel) of the scalograms in $^{28}\text{Si-Ag/Br}$ interaction at 14.5A GeV.

whether there exists any systematic behavior of particle emission, or the clusters formation occurs at random, we investigate the distributions of the extremum points over our entire event sample(s). In Fig. 7.8 we plot the frequency distribution of the scales a_{\max} and a_{\min} at which respectively, the maxima and the minima of the scalograms belonging to individual $^{28}\text{Si-Ag/Br}$ events are graphically seen. The experiments as usual are plotted together with the simulations. Except in Fig. 7.8(b), where the experiment slightly exceeds the simulation at the characteristic scale of $a_{\max} \approx 0.2$, no significant difference between experiment and simulation is observed. In Fig. 7.9 similar histograms for the $^{32}\text{S-Ag/Br}$ events are plotted. In this case also no significant difference between the experiment and the corresponding simulation is seen.

The wavelet analysis is not complete unless we study the distributions of the locations (b), where the local maxima in $W_{\Psi}(a_{\max}, b_{\max})$ are observed. We do this with different choices of scale intervals, cumulative as well as differential. In Fig. 7.10 such distributions for the $^{28}\text{Si-Ag/Br}$ sample (both experiment and simulation) are graphically presented at different cumulative scale windows. The common features of these diagrams are that, at the lowest a_{\max} range the distributions are rapidly fluctuating, and as expected with increasing scale window size the fluctuations get reduced. In comparison with the experiment the UrQMD distributions vary more smoothly. However, when the BEC is incorporated into the UrQMD, to some extent the fluctuating patterns are retrieved. The $^{32}\text{S-Ag/Br}$ sample on the other

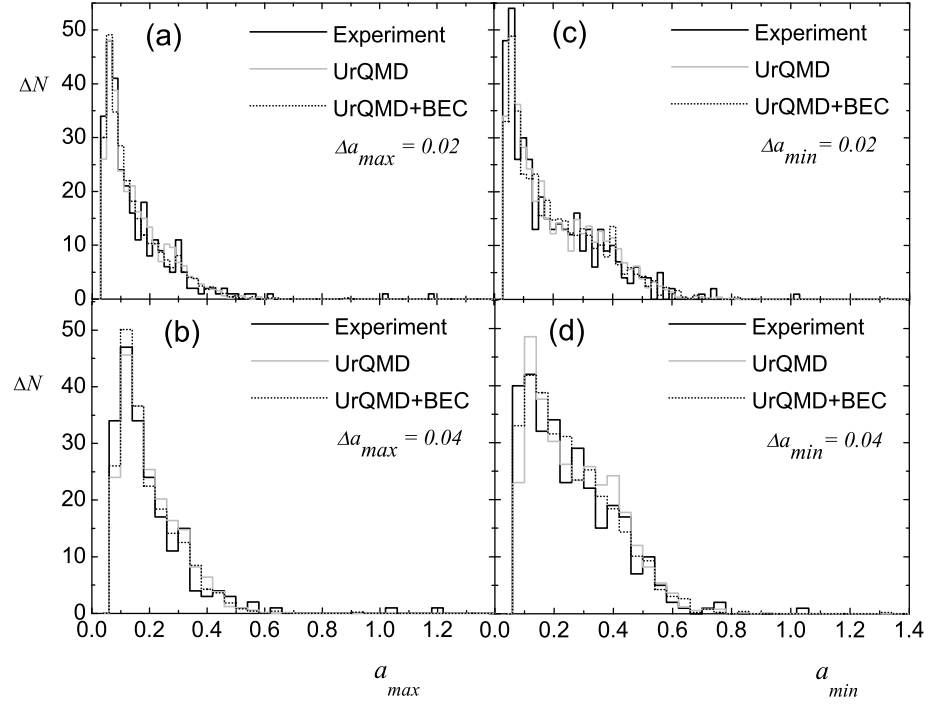


Figure 7.9: Same as Fig. 7.8 but in ^{32}S -Ag/Br interaction at 200A GeV.

hand, behaves a little differently. The distributions are shown in Fig. 7.11. In this case the experimental distribution is still more rapidly fluctuating than both the UrQMD and the UrQMD+BEC plots. It seems that incorporating BEC into UrQMD apparently has little effect in the respective distributions. In Fig. 7.12 and 7.13 the b_{max} distributions respectively, for the ^{28}Si -Ag/Br and ^{32}S -Ag/Br samples are once again graphically shown, where we choose differential scale intervals to draw the histograms. For both sets of data the basic features are more or less same. As expected at the smallest scale window $0.05 \leq a_{\text{max}} \leq 0.1$ most rapid fluctuations are seen, which are systematically smoothed out with increasing a_{max} . The distributions for the ^{32}S -Ag/Br interaction are slightly wider than those for the ^{28}Si -Ag/Br interaction. It seems that the inclusion of BEC into the UrQMD in both interactions increases the heights of the local peaks to a small extent.

7.4 Discussion

Pseudorapidity distributions of singly charged particles coming out of ^{28}Si -Ag/Br and ^{32}S -Ag/Br interactions, respectively at incident energies of 14.5A GeV and 200A GeV, are analyzed by using the continuous wavelet transform technique. Compared to similar other such emulsion investigations [8–11], the target nuclei in the present case have less uncertainties. For background noise elimination the experiments are compared with a set of ordinary

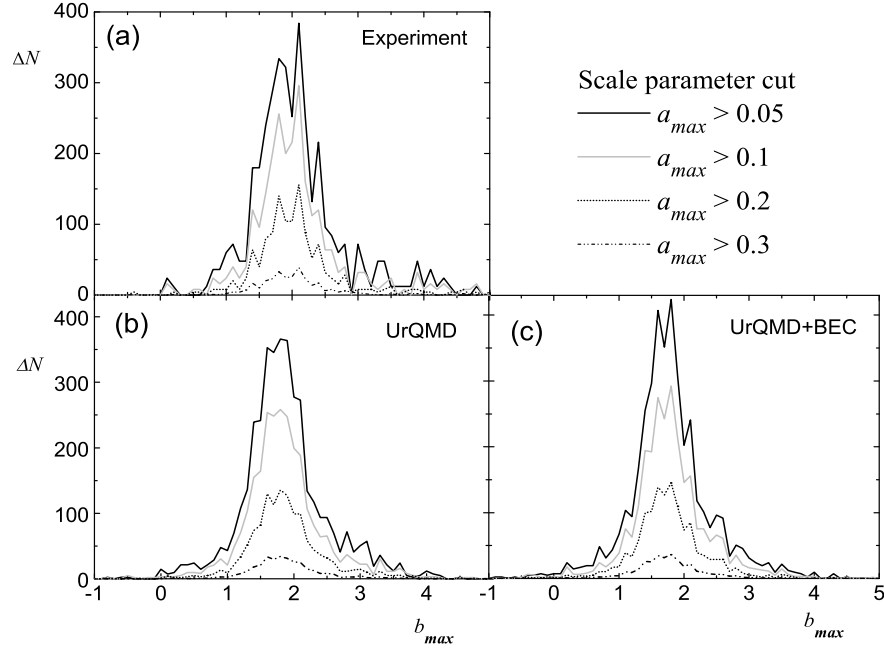


Figure 7.10: b_{\max} distributions for different limiting values of a_{\max} in ^{28}Si -Ag/Br interaction at 14.5A GeV. The distribution plots are so shifted as to avoid mutual overlapping.

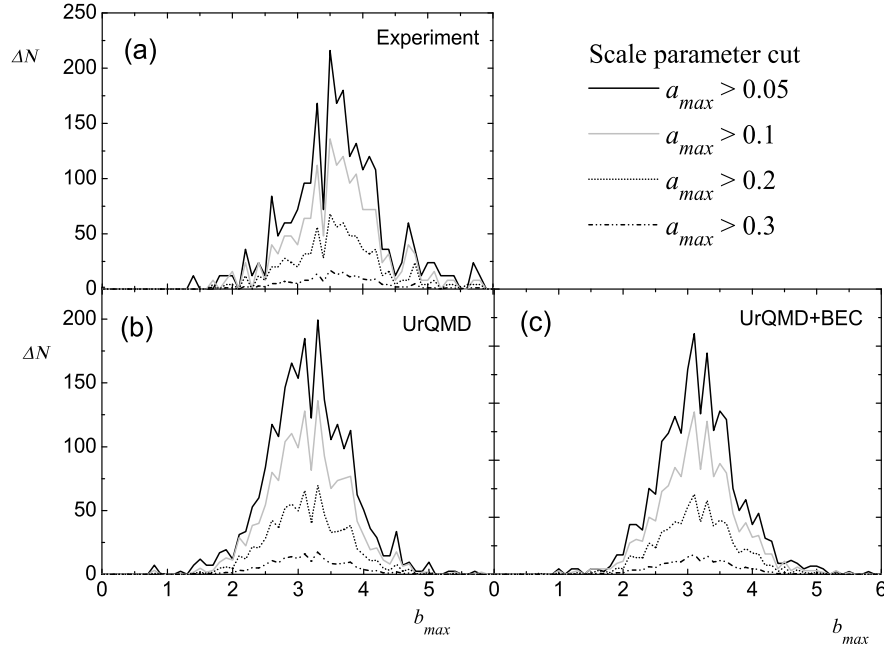


Figure 7.11: Same as Fig. 7.10 but in ^{32}S -Ag/Br interaction at 200A GeV.

UrQMD simulated data, and also with the same set of UrQMD output that is modified by a mimicry of the Bose-Einstein type of correlation. The observed discrepancies between the experiment and the corresponding simulation should therefore, result from nontrivial dynamics like collective flow of hadronic matter. Irregularities in the wavelet pseudorapidity spectra are observed in individual AB events as well, and the cluster characteristics are not reproducible by the simulations. As far as a systematic behavior in many events is

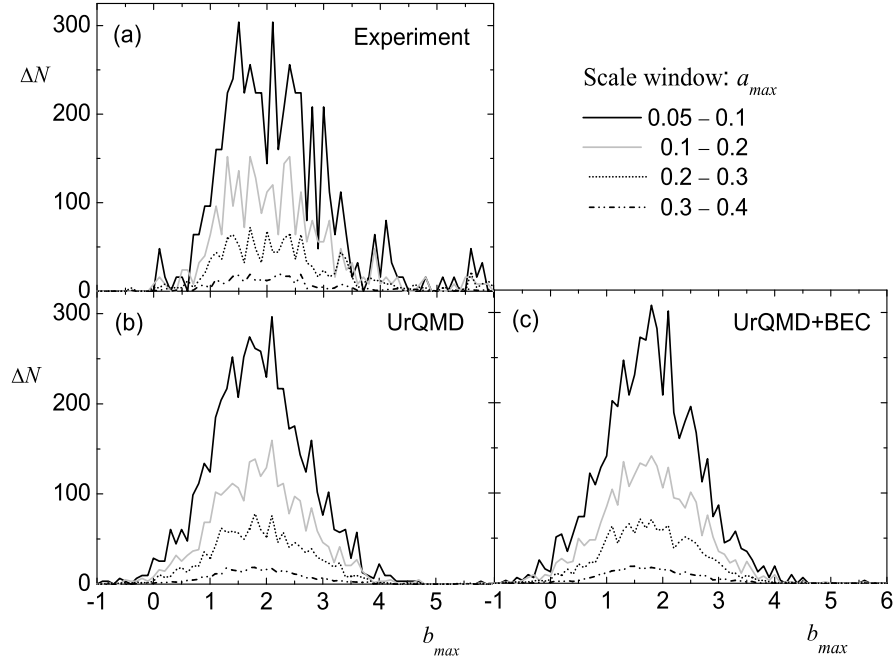


Figure 7.12: b_{\max} distributions for different scale windows in ^{28}Si -Ag/Br interaction at 14.5A GeV. The distributions plots are so shifted as to avoid mutual overlapping.

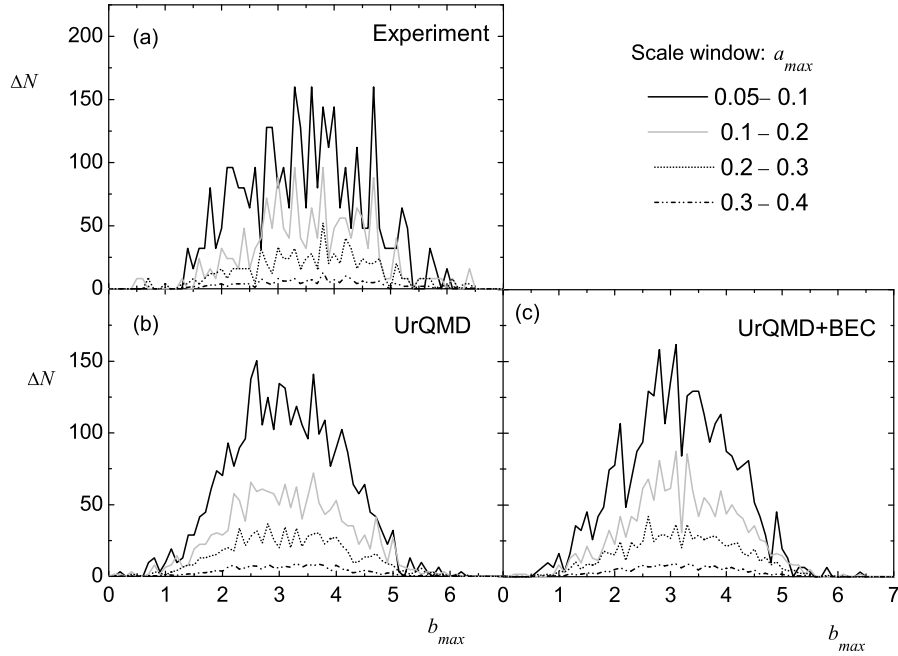


Figure 7.13: Same as Fig. 7.12 but in ^{32}S -Ag/Br interaction at 200A GeV.

concerned, we observed certain difference between experiment and simulation in the ^{28}Si event sample under consideration. The differences with all probability are not a result of ordinary correlations among identical bosons. They should be interpreted in terms of certain nontrivial dynamical reason(s), that is (are) not very much clear from the present analysis. The present study can be extended to the azimuthal angle distribution of shower tracks,

to the 2-dimensional wavelet analysis [12], and with larger statistics to examine the impact parameter dependence of the observed irregularities.

Bibliography

- [1] R. Crandall, *Projects in Scientific Computation* (Springer-Verlag, New York, 1994).
- [2] D. Donoho, *Nonlinear Wavelet Methods for Recovery of Signals, Densities, and Spectra from Indirect and Noisy Data, Different Perspectives on Wavelets*, Proceeding of Symposia in Applied Mathematics, Vol 47, Ed. I. Daubechies, *American Mathematical Society* (Providence, 1993).
- [3] C. K. Chui, *An Introduction to Wavelets* (Academic press, 1992).
- [4] I. Daubechies, *Ten Lectures on Wavelets* (Society for Industrial and Applied Mathematics, Philadelphia, Pennsylvania, 1992).
- [5] P. Mali, *et al.*, *Adv. High Eng. Phys.* **2013**, 759176 (2013).
- [6] N. Suzuki, M. Biyajima and A. Ohsawa, *Prog. Theor. Phys.* **94**, 91 (1995).
- [7] D. Huang, *Phys. Rev.* **D 57**, 3961 (1997).
- [8] I. M. Dremin *et al.*, *Phys. Lett.* **B 499**, 97 (2001).
- [9] V. V. Uzhinsky *et al.*, *Phys. Atom. Nucl.* **67**, 156 (2004).
- [10] J. Fedorišin and S. Vokál, E1-2007-4, JINR Dubna; E1-2007-66, JINR Dubna (2007).
- [11] J. Fedorišin, S. Vokál, *FIZIKA* **B 17**(2), 273 (2008).
- [12] N. M. Astafyeva, I. M. Dremin, K. A. Kotelnikov, *Mod. Phys. Lett.* **A 12**, 1185 (1997).

Concluding Remarks

This thesis is based on some statistical analysis of local density fluctuation and cluster formation of charged particles produced in high-energy nucleus-nucleus interaction(s). Experimental data on angular distribution of shower tracks coming out of $^{28}\text{Si-Ag/Br}$ interaction at an incident energy in the laboratory system $E_{\text{lab}} = 14.5\text{A GeV}$ are used. To understand the mechanism of multiparticle production we systematically compare the experimental results with those obtained from event samples simulated by a microscopic transport model namely the Ultra-relativistic Quantum Molecular Dynamics (UrQMD). For the first time in the history of AB collision, we have also implemented a charge reassignment algorithm that mimics the Bose-Einstein correlation (BEC) to the UrQMD output in the form of an after burner. It has to be however remembered that a real BEC can be incorporated into any model only by appropriately symmetrizing the underlying bosonic fields, which is an extremely difficult task. On more than one occasion our $^{28}\text{Si-Ag/Br}$ results are compared with $^{32}\text{S-Ag/Br}$ results at $E_{\text{lab}} = 200\text{A GeV}$, allowing thereby to examine the effect of different collision energies on colliding systems of more or less same geometrical size. Though at the end of each chapter a section is devoted to discuss the results obtained from a particular method of analysis, we thought that to conclude it would be prudent to summarize the major observations of the present investigation together, and put each of them under a close scrutiny. We are aware that multiparticle production is a soft hadronic process and pertains to very late stages of any high-energy AB collision. Therefore, only by using statistical tools it would be too ambitious a project to probe into the more interesting early evolutionary and/or thermodynamically equilibrated stages of the ‘fireball’. Nevertheless, multiparticle production mechanism itself is a complex dynamical process that should be examined from different perspectives through a colliding system and/or collision energy scan.

First of all we observe that the total $^{28}\text{Si-Ag/Br}$ interaction cross-section at $E_{\text{lab}} = 14.5\text{A GeV}$ incident energy, is consistent with the prediction of a simple participant – spectator model. In this regard a small mismatch between the theoretical estimation and experimental observation can be attributed to personal errors, an aspect inherent to any emulsion experiment. As we have with us only a subsample of $^{28}\text{Si-Ag/Br}$ events and not the entire

minimum bias sample, we have not presented any multiplicity distribution in the thesis. In emulsion experiments the criterion of selecting Ag/Br events ($n_h > 8$) excludes a significant fraction of Ag/Br events. The pseudorapidity distribution of the shower tracks (caused by produced charged mesons moving at relativistic speed) can be approximated by a Gaussian distribution. Corresponding UrQMD generated distribution also possesses this Gaussian nature, though there is a small overall shift between the centroids of the two distributions. The Bjorken's energy density, determined from the central pseudorapidity density of a sub-sample of high multiplicity $^{28}\text{Si-Ag/Br}$ events ($n_s > 50$) is very close to the LQCD estimated value (\sim a few GeV/fm^3) needed to augment the transition from a color neutral hadronic state to a color conducting extended QCD state. However, the single Gaussian description of the pseudorapidity distribution(s) is(are) compatible to significant stopping of the projectile by the target, as expected at such collision energies ($E_{\text{lab}} = 14.5\text{A GeV}$). Therefore, the fireball created in $^{28}\text{Si-Ag/Br}$ collision must be rich in baryon number. The experimental azimuthal angle distribution of shower tracks on the other hand is significantly different from the UrQMD generated one. The azimuthal asymmetry observed in the experimental distribution, can perhaps be attributed to a combination of two effects, (i) some dynamical effect – a collective behavior of shower track emission during the collision process, and (ii) experimental deficiency – small efficiency to detect shower tracks that are moving exactly towards or away from the observer's eyes.

Single particle density distribution of shower tracks in high multiplicity $^{28}\text{Si-Ag/Br}$ events exhibit random fluctuations consisting of sharp peaks and deep valleys. Using the technique of scaled factorial moments (SFM) we could characterize these fluctuations, apparently devoid of any regular pattern, in terms of a finite set of regularly behaving parameters. The SFM can by definition suppress any Poisson distributed statistical background (noise) present in the data. We could identify that the unusually large particle density values, irrespective of their exact analytic form, possess a dynamical component, which with decreasing phase space resolution size (δX) asymptotically approaches a singularity obeying a scale invariant power-law. The UrQMD generated sample does not exhibit any such behavior, i.e. no significant change in the SFM values with phase space resolution size. Even inclusion of BEC in the UrQMD output can only partially recover the power-law type of scaling in simulated data, and that too in the two dimensional analysis. Therefore, certain amount of correlated emission must be present in the experiment which is beyond the known sources of correlation like BEC. In the framework of a simple intermittency model (α model), we observe that within errors intermittency in the $^{28}\text{Si-Ag/Br}$ case is almost as strong as it is in the $^{32}\text{S-Ag/Br}$ case, and slightly stronger in $^{16}\text{O-Ag/Br}$ interaction at $E_{\text{lab}} = 200\text{A GeV}$. Therefore, within the energy range $E_{\text{lab}} \sim 10 - 100\text{A GeV}$, the size of the colliding objects has perhaps a greater influence on the intermittency strength than the collision energy involved. We also observe that in all interactions the intermittency effect in the

azimuthal plane is consistently stronger than that on the pseudorapidity axis. This may be an outcome of the kinematic conservation laws (before collision such transverse degrees of freedom were absent), or a more complicated hitherto unknown dynamical reason. There is a definite indication of non-thermal phase transition in the intermittency pattern in the azimuthal plane. Another important observation is that, while the power-law type of scaling is self similar down to the experimental resolution in one dimension, it is self-affine in two dimension. In $(\eta - \varphi)$ plane) self-similarity is retrieved only when independent phase space directions are partitioned differently by invoking an appropriate ‘roughness’ parameter (H). Two-dimensional intermittency is always stronger than one-dimensional intermittency.

The intermittency technique not only enables us to characterize the local particle densities belonging to a particular bin, but it also allows us to examine the bin-to-bin correlations in terms of the two fold SFM or factorial correlators. Our experimental results in this regard, namely the scaling-laws and sum rules etc., are in conformity with the α -model, and are indicative of short range correlation. UrQMD predictions, even after being supplemented by the BEC, fall short of the experiment. The correlation that we find in these analysis originates mainly from two or three particle correlation, while presence of genuine higher order correlations (of order more than three) are seldom statistically significant. We have also examined the event space fluctuation of the SFM called the erraticity analysis. In the SFM distribution we notice that while most of the single event SFM values are restricted within a small interval, some events have really high SFM values. It is speculated that this kind of event space fluctuation of SFM is chaotic in nature, and should be characterized in terms of a new set of moments called the erraticity moments. We found that the erraticity moments in $^{28}\text{Si-Ag/Br}$ interaction at $E_{\text{lab}} = 14.5\text{A GeV}$ abide by appropriate scaling-law, and the corresponding erraticity parameters also behave as expected. Small difference between the experiment and simulation do exist, and the $^{28}\text{Si-Ag/Br}$ results are qualitatively similar to the $^{32}\text{S-Ag/Br}$ or $^{16}\text{O-Ag/Br}$ results reported earlier.

The self-similar nature of dynamical fluctuation as observed in our intermittency analysis, has inspired us to extend the scope of our investigation to the domain of fractals. Using several statistical techniques we have observed that the shower track distribution both in the experiment and in the simulation(s) are multifractal in nature. The methods of detrended multifractal analysis have so far not been very widely used for AB experiments. As far as multifractal patterns are concerned, on most of the occasions there is hardly any difference between the experiment and the corresponding simulation. There may be more than one reason behind this kind of apparent anomaly between the intermittency results which show some degree of correlated emission in the experiment, and the multifractality results which to a large extent agrees with the uncorrelated UrQMD data. One reason may be that the techniques of multifractal analysis adopted are not very sensitive to correlated emission. The

second reason may be that in multifractal analysis there is no robust technique of eliminating the statistical noise from the data. Only when we take into account the random number generated mass exponent τ_q^{sta} , the (multi)fractal parameter $(q-1-\tau_q)$ drops down very close to its equivalent quantity, the intermittency exponent (ϕ_q) . The third reason may be that the fractal nature of a distribution should actually be examined under the limiting condition $\delta X \rightarrow 0$, which because of the finite event multiplicity cannot in practice be achieved in any real experiment. Notwithstanding these shortcomings it is worthy to mention that there are statistically significant differences in the multifractal singularity spectra and in the generalized dimension values, obtained from the experiment and generated by the simulation. The experimental singularity spectrum is always wider than the simulated one, while the experimentally obtained generalized dimensions change with the order of the (multi)fractal moments and are always smaller than the corresponding UrQMD simulated values. The simulated generalized dimensions also do not always change significantly with its order, and they are closer to the topological dimension of the supporting space.

We have also tried to find out unusual structures in the azimuthal distribution (if there is any) of shower tracks coming out of $^{28}\text{Si-Ag/Br}$ events at $E_{\text{lab}} = 14.5\text{A GeV}$, compared the results with those of $^{32}\text{S-Ag/Br}$ events at $E_{\text{lab}} = 200\text{A GeV}$ as well as with the BEC supplemented UrQMD and RQMD generated events. Except for observing strong correlation(s) in the central particle producing region and occasional formation of jet-like structures, nothing very unusual was found from this analysis. The difference(s) between experiment(s) and simulation(s) is/are often very small. Once again the methodology itself does not allow us to be very conclusive about the probable mechanism(s) of formation of such unusual azimuthal structure(s). Our wavelet analysis of $^{28}\text{Si-Ag/Br}$ and $^{32}\text{S-Ag/Br}$ data once again shows that clusters of particles are formed at different locations on the pseudorapidity axis and at different scales of resolution. The wavelet technique has also not so far been used in many AB experiments, and probably there has so far not been any comparison with any simulated result. The experiments differ from the corresponding UrQMD or UrQMD+BEC predictions. Therefore, with all probability the clusters result from some nontrivial dynamics other than the BEC. As per a norm of our university, at the end we have attached the reprint of one of our published papers on collective flow analysis on $^{28}\text{Si-Ag/Br}$ interaction at $E_{\text{lab}} = 14.5\text{A GeV}$, measured the flow angles and flow parameters, and compared the results with those obtained from $^{84}\text{Kr-Ag/Br}$ interaction at $E_{\text{lab}} = 1.52\text{A GeV}$. Though collective emission of particles is present in both cases the Kr-induced experiment behave in a more systematic manner, and the present results are consistent with those obtained from previous such similar experiments.

The thesis contains some new results on multiparticle emission data obtained from some conventional as well as some not so frequently used statistical tools. An effort however

small it may be, has been made even to modify the simulation technique employed. In view of the upcoming CBM experiment to be held at FAIR, GSI, Germany, designed to study baryon rich ‘fireballs’ produced in AB collisions, in near future these results may eventually come out to be more than useful. In spite the best of our intentions there is no denial that several physics outputs of the present investigation could be put forward only in the form of conjectures. If it were not for the constraint imposed by limited statistics and experimental technique, we could have been more confident and more specific about our conclusions, e.g. by studying the centrality dependence and/or the dependence on the number of binary NN collisions involved in AB collision. As a final statement, one may say that with the advent of new and more sophisticated detecting devices the days of nuclear emulsion technique as an effective tool of experimental nuclear/particle physics research may be numbered, but there are still some scopes of using this age old technique where event statistics is not a very important factor, but direct observation and spatial resolution are.